Bulletin 42
(Part 3 of 5 Parts)

THE SHOCK AND VIBRATION BULLETIN

Part 3
Test Control, Facilities, Techniques

JANUARY 1972

A Publication of
THE SHOCK AND VIBRATION
INFORMATION CENTER
Naval Research Laboratory, Washington, D.C.

Office of
The Director of Defense
Research and Engineering

219

SYMPOSIUM MANAGEMENT

THE SHOCK AND VIBRATION INFORMATION CENTER

William W. Mutch, Director
Henry C. Pusey, Coordinator
Rudolph H. Volin, Coordinator
Edward H. Schell, Coordinator

Bulletin Production

Graphic Arts Branch, Technical Information Division,
Naval Research Laboratory

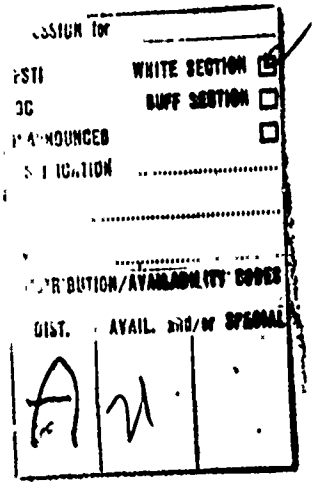

$ 40, the set

Bulletin 42
(Part 3 of 5 Parts)

THE SHOCK AND VIBRATION BULLETIN

JANUARY 1972

A Publication of
THE SHOCK AND VIBRATION
INFORMATION CENTER
Naval Research Laboratory, Washington, D.C.

The 42nd Symposium on Shock and Vibration was held at the U.S. Naval Station, Key West, Florida, on 2-4 November 1971. The U.S. Navy was host.

Office of
The Director of Defense
Research and Engineering

CONTENTS

PAPERS APPEARING IN PART 3

Test Control

Test Facilities and Techniques

PAPERS APPEARING IN PART 1

Invited Papers

Specifications

Measurement and Application of Mechanical Impedance

Transportation and Packaging

PAPERS APPEARING IN PART 2

Ground Motion

Dynamic Analysis

PAPERS APPEARING IN PART 4

Isolation and Damping

Prediction and Experimental Techniques

PAPERS APPEARING IN PART 5

Shock and Vibration Analysis

Structural Analysis

Ship's Problems

TEST CONTROL

ON THE PERFORMANCE OF TDM AVERAGERS IN RANDOM VIBRATION TESTS

Allen J. Curtis
Hughes Aircraft Company
Culver City, California

During random vibration tests in which average control is employed, the averaging device should synthesize a signal whose spectral density is equal to the mean of the spectral densities of the individual control accelerometer signals, i.e., the power average. The most commonly used averaging device is a Time-Division-Multiplexer (TDM) which looks sequentially at each control signal for equal time periods of approximately 100 msecs. Usher has examined mathematically the extent to which the spectral characteristics of the TDM signal vary from those desired. It is believed that the full implications of his analyses for typical laboratory testing are not generally appreciated. This paper provides data to demonstrate the TDM performance to be expected during such testing.

Four factors which influence the performance of the TDM are discussed. The first is the relative phase or polarity of the several inputs to the TDM. The last three, which are very interdependent, are: the relative magnitudes of the several input spectral densities within any control or analysis bandwidth; the type of detection employed to measure the spectral density; the response time and bandwidth of the filters used to analyze the TDM output signal.

It is shown that polarity changes can cause significant (>5 db) over and/or under test due to spectral spreading of peaks and notches. The use of average detection during processing of the TDM signal is analyzed and may often contribute an overtest of at least 3 db. However, compensating errors due to response time of typical filters will tend to counterbalance this error. The virtual elimination of these errors with the use of meansquare detection is demonstrated.

The performance of the TDM during a number of laboratory tests has been analyzed and is shown to be generally satisfactory. Methods to optimize test accuracy during TDM usage are delineated.

INTRODUCTION

During the last several years, it has become almost standard practice to control the spectral density level of random vibration tests to the average of the spectral densities of several control accelerometer signals. This is done whenever significant differences in level, within a particular equalization bandwidth, are expected between several attachment points of the test item to the fixture. The purpose of averaging is to avoid the severe over- and under-testing which can occur at resonances and anti-resonances of a single control point. Averaging can also be used when it is desired to bias the test level as a function of frequency, to account for the attenuation of high frequency excitation with distance from the excitation point.

To use average control, an averaging device is required. This device should

synthesize a signal whose spectral density is equal to the mean (or average) of the spectral densities of the individual control accelerometer signals, i.e., the power average. The most commonly used averaging device is a Time-Division-Multiplexer (TDM) which looks sequentially at each control signal for equal time periods of approximately 100 msec. Usher, (Ref. 1) has examined mathematically the extent to which the spectral characteristics of the TDM signal vary from those desired. It is believed that the full implications of his analyses for typical laboratory testing are not generally appreciated. This paper provides information, mainly empirical, to demonstrate the TDM performance to be expected during such testing based on test data accumulated in the author's laboratory.

The degradation of performance of the TDM, for this paper, is measured by the deviation from unity (either real or apparent) of the ratio of the spectral density of the TDM output signal to the power average of the input spectral densities, i.e., the TDM/Power Average ratio.

Four factors which influence the performance of the TDM are discussed. The first, which is of significance primarily in the low end of the frequency spectrum, concerns the relative phase, or polarity, of the several input signals to the TDM. The last three, while of significance at all frequencies, are most significant at the high end of the spectrum. Without attempting to rank them in importance, these factors are: the relative magnitudes of the several input spectral densities within any control or analysis bandwidth; the type of detection employed to measure the spectral density; the response time and bandwidth of filters used to analyze the TDM output signal.

EFFECTS OF SIGNAL POLARITY

As Usher has shown, the spectral density of the TDM output is a complex function of the spectral densities of the individual input signals and the cross spectral densities between them. To indicate the effects of signal polarity, i.e., a relative phase shift of 180°, he considers the TDM output spectral density when the same narrowband (50 Hz) random signal is applied to two channels of the TDM except the polarity of one signal is inverted. It is shown that significant spectral spreading occurs as the product of the gating time of the TDM and the bandwidth of the narrowband signal decreases.

The cause of this spreading is essentially the discontinuity of the signal which occurs each time the TDM switches to the next channel. Figures 1 and 2 illustrate this phenomenon. In

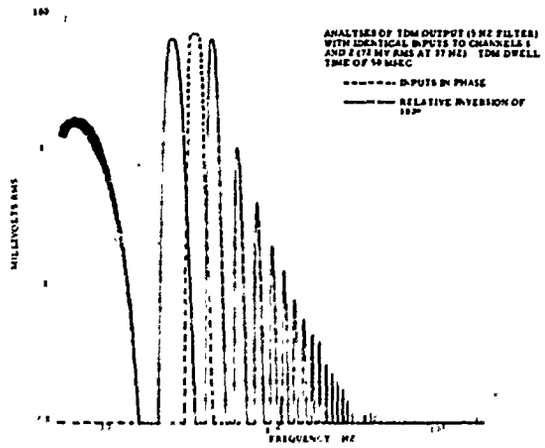

Fig. 1 - Spectral spreading of 37 Hz sinusoid with 50 msec gating time

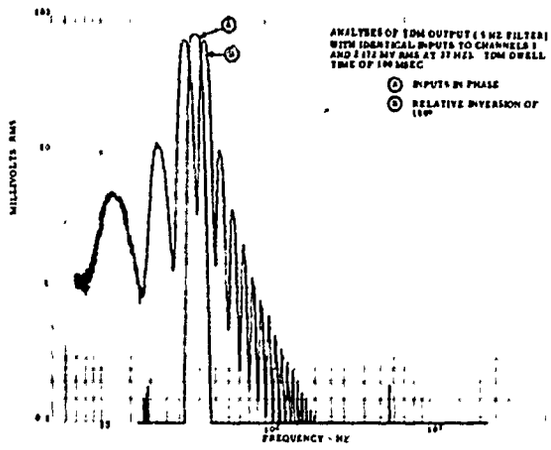

Fig. 2 - Spectral spreading of 37 Hz sinusoid with 100 msec gating time

each case, a 37 Hz sinusoid was applied to two channels of the TDM and a spectral analysis of the TDM output performed, using a 5 Hz filter. This was performed with the signals to each channel in phase and also with the signals 180° out of phase, i.e., with the polarity changed. Figure 1 displays the results for a gating time of 50 msec while Figure 2 is for a gating time of 100 msec. The spectral spreading due to the polarity change is evident in each figure and the greater spreading for the smaller gating time is readily observed. While it is recognized that the TDM is not used in

this unsynchronized manner for sinusoidal tests, these figures do illustrate the effects of polarity change which may occur in random tests and also in sinusoidal tests using fundamental control.

These effects were observed in the laboratory during a random vibration test of a small vibration isolated unit mounted in a rigid fixture on a slip plate. Four control accelerometers were mounted to the fixture. It happened that two pointed in one direction, say North, while the other two pointed South, which effectively created a 180° phase shift between the two pairs of signals. It also happened that these signals were connected to the TDM in a North-South-North-South order.

The spectral densities of the four individual accelerometer signals, obtained from a 10% constant percentage bandwidth analyzer, are plotted in Figure 3. Figure 4 presents a

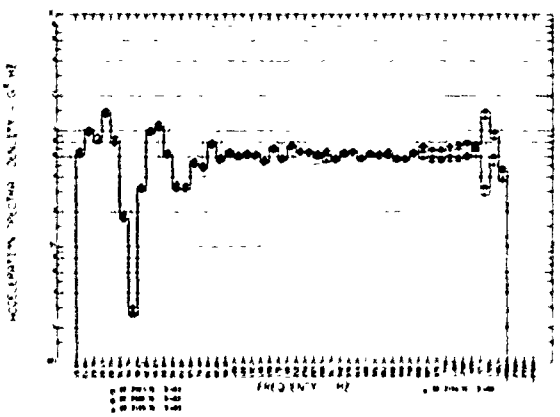

Fig. 3 - Spectral densities of four control accelerometer signals

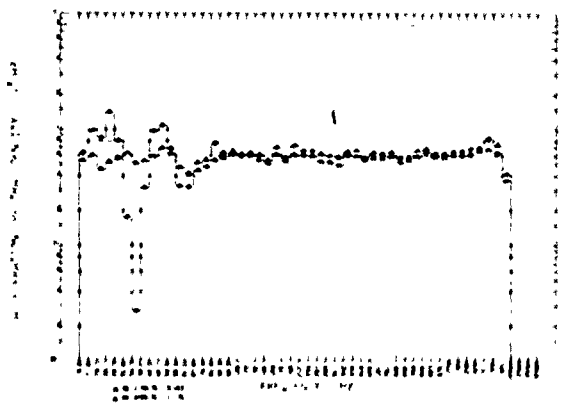

Fig. 4 - Power average and TDM output spectral densities – polarity inverted signals with notch

comparison of the spectral density of the TDM output and the Power Average of the accelerometer signals, computed from Figure 3. The filling in of the notch at approximately 36 Hz, analogous to the spreading of a peak, is evident.

The tape-recorded accelerometer signals were then played back into the TDM after electrically inverting two of the signals so that all four were in phase. A comparison of the spectral density of the TDM output and the Power Average is shown in Figure 5, indicating that if no polarity change had existed, the TDM output spectral density would be as desired.

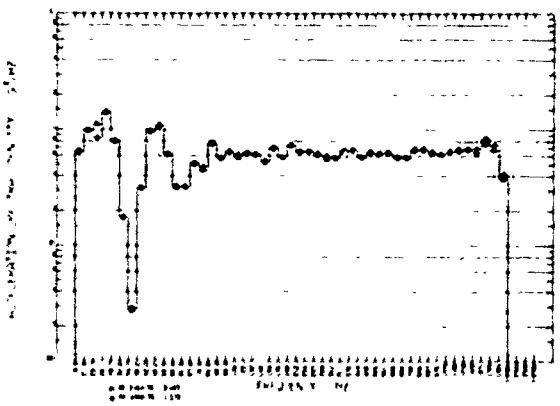

Fig. 5 - Power average and TDM output spectral densities – polarity inversion removed

It should be noted that the notch in these figures was created by the loading down of the shaker at the resonant frequency of the isolated mass. The masking of this notch due to the polarity shift caused an undertest within this resonant bandwidth of as much as 13 db, depending on the frequency band over which the error is averaged. The bandwidth of a typical equalizer-analyzer in this frequency range is about 2.5 times the 10% bandwidth used to obtain the above figures and will tend to average over the undertest and the overtest regions on each side of the notch shown in Figure 4, thus reducing the degree of undertest. However, values of isolator transmissibility, based on the TDM output signal, will obviously be erroneous.

To examine the effect of polarity change near a spectral peak, a signal consisting of white noise plus a 5 Hz narrowband peak centered at 53 Hz and approximately 10 db higher than the white noise, was applied to a TDM, with alternate channels having opposite polarity. Figure 6 shows the spectral densities of the

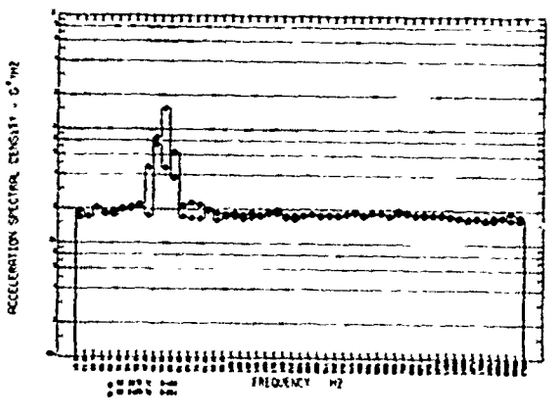

Fig. 6 - TDM input and output spectral densities – polarity inverted signals with peak

TDM input and output while Figure 7 is a plot of the ratio of the TDM output to TDM input spectral density. The spectral spreading of the peak is significant and would cause an overtest of approximately 5 db at the peak and some undertest on each side, depending on the control filter bandwidth.

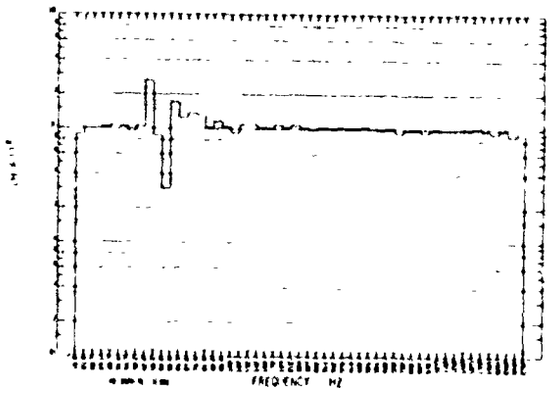

Fig. 7 - Ratio of TDM output to input spectral densities – polarity inverted signals with peak

MEASUREMENT OF TDM PERFORMANCE

Three further factors affecting TDM performance, as previously mentioned, are the relative magnitudes of the input signals, the type of detection employed to process the TDM output, the response time and bandwidth of filters used to analyze the TDM output signal. Before attempting to discuss these factors, which are strongly inter-dependent, the results of some measurements of TDM performance will be presented. These measurements were made using a calibrated noise source as input to one or more TDM channels, with relative attenuation of the spectral density level into certain channels.

In the first set of measurements, the TDM output was analyzed with a 10% constant percentage analyzer. The analyzer employs analog filters and, through multiplexing and A/D conversion, digital detection. To permit on-line analysis and also save core, a software compromise was to compute the average absolute value rather than true r. m. s. value to determine spectral density. (This was justified on the basis that the signals would have Gaussian density functions.) Figures 8 through 10 present plots of the Power Average input

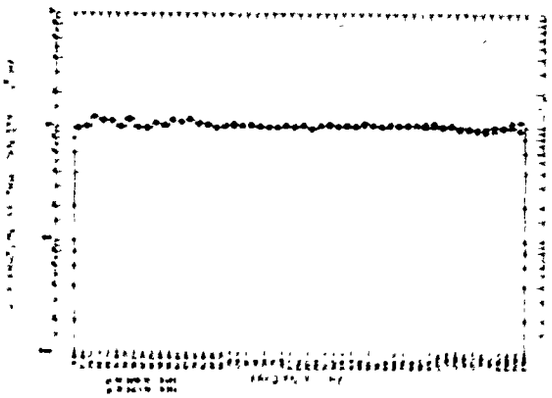

Fig. 8 - Spectral densities of power ave and TDM output – 4 equal input signals

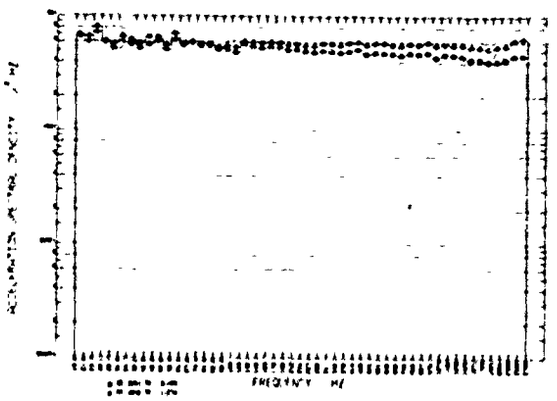

Fig. 9 - Spectral densities of power ave and TDM output – 10 db attenuation of alternate channels

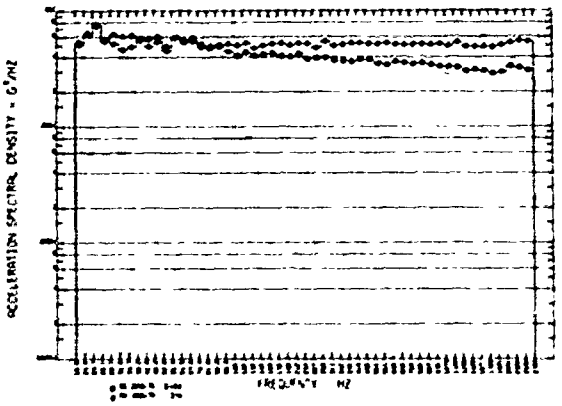

Fig. 10 - Spectral densities of power ave and TDM output – 20 db attenuation of alternate channels

(computed from analysis of the four individual inputs) and the TDM output spectral densities for three conditions: (a) Channels 1 through 4 equal (0.001 g^2/Hz); (b) Channels 2 and 4 attenuated 10 db (i.e., 0.0001 g^2/Hz); and (c) Channels 2 and 4 attenuated 20 db (i.e., 0.00001 g^2/Hz). The roll-off of the TDM output with increasing frequency is evident. The error for the 10 db difference in level of alternate channels ranged from about +0.6 db near 44 Hz to -1.5 db at 2650 Hz. For the 20 db difference, the error ranged from +1.0 db near 33 Hz to -2.5 db at 2650 Hz. A gating time of 100 msecs was employed for these measurements. A variation in gating time between 50 and 200 msecs appeared to make no significant difference to these results.

The second measurements were made using an 80 channel automatic equalization system. The output of the noise source was applied to the equalizer and in turn, to the TDM. The TDM output was applied to the analysis section of the equalization system. With the input applied to two channels of the TDM using 100 msec gating time, the equalizer was adjusted to obtain the "flattest" possible spectrum on the scanner output and a plot made. The input to one TDM channel was removed and a second plot made. These two plots are shown in Figure 11. Theoretically, the second plot should be 3 db below the first. The true rms output of the TDM did reduce exactly 3 db. A repeat of this measurement with the input "shorted" rather than "open" made no change in the curves. At first glance, it appears that the deviation of the lower curve from the desired value increases with frequency. However, a closer examination shows that the deviation is approximately constant at -1.2 db up to about 150 Hz, is constant at approximately -1.7 db up to about 650 Hz and is again constant at approximately -2.2 db up to 2000 Hz. However, these values, particularly the first, may be imprecise since they were scaled from Figure 11.

It should be noted that the filter bandwidths of the equalization system increase from 10 Hz at 10 Hz to 25 Hz at 150 Hz and are constant thereafter. In addition, the detection of the analysis filter outputs employ the average absolute value rather than the true rms value. A test with two equal inputs but with the polarity of the second input reversed with respect to the first, exhibited no change due to polarity. The following sections attempt to explain this performance of the TDM.

RELATIONSHIP BETWEEN AVERAGE ABSOLUTE AND R.M.S. VALUES

It is generally well known that the ratio of the average absolute value, $\overline{|x|}$ to the true rms value, σ, of a signal with zero mean value is a function of the probability density function of the signal. This ratio is of importance, for example, when using an average-detecting meter, with scale indicating r.m.s. volts.

As shown in Ref. 2, for example, the ratio of $\overline{|x|}/\sigma$ for a pure sine wave is 0.900, while for a stationary random process, with Gaussian distribution, this ratio has a value of 0.798. The familiar ratio of these ratios is 1.13, the correction factor for use of an average-detecting meter.

Since many spectral analyzers used for analysis of random processes employ average-detecting circuitry and are also used to analyze the output of a TDM, (e.g., the analysis section of an equalizer-analyzer in random vibration tests), the value of $\overline{|x|}/\sigma$ of a non-stationary signal must be examined. For this immediate discussion, it is unimportant whether the signal is a broadband or narrowband signal. Consider a signal consisting of a series of equal time segments of random signals, each stationary but differing in intensity, i.e., spectral density $W_i(f)$, in each segment, as illustrated in Figure 12.

This signal is typical of the output of a TDM or, neglecting filter response time for the

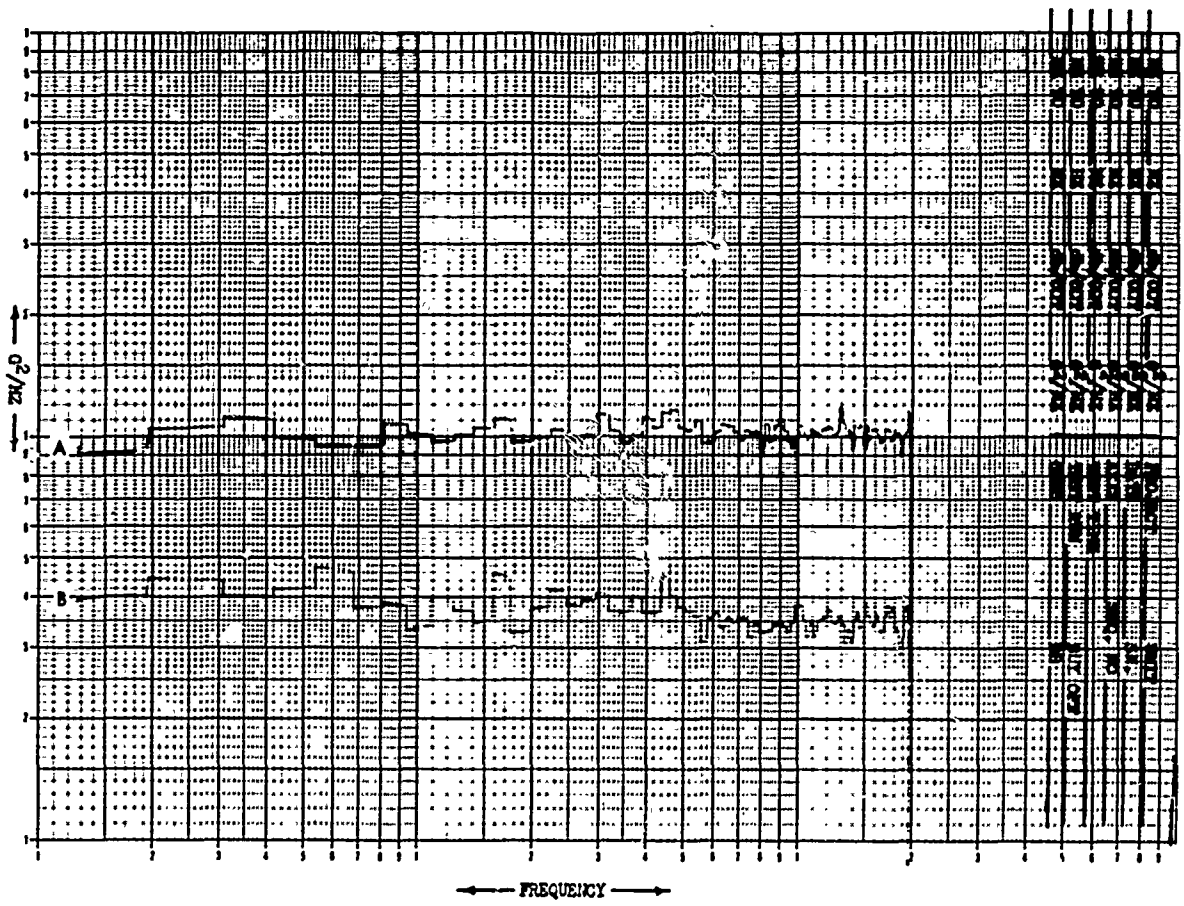

Fig. 11 - Spectral densities from equalization system;
A. Equal inputs to two TDM channels
B. Zero input to second TDM channel

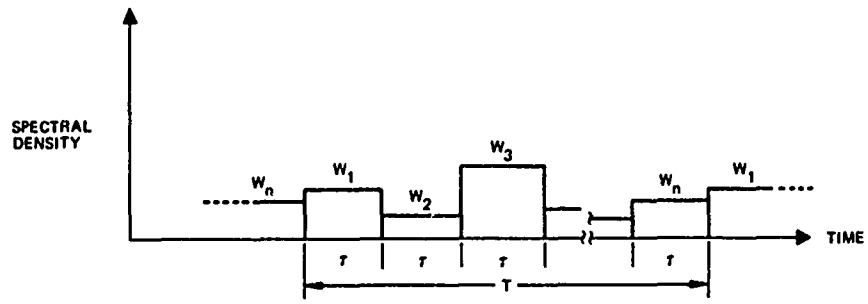

Fig. 12 - Time segmented random process – gating time τ, Scan time T

moment, the output of a filter to which the TDM signal has been applied. For this signal,

$$\sigma^2 = \frac{1}{T}\int_0^T x^2 dt = \frac{1}{T}\sum_{i=1}^{n}\int_{(i-1)\tau}^{(i)\tau} x^2 dt$$

$$= \frac{\tau}{T}\sum_{i=1}^{n}\sigma_i^2$$

$$\overline{|x|} = \frac{1}{T}\int_0^T \overline{|x|}\,dt = \frac{1}{T}\sum_{i=1}^{n}\int_{(i-1)t}^{(i)t} \overline{|x|}dt.$$

$$= \frac{\tau}{T}\sum_{i=1}^{n}\overline{|x|}_i$$

Since in each segment, the process is random, the ratio $(\overline{|x|}/\sigma)_i$ is known and therefore $\overline{|x|}$ can be expressed as:

$$\overline{|x|} = \frac{\tau}{T}\sum_{i=1}^{n} k\sigma_i = \frac{k}{n}\sum_{i=1}^{n}\sigma_i$$

where $k = (\overline{|x|}/\sigma) = 0.798$.

Thus the ratio $\overline{|x|}/\sigma$ for detection over one complete scan of the TDM can be expressed as:

$$\frac{\overline{|x|}}{\sigma} = k\left\{\frac{1}{n}\sum_{i=1}^{n}\sigma_i \Big/ \left[\frac{1}{n}\sum_{i=1}^{n}\sigma_i^2\right]^{1/2}\right\}$$

$$= \frac{k}{\sqrt{n}}\left\{\sum_{i=1}^{n}\sigma_i \Big/ \left[\sum_{i=1}^{n}\sigma_i^2\right]^{1/2}\right\} \quad \text{Eq. 1}$$

If the signal is the same in all channels, Eq. 1 becomes:

$$\frac{\overline{|x|}}{\sigma} = \frac{k}{\sqrt{n}} \cdot \frac{n\sigma_i}{\sqrt{n}\,\sigma_i} = k$$

Consider the extreme case when all time segments except the first are negligibly small, for values of n between 1 and 6. The value of $\overline{|x|}/k\sigma$ becomes $1/\sqrt{n}$ and the values for n = 1 to 6 are shown in Table I.

TABLE 1

n.	$\overline{\lvert x\rvert}/k\sigma$	$\left[\overline{\lvert x\rvert}/k\sigma\right]^2$	db
1	1.0	1.0	0
2	0.707	0.5	-3
3	0.577	0.33	-4.7
4	0.50	0.25	-6
5	0.447	0.20	-7
6	0.408	0.17	-7.7

If, for n even, half the signals have a value σ_1^2 and the other half all have a value σ_2^2, then Eq. 1 becomes

$$\frac{\overline{|x|}}{\sigma} = \frac{k}{\sqrt{2}} \cdot \frac{(\sigma_1 + \sigma_2)}{\left[\sigma_1^2 + \sigma_2^2\right]^{1/2}}$$

$$= \frac{k}{\sqrt{2}} \cdot \frac{\left(1 + \frac{\sigma_2}{\sigma_1}\right)}{\left[1 + \left(\frac{\sigma_2}{\sigma_1}\right)^2\right]^{1/2}} \quad \text{Eq. 2}$$

The value of $\overline{|x|}/k\sigma$ as a function of σ_2/σ_1 is shown in Figure 13. Decibel scales were used to permit interpretation in terms of either rms or spectral density.

EFFECT OF DETECTION METHOD

From Table I and Figure 13, it is evident that if the rms value of the time segmented signal of Figure 12 is measured by use of an averaging detector, the value obtained may be greatly in error, depending on the value of n and the relative values of the σ_i. If the rms value so measured is used to control the spectral density level of vibration during tests, the test level will clearly be in excess of that desired.

From Figure 13, differences of 10, 20 and infinite db in input intensities create errors of -1.05, -2.2 and -3 db respectively, due to changes in $\overline{|x|}/\sigma$. These errors should be independent of bandwidth and center frequency of the analysis filter. The above values do not correspond to the measured errors shown in Figures 9 through 11, and clearly the measured errors are related in some way to filter bandwidth. At a center frequency of 250 Hz,

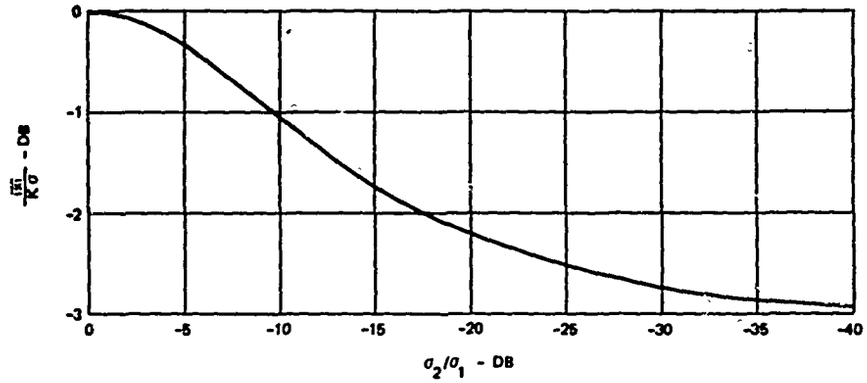

Fig. 13 - $|\bar{x}|/k\sigma$ vs. σ_2/σ_1 - Ref Eq. 2

and therefore at a bandwidth of 25 Hz, equivalent to the equalization system, the errors from Figures 9 and 10 are -0.6 and -1.4 db respectively. The differences between these measured errors and the theoretical errors of Figure 13 are 0.45 db at 10 db, 0.8 db at 20 db and 1.3 db at infinite db difference in TDM input signals.

Thus it appears that errors in TDM performance are a function of the difference in signal level and the analyzer filter bandwidth as well as the type of detection employed. Further these errors appear to be in the opposite direction to the detection error. The remaining known factor which can cause degraded performance is the characteristic of the response of a filter to the TDM signal.

EFFECT OF FILTER RESPONSE CHARACTERISTICS

Consider the response of a filter to a time segmented signal such as Figure 12. The response of a single degree-of-freedom system with viscous damping to a random signal which is rectangularly modulated, i.e., Figure 12, has been studied by Holman and Hart, (Ref. 3). Since, within the resonant bandwidth, this system may be considered as a filter, their results are indicative of what might be expected from a spectral analysis of the output of a TDM.

Figure 14 is a representation of the meansquare input and output of a filter to the TDM output with two unequal channels and a gating time τ. Due to the response and delay times of the filter, the meansquare output, a measure of the spectral density of the input within the filter pass band, does not follow the step changes in input but lags as shown by the dotted line. Holman has shown that for white noise input within the resonant bandwidth, a mechanical system response builds up and decays without overshoot and does so in a time approximately equal to the reciprocal of the bandwidth. If the true meansquare output of the filter were measured, the two shaded areas in Figure 14 are probably approximately equal (Ref. 3) and will be cancelling errors. However, if average detection is used, the degree of cancelling will be less perfect. Furthermore, during these transition periods, the waveform is composed of a mixture of a nonstationary random process and an exponentially decaying simusoid. (When one channel has zero signal, the decaying signal is comprised of the latter only.) It may be difficult to ascertain the probability density function during this time period but it is almost certainly non-Gaussian, thus creating additional error due to variations in $|\bar{x}|/\sigma$.

The response and decay times of a filter are approximately equal to the reciprocal of the filter bandwidth. Thus the narrower the filter, the larger the ratio of transition time to gating time. Therefore, for a given gating time, the error, when using average detection, should increase as the filter bandwidth increases, as shown in Figures 9 and 10, and should be constant for constant bandwidth, as shown, at least approximately, in Figure 11. It was determined from the manufacturer that the filter input connections for the 25 Hz filters up to 500 Hz are slightly different than those above 500 Hz. It is possible that the differences in impedance causes sufficient difference in response and decay times to account for the 0.5 db difference between filter groups mentioned previously.

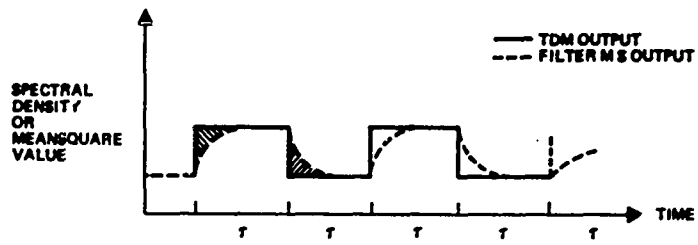

Fig. 14 - Input and response of filter to TDM output

For a gating time of 100 msecs, the ratio of filter response or decay time to gating time is 5 for a 2 Hz bandwidth, 0.40 for a 25 Hz bandwidth and 0.04 for a 265 Hz bandwidth. The large changes in error shown in Figures 9 and 10 as a function of bandwidth are thus credible in terms of filter response time. In addition, the ratio of 0.40 at 25 Hz is compatible with the errors observed for this bandwidth as a function of difference in level between TDM channels. Clearly from Figure 14, the greater the difference in levels, the greater the percentage of the total area under the curve will be represented by the shaded areas.

The above arguments lead to the conclusion that the error, for a given filter bandwidth and ratio of TDM input levels, must be a function of gating time. To examine this, and despite the previous comment with respect to Figures 9 and 10, the measurements presented in Figure 11, using the equalization system, were repeated for three gating times, 40 msecs, 100 msecs and 200 msecs. The difference between the two larger values was too small to observe with the scanner output. The difference between 40 msec and 100 msec is shown by the two lower curves of Figure 15 and amounts to approximately 1 db. (The top curve is the reference curve for equal inputs in both TDM channels.) For the 40 msec gating time, the total error is generally less than 1 db, due to the fortuitous cancelling of errors.

USE OF MEANSQUARE DETECTION

Although available random vibration equalizers do not employ meansquare detection, each factor affecting TDM performance is interdependent with the detection method employed. To attempt to verify some of the previous postulates, a spectral analysis of the TDM output using meansquare detection was made. The calibrated white noise source was applied to the 10% bandwidth filter system through the TDM. The meansquare response of each filter was measured with a true rms meter to which a massive external capacitance was attached. The meansquare values with the TDM dwelling continuously on channel number 1 and then scanning channels 1 and 2, with zero input to channel 2, were obtained. (This essentially repeated the previous experiment with the equalization system.) A gating time of 100 msecs was used.

Figure 16 is a plot of twice the ratio of the measured values when scanning the two channels to those when dwelling on channel 1, i.e., the TDM/Power Average. The variation from unity is thus the error due the combined effects of gating time and filter response time plus experimental error. From this plot, it is concluded that the error is essentially zero if the response time of the filter is less than half the gating time, e.g., 200 Hz in Figure 16. As the filter response time increases, the error increases and approaches 20% when the filter response time is about five times the gating time.

PERFORMANCE DURING TYPICAL LABORATORY TESTS

Chronologically, the data to be presented in this section were acquired prior to most of the special investigations discussed so far and, in fact, were the catalyst for them. Regardless of the explanations for TDM performance, the real question is now well, or poorly, the TDM, in conjunction with the remainder of the vibration system, performs in live tests. To answer this question, data from two groups of tests were gathered. The first group consisted of tests of three hardmounted equipment racks or shelves, each containing 4 or 5 "black boxes", each with a total weight of about 200 lbs. The fixtures were flat plates, with considerable overhang when mounted to the armature for vertical axis tests. Five or six control accelerometers were used in each case and the TDM was set for 100 msecs gating time. A total of eight tests were analyzed. An

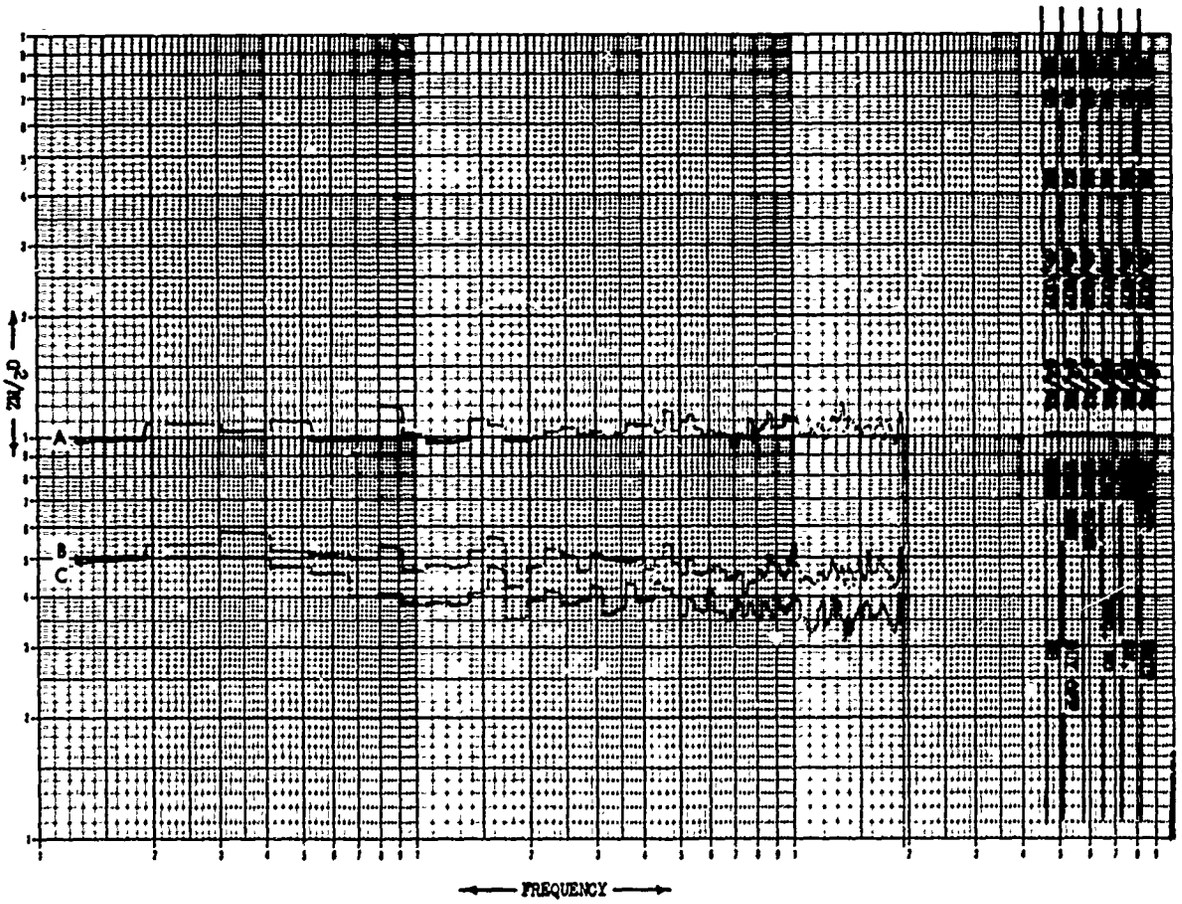

Fig. 15 - Spectral densities from equalization system:
A. Equal inputs to two TDM channels
B. Zero input to second channel - 40 msec gate
C. Zero input to second channel - 100 msec gate

additional rack, weighing about 300 lbs and mounted on vibration isolators was also analyzed for three tests. Four control accelerometers were employed.

The second group of data was gathered from two sets of tests of a missile, approximately 13 ft. long and weighing about 1000 lbs. Each set consisted of four tests normal to the missile axis and one longitudinal. Excitation was at a single point but three control accelerometers were employed in order to bias the spectrum in a desired fashion. Each test involved two levels, so that twenty different tests were analyzed.

For each test, the spectral densities of the individual control accelerometers, C_i and the TDM output were obtained, using the 10% bandwidth analyzer. The Power Average was computed from the C_i and the ratios of the individual signals and the TDM to the Power Average i.e., C_i/Pwr. Ave and TDM/Pwr Ave, were computed. For each group, the envelopes, high and low, of the C_i/Pwr. Ave., and the maximum, mean and minimum of the TDM/Pwr. Ave. were obtained. The envelopes indicate the range of spectral densities among the control accelerometers while the TDM/Pwr. Ave. measures TDM performance.

Figures 17 and 18 present the results for the three hardmounted racks, while Figures 19 and 20 contain the results for the vibration isolated rack. In view of the use of average-detection for computation of the TDM spectral density, the performance of the TDM appears to be satisfactory (Ref. Figure 10 versus Figure 16).

Figures 21 and 22 present the results for longitudinal testing of the missile while

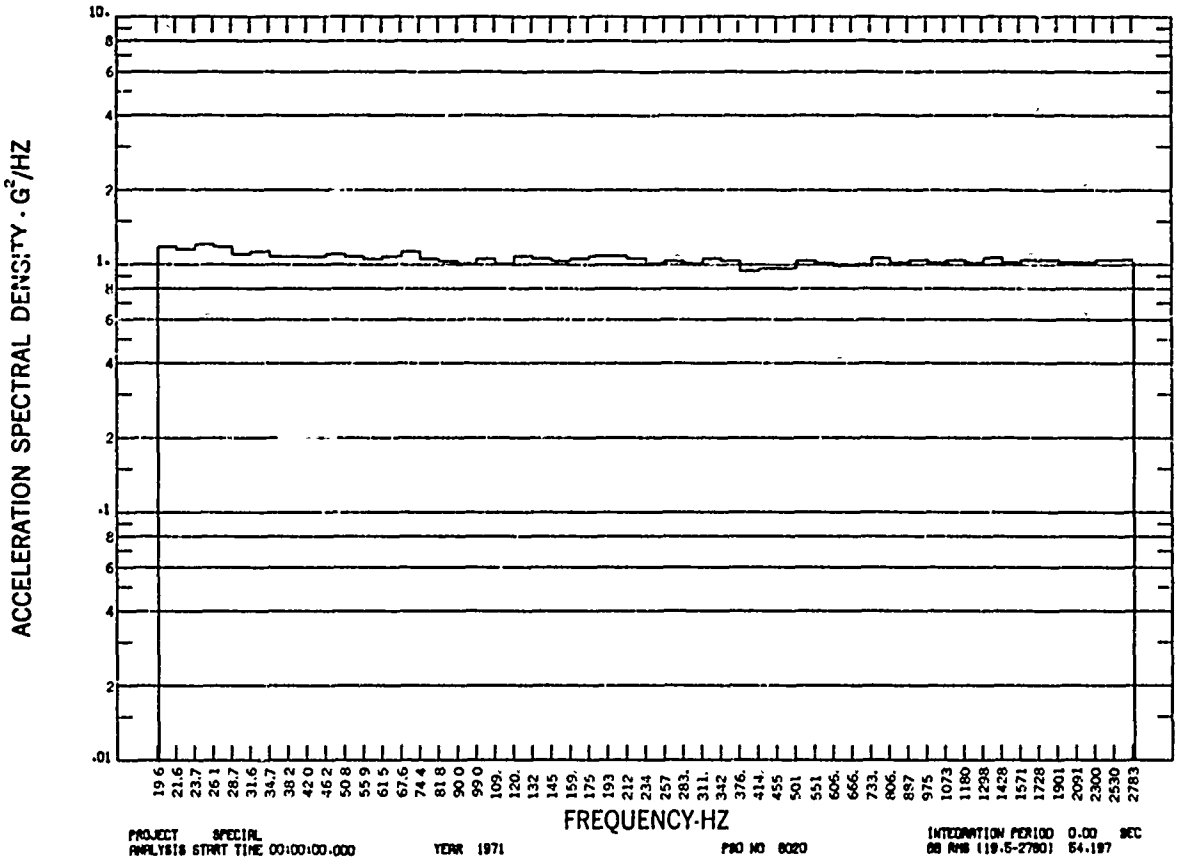

Fig. 16 - TDM/power average ratio with meansquare detection

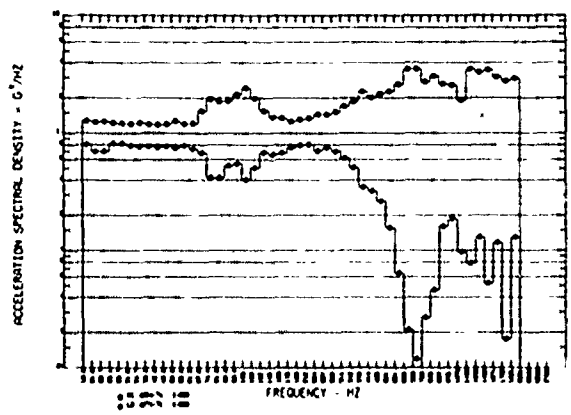

Fig. 17 - Three hardmounted racks - maximum and minimum C_i/pwr. ave.

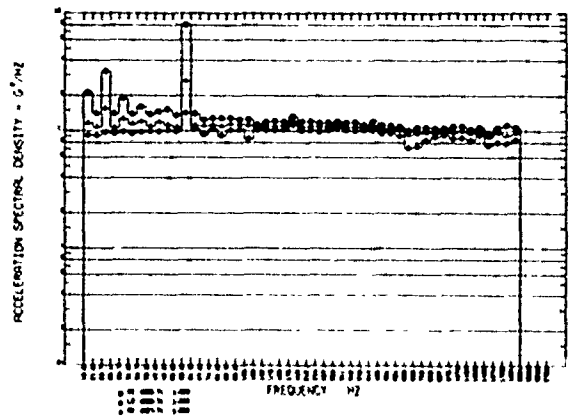

Fig. 18 - Three hardmounted racks - maximum, mean and minimum of TDM/pwr. ave.

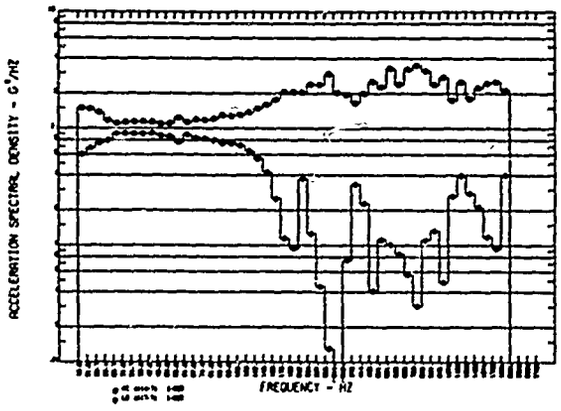

Fig. 19 - Vibration isolated rack - maximum and minimum C_i/pwr. ave.

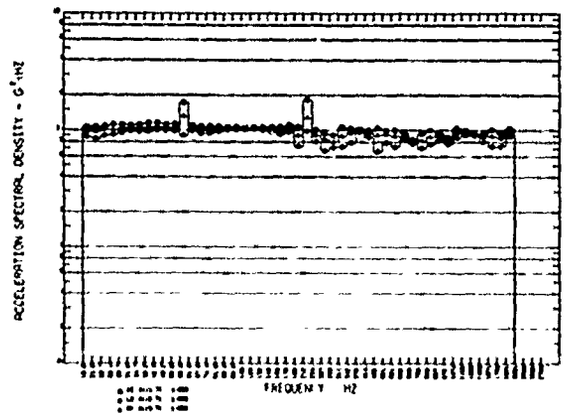

Fig. 20 - Vibration isolated rack - maximum, mean and minimum of TDM/pwr. ave.

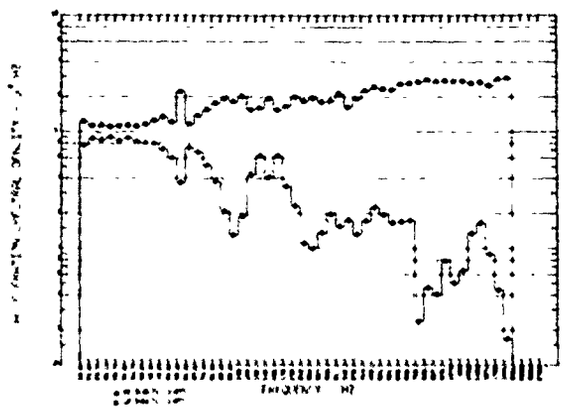

Fig. 21 - Missile - longitudinal - maximum and minimum C_i/pwr. ave.

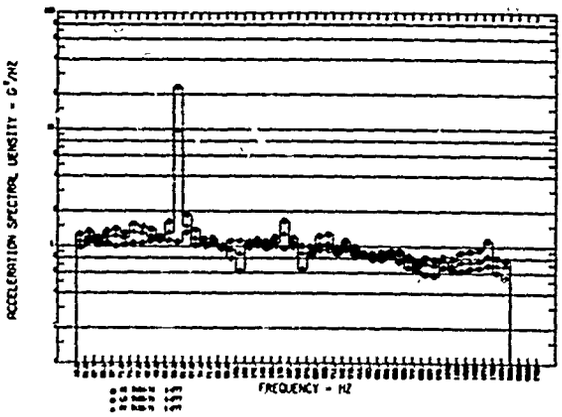

Fig. 22 - Missile - longitudinal - maximum, mean and minimum of TDM/pwr. ave.

Figures 23 and 24 present the results for lateral testing. The greater range of control accelerometer signal levels is evident, in fact the value of three at high frequencies indicates only one accelerometer to be controlling, as was actually intended. The TDM/Pwr. Ave. ratio for longitudinal tests, Figure 22, when compensated for the use of average detection in deriving these plots, is probably quite adequate. However, the results for lateral testing, Figure 24, with much greater range of signal levels, and also effective polarity changes due to rigid body rotation of the missile, are less satisfactory due to the variability of the TDM/Pwr. Ave. ratio. The degree of overtest due to both the variability and the bias of the equalization system at these extreme ranges is difficult to assess but may easily approach 3 db in some frequency ranges for each test.

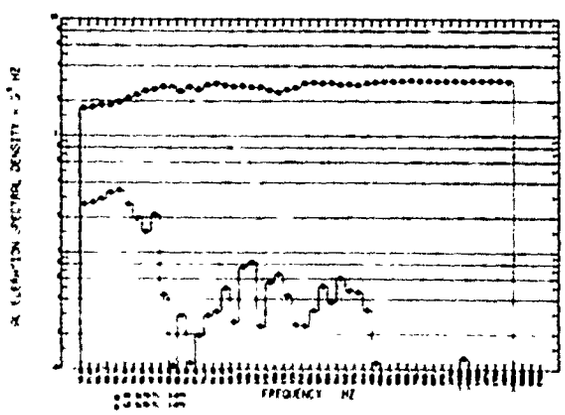

Fig. 23 - Missile - lateral - maximum and minimum C_i/pwr. ave.

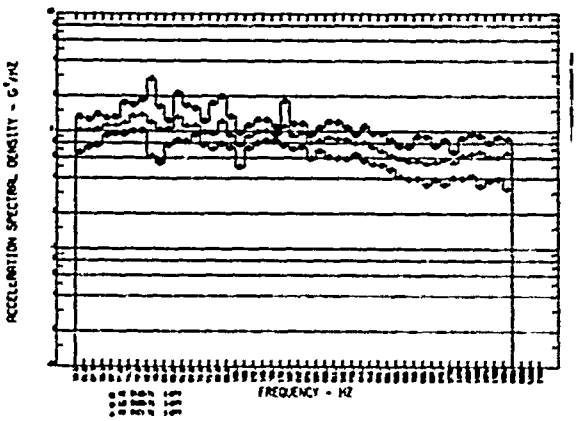

Fig. 24 - Missile - lateral - maximum, mean and minimum of TDM/pwr. ave.

CONCLUSION

In retrospect, it may be that the title of this paper is misleading since it is the performance of the equipment to which the TDM signal is applied more than the TDM performance per se which affects test quality. On the other hand, without the TDM, there is no averaging or performance to evaluate. From the investigations described, a somewhat cynical observation might be that when all TDM input signals are the same in intensity and polarity, i.e., when averaging is unnecessary, TDM performance is perfect. As the need for averaging becomes more acute, i.e., greater variation between control accelerometers, the TDM or rather the vibration system, TDM included, performs less accurately. However, the data gathered from laboratory tests indicates that the overtest which may occur when using a TDM is certainly far preferable to a retrogression to single-point control.

If nothing else, the investigations reported here have re-emphasized the importance, when treating stochastic processes, of following the prescribed mathematical procedures, i.e., computing the meansquare value rather than the average absolute value.

It would be easy, but obviously impractical, to conclude that all random vibration equalization systems must be modified to incorporate meansquare detection. However, there are other practical actions which can help obtain the best performance during TDM usage:

1. Physically orient all accelerometers to avoid polarity differences.
2. When 1) is not possible, electrically invert signals to eliminate polarity differences.
3. Using a shorter gating time rather than longer, particularly for larger filter bandwidths.
4. Never use the TDM output for computation of frequency response functions or for certification of test levels. Use the computed Power Average instead. (See Ref. 4 for alternative Tape Delay Method to obtain Power Average).
5. Preferably avoid, but if unavoidable, use extreme caution when using fundamental control of the TDM output.

Finally, the author would like to acknowledge the valued contributions, both conceptual and in the experimental measurements, of many colleagues, particularly John Olbert, Henry Abstein and Nick Tinling.

REFERENCES

1. T. Usher, "Average Control for Sinusoidal and Random-Vibration Testing", JASA, Vol 41, No. 4 pp 840-849. April 1967.
2. Handbook of Shock and Vibration, Harris and Crede, Ed. McGraw Hill New York, 1961.
3. R. E. Holman, Gary C. Hart, "Dynamic Response of Structures to almost Stationary Excitations". AIAA paper No. 71-348, April 1971.
4. A. J. Curtis, N. G. Tinling, H. T. Abstein Jr., Selection and Performance of Vibration Tests, SVM-8, SVIC, Washington, D. C., 1971.

A MULTIPLE DRIVER ADMITTANCE TECHNIQUE FOR VIBRATION TESTING OF COMPLEX STRUCTURES*

Strether Smith
Lockheed Missiles & Space Company
Palo Alto Research Laboratory
Palo Alto, California

and

A. A. Woods, Jr.
Lockheed Missiles & Space Company
Sunnyvale, California

A technique is presented for conducting and analyzing multiple shaker sine sweep tests to determine the modes of a structure. The approach greatly reduces the cost of performing a modal test program and improves the accuracy of the modal parameters measured.

INTRODUCTION

In dynamic testing of aerospace structures, three distinctly different methods have been employed for the determination of the modal response parameters: frequency, damping, and mode shape. The simplest of these is the sine sweep or resonant search test in which the specimen is forced with a single shaker and total response amplitude data are obtained for analysis purposes. This form of data is often adequate to provide a cursory evaluation of the lower frequency (well separated) modes or to assess the ability of the structure to survive a specific environment when excited in a manner similar to the test.

When more accurate information on the modal parameters is required, or when the modal density is high, more elaborate procedures are required. Two advanced techniques have been derived to satisfy the more complex requirements and have been employed during structural dynamic test programs. The first of these is the powerful complex admittance technique of Kennedy and Pancu [1] which employs phase-dependent response analysis techniques to extract the desired modal information from single shaker tests. With this approach, adequate modal information has been obtained from sine sweep tests in frequency bands where the modal density is moderate (i.e., modal spacing is greater than two bandwidths). Analysis of higher modal density areas requires the use of a matrix separation routine similar to that presented by Stahl [2]. Stahl's technique is based on a model containing multiple, linearly superimposed modes with structural damping. This may not be an accurate representation of the structure. Also, the method is inherently sensitive to experimental errors contained in the data. Consequently, practical problems, such as small specimen nonlinearities and instrumentation errors, greatly reduce resolution and accuracy.

The second advanced method is the multiple driver, tuned dwell approach developed by Lewis and Wrisley [3]. The objective of their approach was to "produce in a complex structure, by means of adjustable forces, oscillations that consist essentially of one natural mode."

To force a normal mode of a damped specimen, it is required that the forcing function be distributed over the structure such that each section of the structure is in energy balance. In simple terms, this requires that energy must be put into the structure at the same points at which it is being dissipated. For uniform viscous damping, the required force is proportional to the local velocity, but in the real case, i.e., the damping is neither uniform nor viscous, a more complex forcing amplitude distribution is required.

Theoretically an infinite number of drivers is required to excite a normal mode as every mass of the structure must be individually driven.

In practice, a limited number of drivers must be used (usually about 10). This precludes the possibility of perfect tuning. Judicious adjustment of the available shakers will result in increased isolation of a mode through the suppression of adjacent interfering modes. The response amplitude of the structure at discrete points is used to define the mode shape and any inadequacies in the tuning will result in errors.

Having used both of the advanced methods in practical situations, the authors concluded that a combination of the two procedures might provide an improvement. Each technique has advantages that overcome shortcomings of the other, i.e., the

*Work sponsored by Lockheed Independent Research Program

complex admittance method can accurately analyze improperly tuned modes if the apparent modal density is not too high, and the tuned dwell approach can produce lower apparent modal density thereby increasing the resolution of the complex admittance method. In addition, the appropriate use of multiple shakers can reduce test-induced nonlinearities that undermine the effectiveness of the Kennedy-Pancu and Stahl analyses.

To use the complex amplitude method with multiple drivers, the analytical tools for the reduction of the data must be developed. The approach used here is to determine the instantaneous power input to the structure and the structural response kinetic energy. These quantities may be represented as vectors in a complex energy plane. A set of energy admittance quantities may be determined from the ratio of these vectors using complex vector algebra. The resulting admittance quantities then may be used in the conventional complex amplitude method to determine the modal parameters.

DERIVATION

In the derivation of the energy admittance relationships, the following assumptions are used:

- Each structural mode behaves as a single-degree-of-freedom oscillator with structural damping. The differential equation for modal behavior is

$$m\ddot{x} + k(1+ig)x = Fe^{i\omega t}$$

where

m = generalized mass
k = generalized stiffness
g = structural damping coefficient
i = $\sqrt{-1}$
x = generalized response
F = generalized force (may be complex)
ω = driving frequency
t = time

- The structural responses may be superimposed.
- The forces applied to the structure are sinusoidal and coherently phased, i.e., in phase or at 180 degrees.
- All of the responses are sinusoidal and coherently phased.

Using these assumptions, it may be shown that the complex velocity response at a point j on the structure, due to a force applied at point i, is represented by

$$V_j = \omega(F_i)A_{ij}\left[\frac{g + i(1-\beta^2)}{(1-\beta^2)^2 + g^2}\right] \qquad (1)$$

where

V_j = complex velocity of the j^{th} point
F_i = complex force at the i^{th} point
$\beta = \omega/\omega_n$

$$A_{ij} = \frac{gV_j}{\omega_n F_i}\bigg|_{\beta=1} = \text{constant}$$

$$\omega_n = \sqrt{k/m}$$

By superposition, the response at j when driven by M drivers is

$$V_j = \omega\sum_{i=1}^{M} F_i A_{ij}\left[\frac{g + i(1-\beta^2)}{(1-\beta^2)^2 + g^2}\right] \qquad (2)$$

To calculate the time average of the kinetic energy and power we will use the following relationship for determining the time average of the product of two complex vectors

$$\langle a \cdot b \rangle = \frac{ab^*}{2} \qquad (3)$$

where b^* = the complex conjugate of b. We determine the kinetic energy of the j^{th} point

$$\langle T_j \rangle = \frac{m_j V_j V_j^*}{4}$$

$$= \frac{m_j\omega^2}{4}\left[\sum_{i=1}^{M} \bar{F}_i A_{ij}\right]^2\left[\frac{1}{(1-\beta^2)^2 + g^2}\right] \qquad (4)$$

where

$\bar{F}_i$ = modulus of F_i
m_j = mass of the j^{th} point

The total kinetic energy of the vehicle may be determined by summing the N individual kinetic energies

$$\langle T_T \rangle = \frac{\omega^2}{4}\sum_{j=1}^{N} m_j\left[\sum_{i=1}^{M} \bar{F}_i A_{ij}\right]^2\left[\frac{1}{(1-\beta^2)^2 + g^2}\right] \qquad (5)$$

Again using Eq. (3), we calculate the complex power input at the k^{th} drive point

$$\langle P_k \rangle \quad \frac{F_k V_k^*}{2} \quad \frac{\omega}{2}\bar{F}_k \sum_{i}^{M} \bar{F}_i A_{ik}\left[\frac{g - i(1-\beta^2)}{(1-\beta^2)^2 + g^2}\right] \qquad (6)$$

This is a complex quantity, whose angle from the real axis (kinetic energy) is equal to the phase angle between the force and velocity systems.

The total power input to the structure is determined by summing the individual powers.

$$\langle P_T \rangle = \frac{\omega}{2}\sum_{k=1}^{M} \bar{F}_k \sum_{i=1}^{M} \bar{F}_i A_{ik}\left[\frac{g - i(1-\beta^2)}{(1-\beta^2)^2 + g^2}\right] \qquad (7)$$

We now define an energy-power admittance quantity by dividing the kinetic energy by the total power

$$A_E = \frac{2\langle T \rangle}{\omega i \langle P_T \rangle} \qquad (8)$$

The division by ωi converts the admittance quantity into units of displacement per unit force, for reasons that will become clear.

The individual mass energy admittance is given by

$$A_{E_j} = \frac{m_j \left[\sum_{i=1}^{M} \overline{F}_i A_{ij}\right]^2}{\sum_{k=1}^{M} \overline{F}_k \left[\sum_{i=1}^{M} \overline{F}_i A_{ik}\right]} \left[\frac{(1-\beta^2) - ig}{(1-\beta^2)^2 + g^2}\right] \qquad (9)$$

If forces are maintained proportional during the sweep, then

$$\frac{\left[\sum_{j=1}^{M} \overline{F}_i A_{ij}\right]^2}{\sum_{k=1}^{M} \overline{F}_k \sum_{i=1}^{M} \overline{F}_i A_{ik}} = b_j = \text{constant}$$

The total energy admittance is:

$$A_{ET} = \sum_{j=1}^{M} m_j b_j \left[\frac{(1-\beta^2) - ig}{(1-\beta^2)^2 + g^2}\right] \qquad (10)$$

These relationships are of the same form as the displacement admittances derived by Kennedy and Pancu (which explains the reasons for dividing by ωi).

The complex plane admittance plot is presented in Fig. 1. This figure shows the more general case of the velocities and/or forces not having perfect phase coherency. The errors will be small if the phase scatter is small.

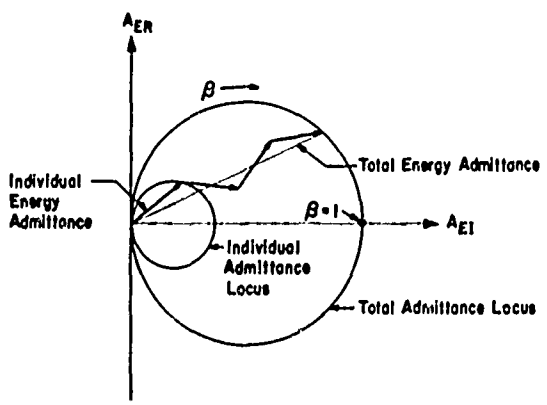

Fig. 1 - Energy admittance in the complex plane

To obtain the modal data from the energy admittance information, the Kennedy and Pancu recommendations to find the modal frequency and mode shape are used.

The modal frequency is found by a maximum of the function

$$\frac{ds}{d\beta^2} \qquad (11)$$

where

s = path length in the complex plane

This quantity should be evaluated from the total energy admittance plot. This will reflect the overall vehicle behavior.

The mode shape is found by determining the radius of curvature of the individual energy admittance locus at the indicated resonance. The modal response at the j^{th} point is determined by converting the energy admittance to relative displacement.

$$x_j = N\sqrt{\frac{2\rho_j}{m_j}}\left|\frac{ds}{d\beta^2}\right| = \text{max.} \qquad (12)$$

where

ρ_j = radius of curvature of the j^{th} individual admittance locus
N = normalizing constant

The normalization is performed to obtain conventional mode shape information.

The overall structural damping is determined from the total energy admittance information by the relationship:

$$g = \frac{4\rho_T}{ds/d\beta}\left|\frac{ds}{d\beta^2}\right| = \text{max.} \qquad (13)$$

where

ρ_T = the radius of curvature of the total admittance locus

There is an alternative method for determining the damping of a mode using energy techniques. If an estimate of the instantaneous vehicle kinetic energy is calculated in real-time (i.e., by analog computation), a decay of this quantity may be determined. This decay is given by

$$T_{DECAY} = \sum_j \frac{m_j V_{jo}}{2} e^{-g\omega_n t} \sin^2 \omega_n t \qquad (14)$$

where V_{jo} is the initial velocity. Thus, the energy decay time constant is

$$\tau_E = 1/g\,\omega_n \qquad (15)$$

This decay method results in an overall structural damping coefficient.

DATA ANALYSIS METHOD

The relationships used to apply the energy admittance method are an extension of the so-called Co-Quad admittance techniques. It is convenient to refer all raw measurements to a fixed amplitude sine wave that is oscillating at the specimen drive frequency. We will define this reference signal as

$$\bar{R} = R \sin \omega t \tag{16}$$

It is assumed that all of the responses and forces are at the same frequency but have their own amplitude and phase. Thus, the force at the i^{th} input and the velocity response at the j^{th} point are defined as

$$f_i = F_i \sin (\omega t + \phi_{F_i}) \tag{17}$$

$$v_j = V_j \sin (\omega t + \phi_{V_j}) \tag{18}$$

If we then perform a conventional Co-Quad analysis between each of these signals and the reference, we obtain

$$\begin{aligned} C_{F_i} &= R \cdot F_i \cos \phi_{F_i} \\ Q_{F_i} &= R \cdot F_i \sin \phi_{F_i} \\ C_{V_j} &= R \cdot V_j \cos \phi_{V_j} \\ Q_{V_j} &= R \cdot V_j \sin \phi_{V_j} \end{aligned} \tag{19}$$

where

C = filtered coincident product
Q = filtered quadrature product

If we square C_{V_j} and Q_{V_j} and sum them, we find

$$C_{V_j}^2 + Q_{V_j}^2 = R^2 V_j^2$$

which, if we divide by $2R^2$ and multiply by m_j (the mass associated with the j^{th} structure point), yields the kinetic energy of the j^{th} point

$$\left\langle T_j \right\rangle = \frac{m_j}{2R^2} \left(C_{V_j}^2 + Q_{V_j}^2 \right) \tag{20}$$

The total kinetic energy of the structure is obtained by summing the individual contributions

$$\left\langle T_T \right\rangle = \sum_j \left\langle T_j \right\rangle \tag{21}$$

where the summation is made over all of the structural mass points.

For structures in which rotational motions are important, these relations may be generalized to include rotational kinetic energy terms.

The complex power is determined using the responses measured at the forcing points (i.e., $i = j$).

$$\begin{aligned} C_{F_i} \cdot C_{V_i} + Q_{F_i} \cdot Q_{V_i} &= R^2 (F_i \cos \phi_{F_i} \cdot V_i \cos \phi_{V_i} \\ &\quad + F_i \sin \phi_{F_i} \cdot V_i \sin \phi_{V_i}) \\ &= R^2 F_i V_i \cos (\phi_{F_i} - \phi_{V_i}) \\ &= R^2 F_i V_i \cos \phi_i \end{aligned}$$

where ϕ_i is the phase angle between the velocity and force at point i.

This, when divided by R^2, is the real component of the power input at the i^{th} forcing point.

$$\left\langle P_{i_{RE}} \right\rangle = \frac{1}{R^2} \left(C_{F_i} \cdot C_{V_i} + Q_{F_i} \cdot Q_{V_i} \right) \tag{22}$$

Similarly, if we calculate:

$$\begin{aligned} C_{V_i} \cdot Q_{F_i} - Q_{V_i} \cdot C_{F_i} &= R^2 F_i V_i \sin (\phi_{F_i} - \phi_{V_i}) \\ &= R^2 F_i V_i \sin \phi_i \end{aligned}$$

Again, dividing by R^2, we determine the imaginary component of the power.

$$\left\langle P_{i_{IM}} \right\rangle = \frac{1}{R^2} \left(Q_{F_i} \cdot C_{V_i} - C_{F_i} \cdot Q_{V_i} \right) \tag{23}$$

To determine the total complex vector in the energy plane, we sum the individual components

$$\begin{aligned} \left\langle P_{T_{RE}} \right\rangle &= \sum_i \left\langle P_{i_{RE}} \right\rangle \\ \left\langle P_{T_{IM}} \right\rangle &= \sum_i \left\langle P_{i_{IM}} \right\rangle \end{aligned} \tag{24}$$

The magnitude of the total power from all drivers is

$$|P_T| = \left(\left\langle P_{T_{RE}} \right\rangle^2 + \left\langle P_{T_{IM}} \right\rangle^2 \right)^{1/2} \tag{25}$$

We now have two time average vectors in the complex energy plane: the kinetic energy (individual and total) and the power.

Using these quantities, we determine the desired admittance pair by dividing the kinetic energy by the power and multiplying by $2/i\omega$. The components of the admittance may be expressed as shown in Eqs. (26) and (27).

$$\begin{aligned} A_{ET_{RE}} &= \frac{2 \left\langle P_{T_{IM}} \right\rangle \left\langle T_T \right\rangle}{\omega |P_T|^2} \\ A_{ET_{IM}} &= \frac{-2 \left\langle P_{T_{RE}} \right\rangle \left\langle T_T \right\rangle}{\omega |P_T|^2} \end{aligned} \tag{26}$$

for the total vehicle energy admittance, and

$$A_{Ej_{RE}} = \frac{2\left\langle P_{T_{IM}}\right\rangle \left\langle T_j\right\rangle}{\omega |P_T|^2}$$

$$A_{Ej_{IM}} = \frac{-2\left\langle P_{T_{RE}}\right\rangle \left\langle T_j\right\rangle}{\omega |P_T|^2} \qquad (27)$$

for each individual mass point admittance.

We may determine the desired admittance quantities in terms of the original measured variables by vector summing the components

THE TUNED SWEEP TECHNIQUE

The energy admittance relationships derived provide the tools for applying complex amplitude techniques to multiple-driver sine sweep data. This section will describe one method for using this capability to advantage.

The tuning approach used by Lewis and Wrisley [3] was to perform a rough tuning by adjusting each shaker so that its amplitude was proportional to the relative velocity and phased such that the power is positive at the drive point. They then attempted additionally to adjust each shaker to improve the modal isolation. This second step is achieved by an extremely tedious trial and error procedure – one that is necessary if the tuned dwell method is to successfully separate the modes. The use of complex energy admittance techniques eliminates the necessity for exact modal tuning to accurately determine modal information. The straightforward adjustment of force amplitude proportional to local relative velocity is usually sufficient. However, it is recommended that a modification of Lewis and Wrisley's approach be implemented. This refinement is to proportion the force to the in-phase component of the velocity. The procedure is straightforward and easily automated and provides somewhat better modal separation by reducing the drive amplitude at drive points where phase relationships are poor.

There are two secondary improvements that result from the use of multiple drivers and energy techniques. They are related to nonlinearities – one type is test induced (to be avoided) and the other true to the structure (to be measured).

A major contributor to test-induced nonlinearity is improper driving. If an attempt is made to drive a mode at a point where the acceptance is low, energy is inserted into the mode through local specimen action which is almost always very nonlinear. This problem is greatly reduced or eliminated by using multiple drivers and proportioning their amplitude according to the local in-phase acceptance.

Structures that do exhibit moderately nonlinear stiffness and damping may be analyzed by quasi-linear techniques if the modal amplitude is maintained constant during the sweep through the mode. When the test is controlled in this way, the complex energy admittance techniques may be used for determination of the modal parameters.

In conventional testing practice, the amplitude is usually controlled by one response point. In general, this is not a good indicator of modal amplitude.

The kinetic energy of the vehicle is an excellent measure of total modal action. It is possible to calculate the specimen energy based on ten or more measured responses by using analog techniques. This quantity may then be used as the test amplitude control parameter.

For systems that do exhibit moderately nonlinear behavior, as is common in many aerospace vehicles, sweeps should be run at several kinetic energy levels to determine the indicated modal frequency, damping, and mode shape as a function of amplitude. This allows for amplitude-dependent linear definition of the modal parameters.

EXPERIMENTAL VERIFICATION

To explore the feasibility of the complex energy-tuned sweep method, a bar-mass test specimen was constructed. This structure, shown in Fig. 2, was driven at each of the six major masses by permanent magnet shakers. The response was measured at each of these locations with velocimeters. A detailed specimen description is contained in Ref. [4].

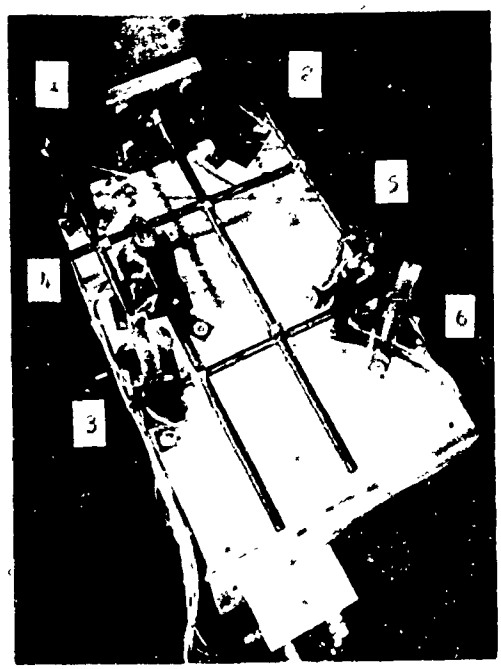

Fig. 2 - Test specimen

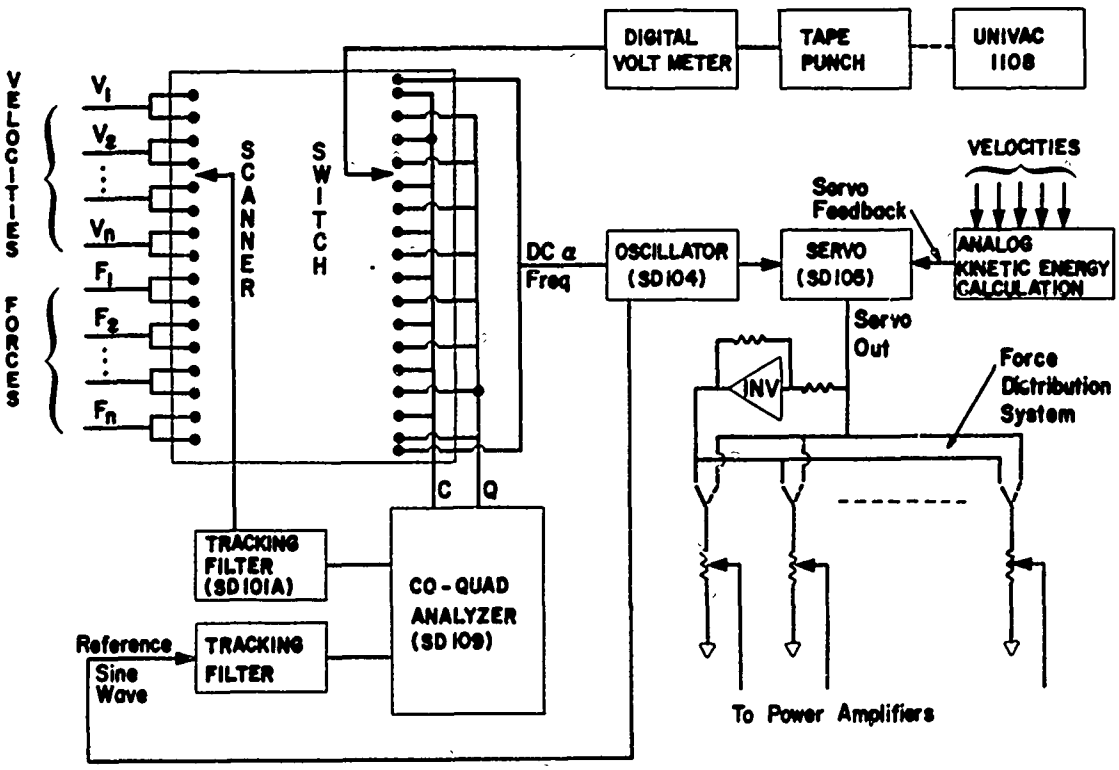

Fig. 3 - Instrumentation system

The instrumentation system is presented in Fig. 3. The filter Co-Quad devices are configured to provide dc voltages for the C and Q quantities. These voltages are measured with a digital voltmeter and recorded on punched paper tape. The data are then reduced on a Univac 1108 and the modal parameters are listed and plotted.

An analog computer was used to calculate an estimate of the specimen kinetic energy from the responses indicated by the six velocimeters. This quantity was employed for servo feedback to control overall driving amplitude during the sweep tests and for kinetic energy decay damping analysis.

During this investigation the following manual tuning procedure was employed. The drive frequency was set at an apparent natural frequency of the specimen. The drivers were then adjusted individually so that their amplitudes were proportional to the in-phase component of the velocity at each drive point. During this adjustment process, the frequency was changed, as necessary, to maintain the apparent mode. The frequency was then stepped in small increments through the mode while the overall level was controlled to maintain constant indicated kinetic energy. Force and response data were recorded at each step.

Typical results, in the form of individual and total energy admittance are presented in Figs. 4 and 5. This data set for the 3rd, 4th, and 5th modes of the structure is a composite made up of three tuned sweeps.

To determine the damping by the energy decay method, each mode was tuned and then the decay of the kinetic energy was recorded. A typical energy decay is shown in Fig. 6.

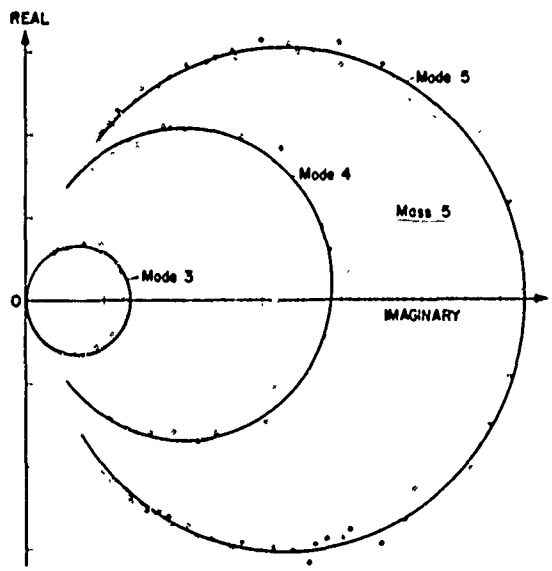

Fig. 4 - Individual energy admittance

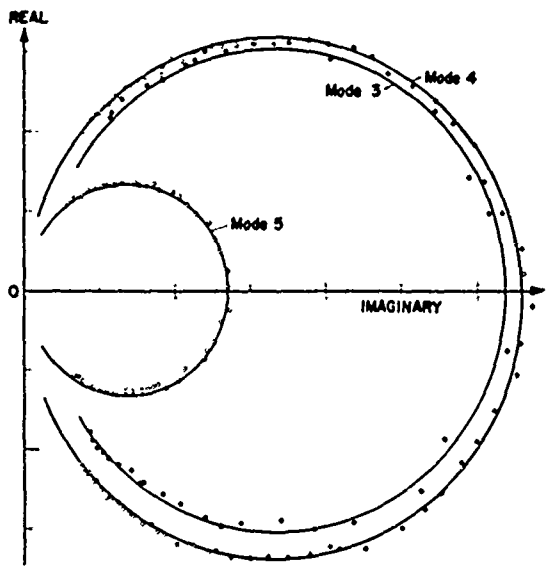

Fig. 5 - Total energy admittance

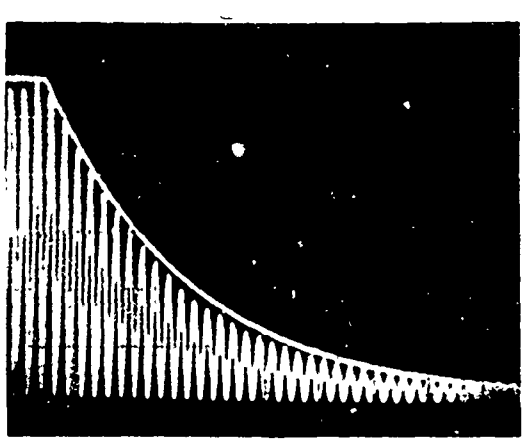

Fig. 6 - Kinetic energy decay

The specimen was analyzed with the LMSC REXBAT-5 finite element computer program. A 102-degree-of-freedom model was constructed from the test specimen dimensions and mass distribution. For modeling purposes, the joints were assumed rigid. The six disk masses (which included the masses of the shaker and velocimeter magnets) were modeled as rigid lumps with translational and rotary inertia.

The mode shapes, natural frequencies, and damping for the three modes studied here are presented in Table 1. The comparison between the test and analytical mode shapes and frequencies is very good.

SUMMARY

As has been discussed in the preceding sections, previously available experimental techniques for modal definition have several disadvantages. Single driver tests, regardless of analysis technique, will not yield accurate results in the presence of nonlinear behavior, closely spaced modes, or poorly conditioned force application. Multiple shaker dwell techniques suffer from the lack of a suitable fine tuning criterion and a method for recognizing and dealing with nonlinear behavior. In addition, the dwell method is extremely time consuming and, consequently, expensive.

The complex energy admittance data analysis technique when combined with the tuned sweep method retains many of the advantages of the tuned dwell and complex admittance procedures and eliminates many of their disadvantages.

A piece-wise tuned sweep method has been demonstrated in which the structure is tuned for an apparent mode by adjusting the shakers using a simple procedure. A sine sweep is then performed while the tuning is maintained. This method yields excellent modal data and the testing time required is considerably less than the conventional tuned dwell method.

The data are analyzed using the relationships derived with the aid of a digital computer. In essence, this method shifts the main burden of work from the expensive test procedure to a relatively inexpensive computer data processing operation.

A further improvement in the method, which has not yet been fully explored, would be derived from automation of the tuning process. This would provide a twofold advantage – first, the tuning should be more accurate (and less mistake prone), and second, a further time saving can be achieved.

A six-channel automatic analog tuning device is presently being built. This unit is designed to proportion the shaker amplitude such that

$$\left[F_{i_{Command}}\right] = \left[D\right]\left[F_{i_{Measured}}\right]\left[V_i\right]\left[\cos\phi\right]$$

where D is determined by overall specimen amplitude, i.e., maintaining the specimen kinetic energy constant. Thus for $F_{i_{Command}} = F_{i_{Measured}}$, as occurs when the system is stationary, we obtain

$$F_i = D^2 \cdot V_i \cos\phi$$

It is expected that this system will provide an accurate "automatic" modal test for systems with modal spacing greater than one bandwidth. For finer spacing, the manual tuning procedure used in this investigation will probably be necessary. Results of the automatic tuning program are expected in the near future.

ACKNOWLEDGMENT

Many people at the Lockheed Palo Alto Research Laboratory have contributed to this work. The authors would like to thank, in particular, Miss Jessie Vosti and W. W. Lee for their help.

TABLE 1
Tuned Sweep Modal Test Results

			Mode Number		
			3	4	5
Natural Frequency (Hz)	Test		16.9	20.2	21.4
	Analysis		16.6	19.7	20.8
Normalized Mode Shape	Test	1	0.86	-0.67	~0
	Analysis		0.867	-0.647	-0.002
	Test	2	-0.25	-0.29	1.00
	Analysis		-0.270	-0.180	1.000
	Test	3	-0.03	1.00	~0
	Analysis		-0.031	1.000	-0.067
	Test	4	-0.71	-0.62	0.18
	Analysis		-0.756	-0.535	0.266
	Test	5	-0.35	-0.63	-1.01
	Analysis		-0.401	-0.734	-0.801
	Test	6	-0.58	-0.32	0.30
	Analysis		-0.526	-0.278	0.253
Structural Damping Coefficient	Eq. (13)		0.013	0.012	0.023
	Eq. (15)		0.022	0.017	0.032

REFERENCES

1. Kennedy, C. C. and Pancu, C. D. P., "Use of Vectors in Vibration Measurements and Analysis," Journal of the Aerospace Sciences, Vol. 14, No. 11, Nov 1947

2. Stahl, C. V., Jr., "Phase Separation Technique for Ground Vibration Testing," Aerospace Engineering, Jul 1962

3. Lewis, R. C., and Wrisley, D. L., "A System for the Excitation of Pure Natural Modes of Complex Structures," Journal of Aerospace Sciences, Vol. 17, No. 11, Nov 1950

4. Smith, S. and Woods, A. A., Jr., "An Energy Technique for Use In the Vibration Testing of Complex Structures," LMSC-A973847, Oct 1970 (to be published in Experimental Mechanics)

DISCUSSION

Mr. Blake (Naval Ship Research and Development Center): Did you set the magnitude of the force or the real part of the force proportional to the real part of the velocity?

Mr. Smith: It is the amplitude of the force and it winds up being the same thing if I heard you right. I believe the amplitude of the force in this case is proportional to the imaginary part. If we use Kennedy and Pancu's complex energy notation I believe its the imaginary part of the force.

Mr. Blake: In the normal impedance relationship are not the magnitudes of the force and the velocity proportional?

Mr. Smith: No, this is a special case. We are not adjusting the force relationship as we sweep through the mode. This is set at the modal frequency. Remember that we are using multiple shakers and this is a relationship between shaker levels. It is not the overall shaker level. We adjust individual shaker levels up and down relative to one another according to this criterion, and the over-all shaker level is controlled by the specimen kinetic energy. We adjust the shaker levels manually at the natural frequency or at an apparent natural frequency. It is only done once for each mode. We are building an automatic tuning box which will do this. It will hunt for a natural frequency, it will set our shakers up automatically to the natural frequency, lock them in that position, and then we will back the frequency off and sweep through the mode automatically instead of manually. This is a very easily applied criterion to use automatically.

Mr. Curtis (Hughes Aircraft Company): Do you attempt to adjust the phase angle between the individual shakers or are they all in phase?

Mr. Smith: They are all in phase. For a linear vehicle it has been shown that this is the condition that we want to have. Now a nonlinear vehicle is a different case entirely and we have not worked on that. Our problem is that the mathematics gets extremely messy using this technique if we allow phase angle variations in the shakers. This technique can be generalized to handle that type of thing but it is something we have not done yet, and I am not sure that we want to either.

Mr. Zudans (Franklin Institute): If you test real vehicles how many mass points do you need? It seems if you would need thousands of them. Can you put that much instrumentation on and process the data the same way you did for the six or eight mass points?

Mr. Smith: That is correct and obviously we have to cut ourselves off at some point. It can also be said that we need thousands of shakers. If we can cover 75 or 80 per cent of the mass points on the vehicle, or of the mass on the vehicle, I think that we have a pretty good criterion. It is a matter of financial problems rather than theoretical problems.

Mr. Zudans: I do not question the financial problem but it is just a sheer space problem. How can you accomodate all these things in a structure which is relatively dense in itself? Think about an airplane that was analyzed to 10,000 degrees of freedom for structural analysis, now you want to verify the mode shape by this modeling what would you do then?

Mr. Smith: Modal tests of large vehicles that have been done in the past have been satisfied with something between 100 and 200 response points. This is not going to verify everyone of the analytical degrees of freedom. It is a spot check on the analytical model and this is all anybody is ever going to do I think.

EQUIPMENT CONSIDERATIONS FOR ULTRA LOW FREQUENCY MODAL TESTS

R. G. SHOULBERG
R. H. TUFT
GENERAL ELECTRIC COMPANY
VALLEY FORGE, PENNSYLVANIA

A vibration system was developed for determining dynamic characteristics of flexible light weight structures with inherently low frequency vibration modes, and low internal damping relative to windage effects. System elements developed and integrated were:

- DC coupled, high displacement vacuum rated electrodynamic vibration exciter
- Low frequency sweep oscillator
  Range .008 Hz to 10k Hz
  Sweep rates 6 x 10^{-5} to 6 decades/min.
  Linear, logarithmic and hyperbolic
- Non-contacting, vacuum rated vibration sensors
- Signal analyzer for determining coincident/quadrature amplitude relation between forcing and response parameters
- Servo control for maintaining constant forcing function

These elements were integrated and applied during extensive dynamic testing of a large Roll-Up Solar Array at absolute pressures of approximately 1 Torr.

INTRODUCTION

A study resulting in development hardware was completed recently by the Space Division of the General Electric Company. The objective of the program, under JPL Contract 952314, was to develop a 30 watt per pound solar cell array for energy conversion in general space application. Preparation of a detailed design performance of required analyses and subjection of the engineering model to a comprehensive test program were included in the scope of the effort.

TEST ARTICLE DESCRIPTION

The configuration, following a roll-up approach for stowing the required 250 square foot array, is shown in Figure 1. Comprised of two storage drums, the unit is mounted on a central support structure. Each drum has a bearing, a slip ring assembly for power and sensor signal transfer, and a Negator spring motor to provide constant tension in the solar cell blanket. One blanket, an interconnected assembly of cells mounted on a flexible substrate, is rolled onto each drum with the outboard edge attached to the leading edge member. A deployable boom mounted on the center support is also attached to this leading edge member. The array is deployed by extending the boom. Outboard end supports are provided in the launch configuration, and are pyrotechnically released before deployment.

An interplanetary spacecraft was used as a baseline for the study and four arrays would be mounted on its square cross section. This spacecraft concept was for reference only, as the array design is intended to be adaptable to a variety of spacecraft configurations and missions. Weight was a primary consideration in all design tradeoffs and decisions.

DYNAMIC CHARACTERISTICS OF DEPLOYED ARRAY

The solar cell array has a maximum deployed length slightly more than 34 feet. This, coupled with the low weight allowance - nominally 82.5 pounds, results in very low natural frequencies. Separation of these frequencies from nominal "on orbit" control modes dictated a design goal for the first resonance of no less than 0.04 Hz.

Determination of the first ten vibration modes through measurement was an important requirement of the program. The very low frequency range presented several problems relative to vibration excitation, instrumentation and data analysis equipment. In addition, the effect of "zero G" conditions of space had to be considered.

TEST APPROACH FEASIBILITY

During the Phase I study, some initial ambient pressure modal tests were performed. These were exploratory with the principal objectives to demonstrate the feasibility of the proposed Phase II test methods.

A 20-foot simulated array, deployed upward, was used for the specimen. Base excitation was accomplished with a small (50 pound force) permanent magnet electrodynamic shaker and a D-C coupled power amplifier.

Input and response displacements were measured with optical tracking devices (Physitech Model 39 and 39A) used in conjunction with light weight targets mounted on the array. The test arrangement is shown in Figure 2.

The base of the array was mounted to a fixture plate supported on a lateral hydrostatic bearing for translational excitation. A rotational bearing was used for mounting when determining torsional modes. Vibration signals of 0.04 Hz and higher were generated with a Spectral Dynamics Sweep Oscillator Model 104-2. Servo control was provided with "a man closing the displacement sensing loop". Base excitation and target displacement signals were recorded during swept vibration with magnetic tape speed set at 3-3/4 ips. During playback, however, the speed was 120 ips. In this manner, a time compression ratio of 32:1 was realized. In effect the test frequencies were raised above the 2 Hz low frequency limit of the equipment used to obtain phase relations between the input and responses.

Figures 3 and 4 are plots of the in-phase coincident and quadrature response of translational excitation. These clearly indicated that use of phase separation techniques would provide adequate data to define the modes.

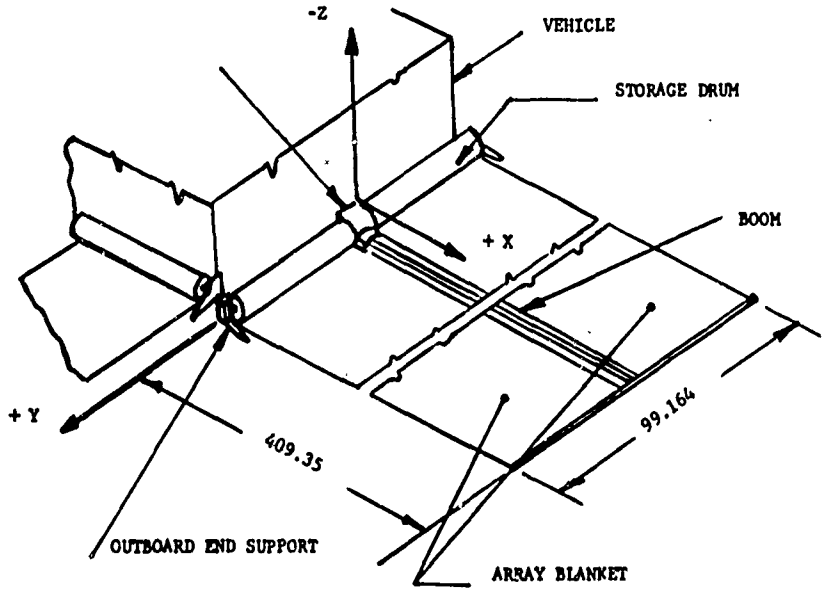

Figure 1. Roll-Up Solar Array Configuration (Coordinate System Shown)

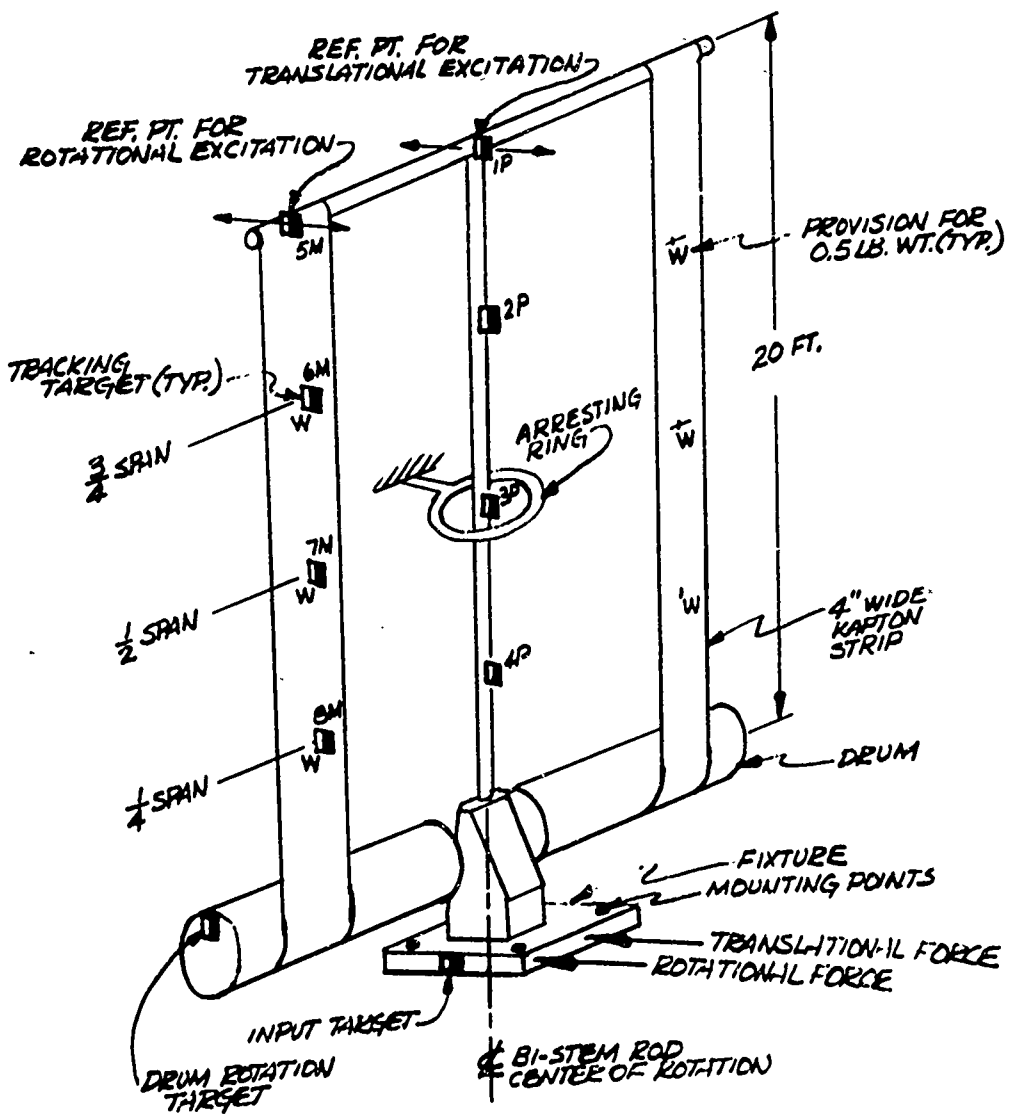

Figure 2. Phase I Test Arrangement

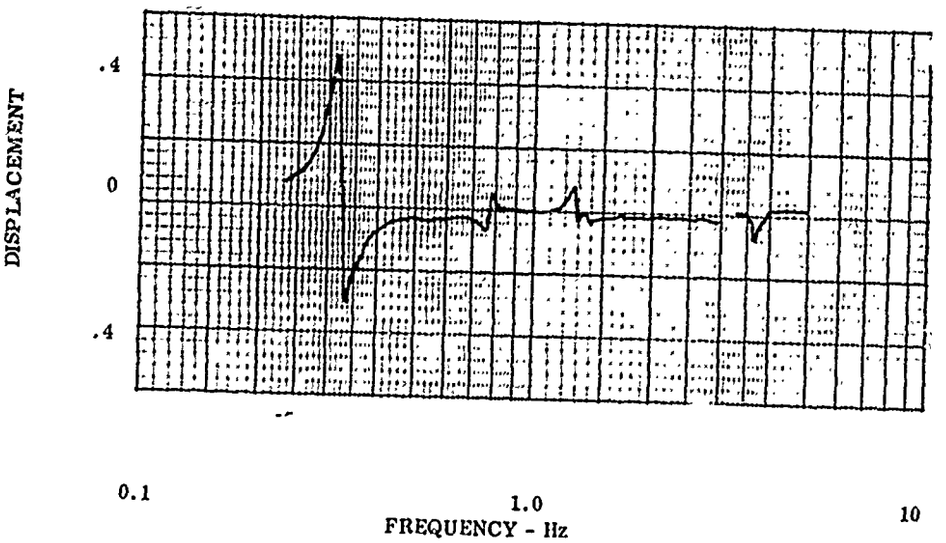

Figure 3. In-Phase Response - Translational Excitation

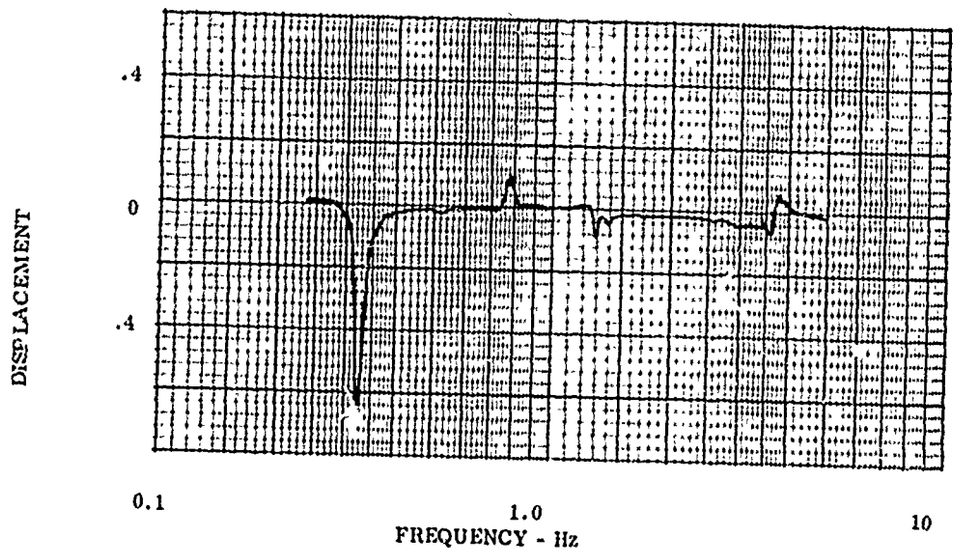

Figure 4. Quadrature Response - Translational Excitation

EQUIPMENT CONSIDERATIONS

As anticipated, the test also confirmed that one major requirement for modal testing of the deployed array was the reduction of the damping and virtual mass of the atmosphere. This could be satisfied by testing in vacuum, although the low pressure environment added complexity to the test and the equipment required. The atmospheric pressure test revealed several desirable equipment features which would reduce test time and improve data validity. These equipment considerations will be discussed.

- Vacuum Test Facility for test pressure of approximately 1 Torr.
- D-C coupled, high displacement, vacuum rated vibration exciter
- Non-contacting, vacuum rated vibration sensors
- Low frequency sweep oscillator
- Signal analyzer for determining in-phase and quadrature ratios of response and forcing parameters
- Servo control for maintaining a constant forcing function during vibration sweeps.

A block diagram of the interrelation of these is shown in Figure 5.

VACUUM TEST FACILITY

A pressure of nominally 1 Torr was considered to have negligible effect on both the external damping and the virtual increase of mass caused by the atmosphere. This pressure can be readily achieved in any of four large test chambers at the General Electric Space Center. The size of the array and the test arrangement were the major factors for the selection of the Valley Forge Space Simulation Facility. Shown schematically in Figure 6, this chamber affords ample provision for shaker support above the walkway elevation. This was required to enable a vertically downward deployment. In this manner, gravity could effectively be correlated with the mathematical model. Good coorelation of test data with analytical results, gravity considered, would provide confidence in the analysis when extended to the "zero G" case. The test configuration is "fixed-free"; affording a free boundary condition at the leading edge. This is the condition of the array in an orbiting application.

The length of the partially deployed array was governed by the facility size and set at 26 feet. This length was factored into the mathematical model and the analytical study. Required pressure of approximately 1 Torr was readily achieved with the mechanical pumping system associated with the

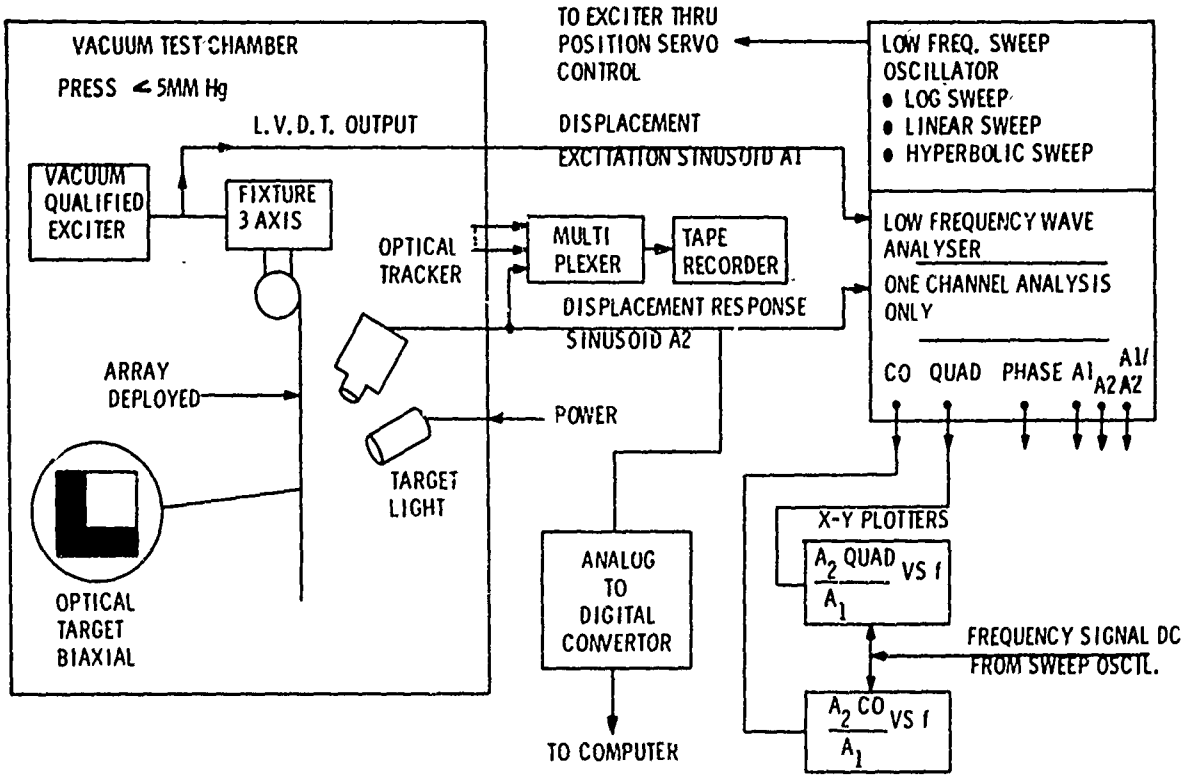

Figure 5. Block Diagram of Equipment Interrelation

test facility. Pumping speed is 2,500 cfm with a blank-off of the roughing pumps in the micron range.

VIBRATION EXCITER

Translational and torsional vibrations were required at very low frequencies - virtually DC. Double amplitude (DA) displacements greater than 1/2 inch were also desired in order to generate significant responses at the higher modes.

To minimize shaker complexity, recognizing that a high force was not necessary, an air cooled exciter was best suited for the application. The specifications prepared for procurement bids received no response. One manufacturer, Ling Electronics, offered a 150# force, 4 inch stroke Model 370 Thruster for evaluation at low pressure. A DC coupled Model TP850 Amplifier was also provided. With the shaker operating in a blocked armature model testing was conducted at pressures of 35 Torr and 22 microns. Derated to 30#, operation proved that at 22 microns, the allowable temperature rise will not be exceeded before 10 hours of continuous operation. As this time period appeared sufficiently long, the Ling Model 370 was procured and used. To assure operation within the recommended temperature limits, the field coil temperature was monitored throughout the modal tests.

NON-CONTACTING VIBRATION SENSORS

Feasibility test results demonstrated that optical trackers would provide non-contacting vibration sensing signals. Standard units, however, would not satisfy all of the requirements and special modifications were necessary. These were primarily to afford operation in a vacuum. All candidate trackers use photo-multiplier tubes, and the required high voltage proved the major problem for low pressure operation. The design eliminated arc-over and corona discharge when operating through a pressure range from 760 Torr to 10^{-7} Torr. Construction materials also precluded outgassing products which could result in contamination of the lenses.

As the modal test sweep times were significantly long, and the tracker heads inaccessible for periods of several days, provisions were made for

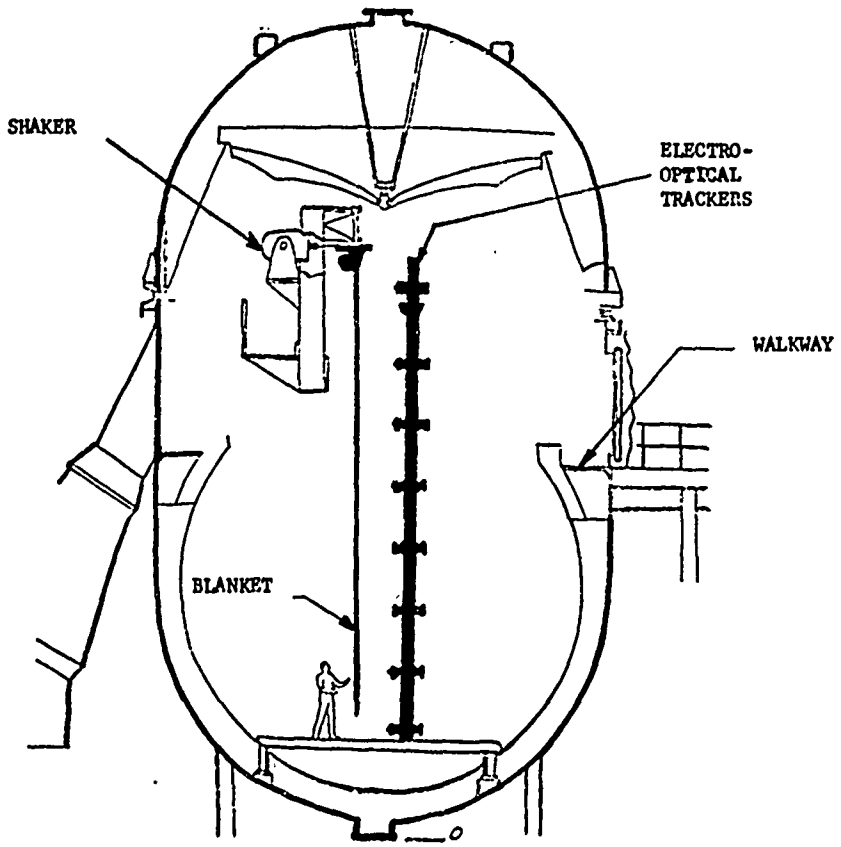

Figure 6. Deployed Modal Test Set Up

a common external calibration signal. This allowed periodic verification of proper operation.

The final arrangement utilized eight two-axis Optron Model 800 Trackers modified to specifications. These have the capability of measuring displacements in two orthogonal directions normal to the optical axis. The frequency response range is from DC to 10kHz. Sensitivity is dependent on the lens system, and for this application resolution was set at 0.001 inch. Two of the trackers were fixed and focused on the ends of the leading edge member. Six were mounted on a horizontal scanning bar which vertically traversed the deployed length. This bar can be remotely positioned during the test to any of ten equally spaced locations. Target placement is shown in Figure 7.

The targets were white paper mounted on the solar cell side of the array blankets. Contrast at the edge of the targets is necessary for tracker operation. The edge, which must be illuminated, is sensed by the tracker. Essentially a "camera", the tracker head contains an image dissector tube on which the target interface is imaged. Electrons are emitted in a beam from the photo cathode proportional to the intensity of the projected light. The electron beam is accelerated to refocus on a small aperture. Electron density is proportional to the light intensity of the image. A servo loop controls the electron beam through two deflection yokes to maintain the target edge centered in the aperture. The deflection current required is then used as a measure of the target displacement.

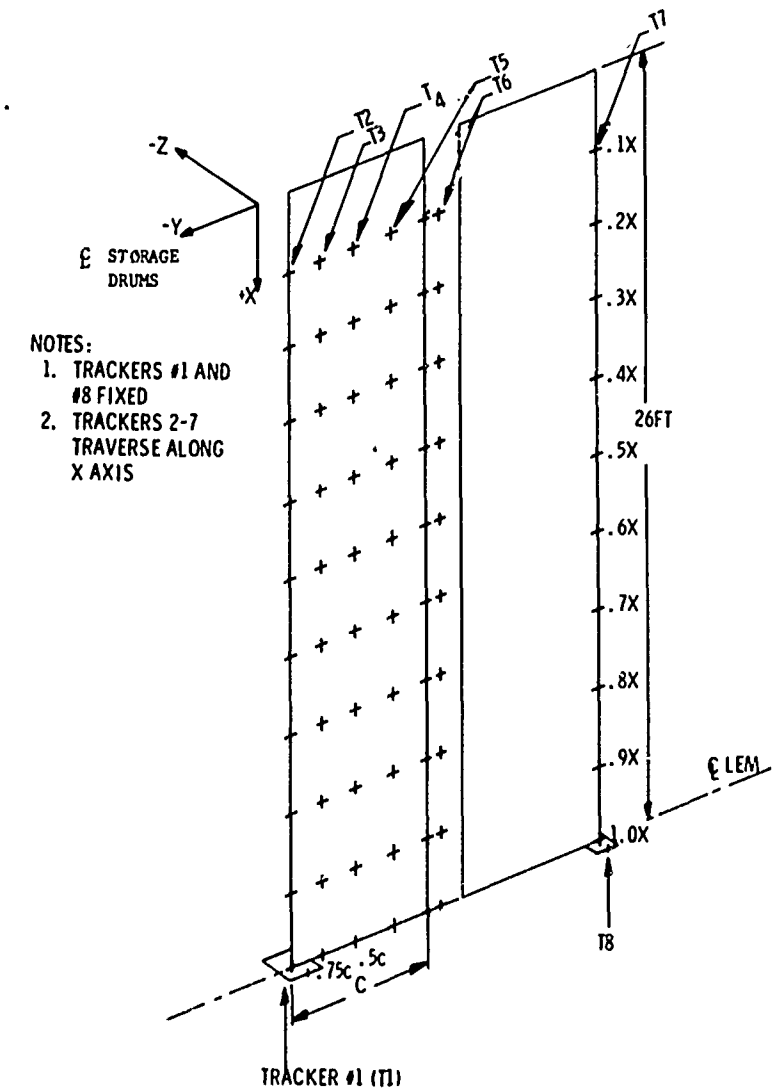

Figure 7. Target and Tracker Locations

As motion had to be monitored in the "Z" axis, the trackers were mounted at an angle relative to the blanket. Shown in Figure 8, this motion resulted in apparent motion (ξ). This arrangement was quite successful as the actual "X" motion was negligible; thus the apparent motion detected by the tracker was the result of blanket "Z" motion. Each tracker was individually calibrated for its test position.

As the tracker will detect any change in light intensity, stable direct current illumination is mandatory. Each tracker had an associated 12 volt illuminator. To reduce heat input to the specimen, the lamps were type V-12 PAR 56/WFL "Cool Beam". A multi-layer coating on the inside of the reflector surface acts as a filter, passing infrared energy through the reflector but reflecting the visible energy back into the light beam.

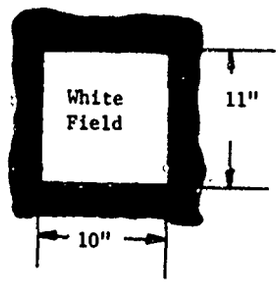

(a) Sketch of Target

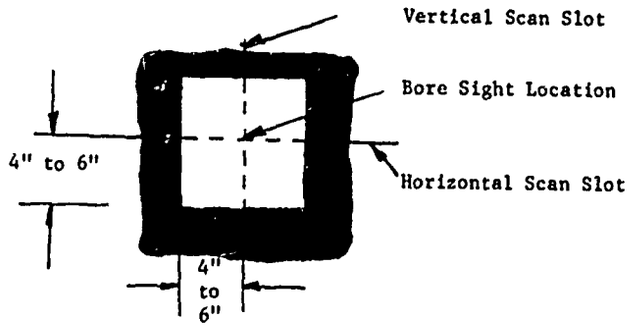

(b) Bore Sight Location

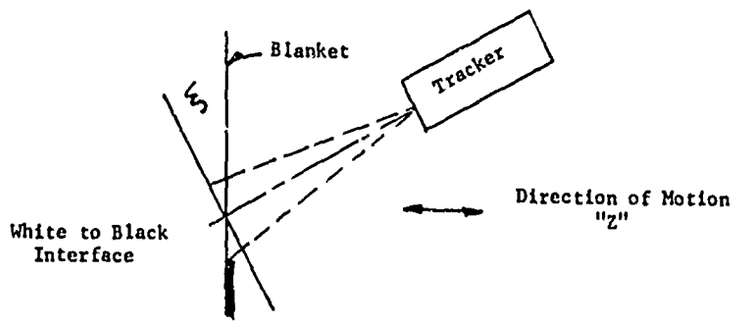

(c) Apparent Motion in ξ Direction

Figure 8. Target and Tracker Relation

SWEEP OSCILLATOR - SIGNAL ANALYZER

Problems had been anticipated in both the generation of low frequency signals, low frequency sweep rates and low frequency signal analysis. With no data available on the array damping coefficient in vacuum, and in light of using new testing techniques, the provision for sufficiently slow sweep rates was a prime consideration. The rate should be slow enough to avoid "beating" near resonant modes, yet it was desirable to sweep as fast as possible to reduce test time.

An in-depth analysis, not covered herein, [1] indicated that a hyperbolic sweep rate would be attractive. This is a logarithmic sweep in which the logarithmic sweep rate varies linearly with frequency. It can be expressed as:

$$\log_{10} \frac{f_1}{f_2} = K_{log}\,(f)t$$

Where $K_{log}\,(f)$ is a logarithmic sweep rate as a function of frequency. The sweep rate results in the number of cycles in a constant band width to be inversely proportional to frequency. Recall that a logarithmic sweep affords a constant number of cycles in a constant bandwidth. Damping was not expected to vary significantly with frequency; therefore, this sweep appeared favorable. In a hyperbolic sweep the same number of cycles occurs between the half power points of a constant Q system regardless of the resonant frequency. This results in the same amplitude build-up at each resonance as the amplitude is a function of the number of cycles at resonance. The hyperbolic sweep is also faster than either the log or linear sweeps. In sweeping from 0.02 Hz to 10 Hz, the hyperbolic sweep requires about 2-3/4 hours in contrast with a log sweep time of about 13-3/4 hours.

Another requirement in determining resonances and damping coefficients was the ability to obtain, measure and display the in-phase and quadrature components of response signals with respect to the forcing input signal. Here again, "off-the-shelf" equipment was not available to generate the hyperbolic sweep nor to provide phase information between low frequency signals.

A frequency response analyzer which had been recently introduced by BAFCO, Inc. appeared to have some of the elements necessary. This two-channel unit was designed to perform Fourier analysis on the output of two signals from an item under test. In accomplishing this, it generates the signal to the test item and provides internal sine and cosine reference functions. Modifications to the basic design were provided by the manufacturer to satisfy the specific requirements. These are:

- Frequency Range - 0.008 Hz to 10 Hz
- Sweep Range - 10 to 10^{-6} sec/decade
- Sweep Type - Linear, logarithmic and hyperbolic
- Return Signal Range - 10 mV to 10 V peak
- Output Signals
  - Each Channel Amplitude
  - In-Phase Component Ch 2 vs Ch 1
  - Quadrature Component Ch 2 vs Ch 1
  - DC Proportional to Frequency
  - DC Proportional to Log Frequency
  - Log of ch 2/Ch 1 Amplitude Ratio
  - Log of Ch/Ch 1 Amplitude Ratio (Absolute)
  - Log of Quad/Ch 1 Amplitude Ratio (Absolute)
  - Sign of In-Phase Component
  - Sign of Quadrature Component

Detailed theory of operation is not presented here. Reference [2] has a complete description. Briefly, the analog analyzer is based on a precision DC to frequency converter. The DC source establishes the sweep law and whether the signal is swept or constant. The output of the converter is a triangular wave of constant amplitude. This is shaped to a sine wave by a function generator and used for reference and output signal generation. The cosine reference is generated from the converter output through a second triangular wave, 90 degrees out of phase. A second diode function generator shapes the cosine wave. Signals from the item under test are then multiplied by the sine and cosine reference, attenuated for scaling, integrated or averaged to provide in-phase and quadrature components with respect to the excitation signal.

The unit also provides reference signals which can be recorded on tape in conjunction with other channels of test item data.

POSITION SERVO CONTROLLER

To maintain a constant displacement vibration input during swept frequency testing, some form of servo control is necessary. The conventional electrodynamic shaker control is generally limited to about 2 Hz, and therefore not applicable. In addition, the feed-back signal is normally generated by an accelerometer and integrated twice for displacement control. Accelerometers in the range of interest with double integration can only result in more complexity.

The servo control finally applied used a linear variable differential transformer (LVDT) for sensing

[1] See Reference at the end of this paper.

displacement and employed a relatively straight forward position controller. This approach was satisfactory for the test, however more development is necessary to afford a frequency response comparable to the other elements.

DISCUSSION OF RESULTS

Each element required development - not beyond the state of the art, yet heretofore not reduced to functional hardware. Design, fabrication and the integration into a workable tool was a challenge successfully achieved through the efforts of many.

The tool, however, is not the measure of the results and some indications of the outcome of the modal testing are presented.

The use of the hyperbolic sweep proved effective for the ambient pressure sweep. On the basis of an assumed damping ratio $\beta = c/c_r$ of 0.10 and a Hok's sweep rate parameter in excess of 2.0, the sweep rate was selected. Twenty-six minutes were required to vibrate from 0.13 Hz to 1.0 Hz. Hok concludes that this sweep is slow enough to allow the response to build up with acceptable distortion. [1]

Figures 9 and 10 are the on-line in-phase and quadrature response plots of the ambient pressure sweep. At the fundamental resonance (0.16 Hz) a peak quadrature response of 3.06 inch D.A. was recorded. Assuming the predicted mode shape to be correct, this corresponds to a damping ratio of about 0.1. Thus Hok's parameter was validated.

In vacuum, the hyperbolic sweep generally was too fast for the initial rates selected. The first sweep from 0.13 Hz to 0.25 Hz was not satisfactory with a rate of 2,050 sec/decade as severe beating was noted. Beating did not cease until a rate of 2 hours/decade was used between 0.29 Hz and 1.0 Hz. An additional reduction of sweep rate to 14,700 sec/decade was necessary in the range of 0.22 Hz to 0.29 Hz before beating ceased. Final resolution of the primary mode was established with a 71 minute sweep from 0.236 Hz to 0.256 Hz. This is a sweep rate of 175,100 seconds (over two days) per decade. It was also linear. This more than anything justified the initial concern over obtaining broad flexibility in the sweep oscillator. Plots of this sweep are shown in Figures 11 and 12.

The predicted resonant frequencies compared to those measured are shown in Table 1. It can be seen that the difference in natural frequencies between the ambient pressure and vacuum anticipated influence of the virtual air mass.

Damping coefficients varied for the primary mode, depending on the method used for determination, from 0.003 to 0.0055. Table 2 summarizes the results for the out of plane modes with translational excitation. The damping factor in vacuum is about 1/20th that determined at atmospheric pressure.

CONCLUSIONS

Through the performance of this test program, the development of low frequency vibration equip-

Table 1. Summary of Resonant Frequencies from Deployed Dynamic Tests

	Mode Number					
	Measured			Predicted*		
	1	2	3	1	2	3
A. Out-of-Plane Symmetric Excitation						
Ambient	.16	.55			**	
Vacuum	.252	.632	.781	.248	.55	.94
B. Out-of-Plane Ant-Symmetric Excitation						
Ambient	.12	.50	.99		**	
Vacuum	.174	.65	.74	.232	.58	.96
C. In-Plane Excitation						
Ambient	1.00				**	
Vacuum	1.015			.38		

*Blanket membrane modes omitted

**No analysis was made which included aerodynamic effects

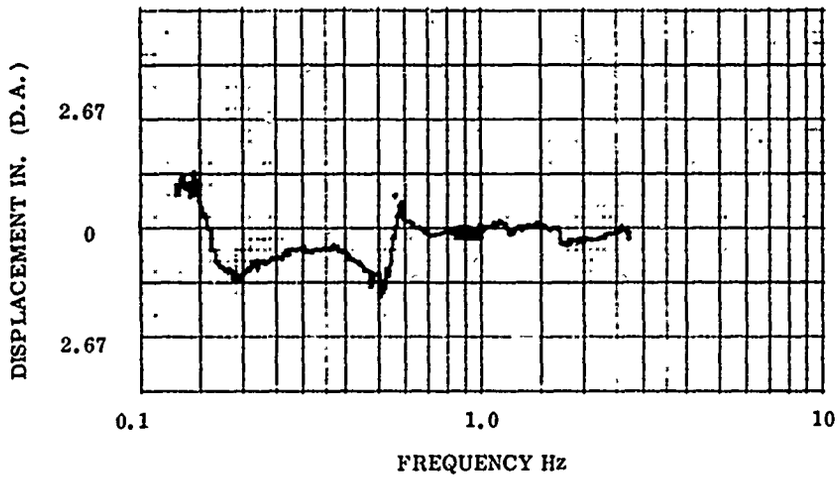

Figure 9. In-Phase Response - Translational Excitation
Ambient Pressure

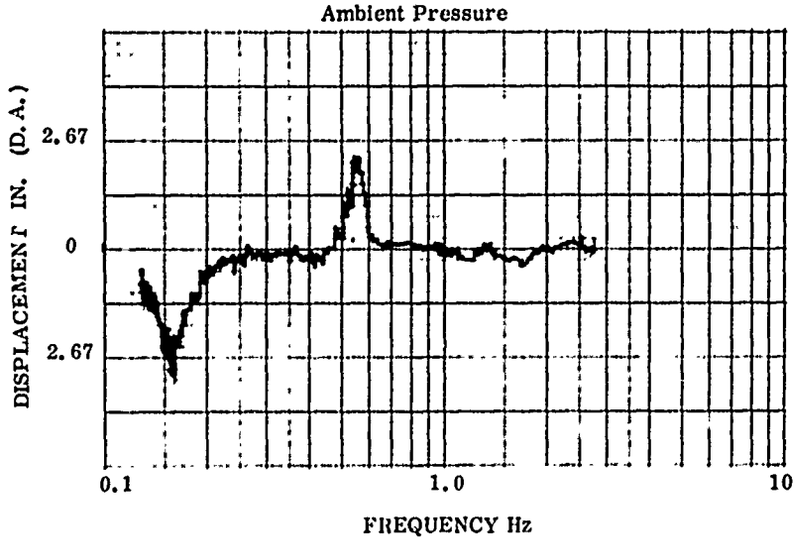

Figure 10. Quadrature Response - Translational Excitation
Ambient Pressure

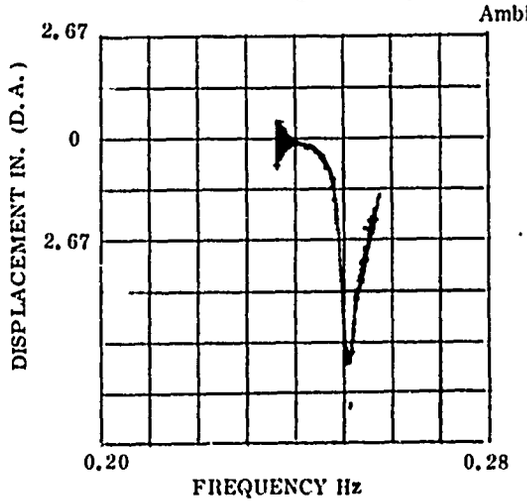

Figure 11. Quadrature Response

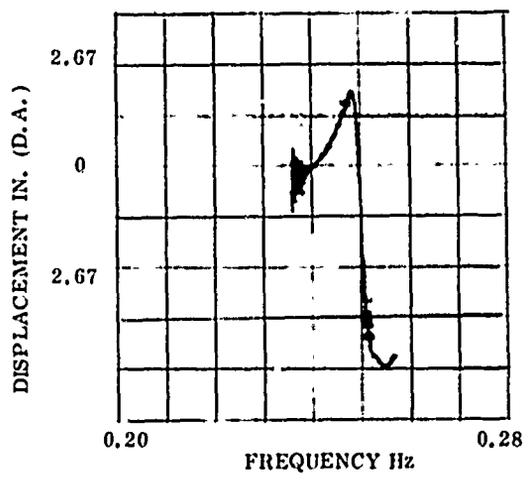

Figure 12. Quadrature Response

ment has been advanced significantly. Work is still required, particularly, when larger, lighter structures for space application are considered.

Table 2. Damping Coefficients for Out of Plane Modes - Symmetric Excitation

Modal Frequency (Hz)	Damping Coefficients				
	Method 1		Method 2		Method 3
	β 1.a	β 1.b	Input Level in DA	β	β
0.251	0.003	0.0042 0.0053	0.025 0.050	0.003 0.0055	0.0055
0.632	-	-	-	-	-
0.781	-	-	0.10 0.20	0.0275 0.0026	- -

Notes: Method 1 determined from decay of motion is a decay from response to step input out, and 1.b is decay from dwells at a natural frequency.

Method 2 is determined from frequencies of peak in-phase response to a slew sinusoidal sweep.

Method 3 is determined from comparison of response with analytical responses.

REFERENCES

1. Hok, Gunnar, "Response of Linear Resonant Systems to Excitation of a Frequency Varying Linearly with Time", Journal of Applied Physics, August, 1947.

2. Instruction Manual - Sweep Modal Vibration Analyzer System Model 911 G, BAFCO, Inc., Southampton, Penna. 18966, January 1970.

ACKNOWLEDGEMENTS

The program requiring the equipment described was conducted for NASA and managed for the General Electric Space Systems Operation by K. Hanson. Thanks are due to R. Barr, R. Carr, D. Grady, J. Quinter, R. Sipple and C. Stahle for their many and various technical contributions.

BIBLIOGRAPHY

1. Rollup Array Phase I Modal Test Report, Addendum to GE-MSD Proposal No. F-20430 JPL RFP EU2-9056, General Electric DIN 68SD4262, 27 May 1968.

2. Final Report - Rollup Subsolar Array-GE-SSO 70SD4286, February 1, 1971.

3. Instruction and Service Manual for General Electric Co. Model 800 Tracking System P.O. #028-H59112, Optron Corporation, 50 Fitch Street, New Haven, Conn. 06515.

DISCUSSION

Mr. Wrenn (Lockheed Missiles and Space Company): How did gravity affect the modes and the results that you obtained? How did the orthogonality of the modes that you obtained with a single shaker check out with the orthogonality that you had obtained from the analysis which would be much more accurate?

Mr. Shoulberg: The first mode was predicted at 0.248 Hz as compared to the measured 0.252 Hz which I feel is quite close.

Mr. Wrenn: I was not thinking so much about the frequency as the mode shape, because as you get to the higher modes, not necessarily the fundamental, the shape would be important. Did you run an orthogonality analysis check on your experimentally developed modes?

Mr. Shoulberg: I can not answer that question but I do know that the results were very close to prediction.

Mr. Wrenn: So that gravity had very little effect?

Mr. Shoulberg: Gravity had an effect but not in the test. It certainly affects the actual mode shape, for zero gravity this frequency was considerably lower. There was a decided effect of gravity in the math model. We took gravity into consideration during the test and it checked out with the math model, of course we had the tension in the math model.

COMBINED-AXIS VIBRATION TESTING OF THE SRAM MISSILE

W. D. TROTTER AND D. V. MUTH
THE BOEING COMPANY, AEROSPACE GROUP
SEATTLE, WASHINGTON

(U) The requirement of the Short Range Attack Missile assembly vibration test, as part of a test series including structural static and fatigue load tests and a sonic fatigue test, was to demonstrate system operability during a simulated free flight mission after long-duration exposure to ground operation and captive flight environments. Flight test data showed that vibration levels were low and that conventional "black box" test procedures would be inappropriate. The technique described represents a departure from conventional test methods and is particularly well suited to the unique requirements of relatively large air launch missiles.

INTRODUCTION

(U) This paper describes the vibration test procedures that were used in qualifying the Short Range Attack Missile (SRAM) assembly. Its significance lies in the departure from conventional vibration test procedures that are applicable to small "black boxes" and standardized levels that do not represent the service environment. The test was unique in that it included simultaneous excitation in all axes, utilized all random input, and controlled input from multiple response accelerometers.

(U) SRAM is an air launched solid propellant missile that weighs approximately 2200 lbs. Its physical dimensions and component locations are shown on Figure 1. The overall length is 14 ft. to 16 ft., depending upon configuration, and its maximum diameter is 17.5 inches. It has the requirement, typical of air launched missiles, of long duration exposure to captive flight environments prior to missile operation. Its carriage environment is the product of external and internal carriage on FB-111 and B-52 aircraft, and flight envelopes that include low and high altitude supersonic velocity. Carriage configurations of SRAM are shown on Figures 2 through 5.

(U) The SRAM vibration qualification test was based upon extensive flight test

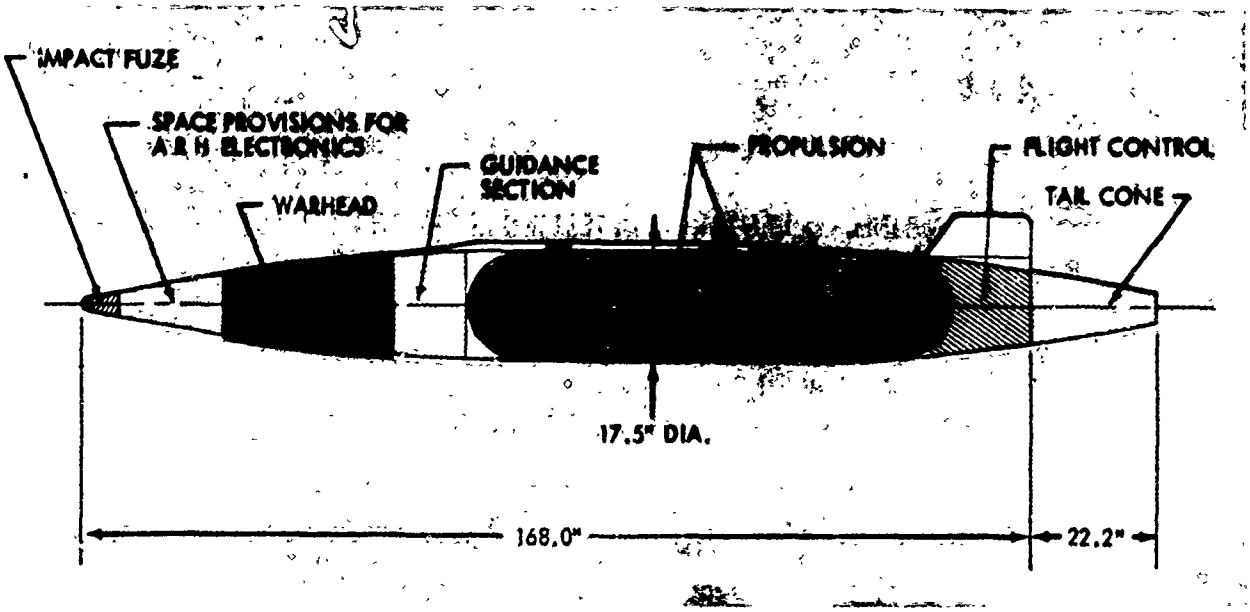

FIGURE 1 SRAM INBOARD PROFILE

measurements and logically combined with structural fatigue tests, and sonic fatigue tests to fully cover the environment frequency spectrum.

REQUIREMENT/OBJECTIVE

(U) The requirement of the vibration test as part of a test series, including structural static and fatigue load tests and sonic fatigue tests, was to demonstrate the missile system operability during a simulated free-flight mission after long-duration exposure to the ground operation and captive flight environments equivalent to four service lives.

(U) Two very important considerations in meeting this requirement were the quality of the environmental simulation and the risk of overtest. The missile test specification required that test levels were to be derived from flight test measurements. Accordingly, acoustic and vibration surveys were conducted for the significant phases of ground operation, captive flight and free flight to obtain the necessary data to derive test envelopes.

(U) The requirement to test to levels derived from flight tests favored a test set-up which properly simulated the missile restraint conditions, i.e., missile supported on the ejector for captive flight and missile soft mounted for free flight in order to preserve the fundamental resonance frequencies of the system. It was reasoned that the random vibrations measured in the payload, on the motor case and elsewhere in the missile, could not be realistically or safely reproduced by the conventional test using a rigid vibration fixture and a prescribed "input" motion at the clevises on the motor case because:

1. The test fixture would be very large, and fixture resonances at low frequencies would be unavoidable. The fixture resonances would be difficult or impossible to control.

2. A prescribed input motion spectrum would result in large resonant

FIGURE 2 FB-111/SRAM EXTERNAL CARRIAGE CONFIGURATION

FIGURE 3 B-52/SRAM EXTERNAL CARRIAGE CONFIGURATION

FIGURE 4 B-52/SRAM PYLON ARRANGEMENT

FIGURE 5 B-52/SRAM INTERNAL CARRIAGE CONFIGURATION (MOCKUP)

responses at system antinodes, for which the missile and its components were not designed. For example, the airframe was designed for the captive flight and free flight loads and ejection, but not for artificially induced resonant missile bending responses which could well exceed the service loads.

3. A single "input" could not be expected to reproduce the local vibrations measured at the various locations in the missile.

(U) To have attempted a conventional vibration test set-up with the missile mounted to a large rigid fixture, and the forces applied through the fixture, would have resulted in a complete distortion of the spatial distribution of the vibration responses along the missile and would have met neither the letter nor the intent of the test specification.

APPROACH/IMPLEMENTATION

(U) In view of the defects of a conventional test and the availability of service vibration measurement, from which to derive test levels, it was decided to use multi-point excitation employing moderate-size vibrators. This made it possible to adjust the individual inputs so as to reproduce, with appropriate margins, the measured service vibrations at the various locations throughout the missile.

(U) Service vibration measurements were available from the forward and aft ends of the payload, from the electronics section, and from the motor case. Typical data are illustrated on Figures 6, 7 and 8. Measurements at most locations had been recorded during all significant captive flight conditions as well as during free flight. Vibration measurements at all flight conditions and carriage positions were low. The significant service conditions - those that generated the highest internal vibration levels - were:

Captive flight, aft outboard on the B-52 wing pylon, during takeoff and climb to 25,000 feet. (long duration of exposure)

Captive flight, in the FB-111 weapons bay, with the doors open (weapons bay buffet) (brief exposure)

Free flight, at maximum aerodynamic pressure (short duration)

(U) The sequence of test conditions was set up to reflect worst-case environments. This conservative test assumed a missile exposed for its entire design service life to the B-52 pylon environment, then transferred to an FB-111 weapons bay for launch and free flight.

(U) Test durations were reduced for the captive flight test phase in order to complete the test in a realistic time span. Accordingly, the test levels were increased by an amount necessary to correct for the shorter test duration. This adjustment was made by using appropriate random loading S-N curves for the critical materials and determining the proper stress ratio at various frequencies for the test to produce equivalent fatigue damage. The corrections are shown in Figure 9. Smaller adjustments were required for weapons bay buffet and free flight because the test durations were longer than the service exposures.

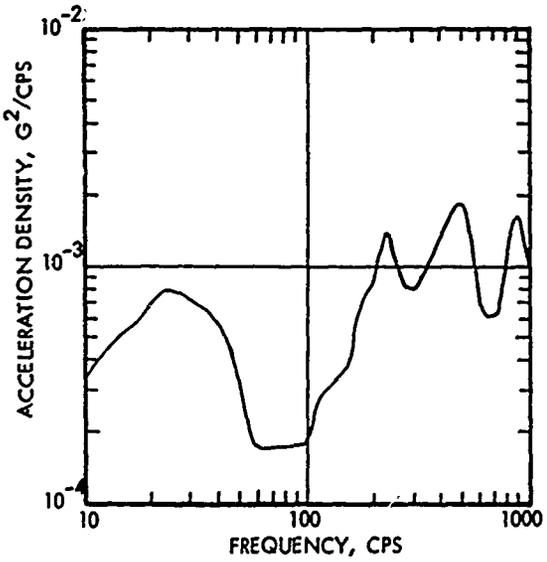

FIGURE 6 ROCKET MOTOR VIBRATION MEASUREMENTS CAPTIVE FLIGHT FB-111 BAY

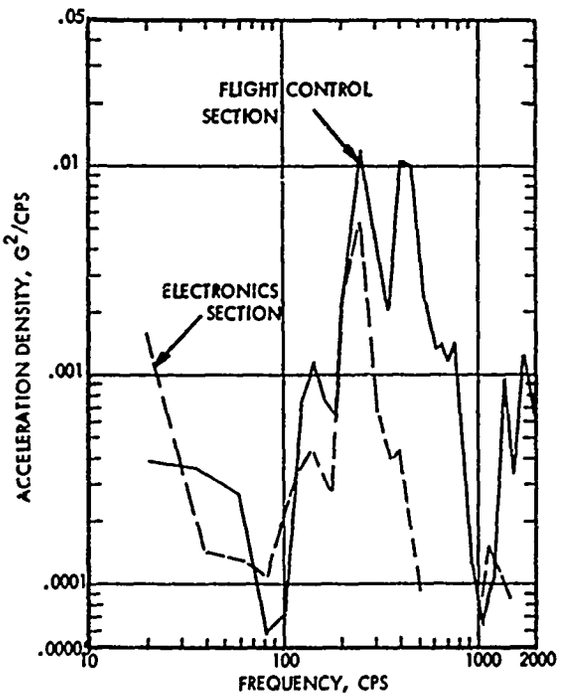

FIGURE 7 MISSILE VIBRATION MEASUREMENTS CAPTIVE FLIGHT B-52 PYLON

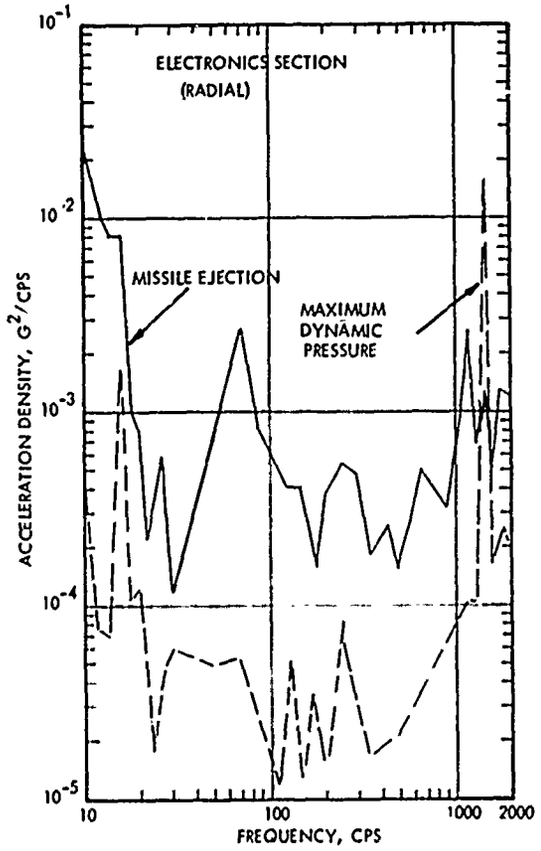

FIGURE 8 MISSILE VIBRATION MEASUREMENTS FREE FLIGHT

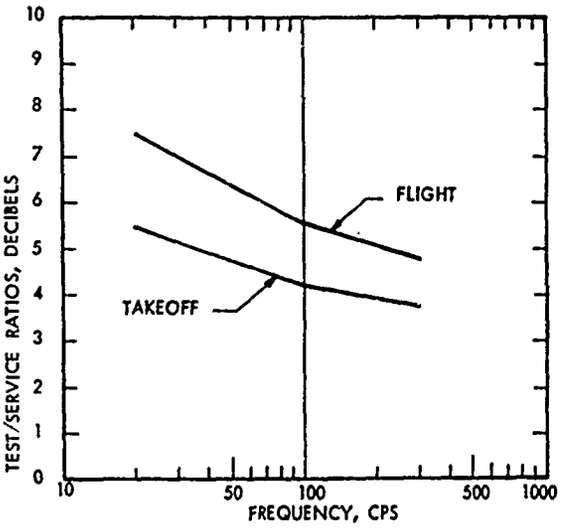

FIGURE 9 CORRECTION FACTORS FOR CAPTIVE FLIGHT MEASUREMENTS

Flight measured data for these test segments were increased by scaling the dynamic pressure to maximum design conditions. The corrections include a factor equivalent to a 4X increase in the design service exposures, which is consistent with the required fatigue design practice. The resulting test durations were 8 hours for captive flight, 5 minutes for weapon bay buffet and 8 minutes for free flight.

(U) Typical service vibration measurements and the corresponding test envelopes are shown in Figures 10 and 11. The lower test envelopes were faired above the data measurements by at least the amount of the correction factors, and the upper test envelopes are at least 6 db above the lower curves. Each pair of envelopes defines the required range of response vibrations to be measured at the given location in the missile during the test. Since, as expected, the spectra of the measured environments showed the missile vibrations to consist entirely or mainly of resonant responses, the test requirement was to bring only the missile resonant peaks at each location into the band between the two envelopes. This contrasts with the conventional practice of forcing the entire smoothed-out spectrum to fall between tolerance limits. A total of 19 spectra were available for the captive flight test and 9 spectra were available for the free flight test.

(U) The missile was suspended to simulate the proper restraint for each test segment and two vibrators were rod-coupled to the missile as shown on Figure 12. Steel rods were used to couple the vibrators to the missile fuse and to the motor case in order to allow the missile to vibrate in all directions without unnecessary restraint. The rods,

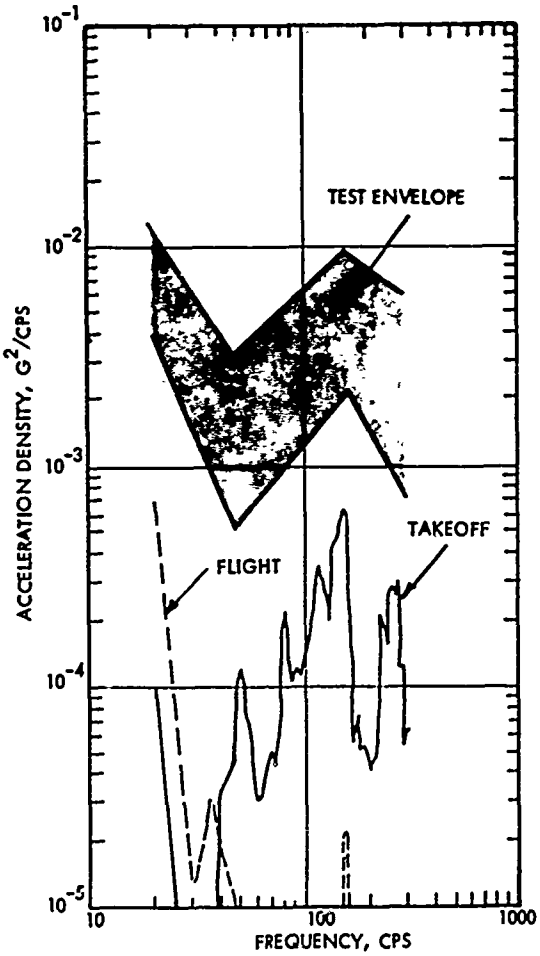

FIGURE 10 DERIVED TEST ENVELOPES WARHEAD AFT MOUNT (LATERAL)

however, tended to act as low-pass filters; that is, high frequency forces (above about 200 to 400 cps) were not efficiently transmitted to the missile. In addition, locally applied high-frequency vibrations were rapidly attenuated along the missile. Therefore the major peaks in the various response spectra generally occurred below 400 cps. With this test set-up, 300 cps is essentially the upper frequency limit of the test equipment, beyond which there was no capability to put the response peaks within the test envelope. High frequency peaks, which in service are due to random sonic pressures on the missile skin, were reproduced in the

missile sonic fatigue tests.

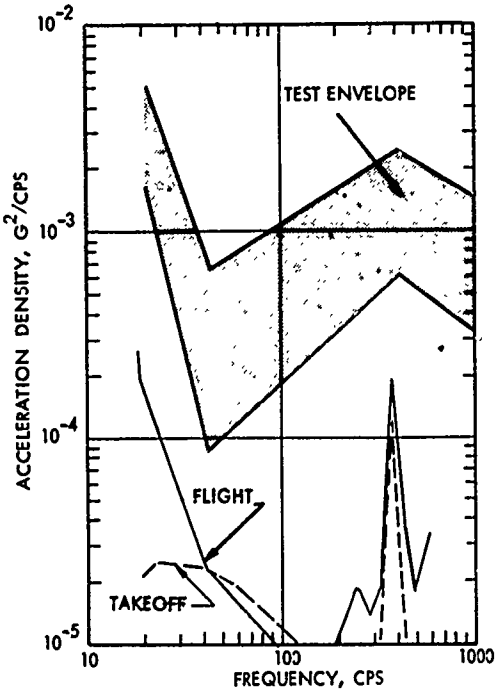

FIGURE 11 DERIVED TEST ENVELOPES ELECTRONICS SECTION CASTING(FORE/AFT)

(U) Initial vibration input equalization iterations were performed on a dummy missile to minimize environmental exposure of the qualification hardware and to acquire confidence in the test procedure.

(U) A special fast-analysis system was used to speed up the otherwise very tedious trial-and-error adjusting of the two vibrator inputs so as to produce the required responses at all the various locations in the missile. The Boeing Dynamic Data Analysis System [1] was used to provide scope-displayed acceleration density spectra very quickly. It was possible to vibrate the missile for less than one minute, and within the next 30 seconds receive scope photos of selected response spectra.

(U) The oscillatory forces applied at the fuse and motor case were adjusted so as to place the major peaks in the response spectrum of the

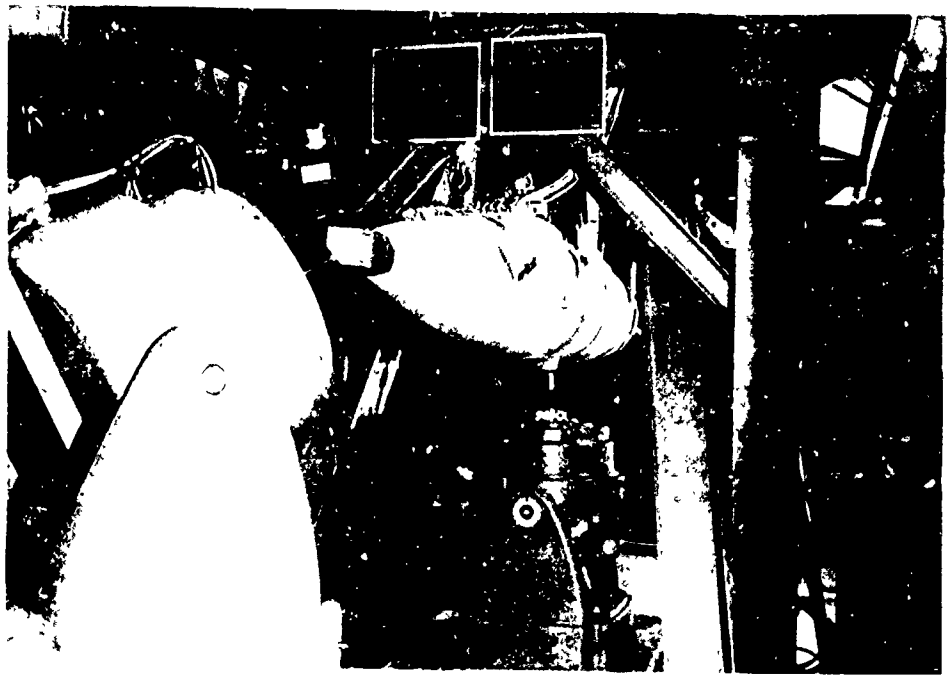

FIGURE 12 MISSILE TEST SETUP -- FREE FLIGHT

primary monitor accelerometer inside or above the band between its test envelopes.

(U) One accelerometer at each vibrator /missile interface and thirty-four accelerometers located in the missile were used to monitor the vibration inputs and responses. These transducer correspond to exact locations and orientations of the flight test transducers. The associated signal conditioning, recording and analysis instrumentation provided the necessary data to verify the vibration environment imposed on the test specimen.

(U) A vertical accelerometer between the warhead and the electronics section was used as the primary monitor because service measurements at that location were available for all test conditions and because it was near two areas of interest: the warhead and the electronics section.

(U) The input forces were further adjusted to get as many other response monitor peaks inside their respective envelopes as possible. Comparisons of the vibration response spectra with the corresponding test envelopes show that at the high frequency beyond the test equipment capability the responses were less than the test envelopes, as expected. Typical test results are shown in Figures 13 and 14. Figures 15 and 16 show the high frequency responses from the sonic test superimposed on vibration test data. The missile sonic fatigue test was conducted in a progressive wave tube configurated to provide the desired sonic energy distribution along the missile length. Overall levels during

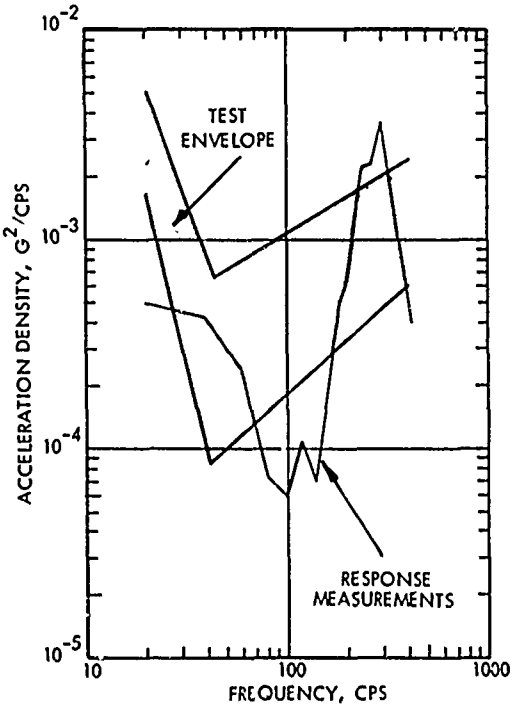

FIGURE 13 TEST RESULTS ELECTRONICS SECTION CASTING (FORE/AFT)

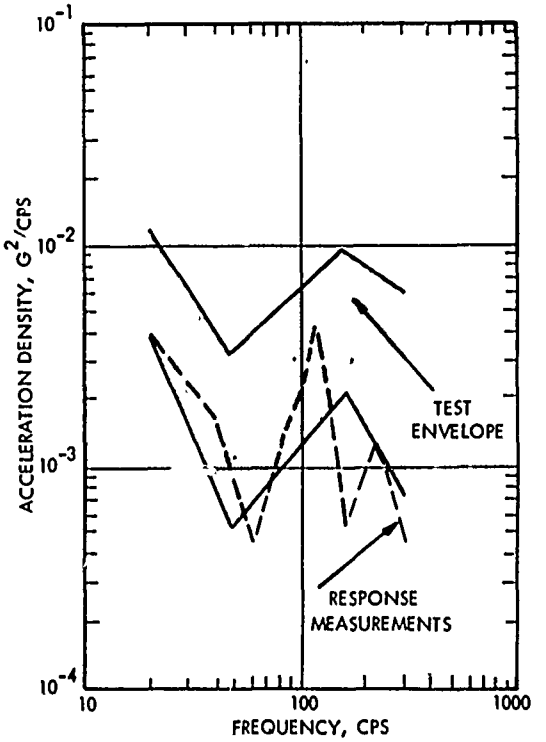

FIGURE 14 TEST RESULTS WARHEAD AFT MOUNT (LATERAL)

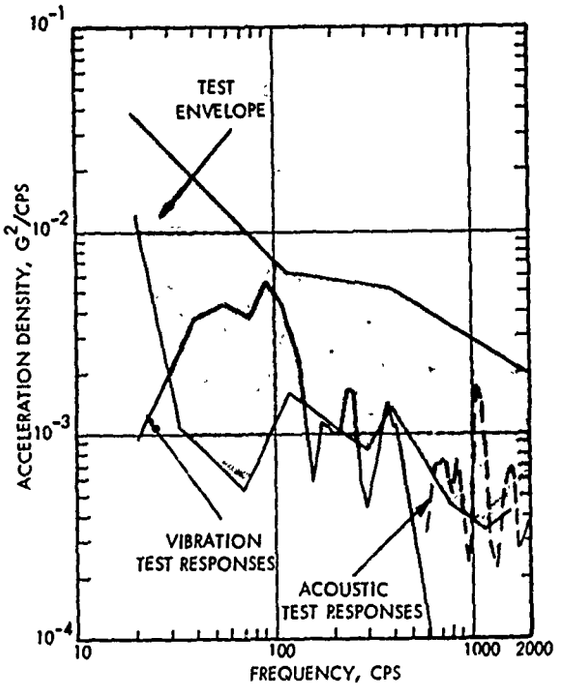

FIGURE 15 COMBINED TEST RESULTS FREE FLIGHT WARHEAD AFT MOUNT (VERTICAL)

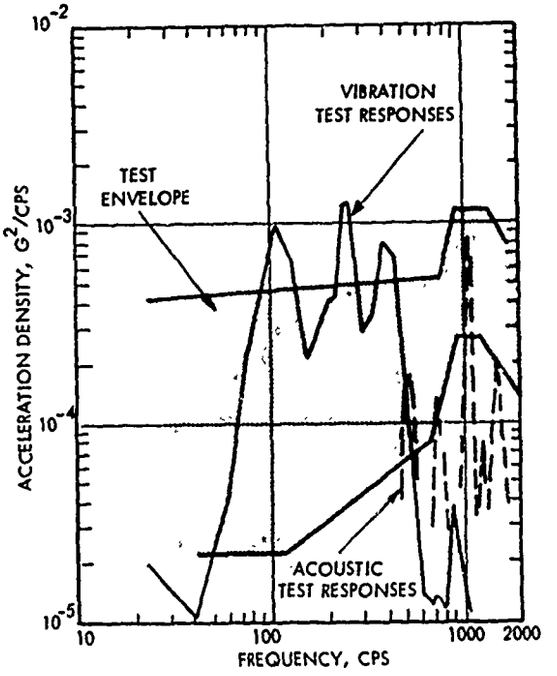

FIGURE 16 COMBINED TEST RESULTS CAPTIVE FLIGHT, WARHEAD AFT MOUNT (VERTICAL)

simulated captive flight were 162 db at the aft end to 156 db at the payload section. The free flight sonic test levels were 145 db to 147 db. The sonic test was culminated in a simulated launch and flight during the sonic free flight environmental exposure.

CONCLUSIONS

(U) The test results showed that this vibration test technique, when combined with acoustic testing for high frequency response and structural fatigue tests for very low frequency response, realistically tested the missile assembly for the broad band vibration fatigue load environment.

(U) The use of flight test measurements permitted realistic simulation of the service loads and minimized the risk of overtest. Typical "black box" vibration levels were shown to be inappropriate for the large mass SRAM assembly.

(U) The use of multiple point excitation with realistically simulated missile restraint conditions was instrumental in minimizing the test cost. The multiple axis excitation minimized test time and the use of moderate sized vibrators place minimum demand on capital facilities.

REFERENCE

(1) Michael O. Michelich, "Dynamic Data Analysis System" Shock & Vibration Bulletin No. 40, Part 7, pp. 115-121, Dec. 1969.

SHOCK TESTING UTILIZING A TIME SHARING DIGITAL COMPUTER (U)

Robert W. Canon
Naval Missile Center
Point Mugu, California

To demonstrate the feasibility of a total experiment being conducted with a timesharing digital computer, a testing arrangement was designed to use a local digital interface processor (the LP-1010) to run a drop-type shock testing machine in the Naval Missile Center's Environmental Laboratory. The system encompasses the complete test routine of process control, data acquisition, and immediate scientific analysis and results.

The main advantages that have been demonstrated by use of a timesharing computer in the Environment Branch are: (1) convenient and easy access; (2) fast results, in a matter of seconds and minutes rather than hours or days; and (3) less expense, since charges are only for the time the computer is used; thus there is no investment in and maintenance of capital equipment.

INTRODUCTION

The Environment Branch at the Naval Missile Center is responsible for conducting all laboratory environmental tests and experiments at the Center. During these tests, weapon systems are subjected to much of the environment of actual flight operations. The value of the test results increases with their promptness.

Prompt results have been obtained through the use of a timesharing computer. The main advantages of a timesharing computer are:

1. Convenient and easy access. In the present test setup, the user merely dials a telephone connected to a dedicated line.

2. Fast results. Results are obtained in a matter of seconds or minutes rather than hours or days.

3. Less expense. Charges are made only for that time the computer is used. In addition, it is the owner who buys, updates, and maintains capital equipment.

Programmers can be trained in a short time, and it is not necessary they have an extensive computer background.

Although a timeshared digital computer has been used in the Environment Branch for over 2 years, only recently did the concept of testing machine control by use of a computer service become possible. With the development of suitable interfaces between the testing device and the timeshared computer, the operations of process control, data acquisition, and immediate scientific analysis are combined into one, and results are available in a few seconds for decision making.

When it became apparent that a timeshared computer could be used to control an entire test, a test machine was chosen for the demonstration run. Because it was to be a demonstration of feasibility as well as a useful experiment, the machine chosen had to be one that would yield a meaningful test and be a graphical demonstration. The machine that was felt to best fulfill these criteria was the laboratory's drop-type shock machine. Although mechanically it is a relatively crude machine, analysis of data it yields can and does become very sophisticated.

The interface chosen for use with the digital computer is the Local Processor 1010 (LP-1010) that is manufactured by Pacific Radionics, Incorporated, of Campbell, California (now a wholly owned subsidiary of Boole & Babbage, Inc.). This particular model of the LP-1010 was designed specifically for use in the Environmental Laboratory and its software was built around the Super Basic and Editor languages of Tymshare, Inc. Further descriptions of the drop-type shock machine and the LP-1010 are given in this paper.

TEST EQUIPMENT AND COMPUTER INTERFACE

Drop Tester

One of the environments frequently simulated in the laboratory is that of shock. One machine that is frequently used is the laboratory's drop-type shock tester (figure 1). The object to be shock-tested is mounted on the top of the movable table of the drop tester. Instrumentation usually consists of one or more accelerometers (or other transducers) mounted on the table and on and in the test item itself. The table may be raised or lowered to any desired height by a motor and pulley and cable arrangement to set the proper dimension before the table is dropped. The table is guided by a pair of vertical rods that prevent lateral table motion, and it is dropped by a capacitor-fired solenoid which releases latching fingers that grip the movable table. The bottom of the table is fashioned into a small hammer that impacts onto a lead pellet atop a mating anvil mounted on a seismic mass at and below the deck level. By selection of the combination free-fall height and pellet size and shape, it is possible to obtain various acceleration versus time histories of the test item on the table. One such acceleration--time history--is shown in figure 2. This is an actual acceleration--time pulse measured on the top of the table and photographed from the screen of a memory oscilloscope.

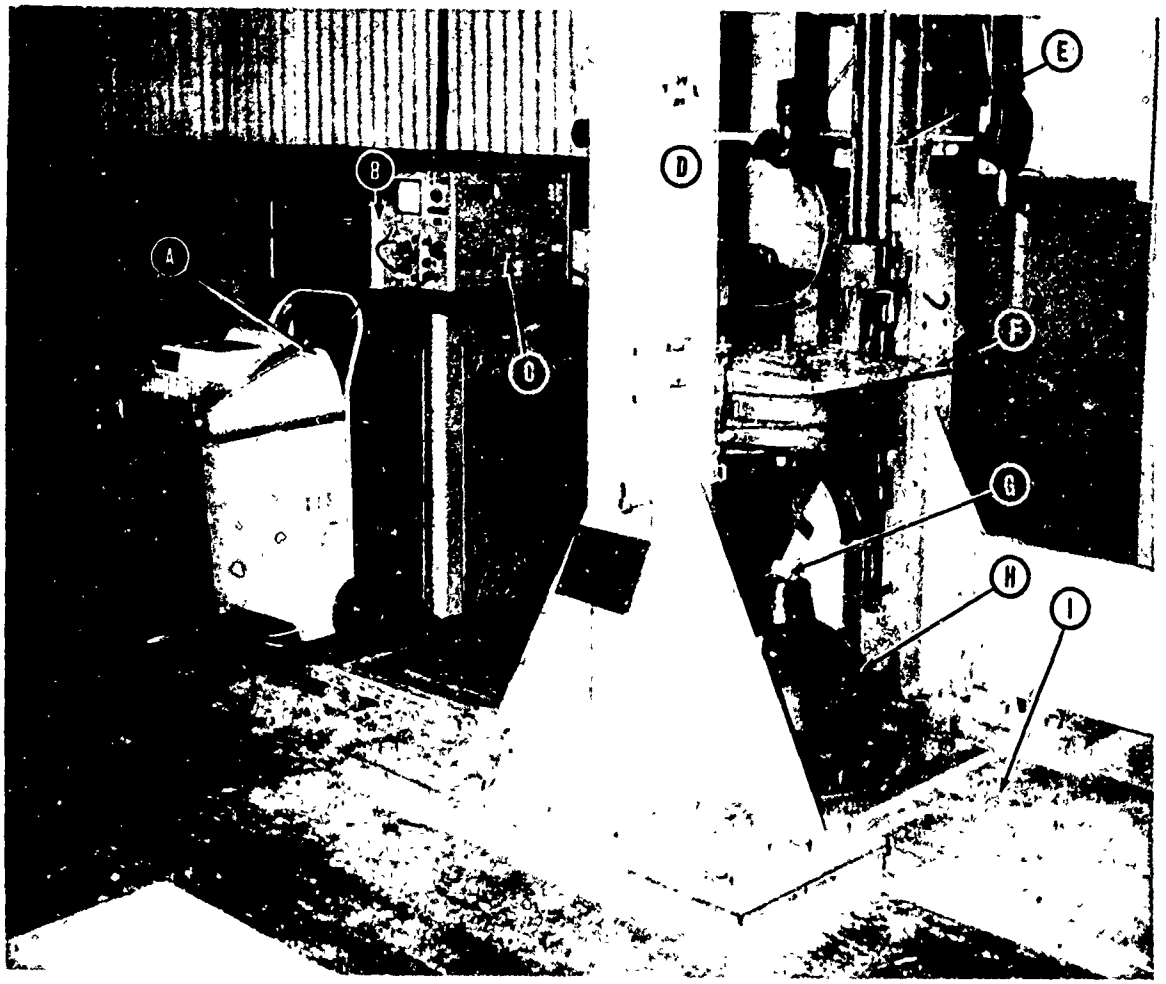

a. Teletype
b. LP-1010 (interface)
c. Memory oscilloscope
d. Frame of drop tester
e. Vertical guide rod (prevents lateral table motion)
f. Movable table top
g. Lead pellet
h. Anvil
i. Deck level

Figure 1. Drop-Type Shock Tester and Related Instrumentation.

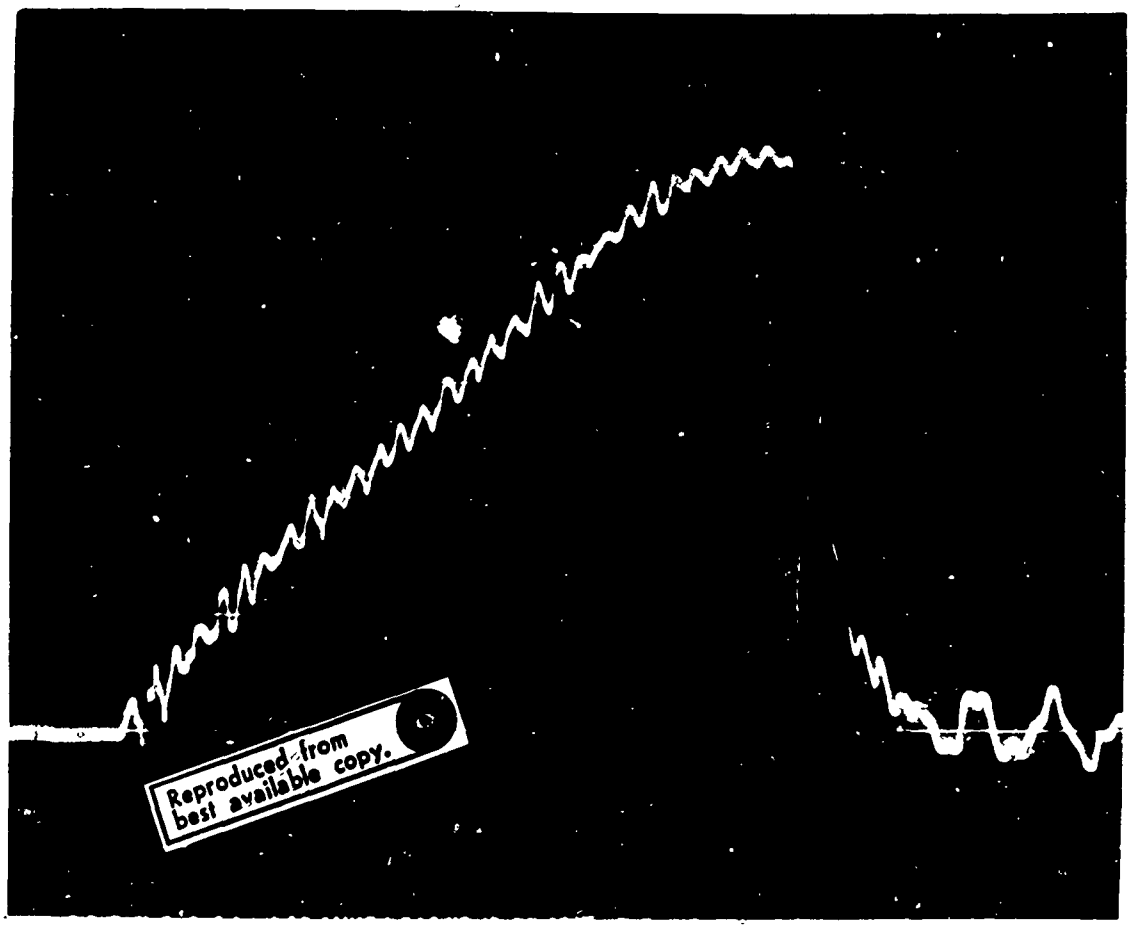

Figure 2. Acceleration Versus Time History of a Shock Input to a Test Item.
Photograph is of memory oscilloscope trace.

Computer programs have been written to perform some analysis of specific shock pulse parameters. One program checks the actual input pulse data to see if the pulse meets MIL-STD-810B. If not, the program selects the best fit within the specification tolerance envelope and informs the user. A second program determines drop height and pellet size required to meet a specified pulse duration and peak acceleration. A third program calculates the height and diameter of conical pellets needed to produce specified sawtooth pulses. Thus the computer is used to remove much of the trial and error process usually involved in beginning shock tests.

The method and extent of the analysis of the shock data thus obtained depends upon the purpose of the test being conducted. If the test is basically to observe whether or not a device operates after undergoing a certain shock input, perhaps only one accelerometer would be used to measure the input to the test item from the table. On the other hand, if extensive information regarding interactions within the test object were desired, the output of several accelerometers or other transducers would be recorded. Analyses of the shock pulse(s) can include, but are not limited to maximum acceleration, time of maximum acceleration, pulse duration, pulse shape, velocity change, displacement during deceleration, energy transfer, momentum transfer, shock spectrum analysis, Fourier spectrum analysis, and ultimately transfer function determination for linear systems.

LP-1010

One of the chief reasons for the selection of a device such as the LP-1010 is its ability to use the higher level computer languages and hence avoid the need for manipulations in cumbersome machine language. However, languages providing for complete string manipulation are suitable, and such languages tend to be more suited to the needs and abilities of most practical engineers.

With the LP-1010, 256 10-bit data words can presently be digitized and recorded in 10.24 milliseconds; subsequently each datum requires 0.3 second to be transmitted to the computer. However, this is still quite fast for this application and data analysis is now provided in a matter of minutes rather than days. Additionally, analyses can now be done quickly and cheaply where formerly they were avoided entirely because of the cost and time required.

Originally the LP-1010 was designed to handle 16 digital outputs to control the environment and 16 time-multiplexed analog inputs from the environment;* however, special features were incorporated to accommodate the unique features of this experiment. The position of the LP-1010 in the drop-tester experiment has been shown in figure 1, a sketch of the simplified system is shown in figure 3, and a front view is given in figure 4.

To implement the drop-tester experiment with merely one accelerometer input, six interactions between the LP-1010 and the environment (basically the drop tester) are required. These are three digital signals and three analog signals. Although the LP-1010 has the capacility of many other interactions, only those mentioned here were used. One digital signal is used to drive the table carriage positioning motor up, one to drive the motor down, and the third to activate the release solenoid.

The three analog signals are somewhat more involved since they are inputs required from the drop tester. One analog signal is a voltage in the 0- to 10-volts-DC-range which gives the indication to the LP-1010 of the height of the table carriage. Figure 5 is a sketch of a 15-turn potentiometer which is driven off the cable wind drum.

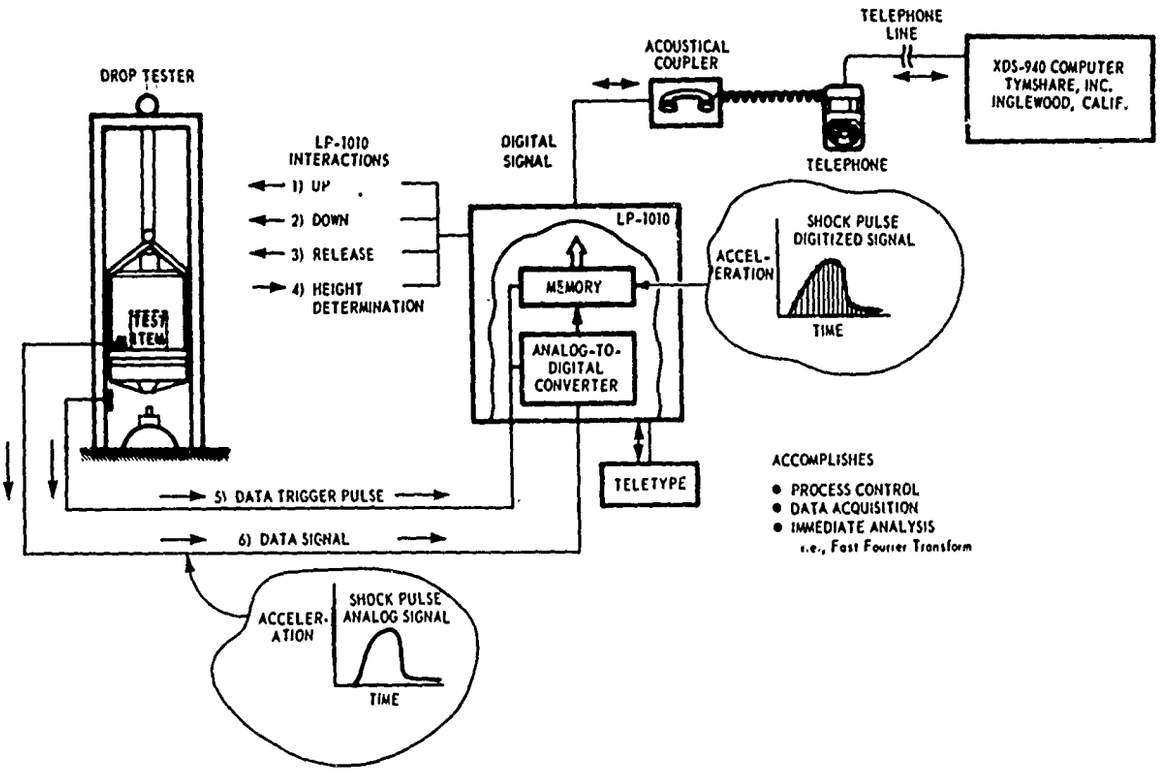

Figure 3. Drop Tester—LP-1010 Setup With Timesharing Digital Computer.

*By use of tape recorded data, virtually an unlimited number of sensor inputs could be accommodated.

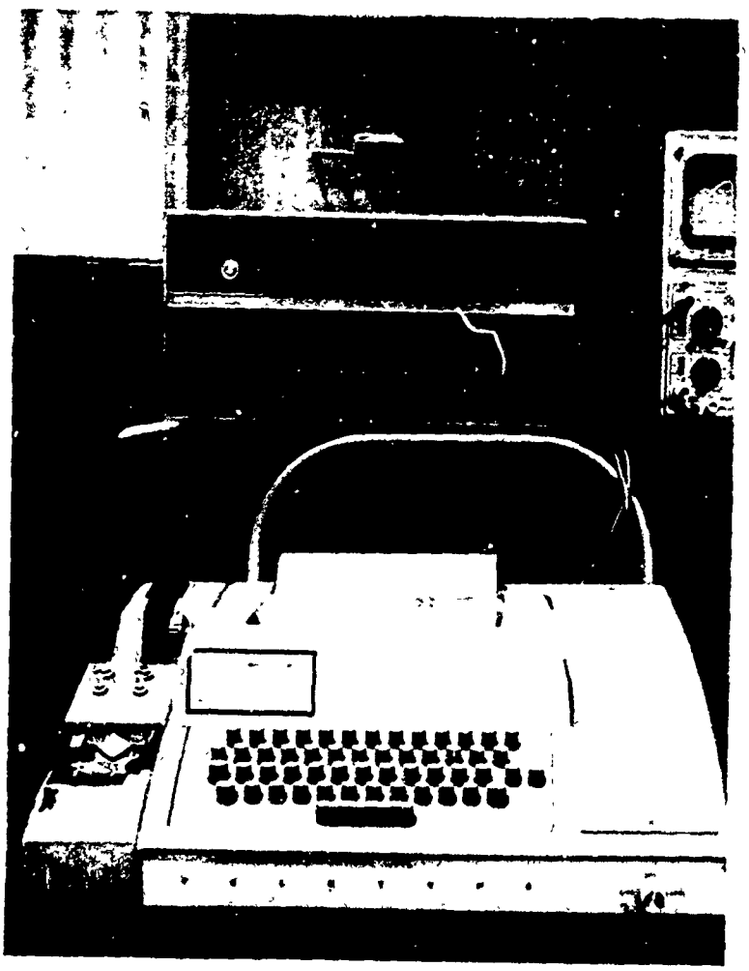

Figure 4. Front View of LP-1010. Teletype is in foreground, memory oscilloscope is to right.

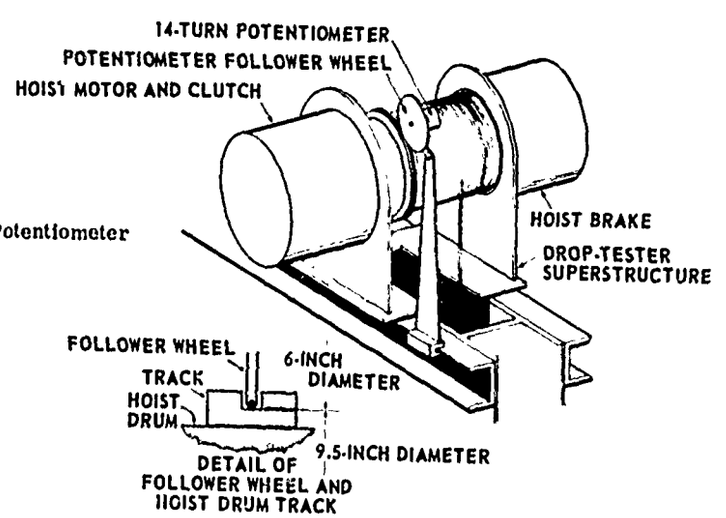

Figure 5. Table Height Potentiometer Installation.

Because certain local actions must be independent of the computer since it might happen to time-share at an inopportune time, table positioning is done in the laboratory by a voltage comparator circuit in the LP-1010. The proper voltage corresponding to a specific height is determined by the timesharing computer, is sent to the LP-1010 where it is converted to an analog signal on one side of the height comparator, the drive motor is started, then the matching or comparing voltage is obtained from the height potentiometer circuit. When the voltages are the same, the relay driver in the LP-1010 that causes activation of the particular carriage drive relay is disabled, which stops or drops the table, as the particular sequence of events requires.

The remaining two analog signals are interrelated since they both are needed in the actual taking of data. As originally designed, the LP-1010 did not make provision for the very rapid data rates necessary to record a shock pulse of only a few milliseconds. To accommodate this fast but short-lived data rate a small 256 10-bit-word buffer memory was added to the LP-1010. Since the accelerometer information is analog, it must be converted to digital form before being sent to the computer for stowage and analysis (see back to figure 3); since the data rate to the computer is relatively slow (110 bits per second in this case--i.e., 10 characters per second X 11 bits/character), a means for local temporary stowage of the data is necessary. Hence, the analog to digital converter and buffer memory must work together in unison. The fastest data can be gathered in the LP-1010 is 256 samples (10-bit words) in 10.24 milliseconds. The slowest time for 256 samples is two or more seconds; this time may be lengthened indefinitely if desired by use of a simple extender program.

One of the two remaining analog signals is a strike pulse which is a signal that actual data will be forthcoming. It is generated by a striker on the falling table that closes a simple microswitch just before the table impacts with the lead pellet (see figure 6 for details). This pulse or switch closure then initiates the analog to digital converter and commences filling the buffer memory with data. The last analog signal is just the accelerometer signal itself. Since the typical accelerometer signal is 0-1 volt DC, an amplifier is provided to multiply the voltage by 10 to make it suitable for input to the LP-1010.

The LP-1010 can be operated on-line with the computer and hence gives completely automatic experiment control, computer-operator interactions, and processing analysis of data obtained. The LP-1010 can also be operated locally (off-line) from the teletype keyboard on a sequential basis by the operator simulating the coded signals from the computer. The local mode of operation is used to check the system operation before going on-line with the computer for an automated run. Off-line operation does not provide for data analysis.

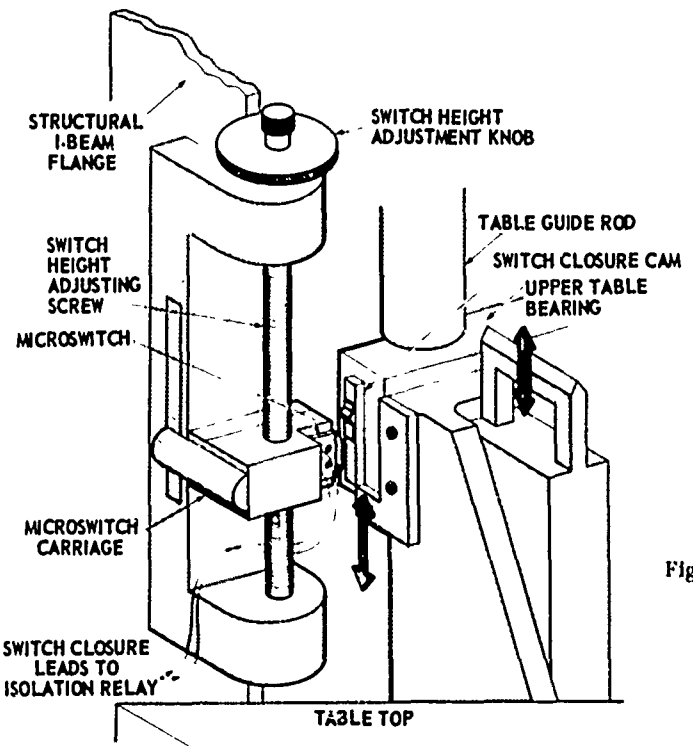

Figure 6. Switch Closure Mechanism.

Once obtained and stored in the LP-1010's buffer memory, the data is then sent to the computer in a rather ingenious fashion. Since the data transmission rate is that determined by the remote terminal/time-sharing computer combination, this also becomes the speed of the LP-1010's operation. The system described here transmits and receives at the rate of 10 characters per second. Each character consists of 11 bits of information: 1 start bit, 8 bits of character description, and 2 stop bits. The 8 bits of character coding are used inside the LP-1010 in two groups of 4 bits each. The 4 most significant bits are used by the LP-1010 to select channel routing, then the 4 least significant bits perform functions within the channel selected. In the specific case of the data channel, the 4 least significant bits carry the data. Ten bits for each data word are distributed among the least significant bits of three characters as shown in figure 7a. A brief explanation of data conversion and readout is given in figure 7b. Figure 7a depicts the distribution of characters in a 40-bit data buffer subsequent to the buffer memory. Each character transfers in parallel to the transmit register and is then transmitted serially to the computer.

SAMPLE TEST RUN

A typical test sequence of this system is as follows.*

Once the operator has gone on-line and logged in with the computer, his first step is to go to the Super Basic language and load the driving program. Once the program is loaded, the operator issues the command "RUN" from the teletype. The computer program then takes control, moves the carriage latch to the engaged position, gives a series of interactive questions, and gets responses from the operator. Once the initial responses are satisfied, such things as drop height and time interval expected for the pulse and number of data samples desired, the computer raises the table to a small predetermined height to allow for insertion of the lead impact pellet. This is a hand operation to ensure proper selection of the pellet and its correct positioning. The operator, if he is satisfied with the situation, types "GO" and the computer takes over, raises the table, drops it, acquires the data from the LP-1010, and returns the desired analysis. To demonstrate how extensive the analysis can

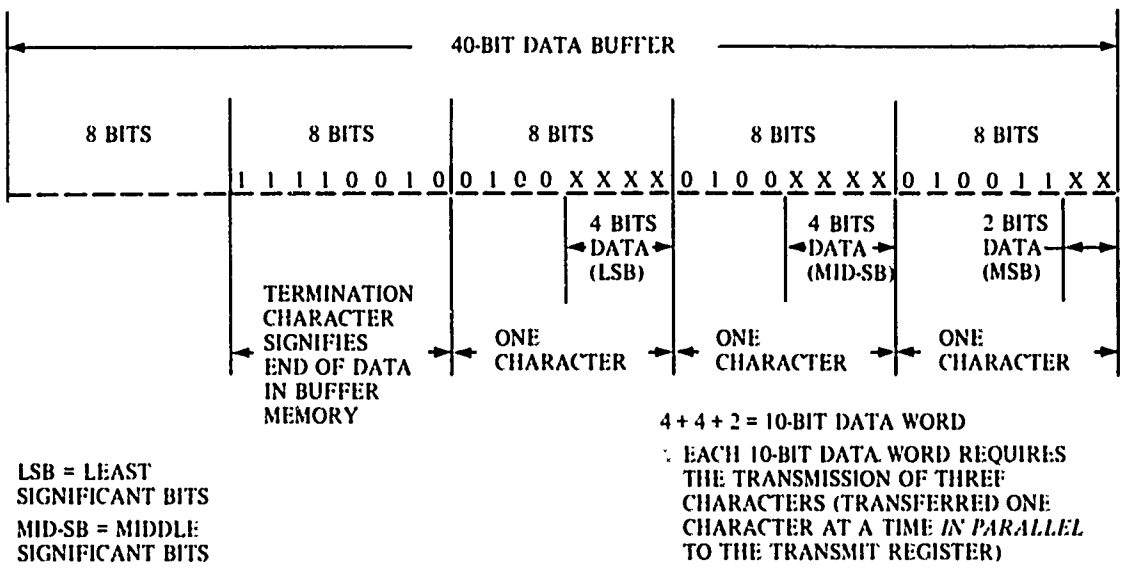

Figure 7a. Forty-Bit Data Buffer.

*A sample of the actual teletype copy and copies of the driving program (written in super Basic) plus a copy of a Fast Fourier Transform (FFT) program (written in Tymshare's Super FORTRAN language using the Cooley-Tukey algorithm) can be found in the Naval Missile Center's technical publication TP-70-74.

BIT NO.	10	9	8	7	6	5	4	3	2	1
POSITION VALUE	$(\ )2^9$	$(\ )2^8$ +	$(\ )2^7$ +	$(\ )2^6$ +	$(\ )2^5$ +			$(\ )2^3$ +	$(\ )2^2$ +	$(\ )2^1$ +	$(\ )2^0$

where ( ) contains either binary 1 or 0 and is the representation for that position in the 10-bit word. ie.,

(1)	(0)	(1)	(1)	(0)	(0)	(0)	(1)	(1)	$(0)_2$ ←
				or					REMEMBER PLACE VALUES
1	0	1	1	0	0	0	1	1	0_2 =
512	0	128	64	0	0	0	4	2	$0_{10} = 710_{10}$

BINARY ⟷ DECIMAL TABLE USED IN 10-BIT WORD A/D AND D/A CONVERSION

BIT NO.	BIT VALUE		RATIO		IF DECIMAL RANGE WERE 10.23 VOLTS	DECIMAL VALUE IS:
10	512	X	$\left(\frac{\text{DECIMAL RANGE}}{1023}\right)$	=	5.12 VOLTS	
9	256	X		=	2.56 VOLTS	
8	128	X		=	1.28 VOLTS	
7	64	X		=	0.64 VOLTS	
6	32	X		=	0.32 VOLTS	
5	16	X		=	0.16 VOLTS	
4	8	X		=	0.08 VOLTS	
3	4	X		=	0.04 VOLTS	
2	2	X		=	0.02 VOLTS	
1	1	X	$\left(\frac{\text{DECIMAL RANGE}}{1023}\right)$	=	0.01 VOLTS	
					Σ = 10.23 VOLTS	

RESOLUTION = ± ½ Least Significant Bit (which means ½ the decimal value for bit no. 1 in any particular decimal range.) Thus the error is $< \pm 0.05\%$.

Figure 7b. Notation for 10-Bit Binary Data Word Used in LP-1010.

be, this run returns the following items: the actual data character string sent to the computer, a tabulation of the acceleration time history, a teletype plot of the acceleration time history, and, by use of the FFT program, a tabulation and plot of the absolute value of the Fourier Transform of the data pulse just acquired.

A typical use of the derived Fourier Transform might be to aid in the determination of a system's response to a given input such as a shock pulse.

For example, the acceleration-time (a versus t) history shown in figure 8a might be a shock pulse that is encountered in practice, but the response of the item to this shock input might be that shown in figure 8b. Usually it is the response of a structure to a certain input which is desired; however, this is not always easily determined theoretically.

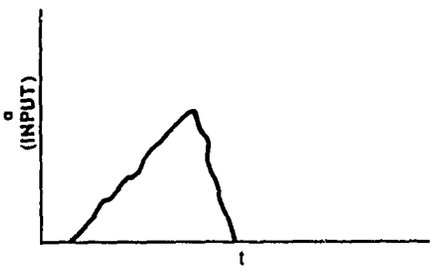

Figure 8a. Input Time History.

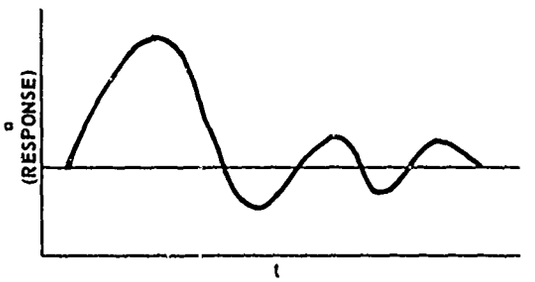

Figure 8b. Response Time History.

To go directly from an input time history to a response time history even for a simple structure is a difficult mathematical problem. However, the problem can be made considerably more simple by computations carried out in the frequency vice the time domain. Hence the time history is transformed to the frequency history and operated on by a transfer function to give a response frequency spectrum. The response spectrum thus obtained is then inverse-transformed back to the time domain to give the sought-after response time history.

Once a shock pulse's time history is recorded, it may be studied to yield other useful information regarding the impact. In addition to the spectral decomposition technique described above, the data also contain simple and straightforward information such as maximum acceleration, time of maximum acceleration, pulse duration, pulse shape, velocity change, displacement, energy transfer, and momentum transfer.

If the outputs from two or more accelerometers are recorded simultaneously, dynamic relationships between different locations in the test item's structure can be obtained. For example, consider two accelerometers placed as shown in figure 9a. When both the input shock pulse to the item being tested and the response to this input at some specific location within the item are measured, a transfer function relating the dynamic characteristics of the intervening structure can be obtained by a simple manipulation of the Fourier Transforms if the system is linear. Figure 9b depicts how the process takes place. Note that the absolute values of the transforms as they might appear are shown, whereas in practice their complex form would actually be used. Once obtained, the transfer function can be used to predict future response time histories at the same location for various other input time histories. This process is shown in figure 9c. Knowledge of such a transfer function was presupposed in the case described above when only one accelerometer was used for an input time history to obtain a response time history.

CONCLUSIONS

Results thus far obtained from the prototype installation demonstrate the feasibility of accomplishing complete tests using a timesharing computer through the steps of process control, data acquisition, and scientific analysis. Furthermore, several side benefits such as convenience and ease of access, faster results in usable form, decreased expense, and less equipment upkeep and maintenance become evident as the installation development progresses. Additionally, it is recognized that testing is now being attempted in areas previously avoided because the analyses are much easier to perform with the system described.

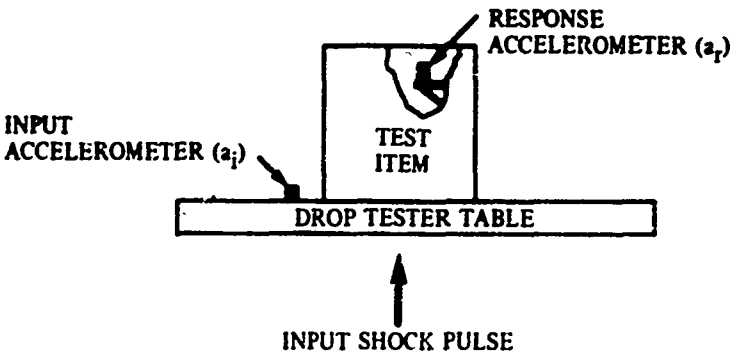

Figure 9a. Accelerometer Placement.

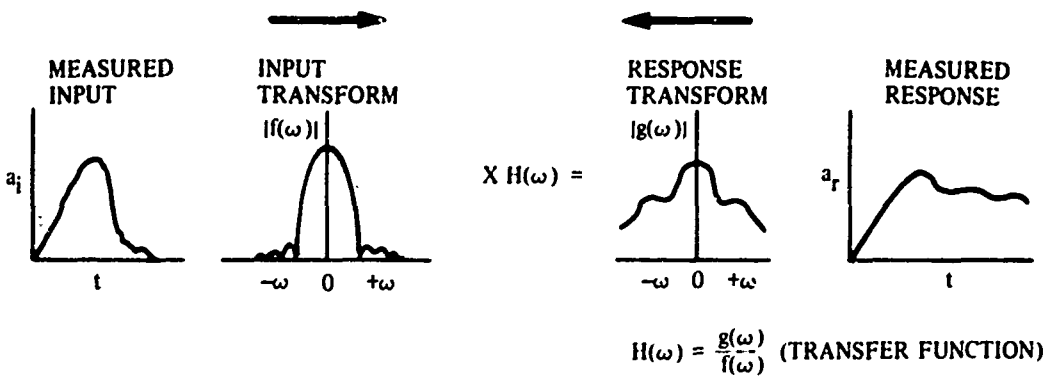

Figure 9b. Determination of the Transfer Function From Two Simultaneous Measurements.

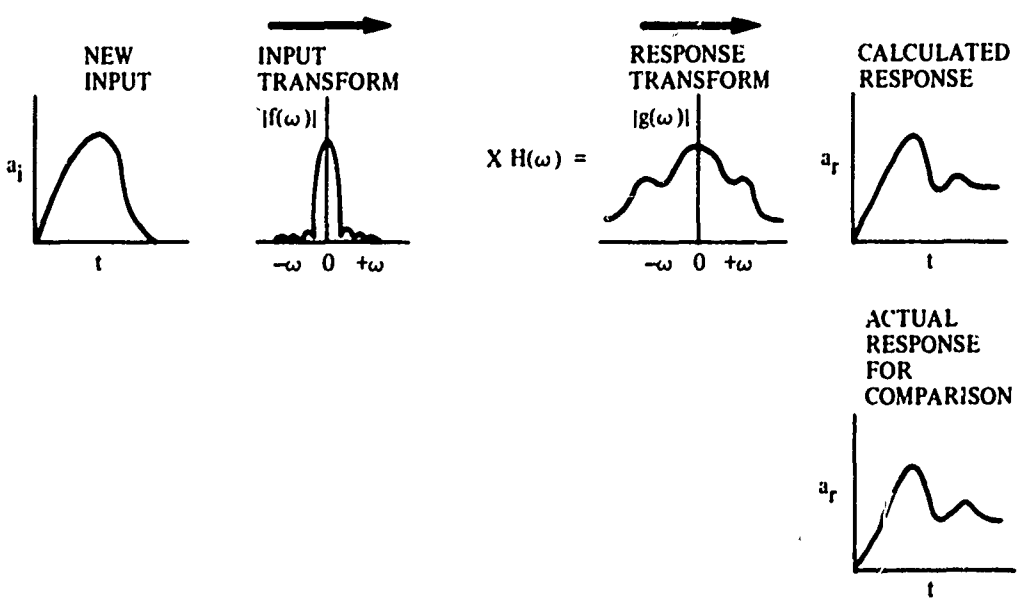

Figure 9c. Use of the Derived Transfer Function to Determine the Response to a New Input.

DISCUSSION

Mr. Luke (Los Alamos Scientific Laboratory): Is the limitation of 256 bits because of the computer? Can you go into shorter time pulses such as 50 to 100 microseconds? You mentioned 10 to 20 milliseconds. What is your limitation in this respect?

Mr. Canon: To answer the question of the limitation on the number of data points, that is not a computer limitation, it is a limitation with a little local processor. We bought a 256 word memory because of the limited money we had available. As far as the time is concerned we can take 256 data points in about 10 1/4 milliseconds and that is as fast as the analog to digital converter will work. If we can take 256 data points in roughly 10 milliseconds, for shorter times we just take what ever proportion of data points we can fit in the shorter time.

Mr. Briggs (General Electric Corporation): I do not quite understand the way you feed the data from the A to D converter back to the teletype. Is there an acoustical coupling, or how do you physically transmit the data through the teletype back to the computer?

Mr. Canon: The data are taken from the accelerometer on the drop tester and it is converted, analog to digital, and stored in a memory in the processor. It never goes to the teletype. The teletype is merely an entry device for us to communicate with the computer. The data go from the memory in the processor via the telephone coupler and the telephone line to the computer. We have a transmit register set up in the front end of the processor which transmits the data just like characters from the processor out to the computer. In fact the computer does not know if the teletype or the processor is talking to it.

Mr. Briggs: Is that something that is optional for the particular teletype that you are working with?

Mr. Canon: The teletype is just an entry device, we could use any kind of teletype. We can actually use a Hazeltine 2000 terminal, or any terminal, as a matter of fact, it does not have to be a teletype.

Mr. Astrike (Naval Ammunition Depot Crane, Indiana): Are you limited to only one accelerometer in collecting data or can you use more than one?

Mr. Canon: No, we can use as many accelerometers as we want. We have done some testing with 2 or 3 accelerometers. However, when it comes to storing the data in the memory, it is stored sequentially like 1,2,3 - 1,2,3. We interlace it. We are still limited by the fact that we have 256 cells available to us locally.

Mr. Astrike: When you program this shock machine are you interested in the repeatability in the duration of the shock test? I noticed that you said that you have a program level each time. Do you get good repeatability by doing this or are you interested in this?

Mr. Canon: With these drop testers, repeatability is a problem that is inherent in the machine. We feel that we can get repeatability that is commensurate with the drop tester and we can eliminate all the little human factors that go toward goofing up the experiment.

A TECHNIQUE FOR CLOSED-LOOP COMPUTER-CONTROLLED REVERSED-BENDING FATIGUE TESTS OF ACOUSTIC TREATMENT MATERIAL

Carl E. Rucker and Robert E. Grandle
NASA Langley Research Center
Hampton, Virginia

(U) A description is given of a computer-controlled fatigue testing system which operated continuously without operator attention during testing. This system was designed to run a reversed-bending fatigue test on flight-weight porous fiber metals to develop fatigue data for this material. Tensile coupons were tested to determine the material properties, and the method of determining these properties is discussed. Fatigue data from one set of fiber-metal tests are also included.

INTRODUCTION

(U) One of the most prevalent forms of noise pollution is the noise produced by jet aircraft upon take-off and landing at airports. The major noise source in aircraft during landing is the fan noise from the turbofan engine. One method by which the fan noise can be reduced is by the use of various forms of acoustic lining materials placed in the inlets of the nacelles [1]. As an example of the application of these materials, Fig. 1 shows the placement of the acoustic liner treatment in the inlet of a McDonnell-Douglas DC-8 turbofan nacelle. In this particular application, the treatment is placed on the interior inlet surface, the center body, and a concentric splitter ring in the inlet, and also in the fan exit duct to achieve reduction of the fan noise.

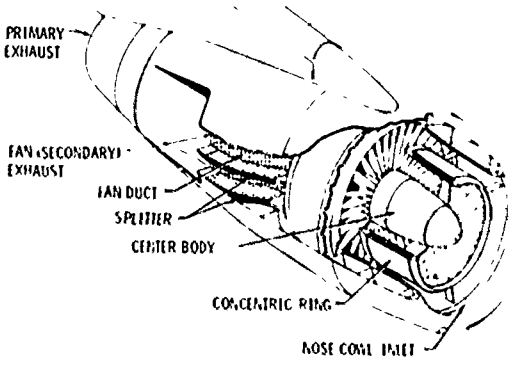

Fig. 1 - Cutaway view of modified turbofan engine nacelle showing treatment of inlet and fan ducts with acoustic material.

Typically, the acoustic treatment used in the nacelles of the turbofan aircraft studied in Ref. [2] was of a sandwich construction. This sandwich consisted of three layers: (1) a porous surface plate for sound absorption, (2) a honeycomb core, to form a Helmholtz resonance chamber, and (3) a solid backing for attachment. To design these sandwiches, fatigue data for the various materials are needed to insure against failures from the low-level, high-cycle-rate stresses which occur in linings in a jet engine inlet.

A candidate material for the porous surface plate of this sandwich is fiber metal. Manual controlled fatigue tests of this material have been performed and were reported in Ref. [3]. Since the material tested in Ref. [3] was too heavy for use as aircraft nacelle treatment material, fatigue tests were needed on the lighter flight-weight fiber metals. Because of the time expended and cost of running the manual fatigue tests on these fiber metals, a computer-controlled fatigue testing system was developed to run the tests on the lighter materials. This system had several advantages which reduced the time and cost of testing: It was tailored to the materials being tested, it ran several fatigue tests simultaneously, and it ran 24 hours a day, 7 days a week without attention during the test.

This paper describes the method of performing multiple fatigue testing of flight-weight samples of fiber metals. It also gives results of tensile tests that determine the material properties and typical S-N fatigue data for the material.

EXPERIMENTAL PROCEDURE

(U) The test specimens were fabricated from commercially available AISI 347 stainless-steel fiber-metal panels. The material of the panel's fibers is composed of a maximum of 0.08 percent carbon, 2.00 percent manganese, 0.045 percent phosphorus, 0.030 percent sulfur, 1.00 percent nickel, columbium plus tantalum at least 10 times the carbon content, plus the balance in iron. The density of the material is 8024 Kg/m^3 (0.29 pound/in^3), the tensile modulus of elasticity is 1.93×10^{10} N/m^2 (28.0×10^6 psi), and endurance limit is 2.68×10^8 N/m^2 (3.94×10^4 psi, annealed) [4]. AISI 347 is an austenitic type (nonhardenable) stainless steel.

The fiber metal for this test was made from random lengths of 0.0051 cm (0.0020 in.) diameter wire bonded in a panel configuration by heating in a reducing atmosphere (sintered). A photomicrograph (amplification 30X) of the material is shown in Fig. 2. The density and

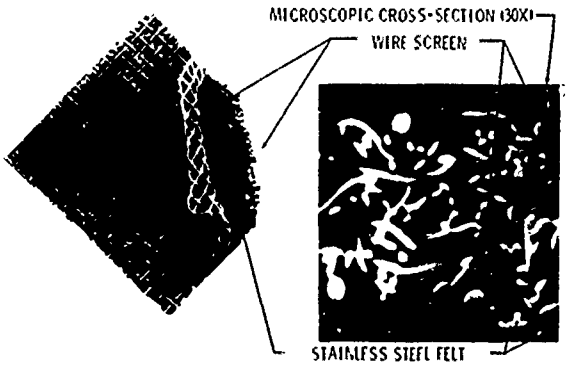

Fig. 2 - Illustration of random wire felt fiber-metal construction showing screen reinforcement and typical cross section.

thickness of this material was 1.93 kg/m^2 (0.40 lb/ft^2) and 0.059 cm (0.023 inch), respectively. The material was also reinforced with 18-mesh-grid wire (0.022 cm diameter wire) of AISI 347 stainless steel sintered to both surfaces of the random wire material.

Twenty-four tensile and 60 fatigue specimens were machined from the commercially available panels. The shape of the specimens used is shown in planform in Fig. 3. These shapes were obtained from each of the panels using an electrodischarge machining technique to avoid disturbing the wire adjacent to the edge of the cut. The tensile and fatigue coupons were cut from the panel so as to obtain 0^o, 45^o, and 90^o orientations to the reinforcing screens.

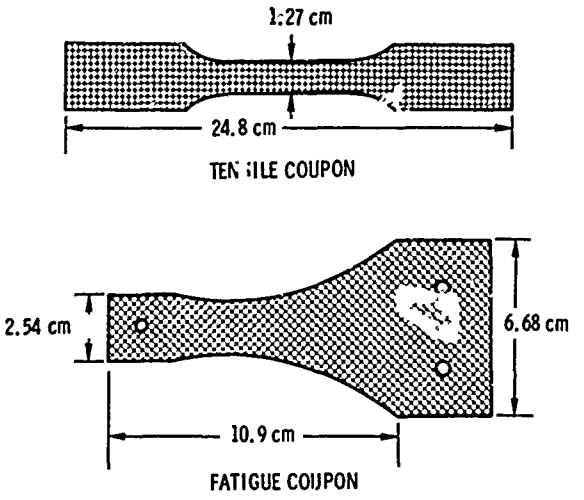

Fig. 3 - Drawings of tensile test and fatigue test models.

Tensile Test

(U) All the tensile specimens were tested in a constant strain-rate tensile testing machine. Load versus strain was recorded on an X-Y plotter. Figure 4 shows a typical stress versus strain curve for this type of thin lightweight fiber metal. The curve in Fig. 4 is not a very

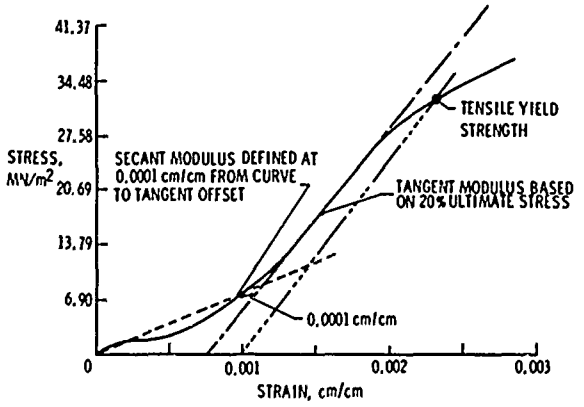

Fig. 4 - Typical stress-strain curve for AISI 347 stainless-steel fiber metal.

typical stress-strain curve for a homogeneous steel. The differences at the low stress levels are caused by the randomly oriented wires in the material reorienting themselves along the lines of the stress. This is shown by the rather low stress increases for a large strain increase at the low stresses. As the fibers are reoriented, the material begins to show the straight-line ess-strain characteristics of steel. The linea portion of the curve above 1.379×10^7 N/m^2

(2000 psi) is more typical of the shape of a homogeneous steel stress-strain curve.

Since the stress-strain curve of this material resembles that of a low modulus material such as plastic, its elastic modulus was defined in a manner similar to that used for plastics in Ref. [5]. The tangent modulus is used to represent the straight-line portion of the stress-strain curve and the secant modulus is used to represent the lower portion of the stress-strain curve. The tangent modulus was defined for this material as the slope of a line tangent to the material stress-strain curve at 20 percent of the ultimate load. As can be seen from Fig. 4, this tangent modulus gives a good approximation of the slope straight-line portion of the stress-strain curve of this material. The secant modulus is defined as the slope of a line which passes through the origin and a point on the stress-strain curve where the first strain deviation between the tangent modulus line and stress-strain curve is 0.0001 cm/cm.

The other material parameters, the tensile yield strength (Ty) and the ultimate tensile strength (Tu), were determined from these stress-strain curves. The Ty was computed from the intersection of the stress-strain curve and a line having the slope of the tangent modulus which intersects the origin at a strain value of 0.001 cm/cm. Tu is the ultimate load divided by the specimen area of 0.0713 cm^2 (0.0115 $inch^2$).

The data from the tensile test of the 24 tensile coupons, shown in Table 1, were arithmetically averaged in groups of eight to get values for the tangent modulus of the material for each screen orientation (Table 2). This tangent modulus was then used as the elastic modulus of the material.

Fatigue Tests

(U) The fatigue coupons were selected for testing at different loads in a random manner to prevent biasing of the data due to the panel selection and location in the panel from which it was cut. The fatigue coupons were tested as a cantilever beam in a reversed-bending fatigue test. The method of load determination and monitoring was reported in Ref. [3] in which an accelerometer at the tip of the cantilever beam is used to determine the load in the beam. With this tip acceleration and the geometry and material properties of the beam, the stress in the beam is computed by the relationship given in Eq. (1), if the beam is near or below first natural mode of resonance.

$$S = \frac{g\, E_t\, h}{0.102\, f^2\, \ell^2} \qquad (1)$$

Where
- f = frequency of vibration
- S = stress in beam
- E_t = tangent modulus
- h = thickness of beam
- g = tip acceleration
- ℓ = length of cantilever beam

For this material and coupon shape, it was found in Ref. [3] that if the magnitude of acceleration was held constant at the tip of the beam the magnitude of the root strain remained relatively constant. Figure 5 shows the relationship between the root strain and the tip acceleration in the beam as reported in Ref. [3] and this relationship was assumed valid for these materials. No strain gages were used to monitor these tests and the "g" loading was determined at the initial test frequency and assigned stress by means of Eq. (1).

A closed-loop computer-controlled testing system was used to run the fatigue tests on these beams near their first mode of resonance (approximately 8 to 10 Hz). This system is capable of testing six coupons simultaneously, at the same or different loads, and continuously without operator supervision.

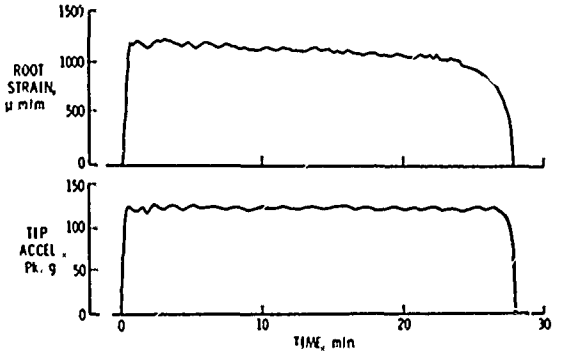

Fig. 5 - Samples of time averaged values of the peak acceleration and strain response time histories for a fiber-metal beam fatigue test.

The computer testing system is shown schematically in Fig. 6. It consists of the following items:

(1) A minicomputer and input typewriter
(2) Six digitally controlled oscillators
(3) Five 100-pound-force and one 50-pound-force electromagnetic shakers and power amplifiers

(4) Six 3-gram, 5.5 mv/g piezoelectric accelerometers and associated signal conditioning equipment

(5) A scanning or multiplexing device with analog to digital converter

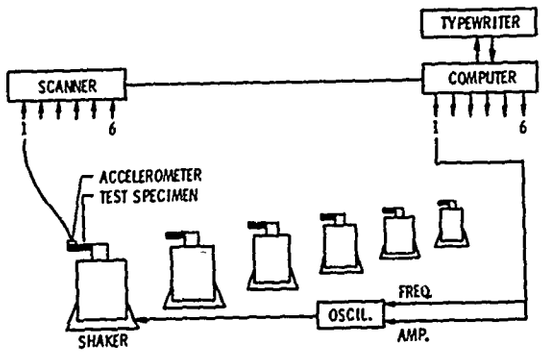

Fig. 6 - Schematic diagram of the computer control for fatigue testing of acoustic materials.

The minicomputer used for this application, Fig. 7, had 8000 words of magnetic core storage, a 16-bit word, and was FORTRAN II programmable.

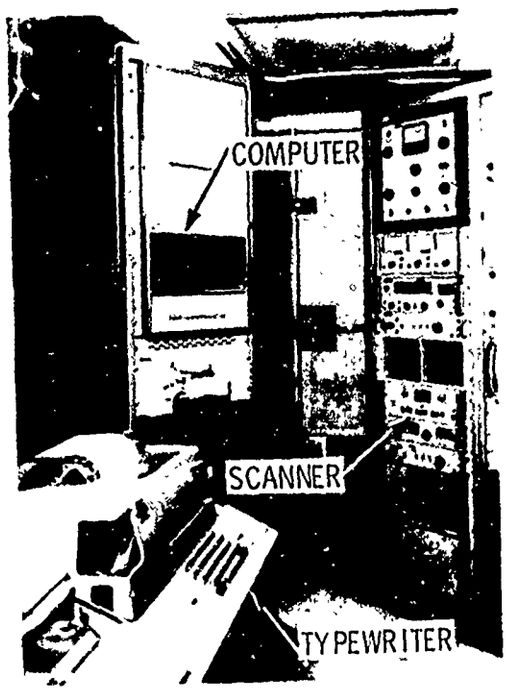

Fig. 7 - Computer and scanning equipment.

The closed-loop computer control system operated in the following manner. A test specimen was mounted on one of the six electromagnetic shakers. Four of these shakers are shown in Fig. 8. The 45° specimens required a slight preload at the end of the beam to prevent an unstable resonance condition from developing. This preloading was achieved by mounting the 45° specimens in the horizontal plane and using the weight of the accelerometer for the preload on the beam. The desired stress, the geometry, and the material properties of the beam were then inputed to the control algorithm or procedure stored in the computer. The computer then used the control algorithm to find the first mode of resonance of the beam by controlling a frequency sweep in the range of that resonance and recording the frequency with the greatest response from the beam. With this information and Eq. (1), the computer then determined the tip acceleration required for the beam to have the desired root stress. The correct voltage amplitude and frequency were then outputed to the digitally controlled oscillator by the computer and the test began.

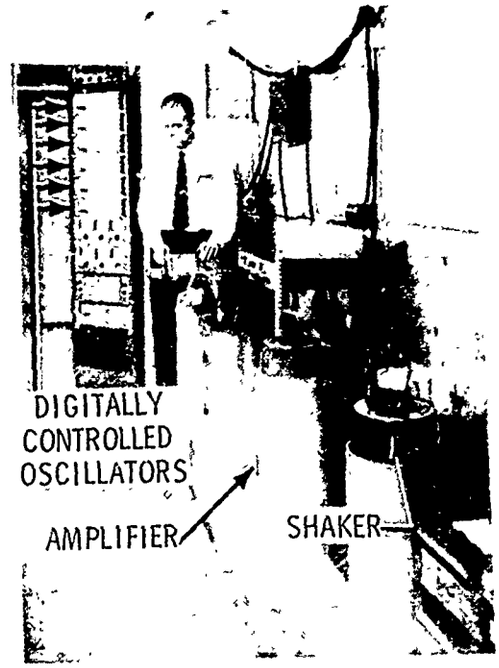

Fig. 8 - Electromagnetic shakers and power amplifiers.

As the testing progressed, the natural frequency of the beam decreased, probably because of the reorientation of the fibers, fracture of fiber bonds, breaking of the fibers, or some combination of these phenomena. Due to this decrease in natural frequency, the tip acceleration also decreased. Since it is necessary to maintain this tip acceleration constant to maintain a constant root stress in the beam,

the computer continually sampled the output of the accelerometer for a change in acceleration. When a decrease below the calculated acceleration was measured by the computer, the frequency of the oscillator was lowered by predetermined increments until the acceleration was again above the desired value. The specimen had failed when a decrease in frequency could not bring the specimen above 50 percent of the desired acceleration and the test was automatically terminated. The results of the tests are printed out in tabular form on the computer's typewriter.

The total number of cycles to failure were determined by the computer through a simple calculation. Product of time and frequency was computed each time the frequency was changed and these products were summed to obtain total number of cycles to failure.

RESULTS AND DISCUSSION

(U) The results of the tensile tests are presented in Table 2. The orientation of the reinforcing screens in a tensile coupon has a large effect on the tangent modulus of the material and was more than 40 percent lower for the 45° bias than for the other two directions of cutting. The ultimate strength exhibits the expected decrease of nominally 40 percent in strength for the 45° screen orientation. The secant modulus shows little response to the screen orientation. This is to be expected since the secant modulus represents the modulus of the material at low load levels and, at this level, most of the load is absorbed by reorientation of the fibers in the material and not by the screen wires. The secant moduli are included to more completely represent the tensile curves.

Figure 9 shows the results from the fatigue test of the coupons. Five groups of coupons were run at 14.13 MN/m^2 (2050 psi), 14.82 MN/m^2 (2150 psi), 15.51 MN/m^2 (2250 psi), 15.86 MN/m^2 (2300 psi), and 16.55 MN/m^2 (2400 psi). It was determined that the constant load fatigue test for each coupon would be terminated after 25 million cycles, due to cost and utility factors. Each specimen still being tested after 25 million cycles had its load increased by 689,500 N/m^2 (100 psi) each 10 million cycles until it failed in order to establish an order to failure. The arrows on the data points in Fig. 9 indicate that these coupons are still being tested after 25×10^6 cycles and have had their loads increased. No coupons were tested beyond 55 million cycles, and the last points at load levels of 14.13 MN/m^2 and 14.82 MN/m^2 did not fail at the increased load.

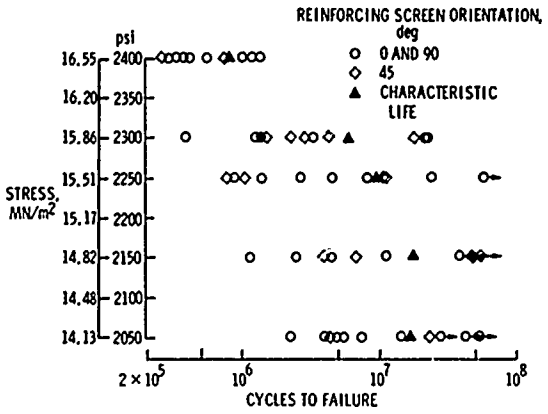

Fig. 9 - Stress-cyclic life data for AISI 347 stainless-steel fiber metal.

The fatigue data show the generally increased life with a decreased stress and exhibit a maximum data spread of about two decades. The fatigue data are represented by a characteristic life plotted in Fig. 9, obtained using Weibull statistical techniques [6]. The three intermediate test stresses demonstrate a possible trend in the data as indicated by the characteristic life, and it should be noted that the Weibull shape parameter for these data was approximately 0.8. The shape parameter for the highest stress was 1.57 and the shape parameter for the lowest load was 1.02. When the shape parameters in the Weibull distribution function are 1, 2, and 3.57, respectively, the distributions are simple exponential, Rayleigh, and normal distribution, respectively. No effects due to the different orientations of the reinforcing screens were noted in the fatigue data. In particular, the 45° orientation bias test is identified to illustrate the absence of trends. Three different elastic moduli corresponding to each separate average tangent modulus determination (Table 2) were used in running these fatigue tests, one for each screen orientation. Use of this modulus in the Eq. (1) computation was assumed, for test purposes, to account for differences in material properties (normalization by the mean). The elastic modulus used to calculate the stress for the 45° coupons was about one-half that used for the 0° and 90° coupons. This resulted in a doubling of the tip deflection of 45° coupons in order to obtain the same stress. It can be seen from Fig. 9 that normalization in this manner was apparently effective since results for the 45° coupons are scattered throughout the data.

The computer-controlled testing of the fatigue coupons has resulted in large savings

in both time and money. Based on the manual testing method reported in Ref. [3], where one coupon was tested at a time, this system has resulted in a 50-percent savings in the cost of the test and has decreased the testing time by a factor of 10. To conduct the tests reported in this paper required approximately 9 months of calendar time, testing (24 hours a day, 7 days a week) continuously much of this time until an average of 3000 hours per shaker (18,000 hours total) were accumulated by this system. During this time, the system was checked daily during the workweek so that any failed coupons could be replaced but operator intervention was not required during actual testing of the coupons.

These fatigue tests have shown that the computer-controlled multiple fatigue tests of composite and sintered materials are advantageous for several reasons:

1. The control algorithm was easily tailored to the material being tested. The algorithm in this test was tailored to follow the decrease in resonance frequency of this particular material and maintain a given stress.
2. Multiple samples were tested and controlled by the same computer hardware without interference between tests.
3. Because of the ability of the machine to make programed decisions, no attention was necessary during the test by an operator.
4. A substantial savings in the time required to run the test was achieved with the use of a closed-loop computer-controlled system, since the computer ran 24 hours a day, 7 days a week.

CONCLUDING REMARKS

(U) These tests have shown that closed-loop computer testing of multiple fatigue specimens is practical and resulted in a savings of both time and money for fatigue testing of this type of fibrous material. Tensile tests were performed to determine the elastic modulus and the results showed that the method of testing used for plastics was applicable. The fatigue data showed considerable scatter; but, considering the type of test (reversed bending), the accuracy of the determination of the material properties, and that the tests were near the fatigue limit for the material, such variations are to be expected. Tests of the material with the 45° bias of the reinforcing screens demonstrated the utility of correcting the elastic modulus by the material properties of the screen orientation. Although grossly different in tangent modulus from the other screen orientation, the 45° orientation demonstrates approximately the same scatter factor in the fatigue test.

REFERENCES

[1] Progress of NASA Research Relating to Noise Alleviation of Large Subsonic Jet Aircraft. A conference held at the Langley Research Center, Hampton, Virginia, October 8-10, 1968, NASA SP-189.

[2] Watson, H. A., Jr., Thompson, J. D., and Rucker, Carl E., "Structural and Environmental Studies of Acoustical Duct-Lining Materials," presented at Progress of NASA Research Relating to Noise Alleviation of Large Subsonic Jet Aircraft. A conference held at Langley Research Center, Hampton, Virginia, October 8-10, 1968, NASA SP-189.

[3] Rucker, Carl E., "Reversed Bending Fatigue Tests of AISI 347 Stainless Steel Fiber Metal," NASA Langley Research Center, presented at 1969 SESA Fall Meeting, Houston, Texas.

[4] Materials in Design Engineering – Materials Selector Issue, Vol. 46, No. 5, 83 (Mid-October 1966-1967).

[5] 1969 Book of ASTM Standards, Part 27, Plastic-General Methods of Testing, Nomenclature.

[6] ASTM STP 91A, 2nd Ed., Guide for Fatigue Testing and the Statistical Analysis of Data, 1963.

TABLE 1
Material Properties for AISI 347 Stainless-Steel Fiber Metal

Coupon Number	Screen Orientation	Tangent Modulus (MN/m^2)	Secant Modulus (MN/m^2)	Ultimate Strength (MN/m^2)
1	0	25143	5084	82.98
2	0	22669	3911	79.38
3	0	25223	7432	71.89
4	0	23383	3876	70.16
5	0	24958	11092	82.07
6	0	21944	6035	72.43
7	0	26262	4542	82.74
8	0	26908	5820	80.73
9	45	12852	10885	54.05
10	45	11822	7783	54.98
11	45	14744	3851	53.08
12	45	13364	3976	56.14
13	45	13068	6715	56.86
14	45	15506	5084	55.83
15	45	14141	5551	55.16
16	45	18655	6955	53.17
17	90	27644	5223	75.27
18	90	24342	5129	80.34
19	90	23592	3962	77.87
20	90	28151	9080	80.24
21	90	23616	6661	77.34
22	90	23614	6256	74.39
23	90	20732	6336	74.35
24	90	35314	6301	79.46

TABLE 2
Average Material Properties for AISI 347 Stainless-Steel Fiber Metal

Reinforcing Screen Orientation in Degrees	Tangent Modulus (MN/m^2)	Secant Modulus (MN/m^2)	Ultimate Strength (MN/m^2)
0	22105	5974	77.80
45	12826	6351	54.91
90	22602	6118	77.41

DISCUSSION

Mr. Silver (Westinghouse Electric Company): How did you manage to hold the resonance frequencies?

Mr. Grandle: The computer looks at the accelerometer output, and since we control on a resonance, there is a rather large peak in acceleration at that point. As the resonance goes downstream the computer looks at it and it decreases the frequency of the digital control oscillator by a given increment. Normally it is small enough so that the computer will not step over this resonance peak until it gets the resonance peak. We do not set right on top of a resonance peak, we usually set to its upper frequency limit.

PROGRAMMING AND CONTROL OF LARGE VIBRATION TABLES IN UNIAXIAL AND BIAXIAL MOTIONS

R. L. Larson
MTS Systems Corporation
Minneapolis, Minnesota

The programming and control of large vibration tables and uniaxial or biaxial motions has long been a problem. Recent developments in servohydraulic analog control technique and digital programming and control methods have made such large systems very practical for performing seismic shock (earthquake) and transportation vibration tests. The topics include the servohydraulic control problems associated with large table systems and some of the programming techniques that are currently available. A large servohydraulically controlled biaxial shock test machine will be discussed to illustrate how the specific problems and requirements are translated into hardware and software to insure an efficient operation of the test facility.

INTRODUCTION

The need for large vibration test facilities is rapidly becoming prominent. The areas of earthquake withstandability and transportation damage of large items have long been sources of unanswered questions. The only way to obtain the answers to some of these questions is to test large, heavy specimens. It is the intent of this paper to present the problems involved with large servohydraulic vibration test systems and indicate what can be done to produce an effective test facility. Of course, not all of the problem areas can be covered in the scope of this work, but it is the intent to provide key points of information about the control and programming methods available.

Servohydraulics is quite suitable for large, heavy specimens because of the large displacements at low frequencies and the total force that is usually required. Unfortunately, a servohydraulic system is actually a positioning device; therefore, direct acceleration control is impossible. The system does not have any zero reference for position in this case. The desired acceleration must be obtained indirectly by achieving a displacement of the vibration table.

Assuming the need for a large vibration table exists, the problems involved in obtaining an effective servohydraulic test system can be outlined. It is interesting to note some historical information about such problems as well as the present techniques used to solve them.

FORCE BALANCE

The first problem is the number of drive actuators used. In a single axis system, the drive system is coupled to a rigid table in a line or a plane. In the horizontal axis case, as seen in Figure 1(a), two points define the horizontal displacement of the edge of the table. If more than two forcing actuators are used, then the force balance between actuators is upset. Because all the actuators are in stroke control on a fairly rigid table, any small errors in calibration, loop gain, etc. will cause the actuators to develop static loads opposing each other. These load levels depend upon the table stiffness and the amount

of control loop errors. It is not uncommon, though, that offsets of 20% to 30% of full load occur. Usually, these load offsets do not change until the dynamic response of the table or oil compliance of the actuators decouples the drive system. The undesirable result of these offsets is the reduction of exciter performance because the servovalves can never produce their full flow capability.

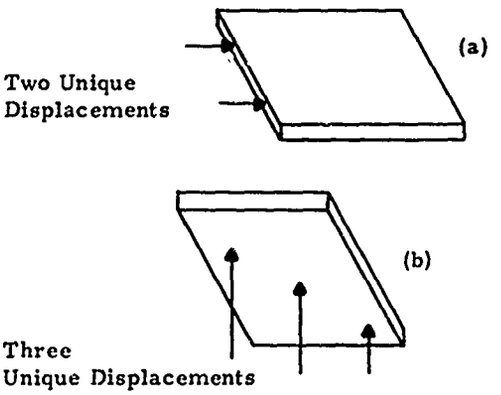

Figure 1

Historically, the problem has been avoided whenever possible. The minimum number of actuators required to define the line or plane have been used to completely avoid the problem. Where more actuators have been used, phase and amplitude controllers have been implemented for a variety of dynamic reasons such as table dynamics, but this does not solve the load offset problem. However, there is a solution to the problem, and this has been incorporated in a new concept of control that will be discussed in a later section after all the problems have been presented.

RESTRAINT

The second major problem is the restraint of undesirable table motions. Some of the motions can be constrained independently from the drive system. For example, the roll, pitch, and true vertical motions can be arbitrarily constrained during horizontal vibration. However, care should be exercised in the constraint of the yaw motion since this relates to the drive system. Similarly, for a vertical drive system the horizontal motions can be arbitrarily constrained, but, in this case, the roll and pitch motions relate to the drive system. Figure 2 illustrates these constraint axes.

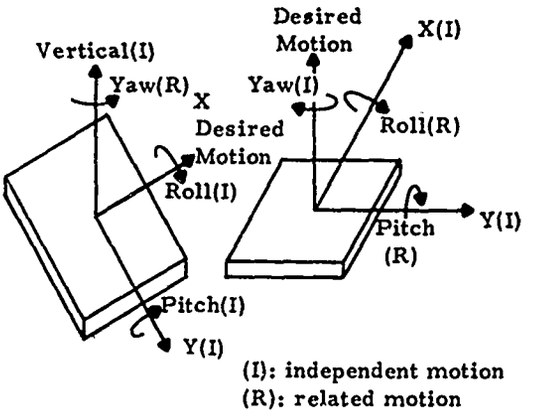

Figure 2

The independent motions should be constrained by a preloaded mechanical system, which usually consists of mechanical or hydrostatic bearings pressing against the table. The restraint system should be designed to not interfere with desired table motions. Proper preloading of the restraint system will be very important in minimizing extraneous motion and reducing backlash problems.

Over-constraint of a related axis of motion can also cause a problem in equal dynamic loading of the drive system. Small errors in the controlled actuators will produce undesired motions without constraint. Excessive constraint can force some of the exciter actuators to carry more of the load than necessary. In this case, it is far better to use an active control system to help minimize the errors inherent in individual actuator control and complement this action with a passive mechanical restraint system just to maintain overall table stability (i.e., keep the table from tipping over on its side). Referring to Figure 2 for the horizontal desired motion, soft mechanical side restraints on both sides of the table parallel to the X axis would prevent any major translations in the Y direction, but could allow slight errors if they should occur. The burden of yaw control would fall upon the exciter system control electronics.

The dead weight load of the table and specimen can be a problem for a vertical drive system. If the exciter system must maintain a heavy load (20% of full load) just to offset gravity, then system performance will suffer and waveform distortion of all dynamic parameters will increase. Just as in the load offset problem, the servovalves

will never allow maximum flow for upwards motion of the table. Waveform distortion will occur from the unsymmetrical force required to produce the desired results. In this case, the best solution is to use actuators with a static lift system operating upon the piston rod. Such a combination must have accumulators to allow the static force to remain fairly constant during dynamic cycling.

A hydraulic exciter system has basically four physical limitations upon performance. Figure 3 illustrates these limiting factors.

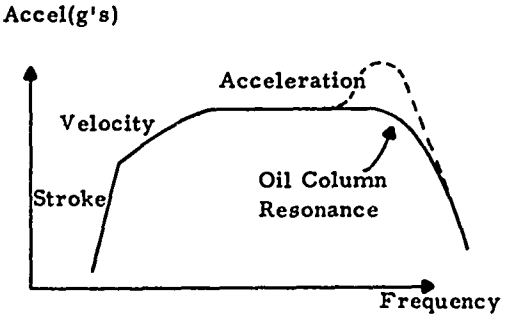

Figure 3

From low to high frequency, the limits are:

1) Stroke limit of actuators.
2) Velocity limit imposed by servovalve peak flow or by pump plus accumulator system.
3) Acceleration limit determined by maximum force possible.
4) Oil column resonance dictated by the hydraulic spring compliance and other system compliances along with the specimen and table mass.

The high frequency roll-off of the exciter system performance will usually be predominated by oil column resonance. Beyond oil column resonance, the oil itself is absorbing the drive energy. Since this resonance is not very heavily damped, provision for stabilization of this condition must be made in the control electronics to maintain system stability for a heavily loaded system or for good performance through the trouble frequency. Properly compensated, the system will work quite satisfactorily through oil column resonance as indicated by the solid line in Figure 3.

Table and reaction mass dynamics are two problems that are not often investigated in sufficient depth. It should be noted that the best control system in the world is not going to help the situation where the vibration table exhibits poor dynamic rigidity in the frequency range of interest. The reaction mass and foundation should be carefully considered to ensure that the exciter system is human comfort and structural integrity of exterior construction.

There are two specimen related problems that, if they are known in advance, will allow the system design to compensate for them. One of the problems is the specimen reflecting loads back into the drive system. If sufficient reserve actuator force capacity is available, this problem is not serious. However, if this factor was not considered in the system sizing, then severe reduction of amplitude response can occur. The other problem of center of gravity location has similar results upon system performance. Large amounts can be induced in the drive system if the excitation drive vector does not point through the center of gravity. Of course, a good restraint system should help minimize these problems, too.

BIAXIAL TABLES

A biaxial vibration test system has a few new problems and extensions of those previously discussed. Biaxial is assumed to mean motion in the vertical axis and one horizontal axis.

The first new problem involves the swivels required on the actuators to allow simultaneous motion. Since these swivels force the actuators to swing through arcs, some compensation is required for the system to achieve true translations without describing these arcs. The swivels should have as little backlash as possible without adding large friction forces. Too much swivel compliance will soften the drive system and lower the oil column natural frequency.

Driving the system with center-of-gravity offsets presents a problem as discussed previously, but now there are more co-ordinate directions with which to be concerned. The difficulty of solid reaction is complicated by the fact that simultaneous operation places a heavier burden on the reaction mass' capability to provide a solid reference with little cross-talk. Of course, without this solid reference, there will be

cross-talk of data through the vibration table. Here again, careful design can put the table trouble frequencies above most test bandwidth requirements.

The most serious control problem in biaxial performance is overturning moment. Driving the horizontal system below the center of-gravity will cause a vertical pitch moment to be generated which will tend to rock the vibration table about the transverse horizontal axis. The vertical drive system's ability to resist this motion depends upon the vertical actuator oil stiffness and the degree of control available on the displacements. This effect is contrary to normal oil column stabilization methods because in this case the desired result is the vertical actuators developing large forces with small resultant displacement changes. If the actuator sizing has included this effect in the choice of actuator force ratings, the problem may have an acceptable solution. This not being the case, the electronic control system must be cross-coupled to help the vertical system anticipate the actual overturning moment. Beyond the pitch oil column resonance of the vertical drive system, the moments will decouple and induce very little pitch error.

NECESSARY DESIGN REQUIREMENTS

From the outline of the problem involved, it is now possible to list the necessary design requirements for the exciter system.

Hydraulic

1. The correct force rating for the drive system should include anticipated loads from center-of-gravity offsets. This will include the pitch overturning moment for a biaxial system.
2. Oil column resonance should be high enough to provide the necessary performance, taking all effective compliances into account.
3. The table should have the lowest resonant mode at a frequency that is higher than the frequency band of interest. The reaction mass should provide the necessary rigid coupling of the system in all major loading axes. Do not forget that pitch moments can be a significant load input to the reaction foundation.
4. Special care should be taken to understand the sources of acceleration distortion, and what can or cannot be done about this effect.

Electronic Controls

A heavy burden is placed upon the electronic control system in order that the system perform satisfactorily.

1. The controls should have the necessary compensation required to operate the system satisfactorily through oil column resonances in all degrees of freedom.
2. Control of the force balance of an over-restrictive drive system is the best means of maximizing lower frequency performance.
3. For best control, the control system should independently have control and stabilization for the principle translation axes, as well as roll, pitch, and yaw motions.

Example

The requirements for the control of a large biaxial vibration table has resulted in the successful design of a control technique that performs the necessary functions.

The system consists of a 20 foot by 20 foot vibration table for seismic shock applications. The drive system has four vertical and three horizontal actuators driving the 90,000 pound test table (see Figure 4). The maximum specimen weight is 60,000 pounds. The total force capability is 100,000 pounds vertically and 150,000 pounds horizontally; the maximum velocities are 38 inches per second vertically and 42 inches per second horizontally. The control system provides overall control of the vertical and horizontal displacements with independent control and stabilization for roll, pitch, and yaw. A force balance of 50 to 100 psi in each actuator is maintained with the exception of the vertical drive resistance to overturning moment. The control system can effectively restrict roll and yaw motions to less than 1% of principle translations. Of course, the control system cannot operate as effectively if the hydraulic system becomes heavily flow limited. In this case, the drive system will be dominated by how well the servovalves are matched and the loading on the actuators at the moment of high demand. The

overturning moment in this system is quite large, but the vertical system can resist this moment until the actuators become force and thus velocity limited. Normally, the pitch can be kept less than 0.1 degree without active cross-coupling compensation.

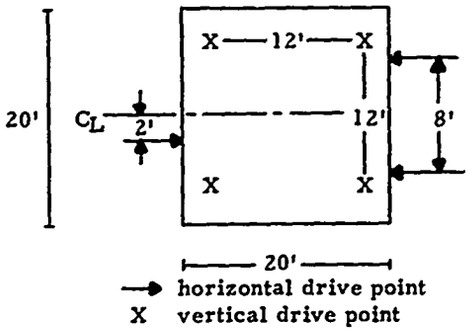

Figure 4

PROGRAMMING

The vibration table system is not very useful unless an effective means of programming is used. The types of programming can be categorized into deterministic and random waveforms. With this in mind, two means of implementation are possible, analog or digital. It is important to note the good and bad points of each method with regard to ease of operation and what the method can do for you.

Analog

Displacement sine sweep testing is very easy to perform, but it does not provide an easy way to control acceleration amplitude. Analog integrators can be used to program a constant velocity or acceleration sweep for resonant search and durability testing. However, analog integration does not perform very well at frequencies below 4 Hz because of practical design problems. To operate at low frequencies, very high quality integrators are required, and they may still not have adequate accuracy or performance.

Amplitude and phase controllers can be used to indirectly program sinusoidal displacement amplitude as a function of the fundamental component of the table acceleration. Frequency breakpoints can be implemented to allow the sine sweep to first have constant displacement at low frequencies; then go to constant velocity and constant acceleration. If the actual acceleration is to be used for amplitude control, the tracking filters to extract the fundamental component are necessary because of high distortion occurring in the drive system.

Analog random generators with 1/3 octave filters provide a method of programming a stationary power spectral density (PSD). Automatic equalizers can provide spectral amplitude control, but are usually difficult and cumbersome to operate. An analog multiplier can give a control of the total RMS of the random generator output, but it is impractical to use 1/3 octave bands with the difficulty of generating the control signals for each multiplier by analog means.

Analog transient function generators can be used for shock spectrum testing. Usually the types of transient waveforms available are quite restricted and variation of the waveform parameters is both costly and sometimes difficult at best.

In general, an analog programming approach to random programming is restricted in its flexibility of types of inputs and is complicated to operate when sophisticated test programs are desired.

Digital Programming

With a dedicated computer system, the problems of flexibility and difficulty of operation are greatly reduced. The computer can be used to pre-process acceleration signals to convert them to the necessary displacement signals. With base line drift corrections, the digital integration process can accurately perform to very low frequencies. Whether the desired command waveforms are deterministic or random, the digital computer system can now provide a very wide range of types of inputs and flexibility of parameter variation. If the input can be described or simulated by a mathematical expression, the digital system can provide the necessary command functions.

Various degrees of capability can be accomplished with a digital system. A simple small computer system can be used to control analog generators, or a more sophisticated system could generate the desired waveforms entirely by digital means. An example of a simple system is shown in Figure 5.

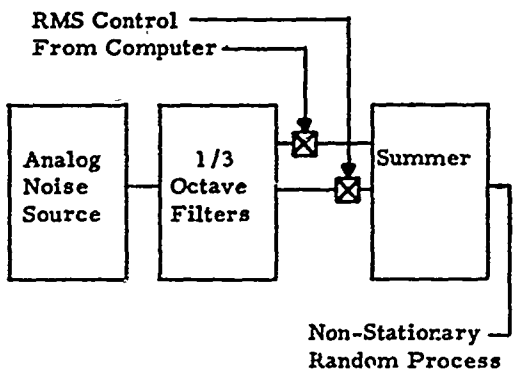

Figure 5

This system uses the digital computer to command the RMS level output of each 1/3 octave filter. A more sophisticated system is one in which the random signal is digitally derived from a given power spectral density. With this capability, it is a logical extension that automatic equalization is possible in the computer system.

A real bonus with a digital system is the system organization that can be accomplished. The computer can be used for data acquisition and analysis functions during a test if desired. The advent of Fast Fourier Transform techniques has reduced rather complicated time series analysis problems to practically a mechanical operation. Real-time analysis and control of power spectral density during a random test or computation on data acquired during a test for any analysis damping of the shock spectrum are quite within the capability of present-day equipment.

The computer could also perform some failsafe functions to automatically shut down the program and/or the hydraulics if certain critical parameter changes are detected. A human operator is not always fast enough to prevent damage to a large, heavy and oftentimes expensive specimen.

A digital system has a great deal to offer in co-ordinating the many tasks to be performed in a large vibration facility, and should not be arbitrarily cast aside for cost reasons without a careful look at what it can do.

THE END?

After noting and considering all of these points, the task of implementing such a system has just begun. It is hoped, however, that the major points discussed have been resolved before any details of construction and/or performance arise. Without the full comprehension and confidence in the basic system organization and capabilities, it will be impossible to determine if detailed test requirements can be achieved.

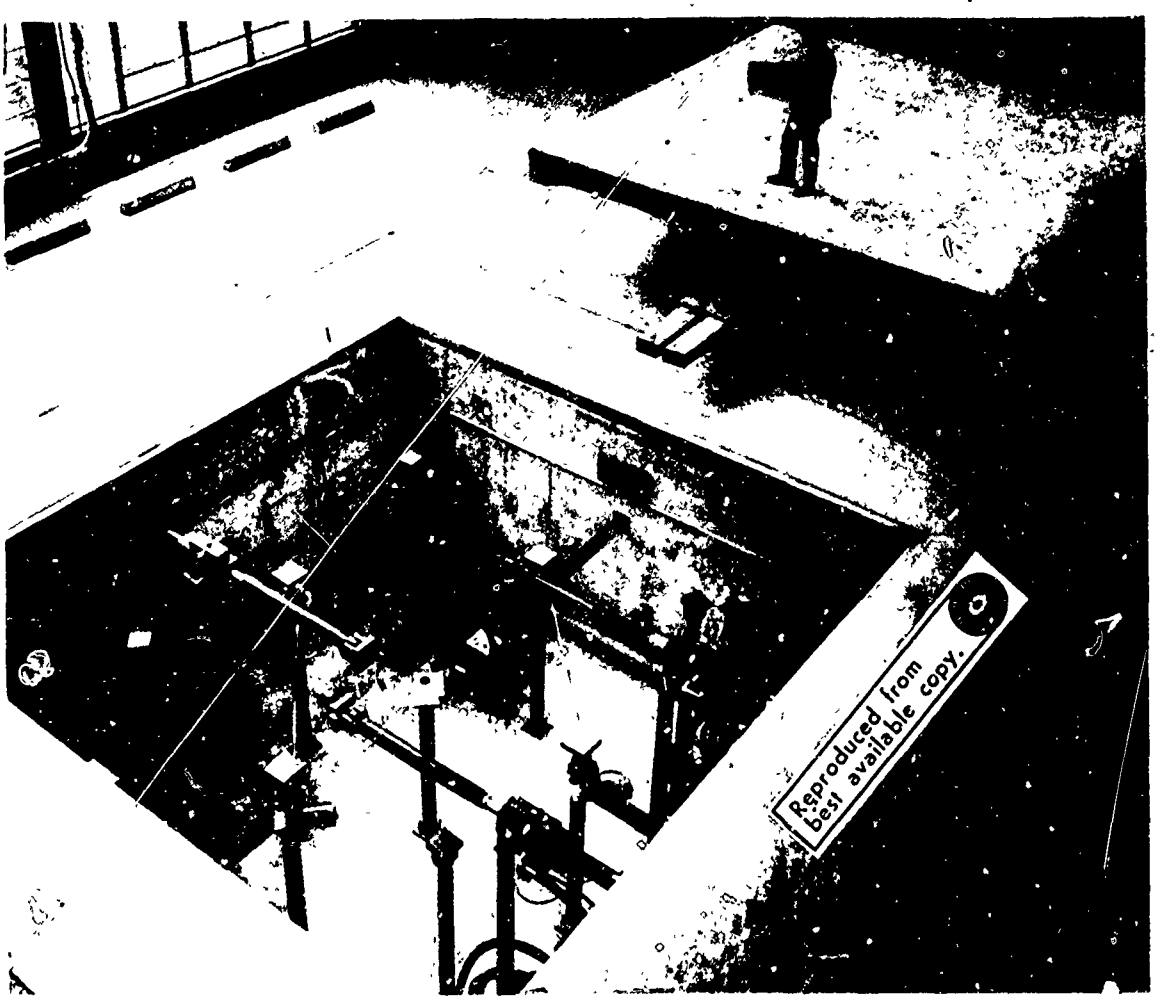

Seismic Shock Test Facility Having a 20 Foot By 20 Foot Table and 100,000 Pound Force Capacity For X-Z Motion.

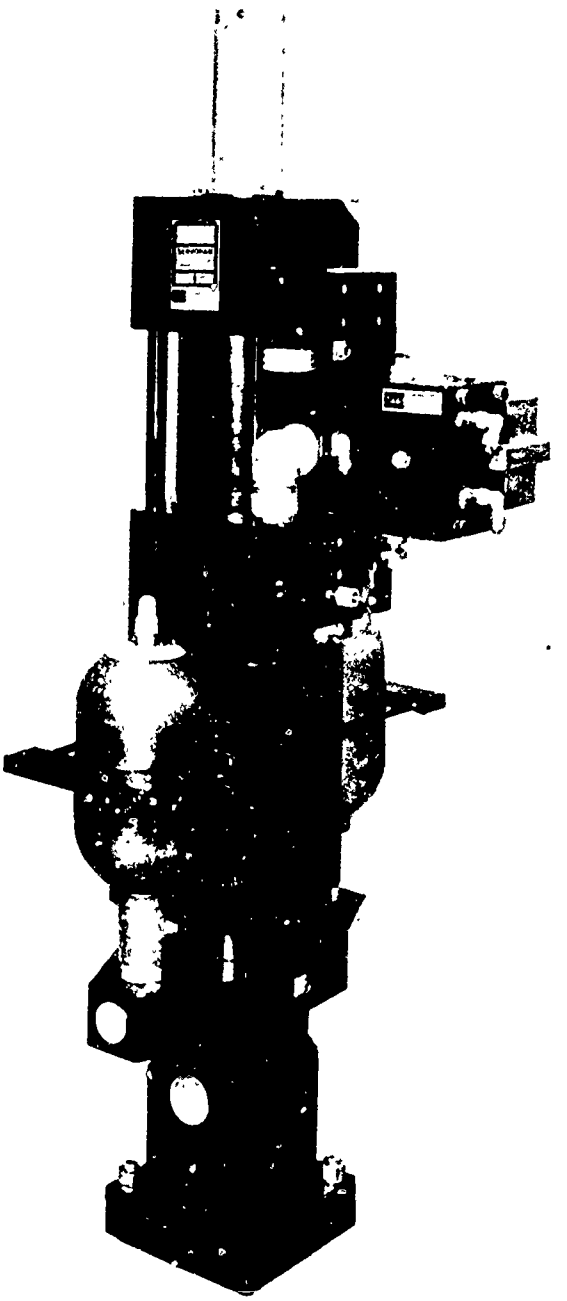

Hydraulic Tandem Actuator Providing Static 1g Support of Specimen in Vertical Direction.

DISCUSSION

Mr. Pakstys (General Dynamics Corporation): What kind of a system does the Berkley facility have, digital or analog?

Mr. Larson: At the moment it is using analog programing only.

A DATA AMPLIFIER GAIN-CODE RECORDING SYSTEM

J. R. Olbert, and T. H. Hammond
Hughes Aircraft Company
Culver City, California

To eliminate the need of an instrumentation operator manually logging amplifier gain settings, a system was designed which would continuously record all amplifier gain information on the same magnetic tape as the actual vibration data. This gain information is multiplexed with an IRIG-B time code signal and recorded on a single tape track.

To accomplish this task, both time and frequency multiplexing schemes are used. Gain code output signals (DC voltage levels representing gain switch position) from data amplifiers are commutated, or time multiplexed, to provide a single output signal containing switch position information for 72 data amplifiers. This signal is then frequency multiplexed with the 1 KC IRIG-B time code. The composite signal, containing both amplifier gain information and time-of-day information is then available to record on a single tape track.

For data reduction, a decoding and readout system is provided. The data reduction operator switch selects the proper accelerometer amplifier channel and a readout is displayed of that amplifier gain at the time of data recording.

Other gain recording systems in use either record the amplifier gain code signal on an adjacent data track or on the same track as the actual data. Recording gain information on a separate data track uses up data recording capability which is usually at a premium. The method of superimposing data signals on a gain code signal reduces the recorder dynamic range available for data. The system developed does not have these objections since no data recording capability is lost nor is the data quality affected in any way.

INTRODUCTION

A record of gain settings used during data recording must be maintained when using variable gain data amplifiers. The most common method of recording gains is probably that of the data acquisition operator maintaining a written log of amplifier settings. Human error problems are, however, always present and the operator can record the gain settings erroneously or forget to record them altogether.

The problem of accurately recording gain settings is particularly acute when many gain changes are made during resonant conditions of a sine sweep vibration test. This condition is further aggravated in a centralized data acquisition facility where one operator may be recording a large number of data channels from several separate test positions simultaneously.

A recording method which would eliminate the human error problem has been of considerable interest in this laboratory for some time. Gain recording systems which are presently in use or have been proposed were all considered unsatisfactory and include:

1) Recording gain code signals for each amplifier on separate tape tracks. This method would reduce tape channels available for recording data by one half.

2) Superimposing the data signal on a DC gain code signal. This method has the advantages of not requiring additional recording

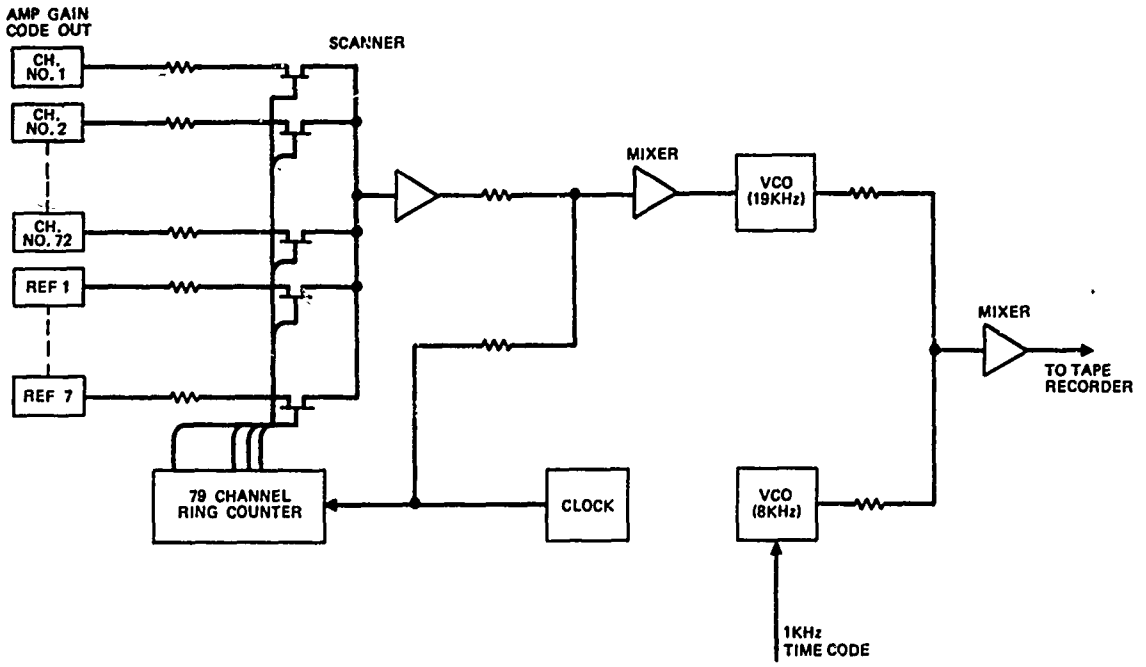

Figure 1 - Encoder Block Diagram

channels and not separating gain information from the data. However, this method was not acceptable because it would appreciably reduce recorder dynamic range available for data.

3) Digital control and recording of amplifier gains. This appears to be a good method for facilities where it can be used. However, adaptation of existing analog equipment to this method does not appear practical.

SYSTEM DESCRIPTION

An amplifier gain recording system which overcomes most of the above mentioned problems was developed. Block diagrams showing the major components of this system are given in Figures 1 and 2.

During operation, DC step voltage gain code signal outputs of all amplifiers are continuously scanned at a rate of once per second. The scanner output signal is then used to frequency modulate a 19 KHz carrier. This signal is then mixed with a 8 KHz carrier which has been modulated with the 1 KHz IRIG-B time code. This composite signal is then recorded on a single tape track using direct record electronics. Since record frequency response of only 25 KHz is required, low band recorders can be used at a tape speed of 15 ips or higher. By mixing the gain and time codes, additional record channels are not required since the time code was already being continuously recorded on each data tape.

During data analyses, both the data track and the tape track containing the multiplexed gain and time information is played back. The multiplexed information is decoded and displayed. The time code is displayed using a standard time code translator/display unit. The gain code is amplitude detected and a lamp indicating amplifier gain corresponding to the detected voltage level, is turned on.

CIRCUIT OPERATION

The amplifier gain code signal is a positive DC voltage varying from 12 volts at 1 G full scale range to 0 volts at 1000 G full scale range. These voltages are obtained from a resistive divider string connected to the amplifier B+ supply, and are switched to an output jack through an additional wafer which was added to the gain range selector switch. A sequential electronic commutator scans the 72 gain code output signals. This scanner is made up of junction FET analog switches driven by an SCR ring counter. A unijunction oscillator serves as a clock to shift the ring counter.

In addition to the 72 gain code (switch

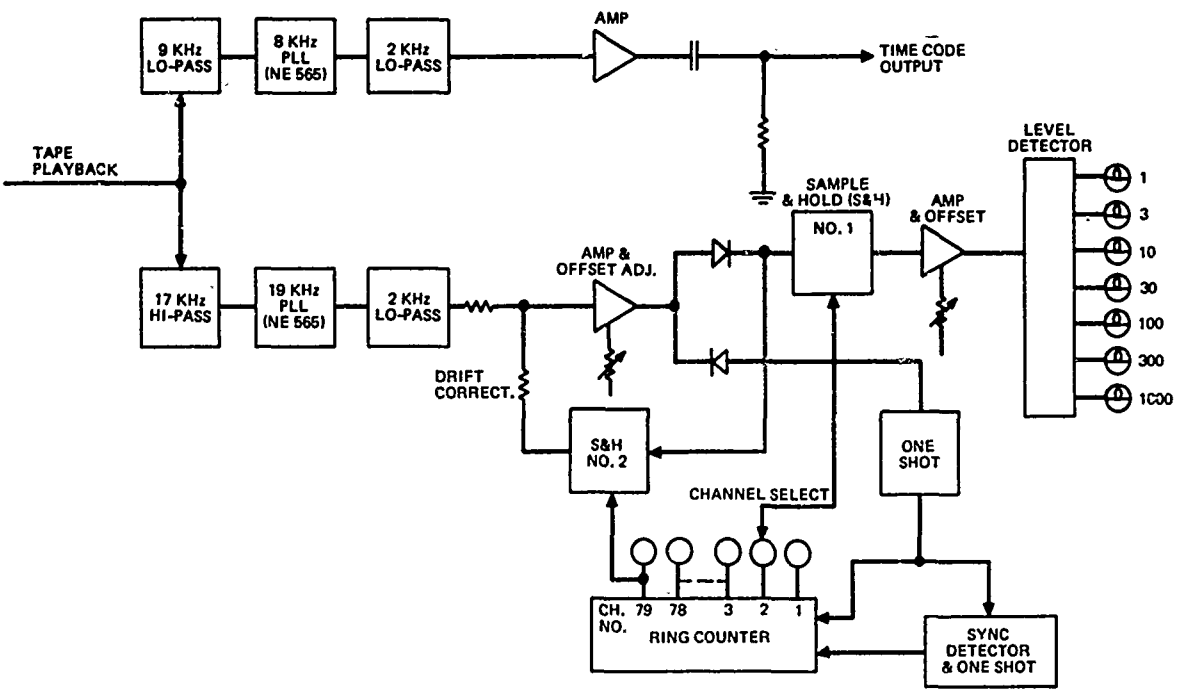

Figure 2 - Decoder Block Diagram

position) signals, the clock pulse, a frame sync pulse, and seven fixed voltage reference levels are also encoded.

A complete scan frame is shown in Figure 3. The clock pulses mark the beginning of each channel and are used in the decoding process as counter shift pulses. The seven reference voltage levels correspond to the switch position gain code values and are used to check and calibrate the decoder. Also, the zero voltage calibrate level is used as a reference for providing automatic system drift correction during decoding.

The scanner output goes to a 19 KHz center-frequency, voltage-controlled oscillator (VCO). The common up-down integrator type oscillator which is used has a triangular wave output. This triangular waveform is shaped into a sinewave by eight biased diodes.

A second similar VCO with a 8 KHz center frequency is provided for the IRIG-B time code signal. Outputs of these two VCO's are linearly mixed and recorded on all tape recorders being used to record vibration data.

During data playback, the multiplexed track must also be reproduced, decoded, and displayed. The decoder/display portion is shown in the block diagram of Figure 2.

The tape playback signal first goes to a pair of four-pole active filters, one being a 17 KHz hi-pass and the other a 9 KHz low-pass filter. Output from the hi-pass filter is the modulated gain code FM carrier and output from the low-pass the modulated time code FM carrier. To demodulate these FM carriers, Signetics Model NE565 phase lock loop discriminators are used. These discriminators (costing under $10) consist of a phase detector, amplifier, and VCO. In operation, the VCO center frequencies are set to the carrier center frequencies (8 and 19 KHz) using an external capacitor and trimpot. As the input frequency shifts with modulation, the phase detector produces a DC output signal. This signal is amplified and filtered and applied as a control voltage to the VCO causing its center frequency to shift and remain locked on the input carrier.

Output of the 19 KHz CF discriminator (amplifier gain code pulse train) is split into positive (gain information) and negative (sync pulse) components. The sync pulses trigger a one-shot which is used as a shift pulse for a 79 stage ring counter. Another one-shot is triggered when three successive sync pulses are absent (resulting from the wide sync pulse at the beginning of each scan frame). This latter one-shot resets the ring counter to channel No. 1.

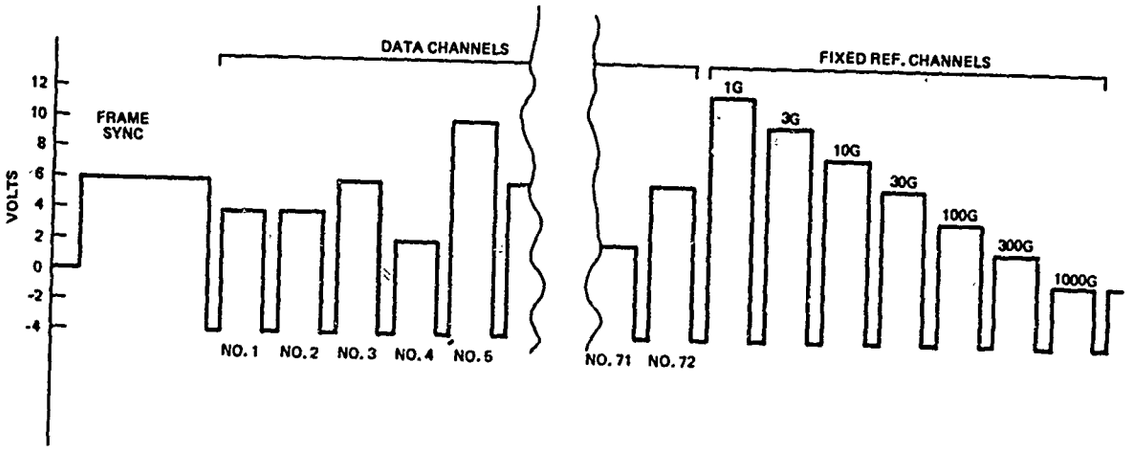

Figure 3 - Typical Scanner Output Frame

Gain information of the desired amplifier channel is gated with a FET switch to the sample and hold circuit. Gating is done at the appropriate time by connecting the proper segment of the 79 stage ring counter to the FET switch. This is accomplished by a bank of four front panel 18-position selector switches (see Figure 4). Output from the FET switch goes to a holding capacitor which holds the signal until the next gating signal arrives one second later (once each frame cycle).

The sample and hold output is applied to a bank of seven parallel amplitude detectors. Each detector is biased to trigger at the appropriate range switch voltage level. Finally, output from each voltage detector drives a front panel lamp, thus displaying the gain range of the selected amplifier number.

CONCLUSIONS

1) Design requirements were met for a system which would provide: a) automatic gain recording, b) permanent records, c) no reduction in amount or quality of data recording capability, d) system reliability, and e) ease of operation.

2) Long lead time problems encountered in acquiring vendor-produced items were eliminated by designing the system so it could be built mainly from store stock items.

3) The system was designed, and performs satisfactorily, for recording gains of a large number of amplifiers. However, for a relatively small system, installation of this type of system would probably not be practical because of its complexity.

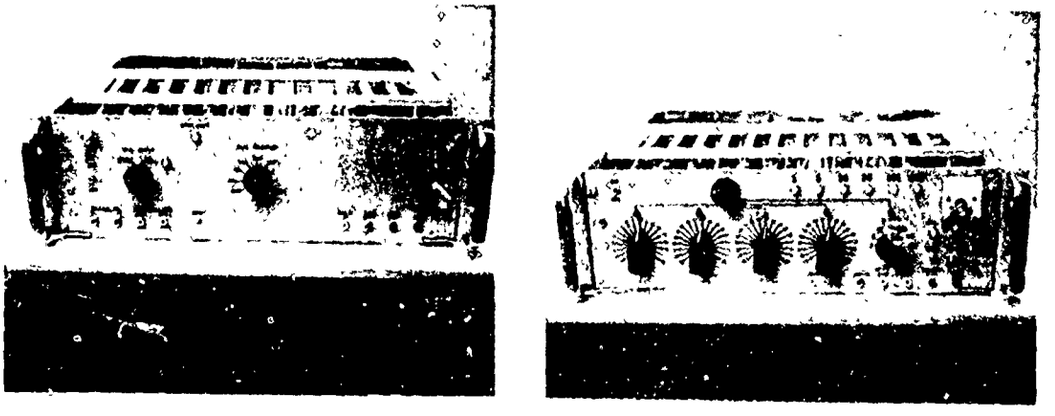

Encoder

Decoder

Figure 4 - Front Panel View of Completed System

STABILITY OF AN AUTOMATIC NOTCH CONTROL SYSTEM IN SPACECRAFT TESTING

B. N. Agrawal
COMSAT Laboratories
Clarksburg, Maryland

In this paper, an automatic notch control system is simulated analytically. The response of the structure is obtained by numerical integration and, at each step of integration, the amplitude of base excitation is modified by the control equation. Such a simulation can be used to predict the stability of the notch control system and to adjust the compression ratio to its optimum value for the sinusoidal vibration testing.

INTRODUCTION

It is recognized that during launch the dynamic response of a large spacecraft will tend to suppress the launch vehicle motion and thus reduce the input level to the spacecraft at the primary spacecraft resonant frequencies. Also, the mechanical impedances during test and when the spacecraft is attached to the booster vehicle are not generally the same; i.e., the booster is more flexible than the relatively inflexible test fixture.

The levels specified for vibration testing do not take into account the possible reduction at resonance, since this effect is a function of dynamic characteristics of each particular spacecraft. To preclude failure due to the application of the unrealistic loads, the input sinusoidal vibration levels are notched at the primary spacecraft resonan frequencies so that the loads at the critical members do not exceed the expected flight loads. An automatic control system, in which the control parameter is automatically switched from input acceleration to allowable response and back as the sweep progresses, is commonly used.

During the acceptance sinusoidal vibration test of the INTELSAT IV, F1 spacecraft, there was an unexpected overshoot of the notched controlled response for certain modes. The problem was alleviated by reducing the sweep rate from 4 to 2 octaves/minute at the resonant bandwidths where the overshoot took place. This solution was chosen since the notching during qualification testing at the slower sweep rate was within tolerance.

To obtain a better understanding of the notch control system, a study was undertaken at COMSAT Laboratories. The notch control system was simulated analytically and the effects of different damping coefficients, sweep rates, natural frequencies, and compression rates on the behavior of the notched controlled response were studied. Experiments were also performed on the cantilever model with the Ling control system. This paper presents the analytical simulation of the notch control system and the notch-controlled responses for various parameters of the structure and the control system.

AUTOMATIC NOTCH CONTROL SYSTEM SIMULATION

Figure 1 is a block diagram of the notch control system at COMSAT Laboratories. The amplitude of base excitation, I(t), is controlled by

$$I(t) = I_0 + \frac{1}{K}\int_0^t [a_c - \bar{a}(t)]\, dt \qquad (1)$$

where D is the differential operator, K is the compression rate, a_c is the allowable response acceleration amplitude, I_0 is the amplitude of unnotched base acceleration, $\theta = \omega(t)$ is the frequency of the base excitation, and $\bar{a}$ is the

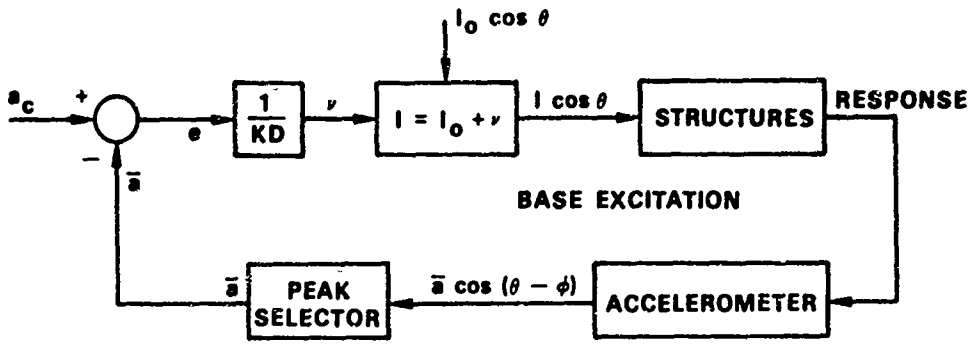

Fig. 1 - Notch control system block diagram

amplitude of response acceleration. Differentiating Eq. (1) with respect to t, we obtain

$$\frac{dI}{dt} = \frac{1}{K} [a_c - \bar{a}(t)] \quad . \qquad (2)$$

The response amplitude, $\bar{a}$, which will be discussed later, is obtained by numerical integration. At each step, the amplitude of the base excitation, I(t), is modified as follows:

$$I_{t+\Delta t} \approx I_t + \frac{dI}{dt} \Delta t$$

$$\approx I_t + \frac{1}{K} (a_c - \bar{a}) \Delta t \quad . \qquad (3)$$

The frequency of excitation, ω, which is swept at a logarithmic sweep rate, is given by

$$\omega = \omega_0 2^{\beta t/60} \qquad (4)$$

where ω_0 is the initial frequency, β is the sweep rate in octaves per minute, and t is the time in seconds.

STRUCTURAL RESPONSE

The structure is simulated by a single-degree-of-freedom mechanical system shown in Fig. 2. No generality is lost, since the modal equations of a multiple-degree-of-freedom system are similar to the equation of motion of a single-degree-of-freedom mechanical system.

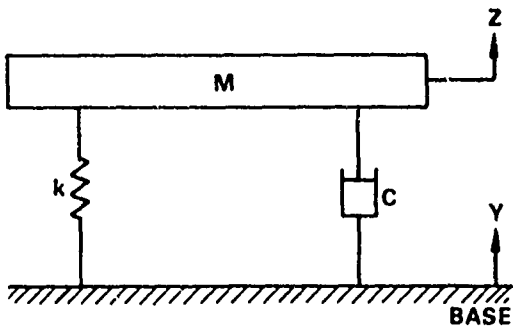

Fig. 2 - Single-degree-of-freedom mechanical system

The equation of motion for the system shown in Fig. 2 is

$$M\ddot{Z} + C(\dot{Z} - \dot{Y}) + k(Z - Y) = 0 \qquad (5)$$

where M is the mass of the system, k is the stiffness of the spring, C is the damping coefficient, Y is the base displacement, and Z is the mass displacement. Let

$$X = Z - Y$$

$$\ddot{Y} = -I \cos\theta \quad . \qquad (6)$$

Substituting X into Eq. (5) results in

$$\ddot{X} + 2\xi\omega_n\dot{X} + \omega_n^2 X = I(t) \cos\theta \qquad (7)$$

where $\xi = \frac{C}{2M\omega_n}$ = fraction of critical damping

$\omega_n = \sqrt{k/M}$ = natural frequency.

The solution of an equation which is similar to Eq. (7) except for an extra cubic nonlinear term in X is obtained in Ref. [1] by using the asymptotic method, developed by Mitropolskii [2]. However, since Eq. (7) is a linear and time-dependent-parameter differential equation, in this paper the solution is obtained by using the direct approach as follows. For constant amplitude and frequency of base excitation, the steady-state solution will have constant amplitude and phase angle; however, for time-dependent amplitude and frequency of base excitation, the solution may have a time-dependent amplitude and phase angle. Hence, we seek the solution of Eq. (7) in the following form:

$$X = a(t) \cos[\theta - \phi(t)] \quad . \qquad (8)$$

The first and second derivatives of X are

$$\dot{X} = \dot{a}\cos(\theta - \phi) - a(\omega - \dot{\phi})\sin(\theta - \phi)$$

$$\ddot{X} = \ddot{a}\cos(\theta - \phi) - 2[\dot{a}(\omega - \dot{\phi})\sin(\theta - \phi)] - a(\omega - \dot{\phi})^2\cos(\theta - \phi) - a(\dot{\omega} - \ddot{\phi})\sin(\theta - \phi) \quad . \quad (9)$$

Substituting the expressions for X, $\dot{X}$, and $\ddot{X}$ into Eq. (7), we obtain

$$\begin{aligned} &\ddot{a}\cos(\theta - \phi) - 2[\dot{a}(\omega - \dot{\phi})\sin(\theta - \phi)] - a(\omega - \dot{\phi})^2\cos(\theta - \phi) - a(\dot{\omega} - \ddot{\phi})\sin(\theta - \phi) \\ &+ 2\xi\omega_n\dot{a}\cos(\theta - \phi) - 2\xi\omega_n a(\omega - \dot{\phi})\sin(\theta - \phi) + \omega_n^2 a\cos(\theta - \phi) \\ &= I\cos\theta \\ &= I[\cos(\theta - \phi)\cos\phi - \sin(\theta - \phi)\sin\phi] \quad . \quad (10) \end{aligned}$$

Neglecting the second-order terms, $\ddot{a}$, $\ddot{\phi}$, $\dot{\phi}^2$, $\dot{a}\xi$, $\xi\dot{\phi}$, and $\dot{a}\dot{\phi}$, and equating the coefficients of $\sin(\theta - \phi)$ and $\cos(\theta - \phi)$ to zero results in

$$2\dot{a}\omega + a\dot{\omega} + 2\xi\omega_n\omega a = I\sin\phi$$

$$-a(\omega^2 - 2\omega\dot{\phi}) + \omega_n^2 a = I\cos\phi \quad . \quad (11)$$

Solving Eq. (11) for $\dot{a}$ and $\dot{\phi}$, we obtain

$$\dot{a} = -\xi\omega_n a - \frac{a\dot{\omega}}{2\omega} + \frac{I\sin\phi}{2\omega}$$

$$\dot{\phi} = \frac{\omega^2 - \omega_n^2}{2\omega} + \frac{I\cos\phi}{2a\omega} \quad . \quad (12)$$

The solution [Eq. (12)] is exactly the same as the solution obtained by using the asymptotic method in Ref. [1]. The steady-state solution corresponding to constant ω and I is obtained with the condition that

$$\dot{a} = 0 \quad \text{or} \quad a = \text{constant} \quad . \quad (13)$$

Using this condition in Eq. (12), we obtain the steady-state solution:

$$a = \frac{I}{\sqrt{(\omega_n^2 - \omega^2)^2 + (2\xi\omega\omega_n)^2}}$$

$$\tan\phi = \frac{2\xi\omega\omega_n}{\omega_n^2 - \omega^2} \quad . \quad (14)$$

This is the exact steady-state solution for Eq. (7). The amplitude, a, and phase angle, ϕ, are obtained by integrating Eq. (12) numerically, and their initial values are obtained from Eq. (14). The amplitude, $\bar{a}$, of the absolute acceleration, $\ddot{Z}$, can be obtained by using the following relationship:

$$\bar{a} = [(a\omega^2 + I\cos\phi)^2 + I^2\sin^2\phi]^{1/2} \quad . \quad (15)$$

RESULTS AND DISCUSSION

The structural response is obtained by using the Runga-Kutta method to integrate Eq. (12) and changing the base excitation at each step according to the control equation [Eq. (3)]. Typical responses are given in Figs. 3 and 4. These responses are calculated by varying the fraction of critical damping, the compression rate, the natural frequency, and the sweep rate. Overshooting factors, which are defined as the ratio of maximum response amplitude to the allowable response amplitude, are plotted vs the fraction of critical damping in Figs. 5 and 6 for various sweep rates, compression rates, and natural frequencies. The notching factor is defined as the ratio of the maximum steady-state response without notching to the allowable response.

The results of the simulation of the notch control system indicate that the characteristics of the structure, such as damping and natural frequencies and test specification sweep rate, and the characteristics of the control system, such as compression rate (gain), influence the overshooting and oscillatory behavior of the response. The overshooting factor increases for higher sweep rates and compression rates and for lower natural frequencies and damping coefficients. The oscillatory behavior of the response amplitude increases for lower compression rates and damping coefficients. For the same compression ratio in the control system, the degree of overshooting and oscillatory behavior will be different for structures at different modes (different damping and mode frequencies) and/or different sweep rates.

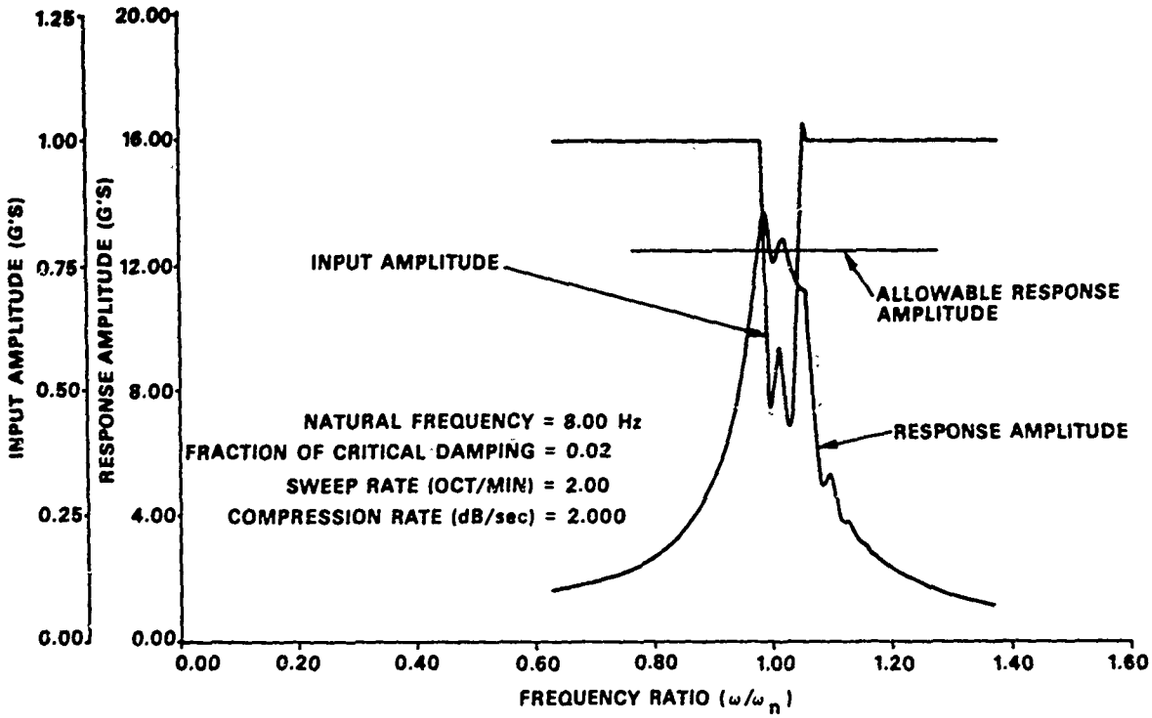

Fig. 3 - Response for swept notched excitation

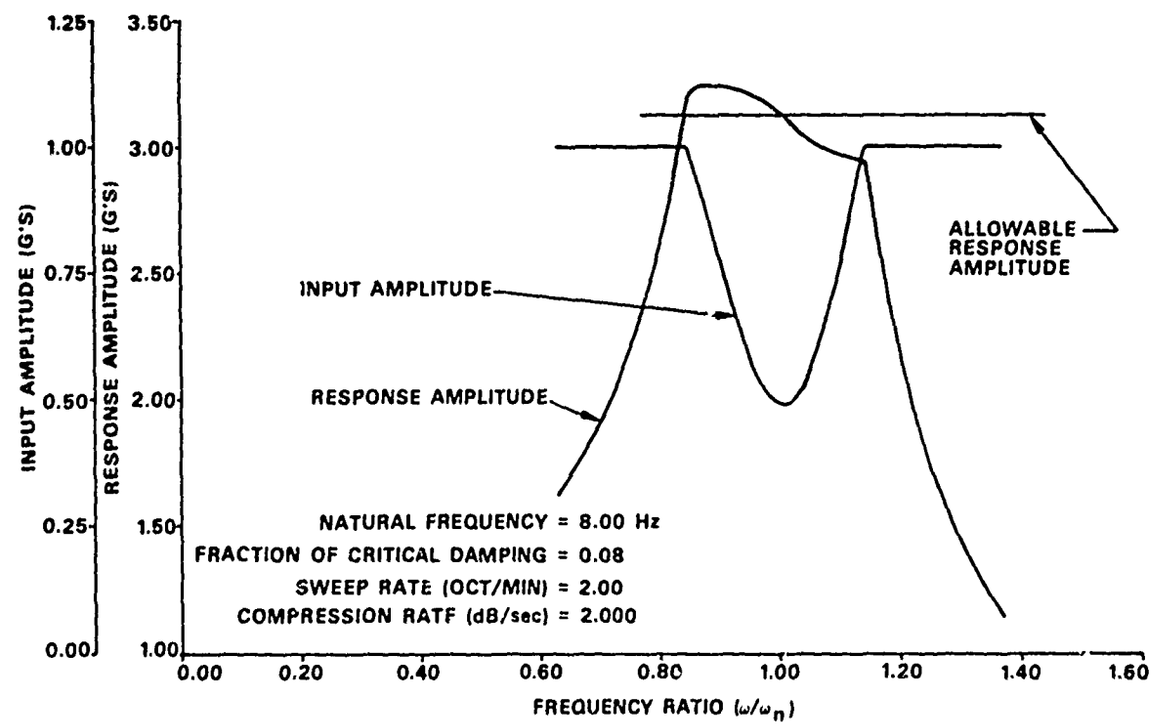

Fig. 4 - Response for swept notched excitation

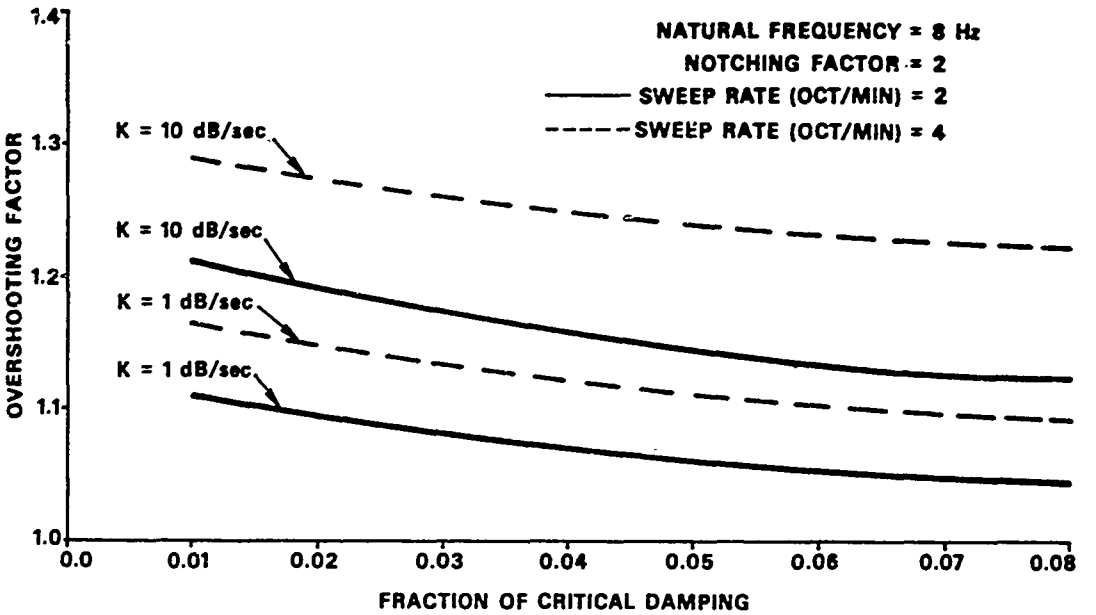

Fig. 5 - Overshooting factor for automatic notch control system

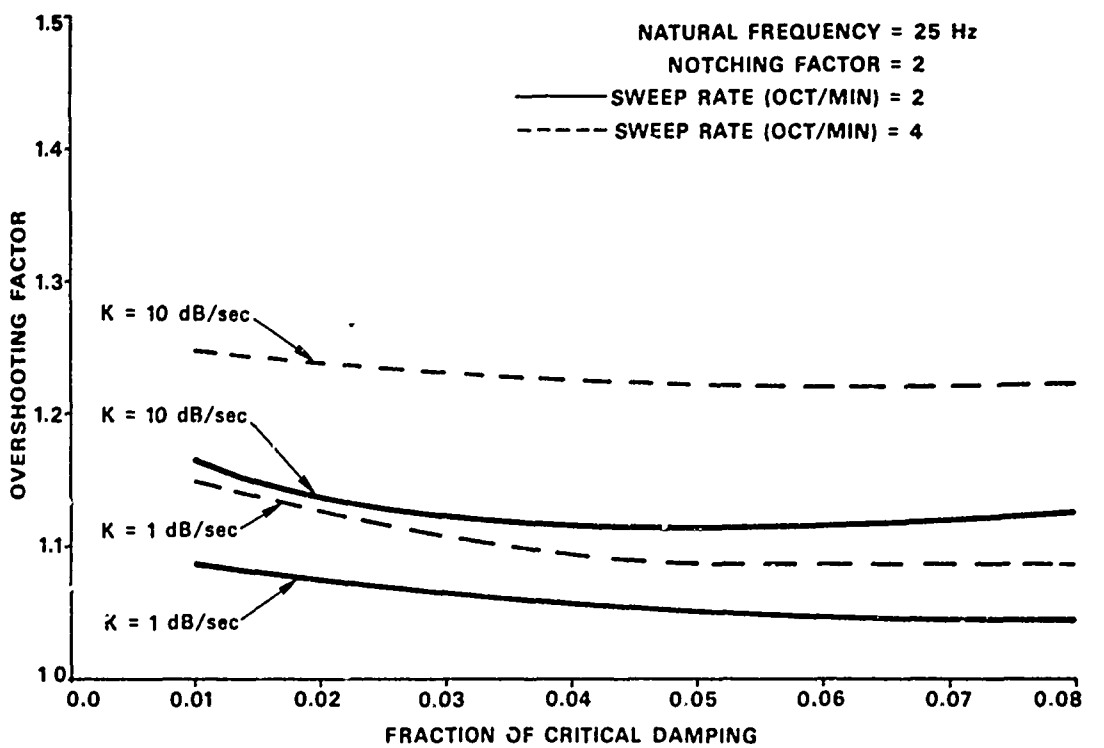

Fig. 6 - Overshooting factor for automatic notch control system

CONCLUSIONS

The automatic notch control system has been simulated analytically for the sinusoidal vibration testing of a spacecraft structure. The results are in good agreement with the test results. Using such a simulation makes it possible to predict the stability of the automatic notch control system and to adjust the compression rate (gain) to its optimum value for the sinusoidal testing.

The present automatic notch control system appears to be ineffective for structures having low modal damping and high sweep rates in sinusoidal vibration testing. Hence, improvements in automatic control system design are needed.

ACKNOWLEDGMENTS

The author wishes to thank Mr. Paul R. Schrantz, Mr. Alberto Ramos, and Mr. Anthony Van Hover for helpful discussions during this work.

This paper is based upon work performed at COMSAT Laboratories under the sponsorship of the International Telecommunications Satellite Consortium (INTELSAT). Any views expressed in this paper are not necessarily those of INTELSAT.

REFERENCES

[1] B.N. Agrawal, "Nonlinear Effects of the Vibration Testing of the Spacecraft Structure," AIAA 9th Aerospace Science Meeting, New York, January 1971, AIAA Paper No. 71-211.

[2] Yu A. Mitropolskii, Problems of the Asymptotic Theory of Nonstationary Vibrations. Izd. Nauka, Moscow, 1964; English translation: D. Davey & Co., Inc., New York, 1965.

TEST FACILITIES AND TECHNIQUES

SINUSOIDAL VIBRATION OF POSEIDON SOLID PROPELLANT MOTORS

by

Lane R. Pendleton
Research Specialist
Lockheed Missiles & Space Company
Sunnyvale, California

The Poseidon first and second stage solid propellant motors generate sinusoidal vibrations which result from acoustic pressure oscillations within the motor chambers. These pressure oscillations are caused by combustion instability and, to a lesser degree, by gas flow turbulence. This paper follows the investigation to determine the cause of these oscillations and describes the effects on missile structure and packages. Acceleration levels measured on the motor domes and on missile packages are presented. It was established through testing and analysis that all missile components could withstand the measured vibration levels with adequate margin. Motor vibration levels will be monitored on future ground tests to ensure that the existing acceptable vibration levels are not exceeded.

DISCOVERY

Ground test firing of developmental motors for the Poseidon missile began in July 1967. The objectives of these static motor tests were to obtain motor performance data and discover areas where improved performance could be gained through design refinements. Vibration instrumentation was included on these tests to measure motor generated environments. Potentially damaging sinusoidal vibrations were observed in the data from both first and second stage motors.

An 80 Hz oscillation was measured on the first stage motor which began 8 seconds after ignition and lasted for about 12 seconds. Figure 1 shows a frequency vs time plot from a typical motor. An envelope of frequencies measured during all ground test firings of tactical configuration motors is also shown. The frequency profile from motor to motor is nearly identical. The peak measured amplitudes were ± 8 g's on the forward dome, ± 10 g's on the aft dome, and ± 22 g's on the nozzle, which is connected to the motor by a flexible joint. The largest accelerations occurred in the longitudinal direction.

A sketch of the Poseidon first stage motor is shown in Figure 2. Flame front contours for progressive times of motor operation are also shown. The motor case is made of fiberglass which expands over two inches during motor pressurization. Some propellant

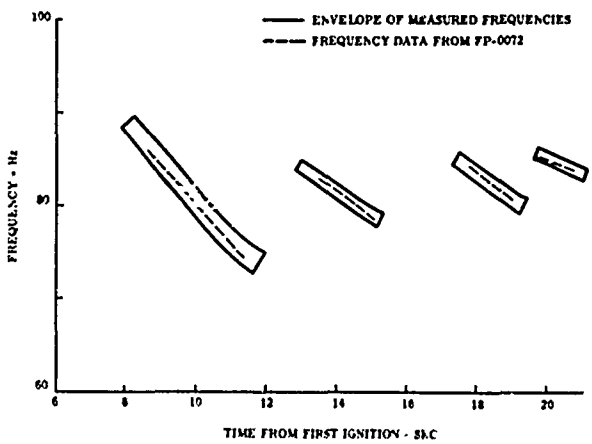

Figure 1 Envelope of Frequencies Measured During First Stage Motor Vibration and Data From a Typical Static Motor Firing

is bonded to the forward dome and is separated from the majority of the propellant by a conical slot called a conocyl. The propellant is not bonded to the aft dome; however, a boot is bonded to the propellant around the aft dome to prevent burning in this area. This design allows the domes to expand during motor pressurization, thus reducing propellant stresses.

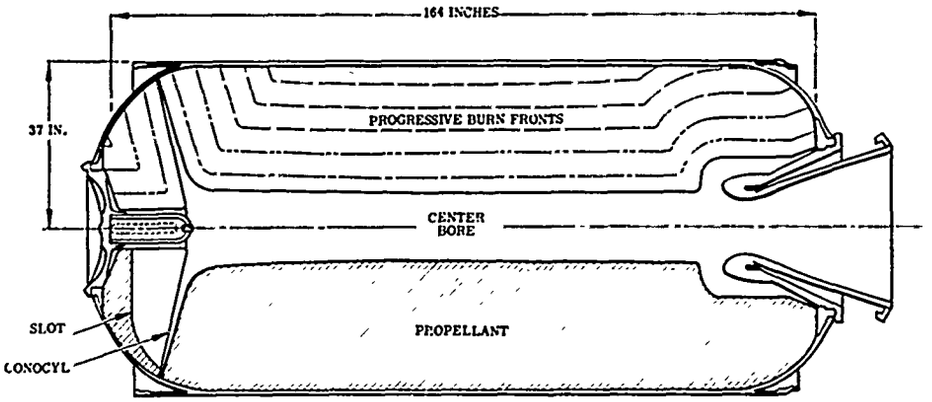

Figure 2 Cross Section of Poseidon First Stage Motor

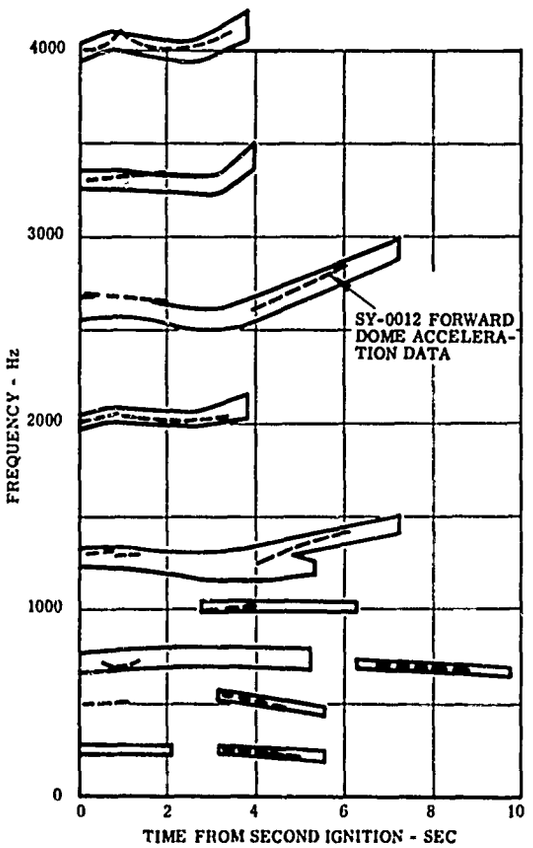

Figure 3 Envelope of Frequencies Measured During Second Stage Motor Vibration and Data From a Typical Static Motor Firing

Sinusoidal vibrations were measured on the Poseidon second stage motor during the first 10 seconds of motor burn. These oscillations were much higher in frequency and amplitude than measured on the first stage motor. Many superimposed sinusoids were observed in the frequency range from 250 Hz to 4000 Hz. Two forward dome locations, forward adapter and thrust termination ports, were chosen early in the program as standard locations to compare motor vibration amplitudes from motor to motor. A typical frequency vs time plot for a second stage motor is shown in Figure 3. This frequency profile was derived from acceleration data measured on the forward dome. Similar frequency profiles occur on each motor with large variations in amplitude at the individual frequencies. Figure 3 also shows envelopes of the standard frequencies measured on the forward dome of tactical configuration motors. Figures 4 and 5 show the peak amplitudes at the two selected locations for the frequency bands defined in Figure 3. Each frequency band was given a nominal frequency as a title for convenience. All available data at these locations for motors static fired before January 1971 are included except SX-0044 which will be discussed later. Note that acceleration amplitudes exceeding ± 300 g's were measured.

A sketch of the Poseidon second stage motor is shown in Figure 6. This motor case is also made of fiberglass. There are 12 slots, or star points, cut in the propellant around the igniter at the forward dome. The motor has a near cylindrical bore down the center with a submerged nozzle at the aft end. A boot is bonded to the propellant around the forward and aft domes, but the boot is not bonded to

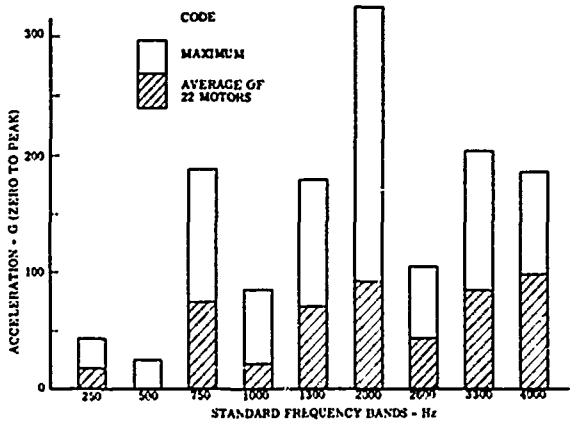

Figure 4 Amplitude of Second Stage Motor Vibration Measured at the Thrust Termination Ports

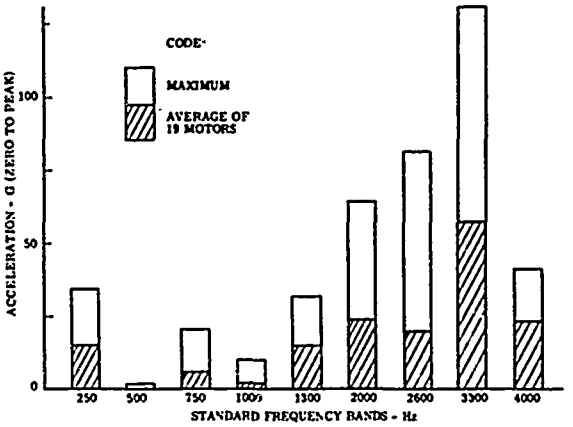

Figure 5 Amplitude of Second Stage Motor Vibration Measured at the Forward Adapter

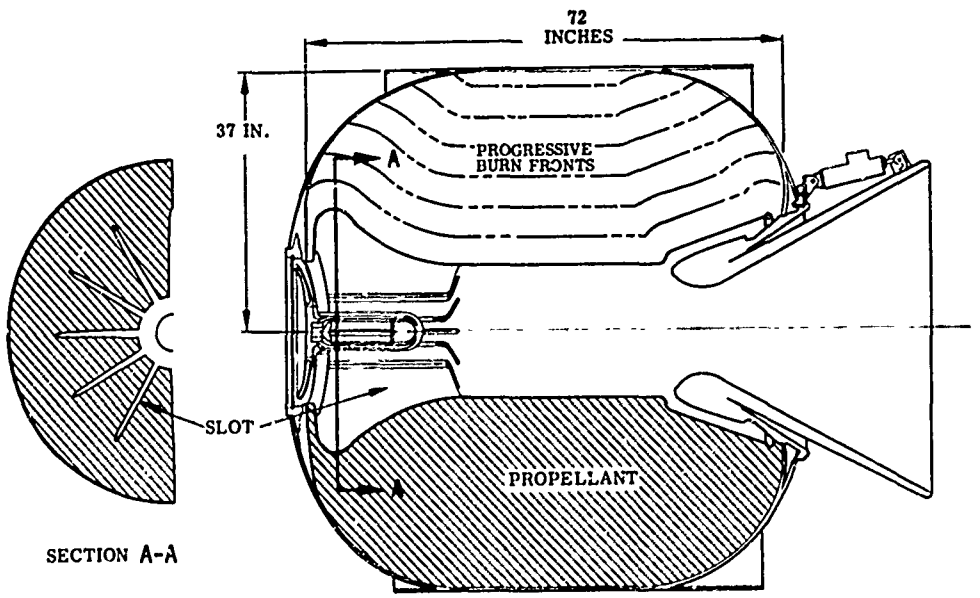

Figure 6 Cross Section of Poseidon Second Stage Motor

the domes. This allows the fiberglass domes to expand away from the propellant when the motor is pressurized. Thus, the chamber pressure acts over the entire forward and aft domes, but there is no burning in these areas.

An investigation into the cause of Poseidon motor vibrations was started in 1968 with the hope that some modification could be made to the motors which would reduce the vibration amplitudes. The minimum objective was to control the manufacturing process to assure that unacceptable vibration levels would not occur on future motors. Concurrent with the Poseidon motor development, the Minuteman missile was also experiencing motor vibration problems.[1] The third stage of Minuteman II had always generated low level 500 Hz vibrations; however, beginning with a particular powder lot, the amplitude increased by a factor of 3. Thus, there was considerable urgency to find the cause of the Poseidon motor vibrations.

CAUSE OF MOTOR VIBRATIONS

Several theories were suggested in trying to explain the cause of these vibrations. It was suggested that the 80 Hz first stage oscillation resulted from aluminum oxide deposited on the exit cone, flaking off and exciting an 80 Hz longitudinal frequency of the nozzle. To resolve this controversy a 153 pound mass was attached to the nozzle on one static motor firing (FX-0032) to significantly reduce the structural frequency of the nozzle. When this motor was fired there was no measureable effect on either frequency or amplitude of the 80 Hz oscillation proving that the nozzle had no significant influence on the motor vibration problem.

According to another theory, oscillations were assumed to be structural modes of the motor domes driven by random motor turbulence. If this were true, the frequencies should remain relatively constant and a random beat pattern should be seen in the amplitude. Neither of these conditions was observed. The frequencies varied with time and the amplitudes were relatively constant for several hundred cycles in many instances. It was also noted that the second stage motor produced harmonic frequencies which is not typical of structural response.

Still another theory postulated that the primary driving force for the second stage motor vibrations was flow turbulence in the region where the gas from the forward star mixed with the gas in the center bore. To verify this theory the forward star configuration of a second stage motor (SX-0044) was modified to streamline and reduce the velocity of flow out of the forward star. The data from this motor showed that the amplitude at some frequencies was greatly increased while the amplitude at other frequencies was unaffected or decreased. Considerable testing and analysis were performed by Dr. L. K. Isaacson, Dr. G. A. Flandro and others at the University of Utah[2] to determine the contribution of flow turbulence to Poseidon second stage vibration and interpret SX-0044 motor test results. The results indicate to this author that flow turbulence does influence second stage motor vibration but is not the primary energy source.

The most widely accepted theory was classical combustion instability, sometimes called acoustic burning. That is, flow oscillations at the acoustic frequencies of the motor cavity are amplified due to pressure sensitivity of the propellant burning process. This is referred to as pressure coupling. Combustion instability also encompasses a related process called velocity coupling which involves amplification of flow oscillations due to changes in burning rate resulting from changes in the flow velocity parallel to the burning surface. The amplitude of the flow oscillations is limited by the damping effects of the aluminum oxide particles in the gas cloud. This theory was supported by the fact that relatively constant amplitudes occurred at each frequency component, and by the fact that harmonic frequencies are a characteristic of acoustic modes. However, if one makes the assumption that the motor cavity could be approximated by a closed-closed circular cylinder, the calculated frequencies do not match the measured frequencies.

Three major efforts were initiated concurrently to confirm the combustion instability theory. One task was to determine the actual acoustic frequencies and mode shapes for the motor cavities. To do this, full scale models of the motor cavities were made for several different motor burn times. The acoustic modes of these cavities were then determined using speakers to excite the air mass and microphones to measure the pressure distributions. These tests were run using air and then the measured frequencies were converted to actual motor conditions using the ratio of the speeds of sound. These tests were performed by the motor manufacturers - Hercules, Inc.[2] for the second stage and Thiokol Chemical Corp. for the first stage.

These tests demonstrated that 84 Hz is the first longitudinal acoustic mode of the first stage motor cavity at 10 seconds burn time. The results also show that the assumption of a closed nozzle matches real motor conditions. The assumption that the first stage could be approximated by a circular cylinder was wrong. The large cavity near the front of the motor during the time of motor vibration (see Figure 2) has a large influence on the acoustic modes.

For the second stage motor the results of the acoustic tests are compared to the motor vibration frequencies in Figure 7. The 250 Hz frequency was identified as the first longitudinal mode in one-sixth scale tests run at Naval Weapons Center, China Lake. This mode should have harmonics at 500 Hz, 750 Hz, and 1000 Hz. The 750 Hz frequency was identified as the third longitudinal mode in the Hercules tests. All frequencies above 1000 Hz are primarily forward star modes. These frequencies and the length of the star points remain constant for the first 3 seconds of motor burning. Then the frequencies increase as the length of the star points decrease. The frequencies end at 7 seconds when the star points have widened so they no longer resemble slots. The radial and tangential modes of the cylindrical bore are not represented (except perhaps momentarily) because the frequencies of these modes continuously decrease with the increasing bore diameter.

The second task to confirm the combustion instability theory was to measure pressure oscillations in the motor chamber. To do this, dynamic pressure transducers were added to the instrumentation on subsequent

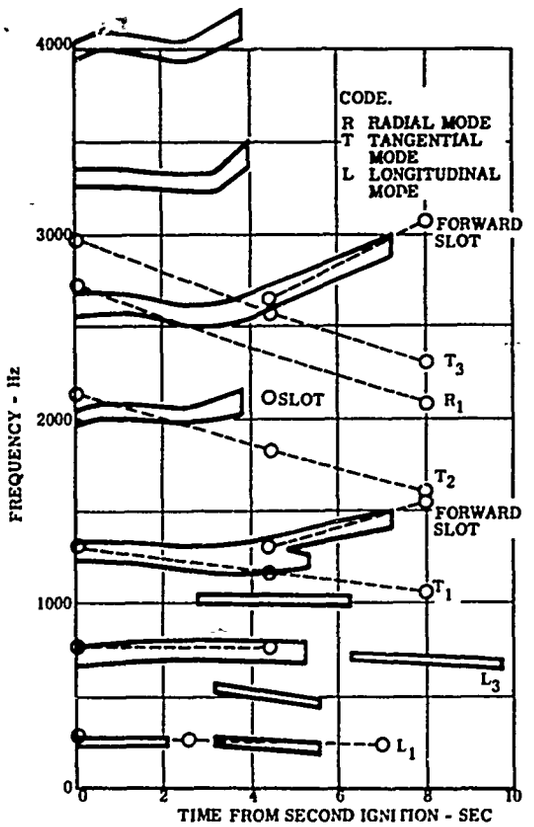

Figure 7 Modal Frequencies Measured During Acoustic Tests Compared with Vibration Data Envelope

static motor tests for both first and second stage motors. A Kistler model 603A pressure transducer was chosen since it had low acceleration sensitivity and the capability to sense only dynamic pressures ignoring the "steady" motor chamber pressure. Thus, the full calibrated band could be used to measure the small (less than ± 10 psi) pressure oscillations superimposed on the approximately 400 psi chamber pressure. To obtain high frequency response the transducer was close coupled (0.75 inch hole length from transducer face to motor chamber) and the hole was filled with silicon grease. Calibration tests run at the Naval Weapons Center, China Lake, revealed acceptably flat frequency response up to the limits of the calibration technique (1400 Hz).

The pressure data from subsequent static motor tests confirmed that chamber pressure oscillations were the cause of motor vibrations. A typical frequency profile of the dynamic pressure data from a second stage static motor test (SP-0038) is compared with the envelope of frequencies from the acceleration data in Figure 8. A one-to-one correspondence is shown.

The maximum and average dynamic pressures measured on 17 second stage static motor tests are shown in Figure 9. It is interesting to note that severe motor vibration amplitudes were caused by these relatively mild pressure oscillations. The reason is the Poseidon motor design permits these pressures to act over the full area of the motor dome producing large forces. These forces, acting on the relatively flexible fiberglass motor case, result in large acceleration levels. The dynamic pressure amplitudes do not form a consistent pattern with the acceleration amplitudes shown in Figures 4 and 5, as expected, since the structural modes as well as acoustic modes would produce different amplitudes at different measurement locations.

Dynamic pressure measurements on the first stage motor recorded a maximum level of ±1.7 psi and an average level of ±1.0 psi for 7 motor tests.

The third task to confirm combustion instability theory was to measure the combustion response and damping of the propellant.

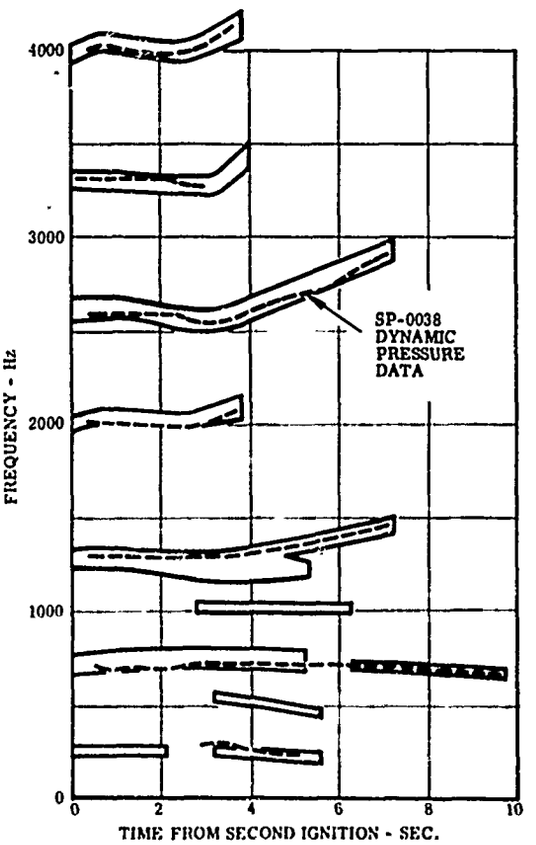

Figure 8 Frequency Profile of Dynamic Pressure Data Compared with Vibration Data Envelope

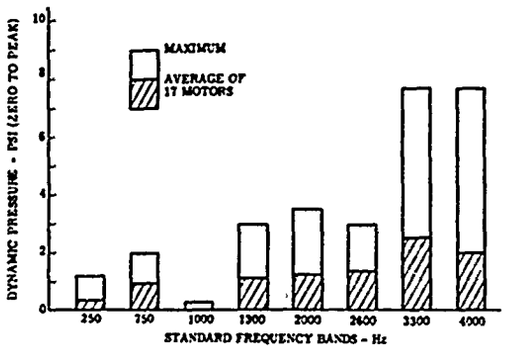

Figure 9 Amplitude of Chamber Pressure Oscillations Measured During Static Tests

T-burner tests and combustion photography were used for this task. A T-burner in simple terms consists of a metal pipe with closed ends and a vent or nozzle at the mid point. The length of the pipe is determined by the frequency of interest. A propellant sample is placed at each end and the pipe is pressurized to some preselected pressure. By burning the propellant samples the ability of the propellant to amplify or damp pressure oscillations can be measured. Extensive T-burner testing and analysis were done by Hercules, Inc.[2], and Naval Weapons Center.[3] The results of these tests indicated large pressure-coupled combustion response, especially in the frequency range from 1000 to 2000 Hz. The basic T-burner does not measure velocity-coupled response, but some experimentation with T-burner modifications indicated that flow velocities parallel to the burning surface had significant effects on combustion stability. As a part of this task, variations were made in some propellant ingredients in an attempt to find the controlling variables. These studies indicated that the quantity of aluminum and the aluminum particle size had significant influences.

A math model which considers all driving and damping influences in the pressure oscillations was derived by Hercules, Inc.[2] It was concluded that a combination of combustion instability and flow turbulence are required to drive the Poseidon motor vibrations. The primary damping influences are particulate damping mainly due to aluminum oxide particles in the combustion gas cloud and acoustic energy loss through the nozzle. No practical method of reducing the oscillation amplitudes was found.

EFFECTS ON MISSILE COMPONENTS

When sinusoidal motor vibrations were discovered an investigation was started to determine the effects on missile structure and packages. Packages attached directly to the motor domes receive the highest acceleration levels. The environments of these packages were measured during static motor tests by installing packages on the motors and making vibration measurements at the package interface. The environment was confirmed by making flight measurements at selected locations. The number of flight measurements was limited by telemetry system capability. A sketch of the Poseidon missile is shown in Figure 10 to illustrate the relative locations of missile components.

Measured data for first and second stage aft dome packages are shown in Figure 11. Both first and second stage motor vibration data are plotted on the same graph since many control system packages are common to both first and second stage motors. Based on this data sinusoidal vibration tests were added to the qualification test program for motor attached packages. A lesson was learned about the setting of frequency band widths for sine sweep testing. When motor vibrations were first discovered, sine sweep tests were specified for packages over the narrow frequency bands measured on the forward dome. However, when measurements were made on several ground and flight tests for all packages attached to the motors, it was necessary to considerably widen the frequency bands to cover the measured data. This expansion of the frequency bands was caused by local structural modes being excited by motor vibrations.

The only packages attached to the forward domes of the motors are the destruct firing units. The 80 Hz accelerations at the first stage forward dome are enveloped by other flight events. However, the motor vibration environment on the second stage forward dome is very severe as is shown in Figure 4. The firing units attached to the second stage forward dome were unable to survive motor vibration tests and a vibration isolator was designed and installed to protect these packages. Vibration measurements taken during both flight and static motor tests on the isolated destruct firing units recorded less than ±10 g's.

The motor vibration environment for the forward portion of the missile (equipment section and re-entry system) could only be measured during missile flight tests. The maximum acceleration levels measured at equipment section packages are shown in Figure 12. A comparison of this environment with existing package and structural capability revealed that no changes were required. A peak amplitude of 2.5 g's was measured in the

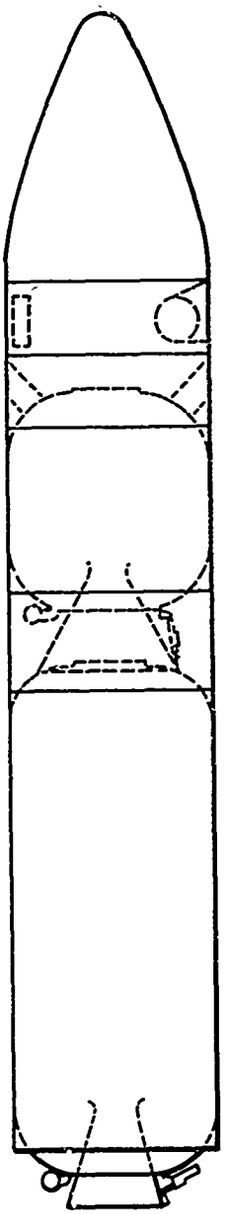

Figure 10 Poseidon Missile

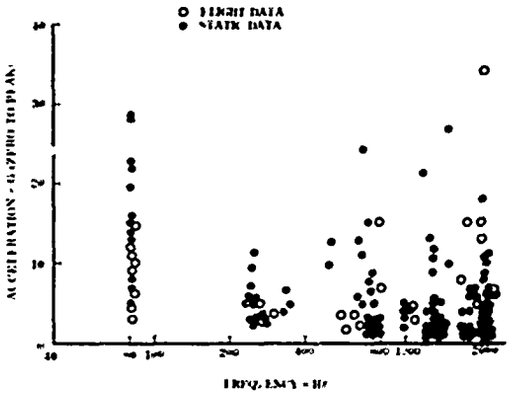

Figure 11 Sinusoidal Vibration Levels Measured on Aft Dome Attached Packages

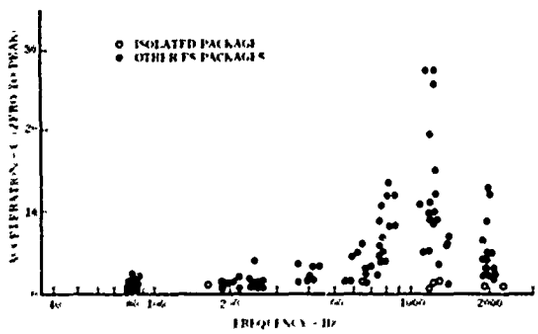

Figure 12 Sinusoidal Vibration Levels Measured on Equipment Section Packages

re-entry bodies. This acceleration level is much lower than other flight and re-entry environments for re-entry system components.

The effect of motor vibration on missile structure, including package attachment brackets, was determined by analysis. Structural load calculations were based on measured accelerations. In each case, it was found that the motor vibration loads were lower than the design load; though by only a small margin for a few package brackets.

No flight failures of Poseidon missiles have been attributed to motor vibration. However, package failures have occurred during qualification testing to 3 sigma predicted motor vibration environments. Most of the package failures occurred in the frequency range above 1000 Hz where the highest acceleration levels were specified. Electro-mechanical relay failures accounted for a high percentage of the failures. This problem was solved by using a relay with less vibration sensitivity. Another problem was fatigue failure of electrical wires

where the wires were carrying some vibration loads. Small packaging design changes were the solution to this problem. Some packages received vibration isolation as a protection from motor vibration as well as other shock and vibration environments during flight.

ROLL TORQUE

As an interesting sidelight to the motor vibration problem, a torque about the missile roll axis was observed during flight for the first seven seconds of second stage motor operation. An envelope of the amplitude of this roll torque for the first 9 flights is shown in Figure 13. The data from a typical flight is also shown. Abrupt changes in amplitude and even changes in direction were observed. Attempts to find a direct correlation of the amplitude of the roll torque with the amplitude of vibration was not conclusive. However, it was discovered that the duration matched the duration of the 1300 Hz and higher modes which were identified in the acoustic model tests as having tangential as well as radial motions in the forward slots. It is probable that traveling torsional modes occur in the center bore during second stage motor vibration. Dr. Flandro, in his Ph.D. Thesis[4], discussed a correlation between roll torque and motor vibration and explained the amplitude by the existence of traveling torsional modes. It is concluded that the roll torque measured during Poseidon flight is caused by the same phenomenon as second stage motor vibration. It is interesting to note that this roll torque temporarily exceeds the roll control capability of the missile. However, this causes no problem since the missile guidance and control systems allow roll excursions. There is ample time after this event for the missile to roll to the required angle before thrust termination.

MONITORING MOTOR VIBRATION

A procedure was established to monitor vibration during future ground tests to insure that a severe environment would not result from some future change in motor production methods. This procedure includes measuring vibration levels at specified locations on each static test motor. For the second stage, four locations on the forward dome were chosen -- two on the forward adapter ring and two on the thrust termination ports. The average amplitude of the two measurements at each location is used for motor to motor comparisons. For the first stage motor, a forward dome location and a nozzle location were chosen. Also, a Kistler dynamic pressure transducer is installed at a standard location on each test motor. The data from these measurements are compared with the data from previous static tests at the same locations. The effect on the missile of any significant deviation from previous data is carefully considered.

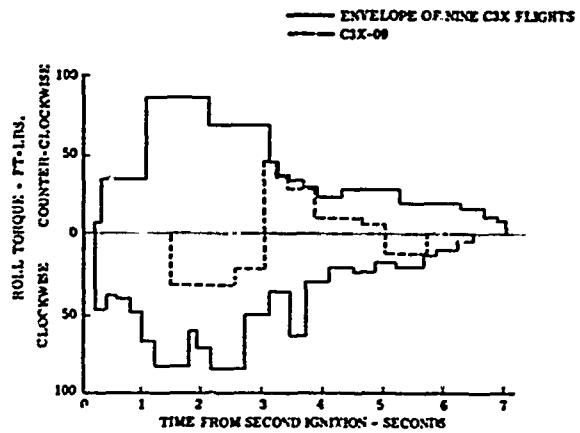

Figure 13 Roll Torque Measured During Poseidon Missile Flights

Another part of the monitoring system is retention of samples of the ingredients used in manufacture of motors. Then if a change in motor vibration occurs these samples can be compared to see if any change in ingredients can be detected. Also, T-burner tests are run on samples of propellant from each powder lot and the results are compared with previous data.[5] If unusually high growth rates are measured, appropriate action will be taken, such as static test firing a motor from the powder lot to measure the resulting vibration levels.

250 HZ PROBLEM

After the monitoring system was established a large amplitude oscillation occurred at 250 Hz on static test number SP-0112 fired on 14 January 1971. The average of the two forward adapter measurements was ± 77 g's at 250 Hz compared with a previous high of 34.5 g's. A study of propellant ingredients and manufacturing procedures was performed by Hercules, Inc.[6] to determine what variables correlated with the increased amplitude at 250 Hz. This study revealed a good correlation with the powder lot used in manufacture. Figure 14 shows the amplitude of 250 Hz mode measured at the forward adapter for all motors when measurements were made. Note that similar amplitudes were measured for motors made from the same powder lot.

A study to determine what affect this increased amplitude would have on missile packages was initiated at LMSC. Specifically, LMSC wanted to know if it was safe to fly missiles using second stage motors made from powder lot 226. A many pronged attack was initiated. The control system packages attached to the second stage aft dome were considered most vulnerable to the increased acceleration levels. A series of sine sweep tests were run on these packages to determine

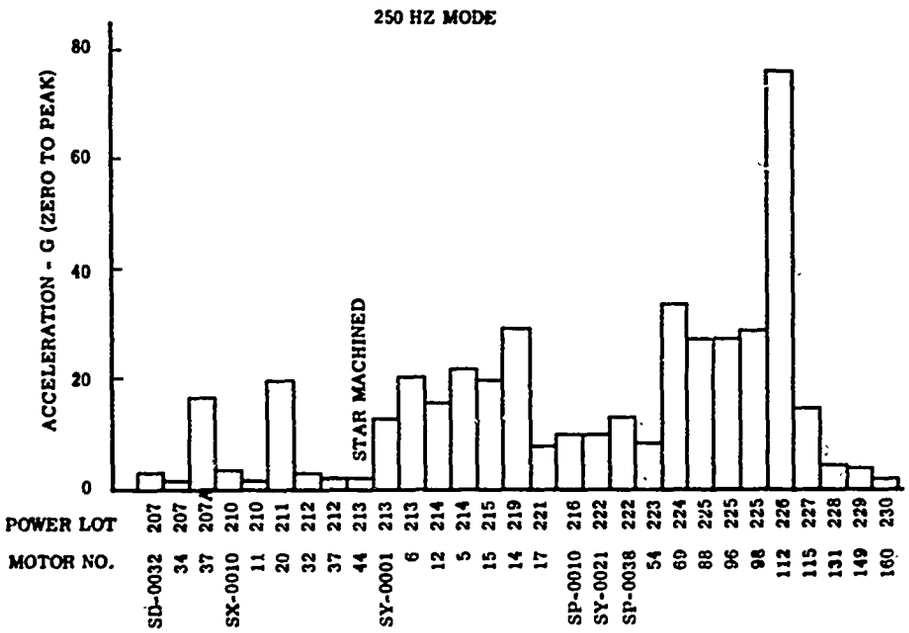

Figure 14 Amplitude of 250 Hertz Mode Measured at the Forward Adapter

the maximum levels they could withstand. A minimum level of ± 30 g's which all packages could withstand was established. At the same time an instrumentation program of static and flight tests was started to establish the expected flight levels for a motor from powder lot 226. A review of existing flight and static data revealed that flight amplitudes at 250 Hz were lower than static amplitudes. Flight measurements were made of the second stage forward adapter, second stage aft adapter and equipment section to accurately measure the amplitude of the 250 Hz mode. A second stage motor from powder lot 224 was chosen for this flight since this lot had shown the highest 250 Hz oscillations except for lot 226 (see Figure 14). An amplitude of ± 5.4 g's was measured on this flight compared with ±34.5 g's on the static test - a ratio of 6. Additional measurements were made on static tests to determine the transmissibility from the aft adapter to each package attached to the aft adapter. Transmissibilities of about 1.0 were measured indicating the package capability of ± 30 g's is certainly adequate. Motor vibration from powder lot 226 motors should have no significant effect on missile reliability.

Figure 15 shows a comparison of flight and static data measured at the same location for the major modes up to 2000 Hz. About the same amplitudes are indicated except for the 250 Hz mode. The reason for a reduction in the 250 Hz mode during flight is unknown. A Kistler pressure transducer was included in the instrumentation on the special flight which used a motor from powder lot 224. A dynamic pressure of ± 0.3 psi was measured at 250 Hz compared with an expected level of ± 1 psi based on static data. This indicates that a reduction in acoustic amplitudes is the primary cause; however, differences in structural loading between static and flight could also influence the reduction in flight amplitudes at 250 Hz.

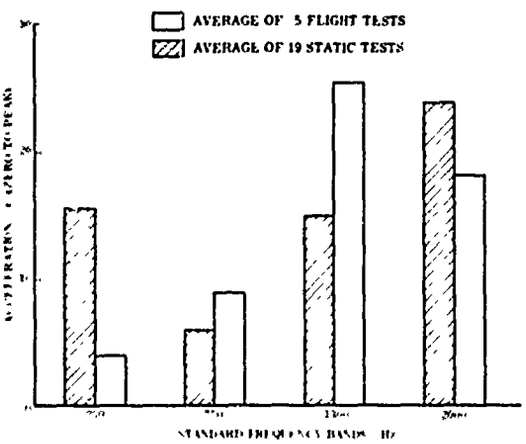

Figure 15 Comparison of Flight and Static Data

SUMMARY

A severe sinusoidal vibration environment was discovered during static test firings of motors to be used for the Poseidon missile. Acoustic pressure oscillation within the motor chamber was established as the cause of these vibrations. No acceptable method of reducing these vibrations was found. The capability of existing missile packages and structure to withstand this environment was determined by testing and analysis. Vibration isolation of some packages, design changes for others, and selection of less vibration sensitive components were among the methods used to qualify packages for this environment. A procedure was established to monitor the levels during ground tests and thereby control the vibration levels expected on tactical missiles. The effectiveness of the monitoring system was demonstrated during the 250 Hz investigation.

REFERENCES

1. J. R. Fowler and J. S. Rosenthal, "Missile Vibration Environment for Solid Propellant Oscillatory Burning," AIAA SAE 7th Propulsion Joint Specialist Conference, Salt Lake City, Utah, June 14-18, 1971.

2. "Final Report on the Poseidon Second Stage Acoustics Investigation," Doc. No. SH015-B3A00HTJ-1, Hercules, Inc., Magna, Utah, March 1971.

3. E. W. Price, H. B. Mathes, O. H. Madden, and B. G. Brown, "Pulsed T-Burner Testing of Combustion Dynamics of Aluminized Solid Propellants," AIAA/SAE 7th Propulsion Joint Specialist Conference, Salt Lake City, Utah, June 14-18, 1971.

4. Flandro, G. A., "Rotating Flows in Acoustically Unstable Rocket Motors," Ph.D. Thesis, Cal. Inst. of Tech., March 1967.

5. M. W. Becksted, D. U. Bennion, L. R. West, and E. C. Jossen, "The Variable Area T-Burner as a Quality Assurance Tool," 8th JANNAF Solid Propellant Combustion Meeting, Monterey, California, September 1971.

6. J. H. Thacher and B. B. Dickinson, "Relationship Between Motor Parameters and Oscillation Response in Poseidon Second Stage Motors," 8th JANNAF Solid Propellant Combustion Meeting, Monterey, California, September 1971.

CONFIDENCE IN PRODUCTION UNITS BASED ON QUALIFICATION VIBRATION (U)

Ralph E. Deitrick
Hughes Aircraft Company
Space and Communications Group
El Segundo, California

This presentation provides equations for the variation in vibration exposure time as a function of input level for equivalent fatigue damage. The derivation uses Miner's Rule accounting for variation in structural damping and incorporates the effect of test tolerances. Considering the statistical characteristics of fatigue failure, the relationship between qualification unit and production unit failure probability is used to define qualification test duration requirements for assuring low failure probability of production units.

An illustration of the application of the procedure is provided and the effect of acceptance/qualification test ratio is illustrated. The Aerospace Industry practice of occasionally using qualification units on the first flight spacecraft is discussed.

INTRODUCTION

This presentation defines a quantitative measure of evaluating the fatigue status of production units based on demonstrated capability during vibration test of a qualification unit. The approach is primarily useful for evaluation of electronic units where there is limited structural analysis of the numerous component installations and a high degree of dependence is placed on past experience and inherent capability of components. The background for this analysis is associated with spacecraft component testing where a single flight configuration unit is subjected to increased vibration levels and extended exposure durations in order to qualify the design mechanically. However, the resulting evaluation method is general and can be applied to other sources of vibration environment. The procedure permits evaluation of confidence in production units based on successfully passing qualification test; it does not predict flight failures unless a failure is exhibited during qualification unit test. The procedure provides a definition of qualification test requirements for level and duration based on specified acceptance and or flight environments; it does not provide a means of establishing the acceptance test levels initially.

The availability of such a tool permits the evaluation of unplanned extended environmental exposure of production units, the significance of premature mechanical failures in the qualification unit, and the loss in confidence resulting from limiting or eliminating qualification vibration test. This permits management to consider the potential decrease in success of a mission during schedule and cost saving exercises. Since by necessity acceptance and qualification specification requirements address the total spectrum of units, this technique permits adjustment of the requirements, where warranted, for special material considerations and can be used to indicate preference in the initial selection of materials.

TIME VERSUS INPUT LEVEL DERIVATION

The objective of the following derivation is to obtain equivalent damage times at different input vibration levels. The accepted theory of fatigue failure [1,2] involves the hypothesis that the rate of progression of a fatigue crack increases with increasing crack depth, h, as expressed by

$$h = As^{-b}e^{cs^{-b}n}$$

where

A, c = constants
s = nominal stress
b = slope of S-N curve
n = number of cycles

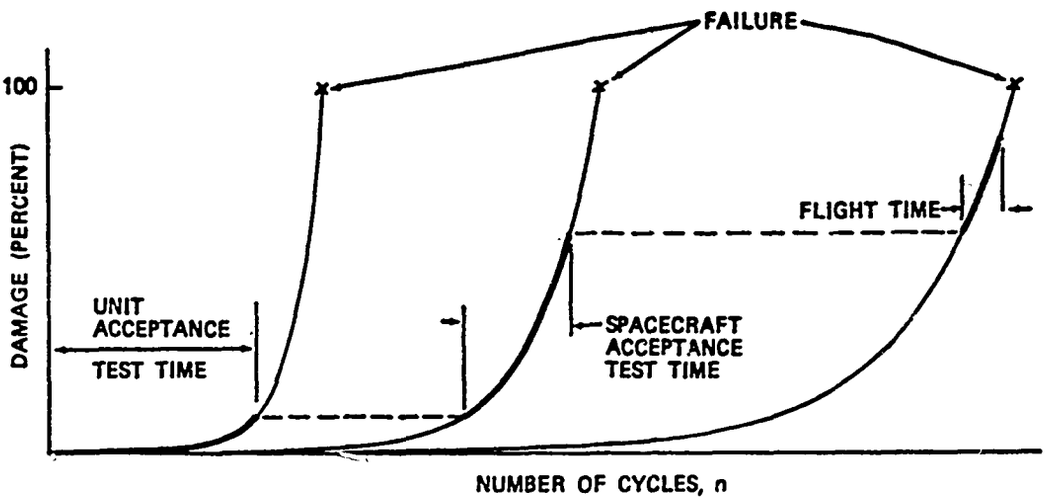

FIGURE 1. FATIGUE DAMAGE ACCUMULATION

The process of accumulation of fatigue damage during the various vibration exposures of a production (flight) unit is illustrated in Figure 1. The same percentage of cycles to failure on each of these curves represents the same amount of crack depth as expounded by Miner's Rule. It is widely recognized that the classical linear damage rule is an inaccurate approximation and may result in erroneous predictions of fatigue life[2]. However, it is used in this analysis in order to retain the equations for conversion of various stress levels of vibration to one reference level in as simple a form as possible. In view of scatter in S-N data and uncertainties in strength capability of units, the potential error introduced by use of Miner's Rule is considered acceptable.

The ratio of applied cycles, n, at two stress levels which result in an equivalent amount of fatigue damage is given by

$$n_1/N_1 = n_2/N_2$$

or

$$n_1/n_2 = N_1/N_2 \qquad (1)$$

where the N_i is the number of cycles which results in failure and is defined by the S-N fatigue curve. Since fatigue curve data is usually given as an average value, the minimum allowable number of cycles at the two levels can be expressed as:

$$\left(\frac{n_1}{n_2}\right)_{min} = \frac{\left\{\frac{N_{1_{min}}}{N_{1_{avg}}}\right\} N_{1_{avg}}}{\left\{\frac{N_{2_{min}}}{N_{2_{avg}}}\right\} N_{2_{avg}}}$$

Based on available information where sufficient data exist to define a scatter band (as illustrated in Figure 2a), the scatter band width relationship shown in Figure 2b can be expressed as:

$$\frac{N_{1_{min}}}{N_{1_{avg}}} = \left(N_{1_{avg}}\right)^a$$

therefore

$$\left(\frac{n_1}{n_2}\right)_{min} = \frac{\left\{N_{1_{avg}}\right\}^a N_{1_{avg}}}{\left\{N_{2_{avg}}\right\}^a N_{2_{avg}}} = \left\{\frac{N_1}{N_2}\right\}^{1+a}_{avg} \qquad (2)$$

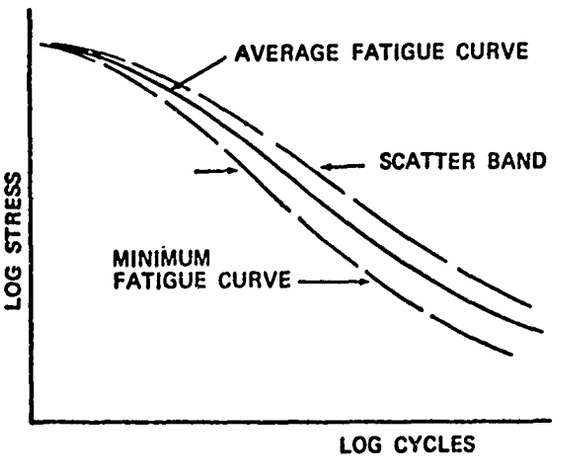

FIGURE 2a. FATIGUE SCATTER BAND ILLUSTRATION

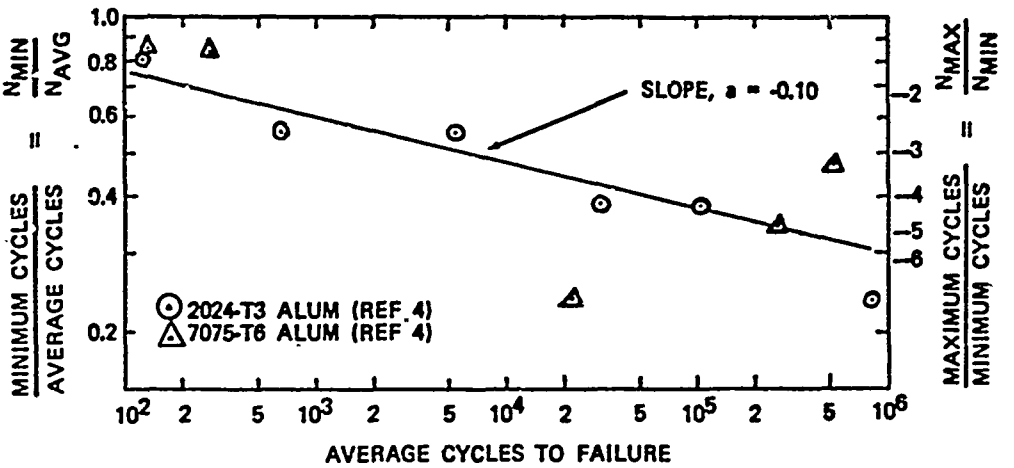

FIGURE 2b. VARIATION IN SCATTER BAND WIDTH

The divergence of these scatter band edges is a recognized characteristic [3, paper 4]. The allowable number of cycles at various stress levels, s, is defined by the accepted relationship

$$N_1/N_2 = \left[s_1/s_2\right]^b \qquad (3)$$

The validity of this equation is illustrated in Figure 3 for a specific material, 2024-T3 Aluminum Alloy [4]. Some important conclusions which can be obtained from this figure are:

(1) The equation truly represents the fatigue curve in the region which doesn't involve low cycle fatigue or endurance limit.

(2) The fatigue curve slope is independent of artifically introduced stress concentrations.

(3) The slope is usually more easily defined by use of notched specimen fatigue test data or a combination of notched and unnotched specimens due to the longer linear portion of the curve.

(4) The artifically introduced notch is equivalent to having imposed additional cycles on an unnotched specimen since the cycles of the S-N curve denote the life until failure from a point of known stress concentration.

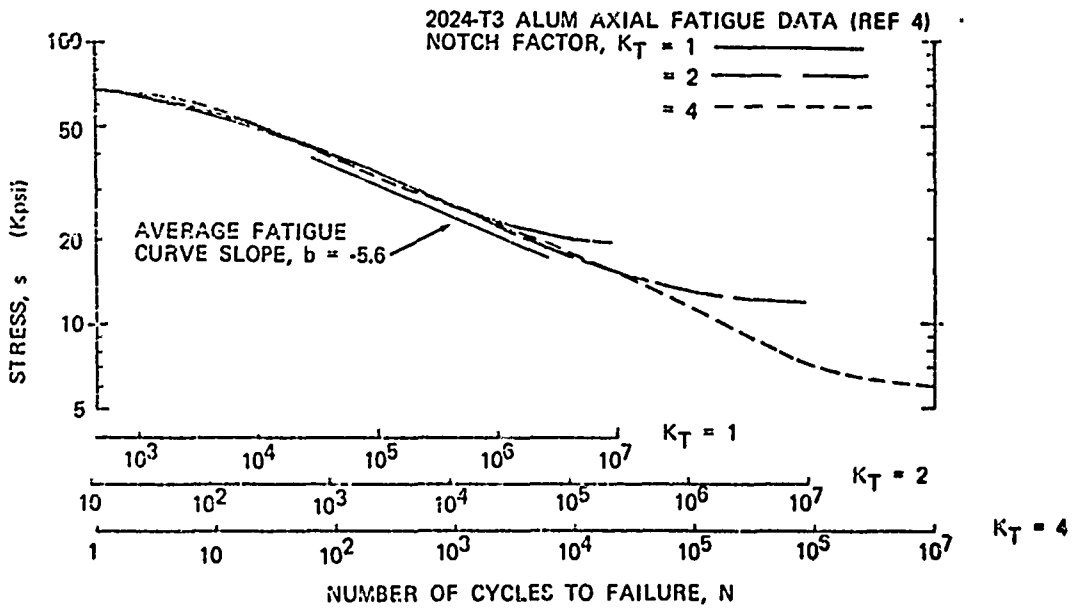

FIGURE 3. FATIGUE CURVE CHARACTERISTICS

(5) There is a reduction in endurance limit stress which is inversely proportional to the induced stress concentration or notch factor.

The last observation indicates that as fatigue damage is incurred at levels above the endurance limit stress the endurance limit is reduced. As fatigue failure is more closely approached (interpreted as an increasing crack depth or stress concentration) the reduction in endurance limit stress indicates that very low level stresses can finally precipitate failure. As an example, in the case of an earth satellite it is possible, if sufficient fatigue damage is done during ground test and flight vibration exposure, that even low level operational vibration on orbit (if of sufficient magnitude) could lead to fatigue failure. In order to account for the detrimental effect of stresses below the initial endurance limit after fatigue damage has been initiated, the existence of endurance limit is ignored. Although introducing some convervatism by accounting for damage accumulation at lower stress levels where it does not initially occur, this prevents complication of the equations to account for a continually decreasing endurance limit.

Table 1 presents values of the S-N curve slope, b, for some representative materials. Many of these values are significantly below the 10 - 25 range which is usually believed to be representative. The multiplication by a factor of 2 of these values is recommended for applications involving multiple stress level conditions [1, pp 37 and 5, Chapter 11]. Increasing the value of b has the effect of shortening the exposure time at higher stress levels which is unconservative when establishing qualification duration requirements, therefore, the additional factor is neglected. Furthermore, there is evidence[6] that the factor is dependent on stress level and possibly can be less than unity.

Another observation possible from Figure 3 is a true representation of the crack growth curve. The stress concentration factors can be interpreted as relative crack depths by means of the formula

$$K_T = 1 + 2\sqrt{\frac{h_o}{r_o}}$$

where h_o is the crack depth and r_o is the root radius. By expressing the cycles to failure of the notched specimens as a percentage of the cycles to failure of the smooth specimens the results can be plotted as shown in Figure 4. The figure illustrates the very rapid deterioration of the specimens

TABLE 1
FATIGUE CURVE SLOPE FOR VARIOUS MATERIALS

MATERIAL	TYPE OF FATIGUE TEST	$\frac{S_{min}}{S_{max}}$	FATIGUE CURVE SLOPE, b
2024-T3 Alum	Axial Load	-1	-5.6
2024-T4 Alum	Rotating Bm	-1	-8.4
7075-T6 Alum	Axial Load	-1	-5.5
6061-T6 Alum	Rotating Bm	-1	-7.0
ZK-60 Mag			-4.8
EK31XA-T6 Mag	Axial Load	0.25	-8.5
	Rotating Bm	-1	-5.8
QE 22-T6 Mag	Wöhler	-1	-3.1
4130 Steel			
Normalized	Axial Load	-1	-4.5
Hardened	Axial Load	-1	-4.1
6Al-4V Ti	Axial Load	-1	-4.9
Beryllium			
Hot Pressed Block	Axial Load	0	-10.8
		0.2	-8.7
		-1	-12.6
Cross Rol Sht	Axial Load	0.2	-9.4
Invar	Axial Load		-4.6
Anneal Copper			-11.2
181 Fiberglass			-6.7

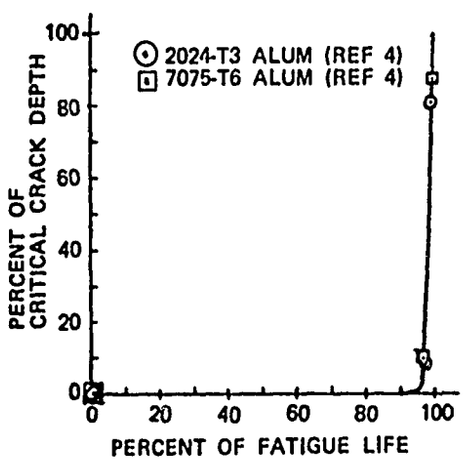

FIGURE 4. FATIGUE CRACK DEPTH GROWTH

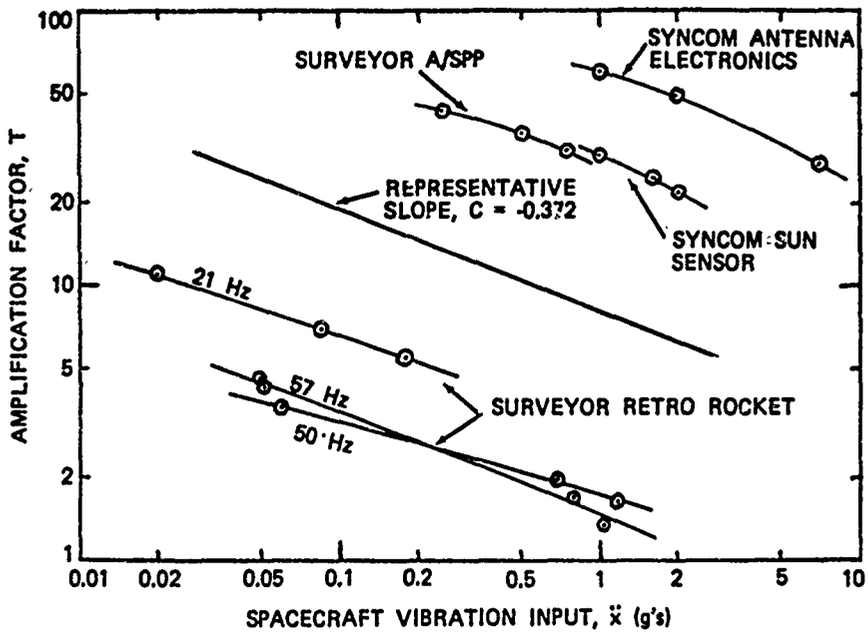

FIGURE 5. EFFECT OF STRUCTURAL DAMPING VARIATION

in the final stages of fatigue failure.

The equation for equal fatigue damage at two levels of stress can now be written as

$$\left(\frac{n_1}{n_2}\right)_{min} = \left\{\left[\frac{s_1}{s_2}\right]^b\right\}^{1+a} \qquad (4)$$

The stress level is a function of the response acceleration of the element of interest. Expressing the response acceleration as input acceleration, $\ddot{x}$, times amplification factor, T, at resonance this becomes

$$\frac{s_1}{s_2} = \frac{\ddot{x}_1 T_1}{\ddot{x}_2 T_2}$$

As input vibration levels are increased there is typically an increase in damping and hence a resonance amplification factor decrease. The damping variation is recognized as a consideration in establishing vibration tests at increased levels [7, section 3.4.5], but the rather significant effect is not generally acknowledged. A summary of some input and response acceleration data for units at different levels of vibration from various programs is given in Figure 5. This figure indicates that the resonant amplification factor can be related to the input acceleration empirically as

$$\frac{T_1}{T_2} = \left(\frac{\ddot{x}_1}{\ddot{x}_2}\right)^c$$

Equation (4) can now be rewritten as

$$\left(\frac{n_1}{n_2}\right)_{min} = \left\{\left[\frac{\ddot{x}_1}{\ddot{x}_2}\left(\frac{\ddot{x}_1}{\ddot{x}_2}\right)^c\right]^b\right\}^{1+a}$$

or

$$\left(\frac{n_1}{n_2}\right)_{min} = \left\{\left[\left(\frac{\ddot{x}_1}{\ddot{x}_2}\right)^{1+c}\right]^b\right\}^{1+a} \qquad (5)$$

In order to express the left hand side of the equation in terms of test time the number of cycles must be expressed as a function of time. Considering the response of a specific element with a resonant frequency f_n at the two levels of vibration, the number of cycles can be expressed as

$$\frac{n_1}{n_2} = \frac{f_{n_1} t_1}{f_{n_2} t_2}$$

where t is the vibration time. For small values of damping, the variation in resonant frequency with input level is minor, so that $f_{n_1} \approx f_{n_2}$ and

$$\left(\frac{t_1}{t_2}\right)_{min} = \left[\frac{\ddot{x}_1}{\ddot{x}_2}\right]^{(1+c)\,b\,(1+a)} \qquad (6)$$

Using the value of $a = -0.010$ from Figure 2b, and $c = -0.372$ from Figure 5 the equation becomes

$$\left(\frac{t_1}{t_2}\right)_{min} = \left[\frac{\ddot{x}_1}{\ddot{x}_2}\right]^{0.565b} \qquad (7)$$

The foregoing analysis is based on vibration at two discrete levels of input for which equations (1) and (3) indicate

$$\frac{n_1}{n_2} = \left(\frac{s_1}{s_2}\right)^b$$

If equivalent fatigue damage at two levels of random vibration is considered

$$\sum_i \frac{n_i}{N_i} = \sum_j \frac{n_j}{N_j}$$

$$\sum_i \frac{n_i}{Ks_i^b} = \sum_j \frac{n_j}{Ks_j^b}$$

Using the Rayleigh probability density distribution to proportion the total number of cycles applied to the various stress levels, these summations are expressed in integral form as

$$\int_0^\infty \frac{s_1}{K}^{-b} \; n_1 \frac{s_1}{\sigma_1} \; e^{-1/2(s_1/\sigma_1)^2} \; d\left(\frac{s_1}{\sigma_1}\right) =$$

$$\int_0^\infty \frac{s_2}{K}^{-b} \; n_2 \frac{s_2}{\sigma_2} \; e^{-1/2(s_2/\sigma_2)^2} \; d\left(\frac{s_2}{\sigma_2}\right)$$

where σ is the standard deviation or rms value. Then

$$n_1\sigma_1^{-b} \int_0^\infty \left(\frac{s_1}{\sigma_1}\right)^{-b+1} e^{-1/2(s_1/\sigma_1)^2} \; d\left(\frac{s_1}{\sigma_1}\right) =$$

$$n_2\sigma_2^{-b} \int_0^\infty \left(\frac{s_2}{\sigma_2}\right)^{-b+1} e^{-1/2(s_2/\sigma_2)^2} \; d\left(\frac{s_2}{\sigma_2}\right)$$

Since the integrals give the same value

$$\frac{n_1}{n_2} = \left(\frac{\sigma_1}{\sigma_2}\right)^b$$

Hence, the conclusions of equation (7) are also applicable to random input conditions where the acceleration ratio is the ratio of the RMS values of the random input provided the two PSD's differ by a constant multiple at all frequencies.

The graphical representation of equation (7) is shown in Figure 6. Use of the equation permits adjustment of exposure time as a function of vibration input level along the lower scatter band line. The curves are essentially the fatigue curves of Figure 3 with the endurance limit characteristics deleted and the slope adjusted for variation in damping with input level.

The times for various environments to which a production unit is exposed (i.e., unit level acceptance test and retest, system level test, transportation, and flight) can be converted to equivalent damage time at a proposed qualification level by means of the equation. This time, t_{Q_E} (see Figure 6) denoted as "equivalent-time-at-qualification-level" represents the required capability for production units.

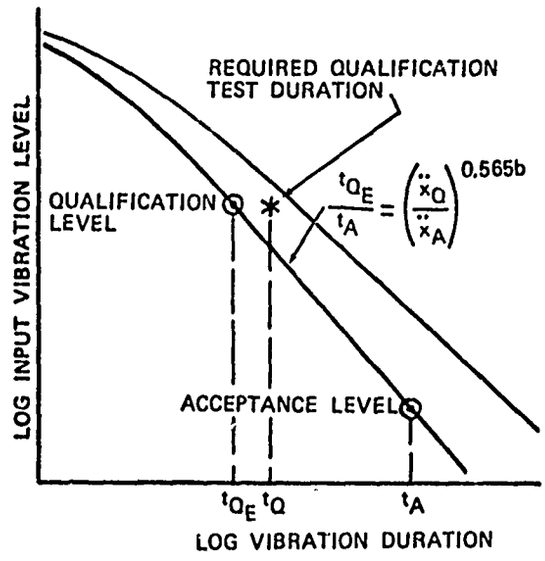

FIGURE 6. ILLUSTRATION OF QUALIFICATION TEST DERIVATION

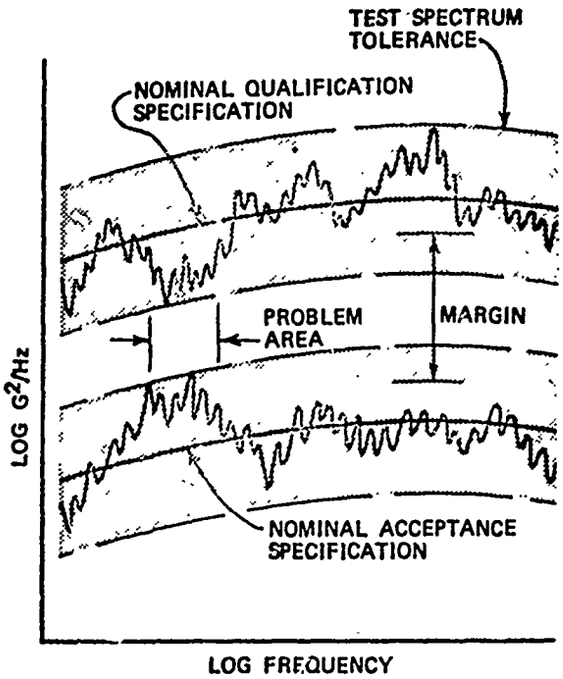

FIGURE 7. DEFINITION OF QUALIFICATION TO ACCEPTANCE TEST LEVEL MARGIN

EFFECT OF VIBRATION TEST TOLERANCES

The application of equation (7) to actual testing conditions requires consideration of variability in the exposure environment associated with input control tolerances. Both in the case of swept sine or random vibration tests, the input at frequencies near each component resonance is the important factor. Therefore, if a specific component resonance is considered, the value of the PSD (power spectral density) spectrum in the bandwidth of the response must be considered in using equation (7). Although a nominal value of the spectrum is ordinarily specified for both qualification and acceptance testing, it is impossible a priori to define exact input levels at a specific frequency closer than control tolerance limitations. Figure 7 illustrates the condition where the qualification spectrum is low and the acceptance spectrum is high at a particular frequency of concern denoted as the problem area. The tolerance band is considered to be a normal distribution with 3σ limits. The joint probability that acceptance and qualification spectra are within the region indicated as margin, dependent on what multiple of standard deviation is used in establishing the margin, is shown in Figure 8. Based on the figure, use of the 1σ points in establishing the margin region

TABLE 2

VIBRATION TEST TOLERANCE SUMMARY

	SINE VIBRATION	RANDOM VIBRATION	
Instrumentation Tolerance, dB	±0.4	±1.0	±1.0
Control Tolerance, dB	±0.9	±2.0	±3.0
Total Tolerance, dB	±0.99	±2.24	±3.16
1σ Value, dB	0.33	0.75	1.05

gives a probability of only 2.5 percent that the acceptance and qualification spectra are not separated by at least the indicated margin. Furthermore, in order to develop the maximum response the spectrum must be outside the 1σ limit over the entire bandwidth of the resonance which further reduces the probability of occurrence. Table 2 summarizes the test tolerances associated with sine and random vibration and indicates the dB values which are used as 3σ limits. Provided the same vibration test fixture is used for both acceptance and qualification vibration testing the spectrum variation from nominal due to fixture resonances need not be held to this close tolerance.

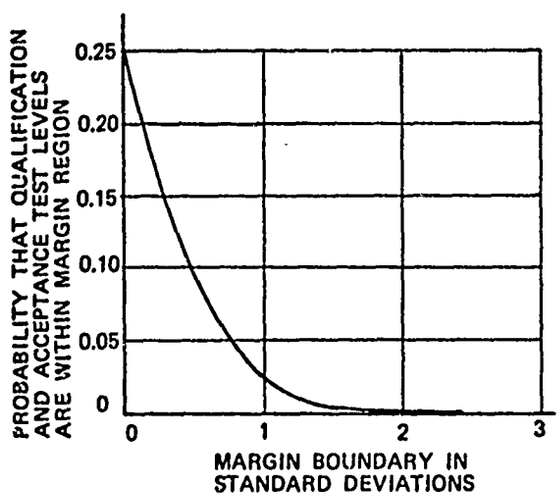

FIGURE 8. PROBABILITY OF VIOLATING QUALIFICATION TO ACCEPTANCE TEST MARGIN

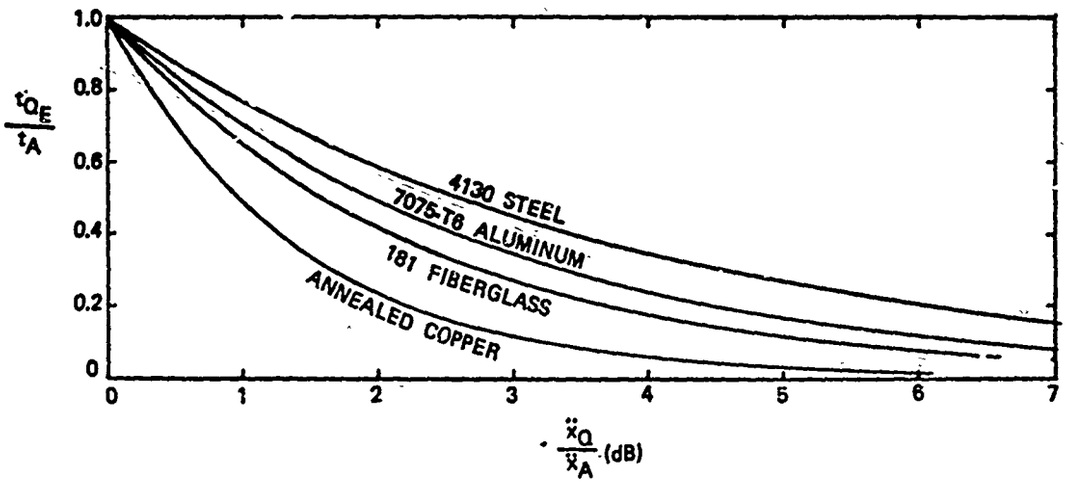

FIGURE 9. EFFECT OF MATERIAL PROPERTIES ON "EQUIVALENT-TIME-AT-QUALIFICATION-LEVEL"

The results of equation (7) are illustrated in Figure 9 for representative materials from Table 1. In using this figure the abscissa value corresponds to the ratio of the margin limits illustrated in Figure 7. This value is obtained by decreasing the nominal specified qualification to acceptance level ratio by the appropriate tolerance correction from Table 2 applied to each spectrum level. (For example, a 6 dB specification ratio with a 1σ tolerance of 1 dB gives a 4 dB margin.)

FAILURE PROBABILITY DERIVATION

Considering the total group of production units and the qualification unit, and assuming there is a fatigue sensitive area in the design, a statistical variation in the vibration time to failure is to be expected between the units. The statistical methods of assigning probability of failure and associated confidence numbers require significant sample sizes and are not applicable to the condition of a single qualification unit. Therefore, in order to define probabilities of failure, a normal distribution with specified mean and standard deviation has been assumed and the probability of failure for production and qualification units determined for various ratios of exposure time of the two types of units. The ratio of the upper to lower 3σ times of the assumed failure distribution are considered to be bounded by factors of 3 to 5, so that

$$\frac{\bar{t}_f + 3\sigma}{\bar{t}_f - 3\sigma} = 3 \text{ or } 5$$

where $\bar{t}_f$ is the mean time-to-failure. These factors of scatter band width result from the variation in stress level existing in component parts with different resonant frequencies which might fail in the unit during testing. Considering one minute of vibration on a 100 Hz resonance (6,000 cycles), the right hand ordinate of Figure 2b gives a scatter band ratio of 3. Considering five minutes of vibration on a 1000 Hz resonance (300,000 cycles), Figure 2b gives a scatter band ratio of 5.

By assuming a mean time-to-failure, $\bar{t}_f$, and using the afore mentioned standard deviation relationship, the normal distribution probability density function can be plotted as shown in Figure 10 for a scatter band width of 3. The cumulative probability of failure for the qualification unit as a function of time, t_Q, is now definable for the assumed $\bar{t}_f$. Since this assumed failure density function is also applicable to

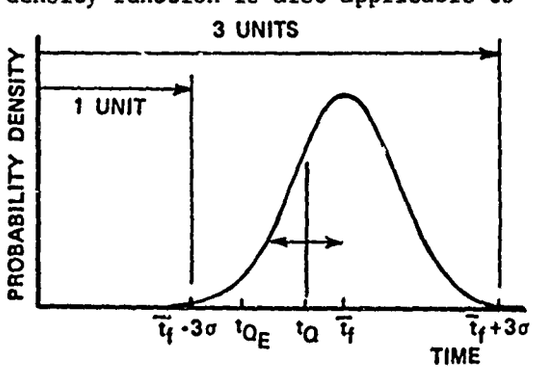

FIGURE 10. REPRESENTATION OF UNIT STRENGTH CAPABILITY

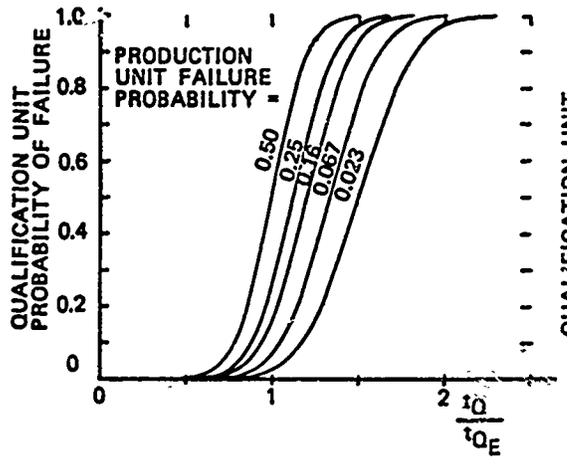

FIGURE 11a. EFFECT OF QUALIFICATION VIBRATION TIME (SCATTER BAND WIDTH = 3)

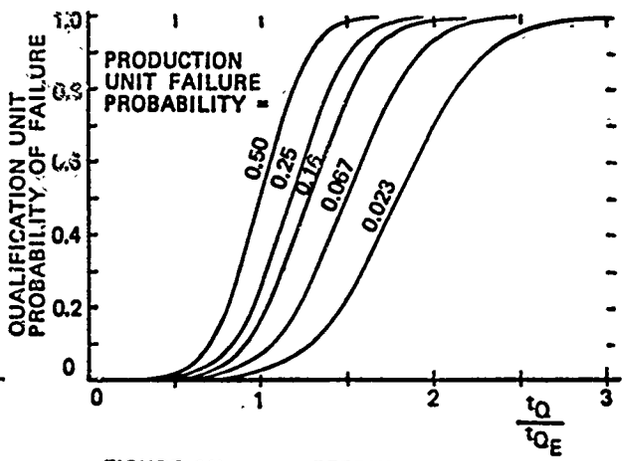

FIGURE 11b. EFFECT OF QUALIFICATION VIBRATION TIME (SCATTER BAND WIDTH = 5)

the production units, the same cumulative probability of failure as a function of time, t_{Q_E}, would exist for the production units. In order to eliminate the assumed parameter ($\bar{t}_f$) which represents the unknown strength capability of the units, the resulting failure probabilities are plotted versus the ratio of qualification time (t_Q) to equivalent-time-at-qualification-level (t_{Q_E}) of production units. The normalized results are achieved by selecting a time for a given probability of failure of the production units and then plotting the qualification unit probability of failure versus the ratio of t_Q/t_{Q_E} as shown in Figure 11. Although the exact value for probability of failure is undefinable since $\bar{t}_f$ is unknown, the figure illustrates that the probability of failure of the qualification unit and production units is identical for a time ratio of unity. The two sets of curves, Figure 11a and 11b illustrate the effect of the previously noted uncertainty in scatter band width.

The lack of a failure in the qualification unit as the probability of failure based on the assumed distribution increases gives an increasing confidence that the production unit probability of failure is not greater than the assumed value. In the absence of a failure, the qualification unit probability of failure is interrupted as a "confidence" in the correctness of the assumed production unit probability of failure. As previously noted, this "confidence" number is not the usual statistical confidence limit which requires a significant sample size in order to evaluate the correctness of the calculated mean and standard deviation.

By use of the curves of Figure 11 and considering various qualification times, the variation in "confidence" with increasing equivalent-time-at-qualification-level of production units can be obtained as shown in Figure 12. These curves represent a 2.3 percent failure

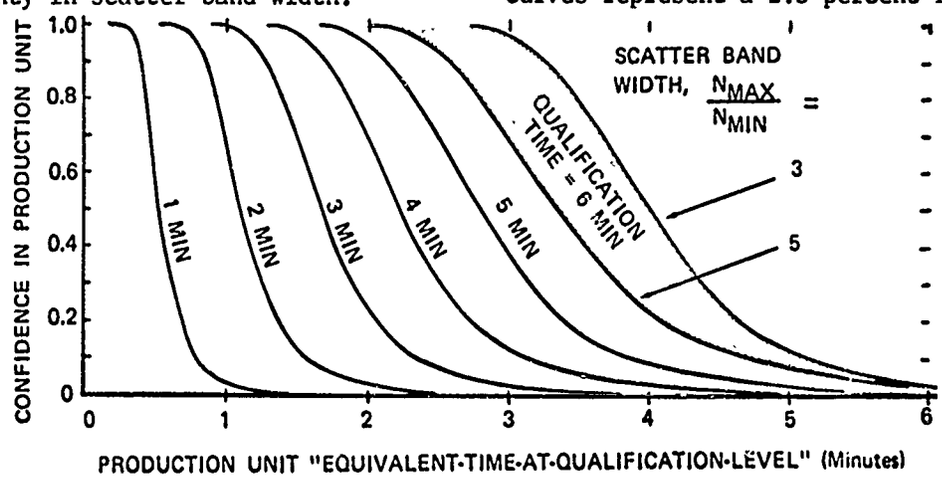

FIGURE 12. EFFECT OF QUALIFICATION TIME ON PRODUCTION UNIT CONFIDENCE (PRODUCTION UNIT FAILURE PROBABILITY = 2.3%)

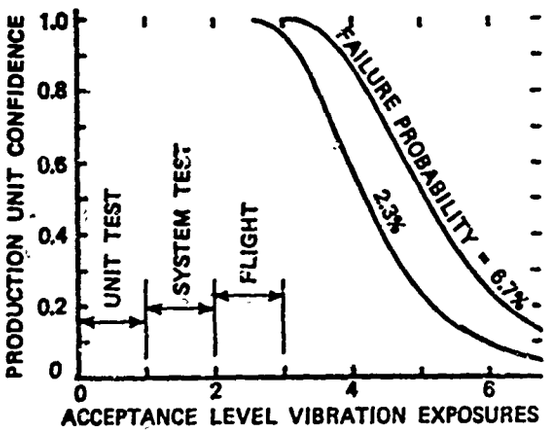

FIGURE 13. EFFECT OF MULTIPLE EXPOSURES ON PRODUCTION UNIT CONFIDENCE

(SEE TEXT FOR ASSUMPTIONS)

probability for production units. The effect of the uncertainty in scatter band width due to the unknown stress level existing during vibration is shown for the six minute qualification time curves.

APPLICATIONS

In order to illustrate the use of this evaluation method, a specific example is presented in Figure 13. The conditions used in arriving at this curve are:

- Unit acceptance test, system acceptance test, and flight environments are assumed identical.
- 7075-T6 aluminum is the material in the unit which has the steepest fatigue curve slope, b = -5.5
- Unit acceptance test is a two minute exposure per axis to a random spectrum.
- The qualification test spectrum is 6 dB higher than acceptance.
- Qualification test duration is three minutes per axis.
- The control tolerance for both acceptance and qualification test is $\pm$ 2 dB (i.e., margin is 4.5 dB).

These assumptions are generally consistent with current spacecraft practice (however, acceptance test is usually one minute per axis). Figure 13 indicates a high confidence in very low flight unit failure probability for the three normal exposures of unit acceptance test, system acceptance test, and flight. However, if workmanship problems during unit acceptance test cause rework of the unit and reacceptance testing resulting in a fourth exposure, the confidence in low probability of failure during flight begins to decrease. A fifth exposure would significantly degrade confidence.

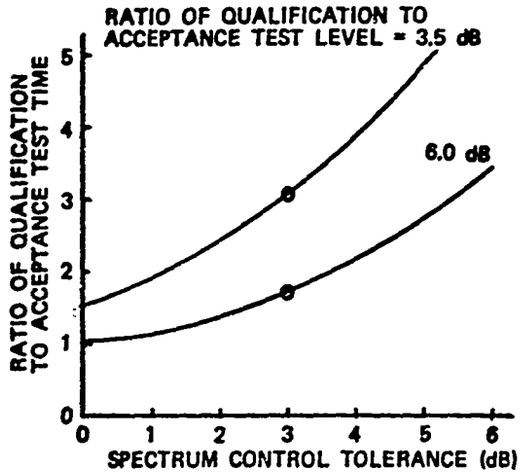

FIGURE 14. EFFECT OF TEST TOLERANCE ON REQUIRED QUALIFICATION TIME

ASSUMPTIONS:
7075-T6 ALUMINUM MATERIAL
3 ACCEPTANCE DURATION EXPOSURES
t_Q/t_{Q_E} = 2.3

The spectrum tolerance can be a relatively large portion of the specified nominal separation between acceptance and qualification testing levels and the effect of this tolerance on required qualification time is shown in Figure 14. The assumptions used in obtaining the curves consist of three acceptance duration exposures with 7075-T6 for the material as in the previous illustration. The two commonly accepted rationales for qualification testing at 1½ or 2 times the acceptance test level are presented for which a test spectrum tolerance of +3 dB is usually specified for random vibration. The figure indicates that for qualification at 50 percent above acceptance test level a duration of approximately twice that necessary for a qualification at twice acceptance level is required to achieve the same confidence for flight units.

The Aerospace Industry presently employs the practice of occasionally flying prototype hardware on one-of-a-kind type spacecraft (referred to as proto-flight). The ingredients of this analysis provide

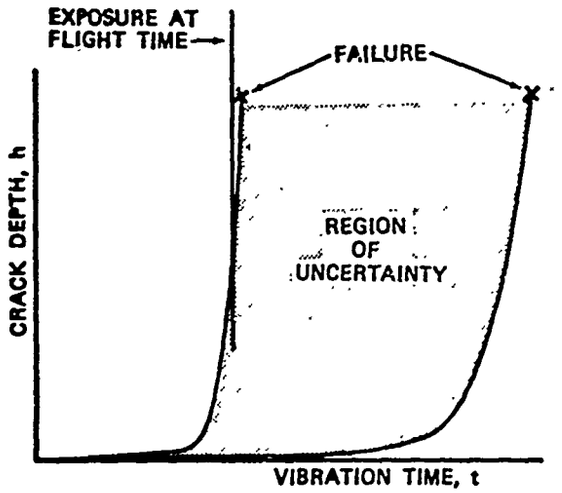

FIGURE 15. RISK OF FLYING PROTOTYPE UNITS

a means for evaluation of this practice. Use of equation (7) permits normalization of all ground vibration environments and the flight environment to one level so that damage versus time can be examined as a single curve for any given component. In the absence of a qualification unit for a reference, only two definitive statements can be made at the start of the ascent flight: (1) the unit is not failed at that time, and (2) past experience indicates a small likelihood of failure during flight. The first statement is illustrated in Figure 15 which shows that the lack of a failure does not give a measure of the amount of fatigue life remaining. Any component in the unit could be close to failure having very little fatigue life left or it could have insignificant damage as indicated by the region of uncertainty in which the actual damage curve lies. If unit acceptance test and spacecraft acceptance test result in the same level and duration of environment, then complete disassembly and inspection of the unit after unit acceptance test would be unlikely to result in discovery of fatigue damage existing at the 50 percent life point on the minimum fatigue life curve. The second statement gives a minimum degree of confidence for a successful flight since a new unit with differences in construction, components used, component and wiring locations, and resonance frequencies can not be guaranteed to be similar in all respects to previous units. Although this practice seems to be reasonably successful, the foregoing analysis approach does not permit evaluating a confidence and would imply that flight failures should not be unexpected. The difficulty of confirming that a significant portion of the fatigue life has not be expended by proto-flight testing has been noted by others [8, section 4.0].

CONCLUSIONS

The foregoing analysis leads to the following observations with respect to definition of qualification test requirements.

1 - The required duration of the qualification vibration test is dependent on the materials used in the unit.

2 - Vibration control tolerances should be taken into account in deriving the qualification test duration.

3 - Allowance should be made for rework and retest of production units when deriving the qualification test duration.

4 - Qualification times of approximately 2 to 2½ times the "equivalent-time-at-qualification-level" of production units are necessary for a high confidence in production unit capability.

5 - If the prototype is the first flight article of a multiple spacecraft program, the full qualification level and duration should be used to obtain confidence in the remaining vehicles.

6 - If the prototype is a one-of-a-kind spacecraft, the qualification level (or slightly less) should be retained and test duration minimized to limit fatigue damage. Additional confidence could be obtained by extended test time on an engineering unit as suggested by A. G. Piersol [8].

REFERENCES

1. F.R.Shanley, "A Theory of Fatigue Based on Unbonding During Reverse Slip," Report P-350, The Rand Corporation, Santa Monica, Calif., November, 1952.

2. S.S.Manson, "Fatigue: A Complex Subject - Some Simple Approximations," Experimental Mechanics, July, 1965.

3. W.M.Murray (Editor), "Fatigue and Fracture of Metals," John Wiley and Sons, Inc., New York, 1952.

REFERENCES (Continued)

4. W.Illg, "Fatigue Tests on Notched and Unnotched Sheet Specimens of 2024-T3 and 7075-T6 Aluminum Alloys and of SAE 4130 Steel with Special Consideration of the Life Range from 2 - 10,000 cycles," NACA TN 3866, Langley Aeronautical Laboratory, Langley Field, Virginia, December, 1956.

5. Harris and Crede (Editors), "Shock and Vibration Handbook," McGraw-Hill Book Company, New York, 1961.

6. S.F.Masri, "Cumulative Fatigue Under Variable-Frequency Excitation," Paper No. 660720, Society of Automotive Engineers, October, 1966.

7. G.H.Klein and A.G.Piersol, The Development of Vibration Test Specifications for Spacecraft Applications," Report CR-234, National Aeronautics and Space Administration, Washington, D.C., May, 1965.

8. A.G.Piersol and J.R.Maurer, "Investigation of Statistical Techniques to Select Optimal Test Levels for Spacecraft Vibration Tests," Report CR-115778, National Aeronautics and Space Administration, Washington, D.C., October, 1970.

DISCUSSION

Mr. Epstein (Endevco Corporation): If you have a systematic error in production units to which the statistics do not really apply, obviously things go astray. Have you found in practice that your statistics really work in terms of flight failures when everything is calculated?

Mr. Deitrick: Yes, that is a problem. Unfortunately qualification units are usually the first ones built. That problems exists in both respects, that is, many try to explain away qual failures by saying "we have corrected this in the production units." Failures in the qual units must be examined very closely with respect to the production unit configuration. If there has been a change from the qual unit configuration this technique will not catch that. The best method is to build all of the units together so that no one knows which is to be pulled for qualification.

SIMULATION TECHNIQUES IN DEVELOPMENT TESTING

Dr. Alexander Hammer
Weapons Laboratory, U. S. Army Weapons Command
Rock Island, Illinois

The need for and the advantages of utilizing simulation technology when armament systems are applied to mobility devices such as armored vehicles, tanks and helicopters are discussed and the various approaches to the solution of the problems emanating from weapon-mount relationship observed during development testing are described. Also presented are the design features of a variable flexibility mount and associated equipment located at the Keith L. Ware Simulation and Experimental Firing Center, U. S. Army Weapons Command, which offer a mechanical solution to these problems, together with the description of the data acquisition, reduction and analysis equipment which control the simulator during actual weapon test firings, provide a limited amount of real-time processing and assure automatic reduction of high frequency data acquired during the test.

INTRODUCTION

On 1 December 1970 the U. S. Army Weapons Command's Keith L. Ware Simulation and Experimental Firing Center named in honor of Major General Keith L. Ware holder of the Congressional Medal of Honor and killed in Vietnam was officially opened. Picture 1 shows the first Army simulation and experimental firing center, completed at the cost of approximately four million dollars and four years of planning, which houses two 1,000 inch firing ranges and two 100 meter ranges.

This Center, in which are located a simulation laboratory and an experimental firing facility, has equipment which simulates all types of motion that may be encountered by weapon-mountings in actual use. Mount-weapon interaction is induced, controlled, measured, analyzed, and recorded within the confines of the simulation laboratory without actually firing the weapon from an armored vehicle, tank or helicopter.

The uniqueness of the mount-weapon simulation equipment lies in the fact that it is not only a motion simulator, which is available at various other facilities, but it is the only one which is able to absorb the forces induced by the fired weapons in the same time frame in which they are created.

No longer will Weapons Command engineers and designers be required to wait for favorable weather conditions . . . no longer will it be necessary to use an actual armored vehicle, tank or helicopter that could be used for important service on the fighting front . . . no longer will researchers be dependent upon the time of day to test a theory that might be just the step necessary to improve a weapon in the hands of our soldiers.

In this building, one finds devices capable of simulating any weather condition . . . from 90 degrees below zero to 200 degrees above zero . . . adjustable lighting that simulates natural lighting conditions 24 hours a day . . . and equipment that enables the engineers to move large tank guns, helicopter frames and other bulky

weaponry items into position for test firing as shown on picture 2.

BACKGROUND

It became well established as far back as 1966 that in the application of armament systems to mobility devices such as armored vehicles, tanks and helicopters, the weapon function including firing rate, stability of rate, and even the ability to fire reliably, can be affected by the characteristics of the mounting system. It was realized that these mount effects were particularly apparent in the flexible range where weapon-mount natural frequencies approach synchronism with the impulse frequency of the weapon. It was recognized that this situation provided significant receiver velocities which, in turn, affected the relative velocities of the operating components and resulted in high weapon malfunction rates and increased forces acting on the mounting structure. It was observed that the large vibration amplitudes caused system malfunctions in the ammunition feeding area, whereby belt separation of link walk-off or belt pull nature occurred, creating problems in ammunition supply.

Obviously, armament system sensitivity to flexible mounting structures had to be identified and eliminated before designs were committed, engineering evaluation tests conducted, and field installations commenced. Delays, costs, and system compromises that occurred when severe corrective actions were required during installation or field stage armament evaluation could have been avoided only by prior knowledge of the significant mounting characteristics to be encountered. The successful fulfillment of the mission to perform research for aircraft weaponization by preparing new concepts and determining the relationship between weapon and mounting depended upon the availability of the aircraft, pilot and ground crew, safe available air space and favorable weather. To have all these elements together at the same place and at the same time proved to be a difficult task. Access to other mobility devices was limited also.

The helicopter armament subsystem interface diagram shown on picture 3 illustrates the essential interfaces existing in helicopter mounted weapon systems. Of these, the gun mount vehicle interface has the greatest effect on weapon-operation reliability. Certain weapons which operate reliably on hard test mounts would not fire when mounted on a helicopter. It was thus learned that far from being a rigid mount, the helicopter behaves flexibly, and any mount attaching a weapon to the helicopter is characterized in part by both an effective spring rate and an effective damping ratio. It is through this flexible coupling that reactions, generated by the recoil forces of the weapon, are transmitted to the helicopter frame and reflected back to the weapon structure. Obviously, those combined forces cause the weapon to be subjected to an environment entirely different from that created by firing the weapon from a completely rigid mount.

This situation created the problem of how to test a weapon under the conditions of flexibility exhibited by helicopter mounts and yet to do this on a conventional ground range without actually flying a helicopter. It seemed obvious that conducting those tests under laboratory type, controlled and repeatable conditions would prove helpful. Although there may be several solutions to the problem, the originator of the idea to be described, with the help of a group of enthusiastic, forward looking scientists and engineers of vision evolved, designed and manufactured a mechanical mount to simulate the actual conditions of flexibility existing in helicopter mounted weapon systems.

VARIABLE FLEXIBILITY GUN MOUNT

The variable flexibility gun mount simulator, shown on pictures 4 and 5 supporting the 20mm, M139 and the 7.62mm, M134 MINIGUN weapon systems, respectively, consists of two rectangular leaf springs with hydraulic pressure pad clamps to provide adjustable spring rate in one-degree-of-freedom (i.e., in the direction of gun recoil). The design is such that the distance of the firing platform to the floor never changes and the change in spring rate is accomplished by moving the pressure pads along the springs. Attached to the firing platform are two variable orifices which provide variable damping ratio. With this equipment it is possible to simulate present and future weapon mount interfaces since the spring rate can readily be varied from 90 to 100,000 pounds per inch and the damping ratio can be changed from 0.05 to 0.80. This simulator is capable of supporting weapons up to and including 40mm, weighing up to 350 pounds, and having a muzzle energy and impulse not to exceed

120,000 foot pounds and 70 pound-seconds, respectively. Under these maximum conditions and nominal damping (damping ratio = 0.10) the simulator is subjected to about 25,000 pounds of force and peak accelerations of 100,000 inches per second squared.

The facility in which the simulator is located is 194 feet long and contains a 1,000-inch range, target drop, sand butt, high bay area with overhead crane and extra high double doors for equipment access. The simulator is located on a reaction mass at one end of the range. Hydraulic power supplies for the simulator, vibration excitation equipment, and other accessories are located near the reaction mass.

The panel shown on picture 6 indicates the flexibility and the damping ratio used for the particular mounting arrangement under consideration. These data are visible not only at the firing range, but are simultaneously recorded on the instruments located in the data acquisition facility, as well.

On picture 7 is shown some of the instrumentation used for the 20mm, M139 weapon system utilizing the latest electronic technology to provide data acquisition, real-time and delayed-time data reduction presentation, and subsequent data analysis in support of all weapon tests performed. Sensing, recording, data-reduction, and analysis equipment permits the simultaneous recording of fourteen different significant parameters such as recoil travel, force, velocity, acceleration, stress, strain and temperature associated with the particular weapon fired in a predetermined mounting condition.

INSTRUMENTATION

The data acquisition, reduction and analysis facility controls the simulator during actual weapon test firings, provides a limited amount of real-time processing and reduction of data, and assures automatic reduction of high frequency data acquired during the test. The block diagram shown on picture 8 indicates how the various components of the acquisition, reduction and analysis are interconnected to accomplish above purpose.

DATA ACQUISITION

The acquisition equipment consists of transducers, signal conditioning and monitoring equipment, magnetic tape and other recording equipment. A time code generator is used to supply precise time signals which are recorded with the test data and later used in the analysis of the data.

Closed circuit television screens are available in each of the facilities to provide visual recording of the firing.

DATA REDUCTION AND ANALYSIS

The reduction equipment shown on picture 9 consists of a magnetic tape playback transport, a time code reader and tape search unit, a digital computer with card reader-punch, paper tape reader-punch, digital tape transport, magnetic disk, line printer, and display units. This equipment is interconnected with the simulator so that the pre-test and post-test calibration, pre-test start-up and post-test shutdown procedures and the weapon test are all performed automatically by the computer with supervisory override control for safety. The analysis equipment comprises specialized analog computer circuits connected with the digital computer for determination of such parameters as spring rate, damping ratio, mechanical impedance, transfer ratio, Fourier coefficients, and power spectral density.

The type of data which are sensed, analyzed, reduced and presented or banked by this equipment are shown on pictures 10 and 11. The recoil force vs. time on picture 10 for an FN Rifle is plotted in engineering units and printed shortly after firing the weapon. Picture 11 shows the effect of mount flexibility upon recoil travel using the same FN Rifle.

MULTIPLE-DEGREE-OF-FREEDOM GUN MOUNT

The one-degree-of-freedom simulator permitted motions only in one direction - that of the line of fire. A more complex simulation equipment shown in an artist's concept in picture 12 has been developed, designed and is being manufactured for December 1971 delivery. It consists of a flexible suspension system having spring and damping characteristics of six-degrees-of-freedom simulation - thus permitting translatory motion along, and rotation around, the three principal axes induced by firing the armament subsystem and resisted by the spring rate and damping ratio that are characteristic of the vehicle in a particular condition. Certain of these motions are coupled together and produce weak or strong interactions.

Some of these interactions are retained as they are similar to the actual motions of mobile devices. Others are eliminated as they are not characteristic of the mobility of a particular mounting setup. As originally conceived, the simulator actually supports sections of full size helicopters and light weight tank cupolas. With the help of this simulator the weapon may be traversed, elevated or depressed, yet it still will be possible to work with a fixed target because the effect of changing the direction of fire is most easily simulated by rotating the weapon while counter-rotating the mount or the mount/carrier structure. The flexible suspension system, cantilevered from a concrete column, consists of six hydraulic actuators attached at both ends by universal joints. By proper excitation, simulating the roll, pitch, and yaw effects of the helicopter - as well as the torque effect of its rotor - will be possible in the Simulation Laboratory when the new equipment has been installed. The size of this equipment is indicated on picture 13 showing the actual suspension support of the multi-degree-of-freedom simulator.

SAVINGS ACCOMPLISHED

It is very important that all these innovations will save the taxpayers' money. Savings that will be effected are in three categories: (1) savings contributed to reduction of development costs, (2) savings that cannot be readily converted into dollar values, such as reduced development time and by not utilizing the armored vehicle, tank and helicopter for weapon systems test purposes when they could be performing the primary function for which they were authorized, and finally (3) savings realized from controlled testing within the confines of the laboratory. For instance, the cost of flight test requirements, estimated to be 40,000 rounds of ammunition fired at the rate of 4,000 per day, with a ratio of 5 to 1 of ground-to-flight time, would be well over $100,000, including helicopter, pilot, ground crew, maintenance, insurance, travel, ammo, links, and handling charges.

Experience obtained from use of comparable simulators shows that a very small sample (20%), under controlled conditions, will furnish more reliable data than field tests in varying, uncontrolled conditions. Simulator test requirements are estimated to be 8,000 rounds of ammunition fired at a rate of 4,000 rounds per day. Estimated cost of one simulated test is about $9,000, leaving a net saving still over $100,000. With three tests required, a saving of $300,000 can be realized for each weapon system.

However, even more important than the reduction of development cost is the reduction of development time, which, of course, means saving money too. Mathematical modeling is one of the newly developed weapons dynamics techniques. Transforming probabilistic models into deterministic ones becomes imperative as soon as one intends to use these complete and reliable models to reduce experimental testing and redesigned prototype fabrication on one hand, and on the other hand wants to determine the multitude of parameters with the help of experimentation.

Thus, it is evident, experimentation still is needed, but only to the extent of permitting the verification of the model at its less sophisticated stages. Such parameters as spring constant, coefficient of friction, gas force, flexibility and damping of the mounting in the basic mathematical model shown on picture 14 must be verified by experiments and not by empirical adjustments. The weapon mount simulator is eminently qualified and fully utilized to determine those parameters which concern flexibility and damping.

ADDITIONAL EQUIPMENT

Spring constants may be determined with the help of a spring simulator shown on picture 15, in which forces of the same magnitude and duration are induced as those which are developed in the actual weapon. Cams in the power train, representing the spring time-displacement in the particular weapon, make the simulation possible. The motion of the spring is visible through a flexiglass cover, which makes it possible to photograph its operation while the test is being conducted. Small arms springs can be developed or tested in this simulator, for a minute amount of the cost of actual firing tests. Also, this system may be used as a dry-cycling machine for endurance testing of complete small arms weapons.

All the high-speed motion-picture records taken and developed in the engineering photo analysis facility of the Laboratory are analyzed frame by frame in a GERBER-READER, resulting in instantaneous typed coordinated or plotted analytical data.

Time-displacement records so determined are differentiated repeatedly, and are utilized as velocity-displacement, acceleration-displacement and force-displacement data, respectively.

Other simulators available at the Center are being used to determine the dynamic coefficient of friction, the interrelationship of natural and superimposed forced vibration in a vibrating medium, feeding and ejection characteristics and optimum power requirements. A small arms components motion simulator which permits the variation of weight, temperature, loading, clearance, speed and acceleration of the test specimen, humidity and temperature of the surrounding medium and the consistency and contamination of the lubricant, is used to determine the dynamic coefficient of friction.

FUTURE PLANS

These pieces of equipment are only stepping stones in a vigorous program shown on picture 16 which permits the U. S. Army Weapons Command to have capability in every facet of simulation testing. The first three projects were accomplished on time; the fourth is progressing well. At the conclusion of the last planned project, complete evaluation of tank and aircraft armament within the confines of the Center not only will be possible, but will also be dictated by economical considerations. Austerity in the defense budget makes it imperative to get the last cent's worth out of every development dollar.

These simulators are essential for a forward-looking program of advanced weapon testing. The first difficult steps toward implementation of laboratory weapon-firing tests simulating actual flight tests have been taken, and actual simulation tests are in progress. Other simulators are being and will be designed for the additional interfaces which were shown in the helicopter armament subsystem interface diagram.

The creative talents of young scientists and engineers, the experience gained from simulated weapon testing, and the technology developed in and the unique equipment of the Keith L. Ware Simulation and Experimental Firing Center are available to all elements of the Army and of the other services. They are also available to private industry to fulfill its contractual obligations.

Keith L. Ware Simulation and Experimental Firing Center

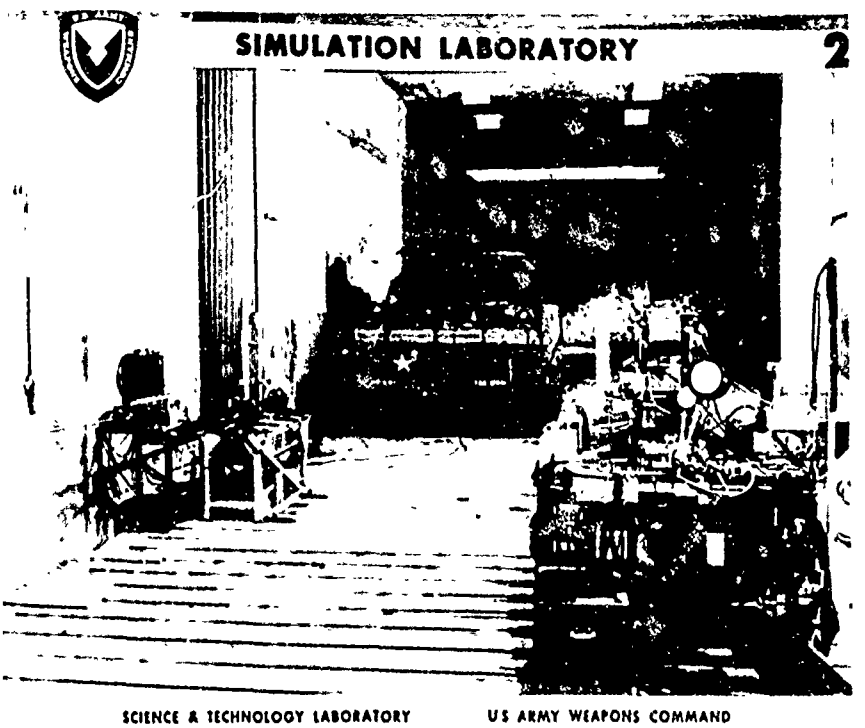

Simulation Laboratory

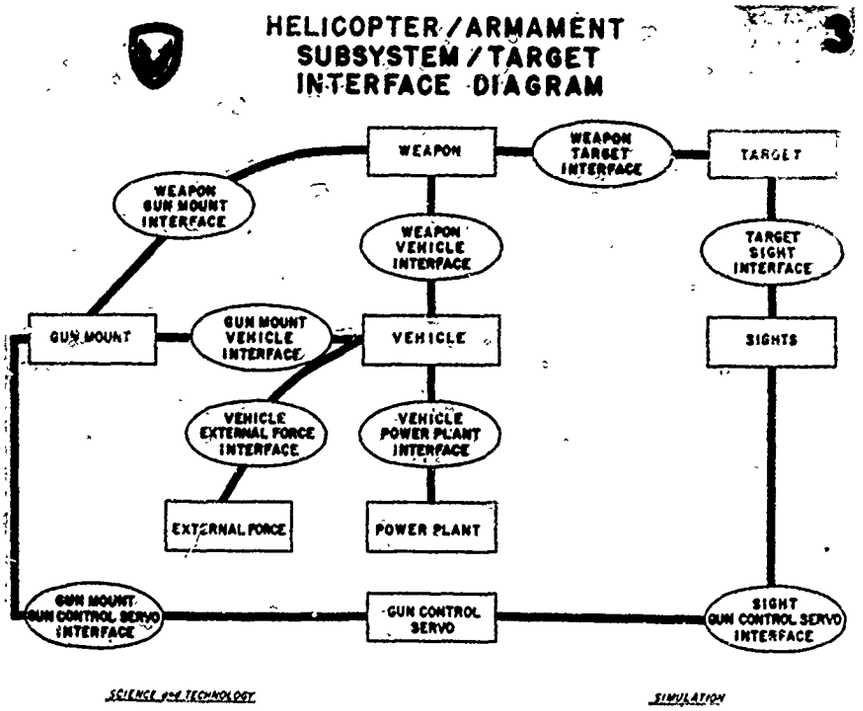

Helicopter Armament Subsystem Target
Interface Diagram

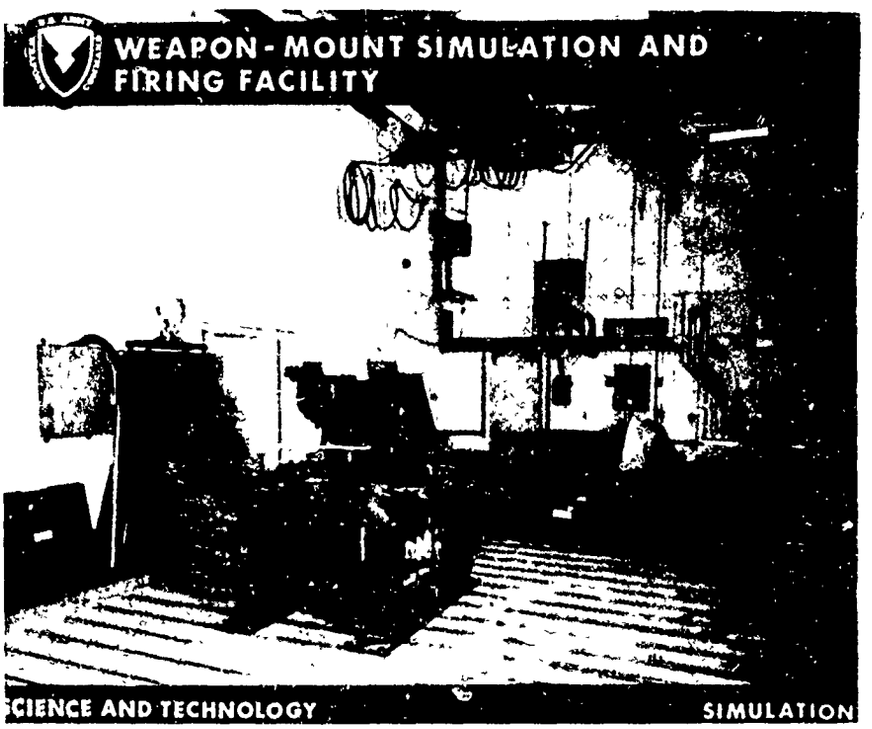

M139 on Weapon-Mount Simulator

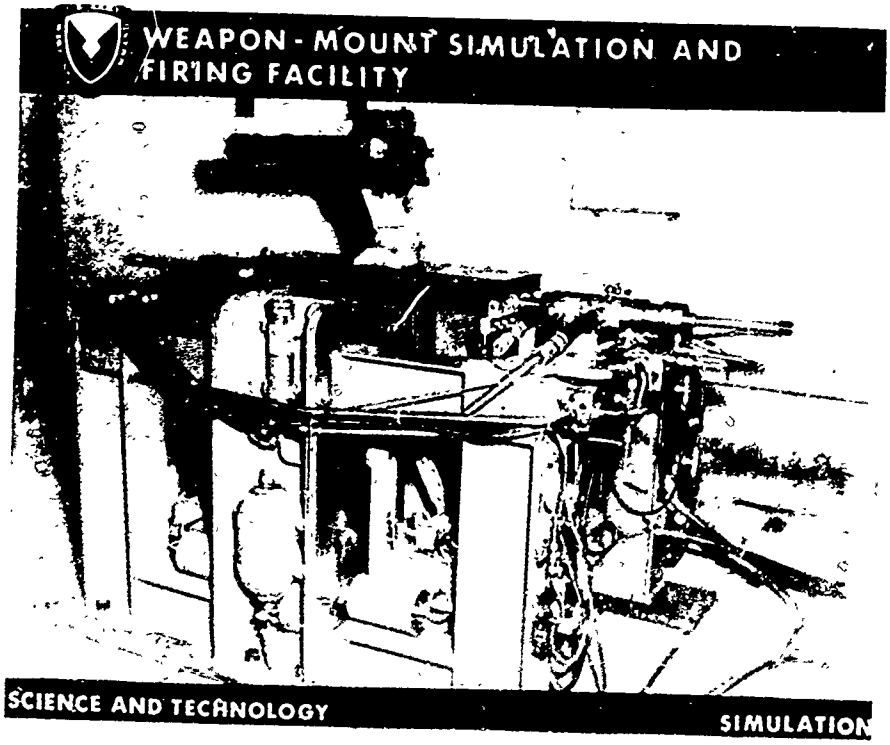

M134 on Weapon-Mount Simulator

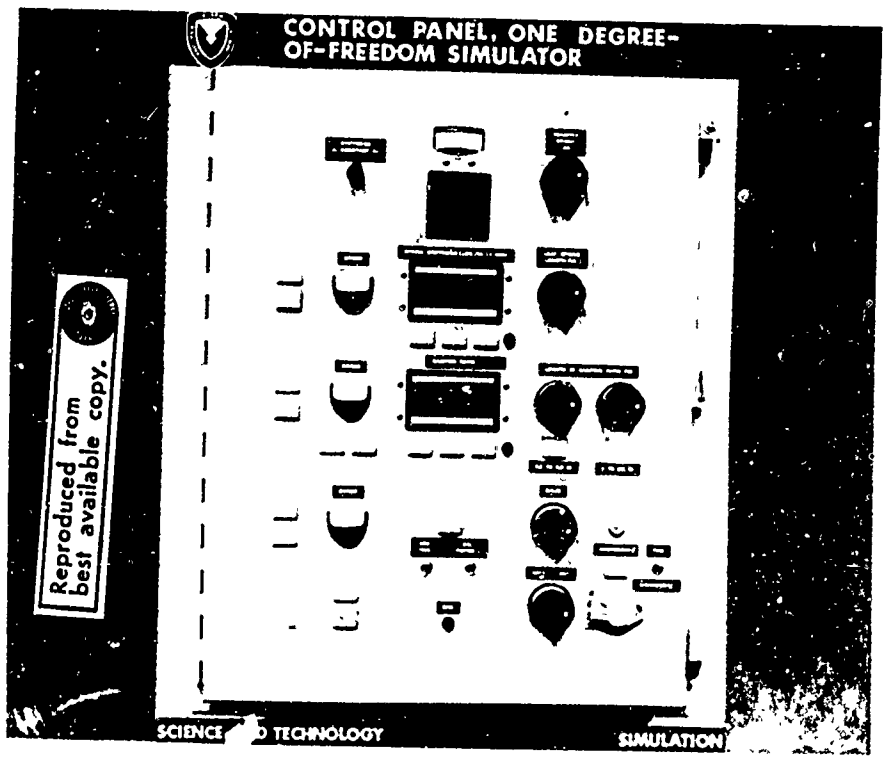

Control Panel

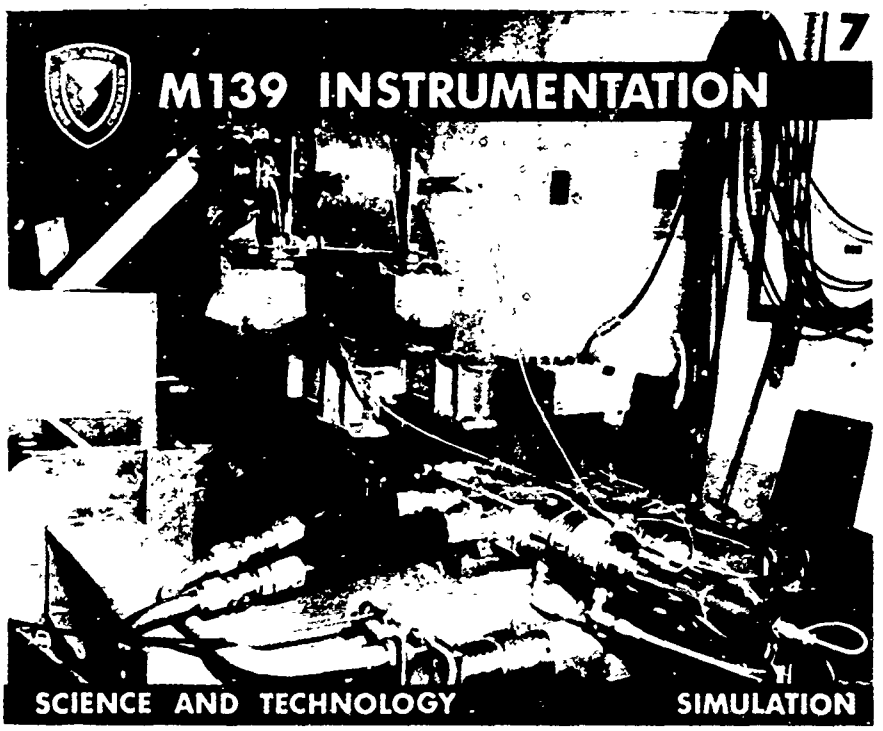

M139 Instrumentation

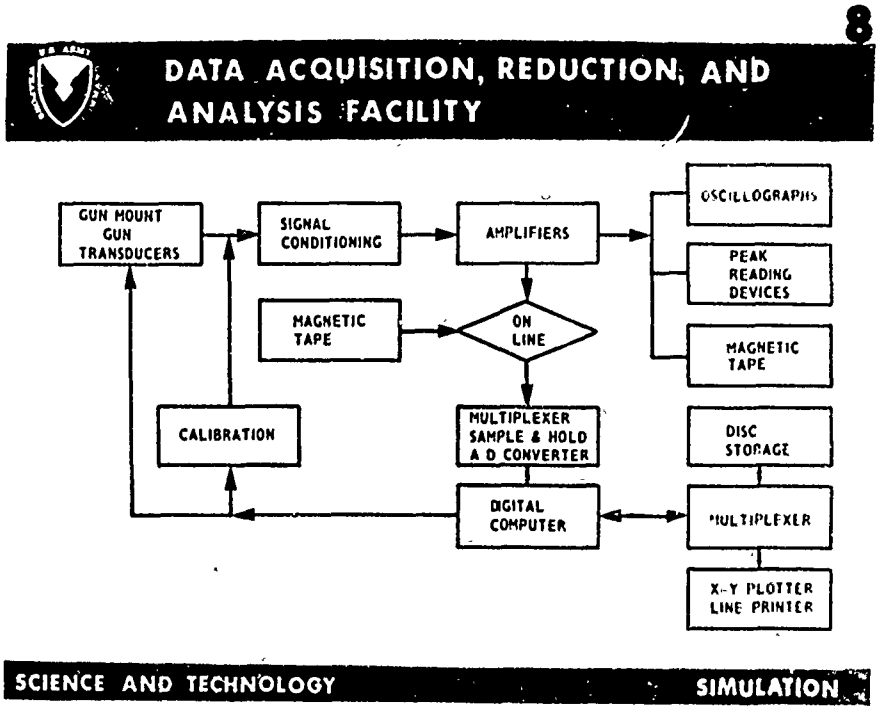

Data Acquisition, Reduction and Analysis Facility

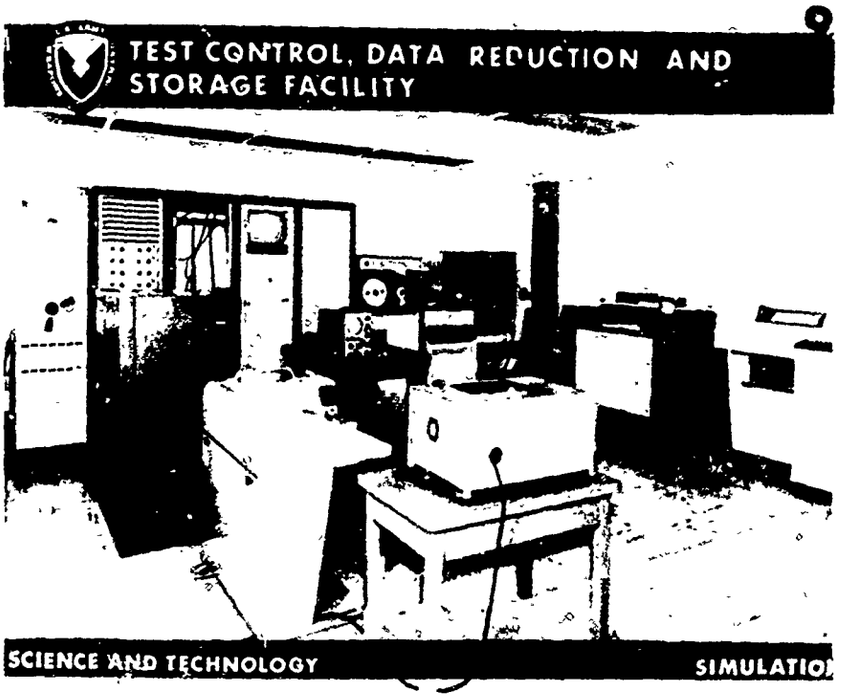

Test Control, Data Reduction and Storage Facility

Reproduced from best available copy.

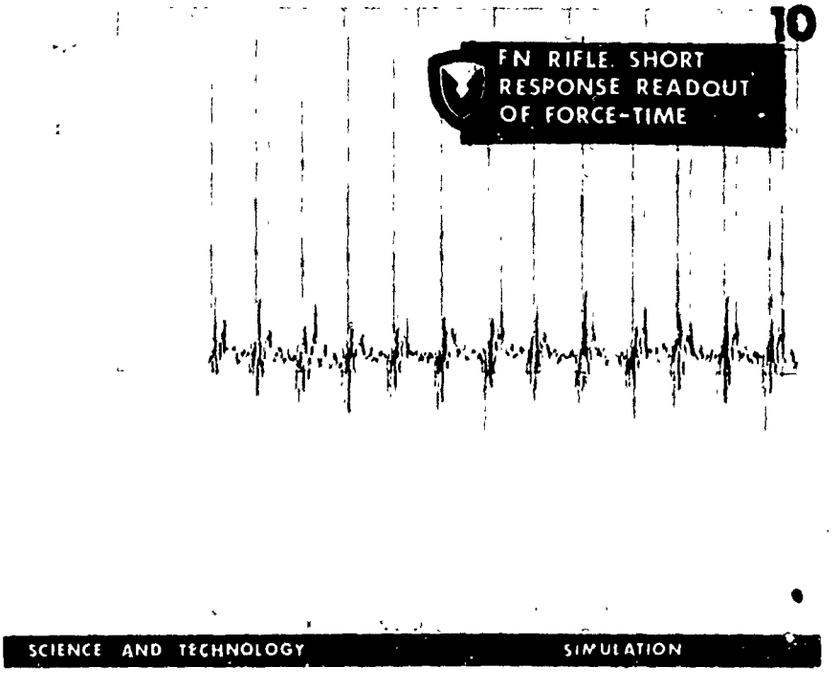

FN Rifle, Short Response Readout of Force-Time

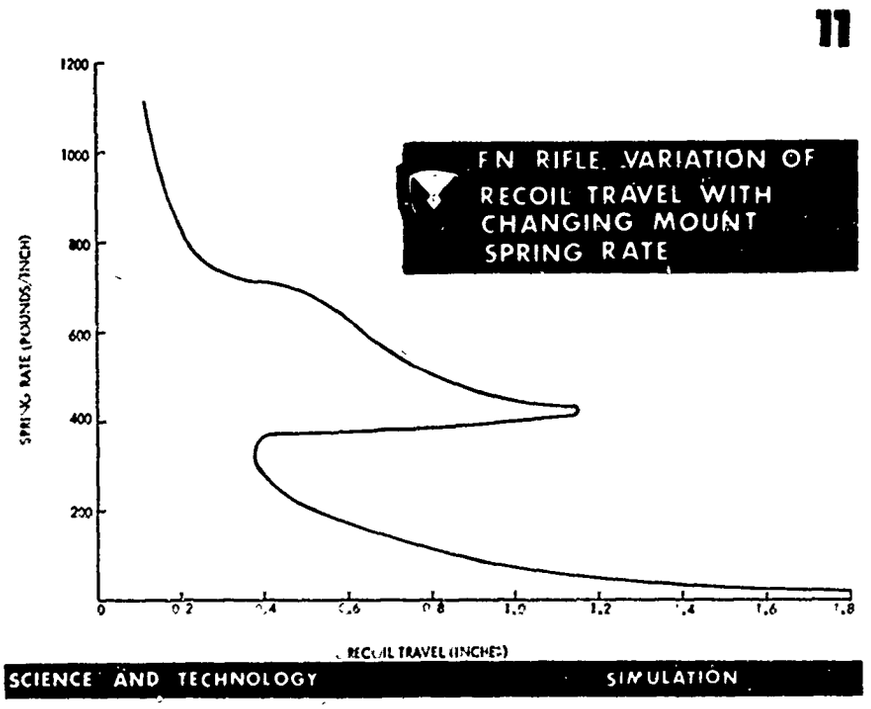

FN Rifle, Variation of Recoil Travel with Changing Mount Spring Rate

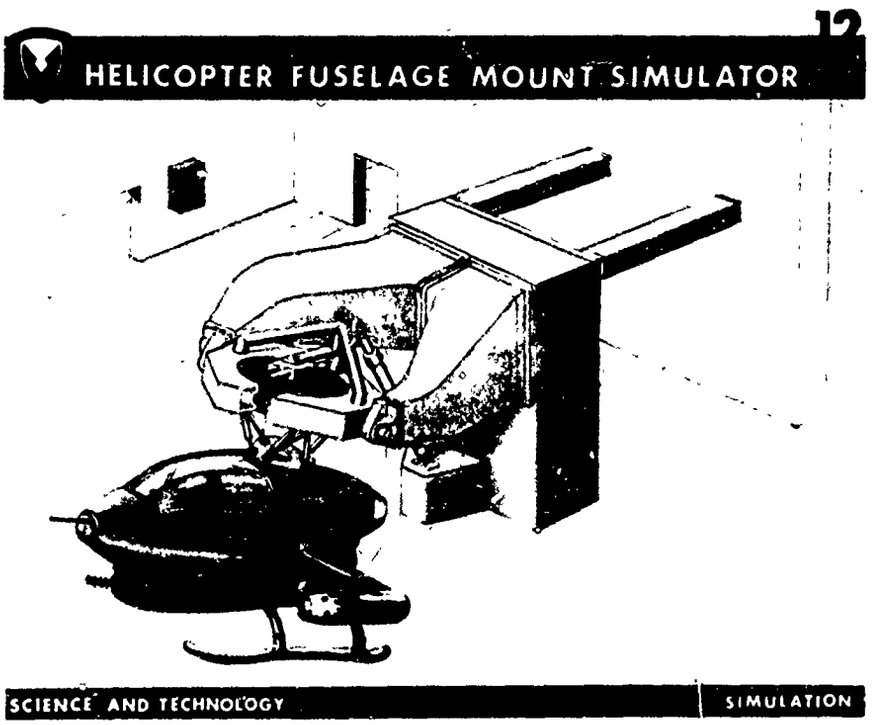

Helicopter Fuselage Mount Simulator

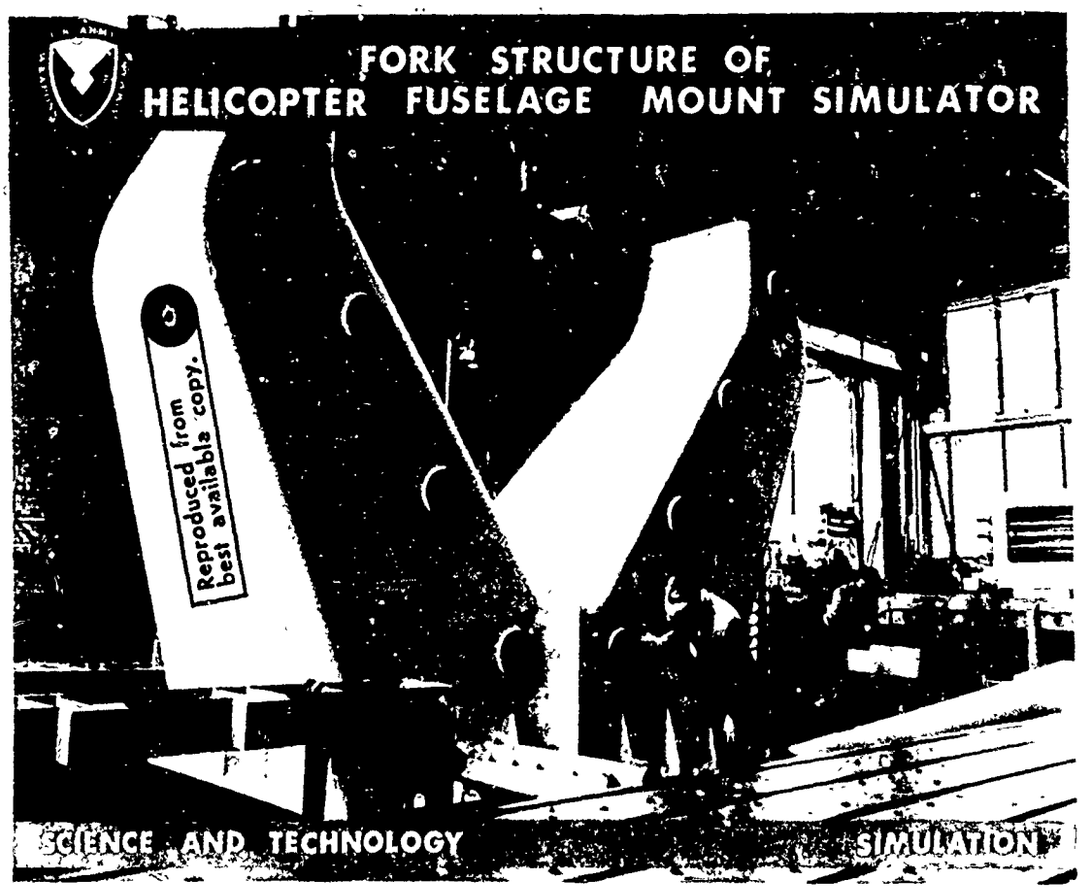

Fork Structure of Helicopter Fuselage
Mount Simulator

PRELIMINARY MODEL 14

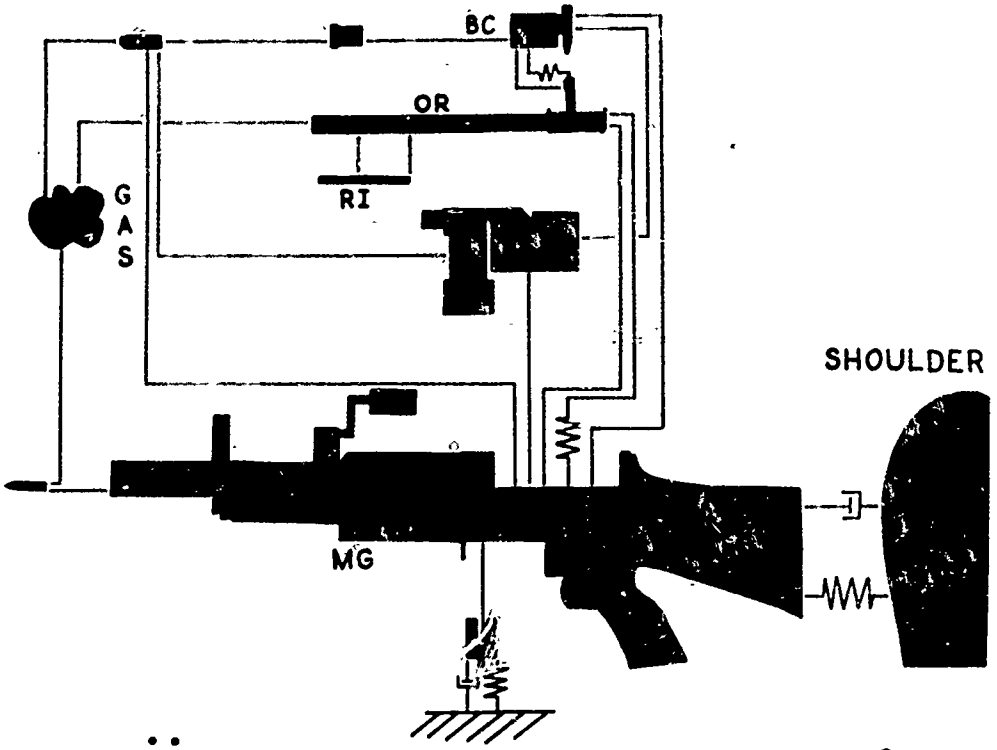

$$(1)\ M_{OR}\ddot{X}_{OR} = K_{\substack{\text{MAIN}\\\text{SPRING}}}(X_{OR} - X_{\substack{OR\\EQ}}) + F_{\substack{\text{GAS}\\\text{PRESS.}\\\text{ON PISTON}}} + f_{OR,MG} + f_{RI,OR} + F^{I}_{RI,OR} + K_{\substack{\text{BELLE-}\\\text{VILLE}}}(X_{OR} - X_{BC} + D_{BC,OR}) + f^{C}_{OR,BC}$$

$$(2)\ M_{RI}\ddot{X}_{RI} = -f_{RI,OR} - F^{I}_{RI,OR}$$

$$(3)\ M_{BC}\ddot{X}_{BC} = -K_{\substack{\text{BELLE-}\\\text{VILLE}}}(X_{OR} - X_{BC} + D_{BC,OR}) + f_{MG,BC} - f^{C}_{OR,BC} + F^{I}_{MG,BC} + F[X_{BC}]_{\substack{\text{FEED CAM}\\\text{\&LINKS}}} + F[X_{BC},t]_{\substack{\text{BLOW}\\\text{BACK}}} + F[X_{BC},t]_{\substack{\text{CARTRIDGE}\\\text{CASE DRAG}}}$$

Mathematical Model

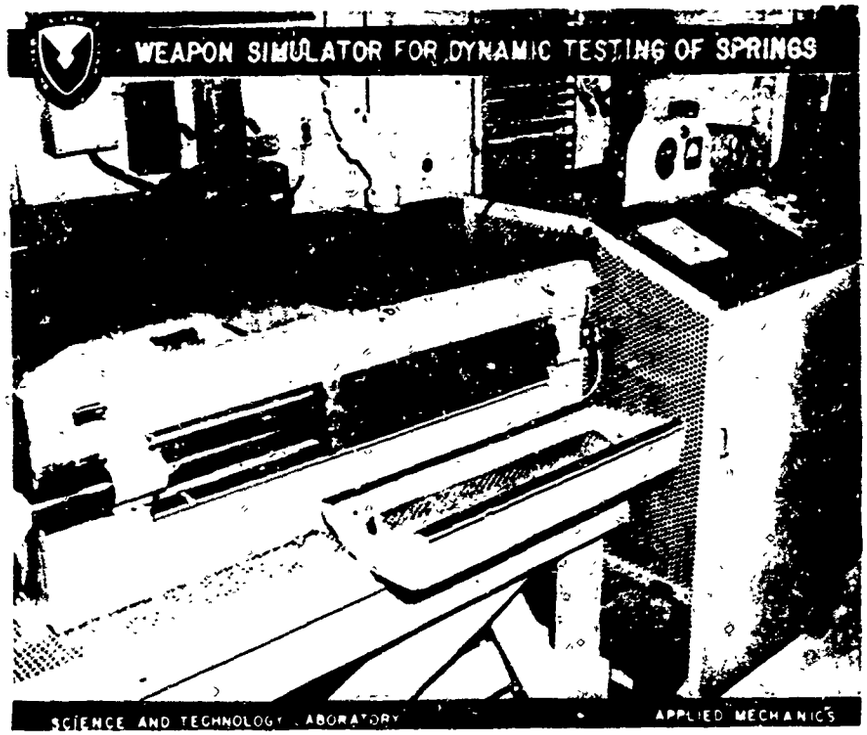

Weapon Simulator for Dynamic Testing of Springs

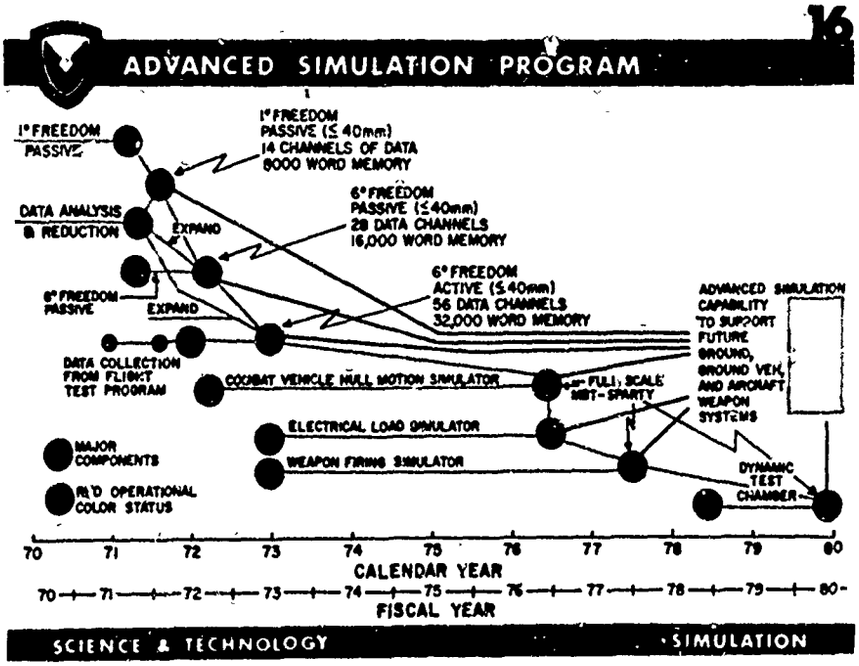

Advanced Simulation Program

A ROTATIONAL SHOCK AND VIBRATION FACILITY

R. T. Fandrich, Jr.

RADIATION INCORPORATED
Melbourne, Florida

This paper describes the design and operation of a rotational shock and vibration facility. The requirement for this facility developed from design problems which emerged from special antenna designs. The paper establishes that, in general, the rotational environment cannot be simulated by the linear environment and generates the rules which describe the difference. These rules can establish if a linear approximation is sufficient or if rotational considerations must be made. The application of these rules to the specific design problem establish the requirement for rotational testing.

A new approach was investigated for this facility, utilizing a rotational, direct current, torque motor as an energy source, instead of a crank mechanism with a linear vibration exciter. This approach allowed a separate location and does not have the linear-to-rotational interface problem. A standard vibration power amplifier and control system can be used since the torque motor has electrical characteristics similar to an electrodynamic linear shaker. This analogy can be carried on for the entire system, flexures being shaft bearings, field windings being stator, etc., so the concept is relatively simple to understand. The feedback signal for closed loop operation is derived from a linear accelerometer which measures circumferencial motion.

The system is plagued by the same design problems as a linear system, these being armature resonance and mass (moment of inertia), field cooling and moving element support stiffness.

This shaker can be used for sine or random testing and can also be used to simulate shock pulses. Since this system has a strong resemblance to a linear system, all common linear shaker techniques can be adapted to it. Shock simulation becomes even simpler since a double amplitude restriction does not exist for a rotational system. Rotational acceleration, that is, circumferencial acceleration, can also be simulated; and this was, in fact, one of the test requirements.

In addition, a heavy-duty rotational shock machine is discussed. This shock machine is designed for heavy, unbalanced loads to be tested at distances of up to six feet from the center of the shock field.

This paper evaluates the systems' performances both theoretically and empirically from results of actual rotational tests and rates the systems in terms similar to linear systems.

THEORY

By the term "Rotational Vibration", we mean an oscillation of a mass about an axis in three dimensional space. For this discussion let us consider sinusoidal rotational vibration remembering that we can expand this concept to any random motion with the mathematical descriptions becoming more complex. A point undergoing this rotational vibration will travel through an arc θ at a circular velocity of ω and a circular acceleration α. If the radius is defined as r, the position of this point is:

$$\theta(t) = \beta \text{ Sin } (2\pi ft) \quad (1)$$

$$\omega(t) = 2\pi f\beta \text{ Cos } (2\pi ft) \quad (2)$$

$$\alpha(t) = -(2\pi f)^2 \beta \text{ Sin } (2\pi ft) \quad (3)$$

t = Time

β = Maximum Angular Deflection

f = Frequency of Oscillation

The acceleration, A, of the point can be defined by its two components.

$$A(t) = A(\text{radial}) \mp A(\text{tangential}) \quad (4)$$

$$= \omega^2 r \mp \alpha r \quad (5)$$

Both components are a linear function of radius, and a square function of frequency. The components differ as a function of β, the radial being a square and the tangential being a linear function. This indicates that the rotational field at the point approaches a tangential linear field as the maximum angular deflection approaches zero, a fact which is intuitively obvious.

Since the "Linear" field is tangential, it is not a linear field for large collections of points; therefore, further restrictions are required to make these fields similar.

The direction of the field is a direct function of the location angle of the points, so the collection of points (or crossectional area) must be enclosed by a small angle to be similar to a linear field.

The magnitude of the field is a direct function of radius so the area must cover a small range of radii, that is, the ratio of the smallest radius to the largest radius defining the area must approach unity.

These three rules for similarity can be simplified and shown in Figure 1.

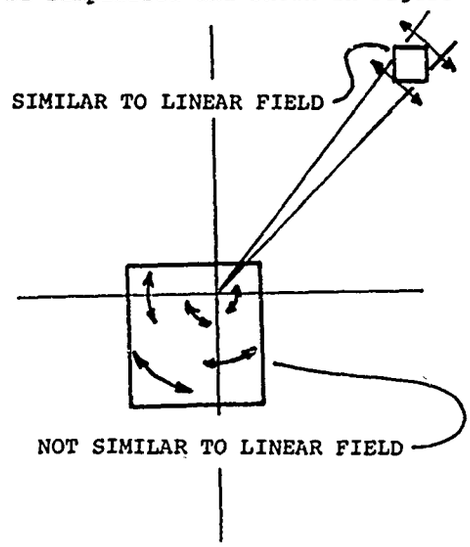

FIGURE 1
ROTATIONAL FIELD

A rotational vibration field will approach a linear vibration field if:

1. The maximum angle of deflection approaches zero;
2. The angle enclosing the area of the field under consideration approaches zero;
3. The ratio of the minimum to the maximum radii enclosing the area of the field under consideration approaches unity.

Observe that many of the dynamic environments imposed on rotating machinery do not fulfill any of the above requirements. If we consider a double gimballed antenna, we see that, contrary to rule number one, large dynamic inputs exist about the elevation and azmuth axes. Contrary to rules number 2 and 3, the antenna completely surrounds both axes. For this case, rotational dynamic considerations cannot be evaluated in terms of linear fields.

HEAVY-DUTY SHOCK MACHINE

A rotational machine was constructed for high-force shock work only. The requirements for this machine were such that a combination shock and vibration machine was unfeasible. The

machine consists of a twelve-foot long beam, pivoted about its center to rotate in a horizontal plane. A heavy-duty automobile wheel assembly provided this pivot. This assembly was cheap, is easily replaceable, readily available and provides the stiffness required about the non-rotating axes. Two linear stroke hydraulic cylinders are used to provide the accelerating torque. (See Figure 2.)

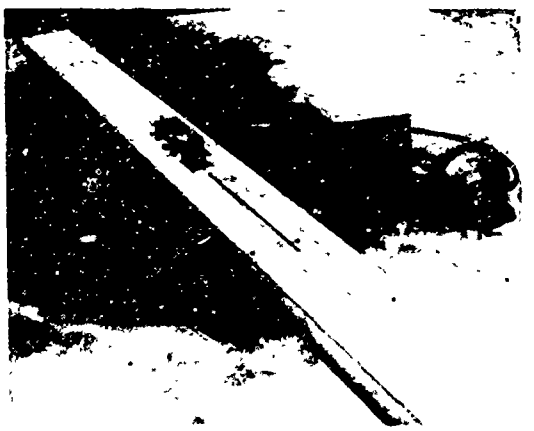

FIGURE 2
ROTATIONAL SHOCK MACHINE

An adjustable moment arm allows optimization of the torque relative to the stroke requirement. The two cylinders are single stroke with 7/8 inch bores. At their rated pressure of 3,000 pounds per square inch, they each provide a force of:

$$\text{Force} = \text{Pressure} \times \text{Area} \qquad (6)$$

$$= 3{,}000 \text{ PSI} \times \frac{\pi(7/8)^2}{4}$$

$$= 1{,}800 \text{ Pounds}$$

Their maximum moment arm is 14 inches; therefore the maximum torque available from the pair of cylinders is:

$$\text{Torque} = \text{Force} \times \text{Moment Arm} \qquad (7)$$

$$= 3{,}600 \text{ Pounds} \times 14 \text{ Inches}$$

$$= 50{,}000 \text{ Inch-Pounds}$$

$$= 4{,}200 \text{ Foot-Pounds}$$

In calculating the machine's capability, three loads must be considered. First, the beam itself must be considered. This is similar to the armature consideration in vibration testing.

Secondly, the test article and fixture must be considered.

Thirdly, the counterweight must be considered. Since the rotational environment is not homogeneous in space, it is imperative that the test article be placed in the same position (relative to the rotational axis) it occupies in its actual application. Since the axis of rotation is not placed arbitrarily relative to the test article, a counterweight is required to balance the load about this axis. The combination of these three loads derates the machine to some fraction of 4,200 foot-pounds effective torque. A sample problem is illustrated below:

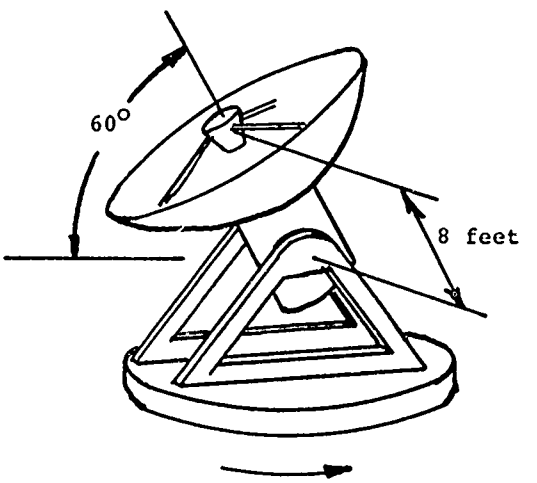

ROTATIONAL SHOCK
OF 10 RADIANS/SECOND^2

FIGURE 3
ANTENNA UNDER ROTATIONAL ACCELERATION

PROBLEM:

Simulate the rotational environment experienced by a 200-pound feed on the antenna shown if a maximum acceleration rate of 10 RAD/sec^2 is expected in the horizontal plane.

SOLUTION:

Due to the inclination on the elevation axis, the radius from the center of rotation is:

$$r = 8 \text{ feet} \times \cos(60^\circ) \quad (8)$$

$$= 4 \text{ feet}$$

A fixture must be designed to hold the feed at 60° to the horizontal. Assuming this fixture weighs 100 pounds, a 300-pound load must be tested at a four-foot radius.

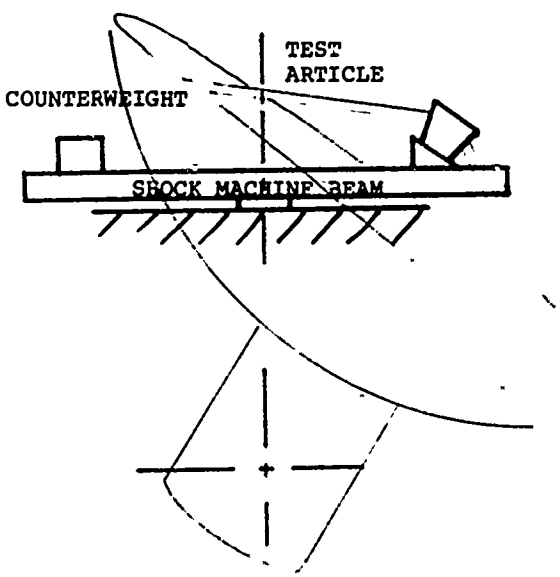

FIGURE 4
ARRANGEMENT OF TEST ARTICLE

The test beam itself has a moment of inertia of 48 foot-pound-seconds^2. The torque required is then:

$$T = \Sigma J\alpha \quad (9)$$

$$J = r^2 \frac{W}{g}$$

$$J(\text{Test Load}) = (4 \text{ feet})^2 \times \frac{300 \text{ pounds}}{32.2 \text{ Feet/Seconds}^2}$$

$$= 149 \text{ Foot-Pound-Seconds}^2$$

$$J(\text{Counterweight}) = 149 \text{ Foot-Pound-Seconds}^2$$

$$J(\text{Beam}) = 48 \text{ Foot-Pound-Seconds}^2$$

$$T = (149 + 149 + 48) \text{ Foot-Pound-Seconds}^2 \times 10 \text{ Radians/Sec}^2$$

$$= 3{,}460 \text{ Foot-Pounds}$$

This torque is less than 4,200 foot-pounds and therefore can be supplied by the existing machine.

This example did not consider the time history of the shock pulse. A programmer must be used to establish pulse shapes and considerations must be made to dissipate the terminal velocity after the shock pulse. If this terminal velocity is high, the machine must be derated because of hydraulic damping of the fluid. The machine has run satisfactorily a 10 Radian/Second^2, 100 millisecond square wave shock test on a 72 foot-pound-second^2 test item.

In the application for which this machine was designed, a square wave pulse was required. The programmer consisted of a pulse actuated solenoid valve. An accumulator was installed just upstream of the valve, and the supply hoses to the cylinders were made as short as possible to minimize hydraulic damping. (See Figure 5.)

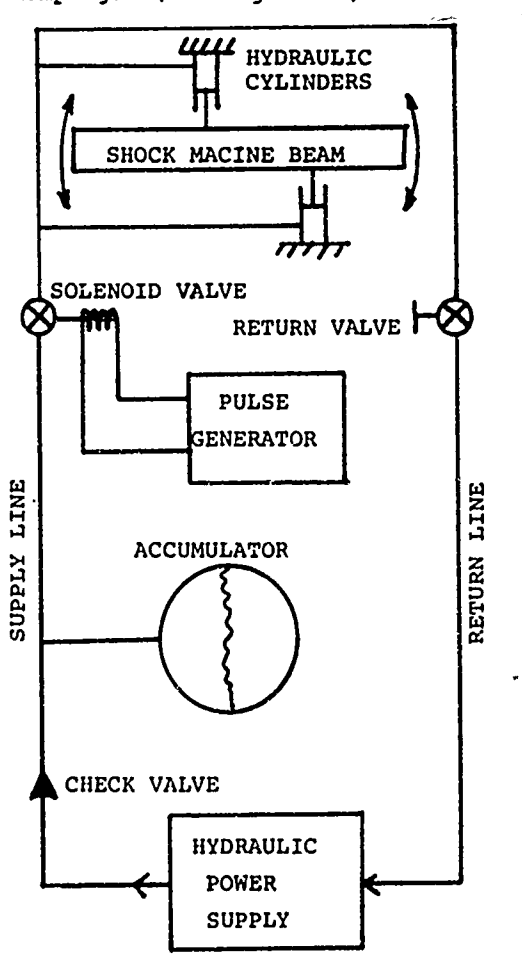

FIGURE 5
HYDRAULIC CIRCUIT

SHOCK AND VIBRATION SHAKER

A smaller machine was constructed to provide both rotational shock and rotational vibration up to 200 Hertz. The motive force for this machine is derived from a direct current torque motor. The particular motor used was a 15 horsepower, 28 volt, series wound, jet engine, starter motor.

The method of application is to excite only the motor field with 500 amps direct current and then provide a control signal to the armature. The shape of this control signal establishes the motion of the armature. This method is typical of linear shakers so a standard shaker amplifier can be used to supply the motor input currents. A control feedback loop can be closed around the motor with a standard linear vibration servo and a feedback transducer. Depending on the frequency range, both accelerometers and position sensors can be used.

Accelerometers mounted to sense circumferencial acceleration provide feedback between 5 and 200 Hertz and rotary potentiometers can be used below 10 Hertz. (See Figure 6.)

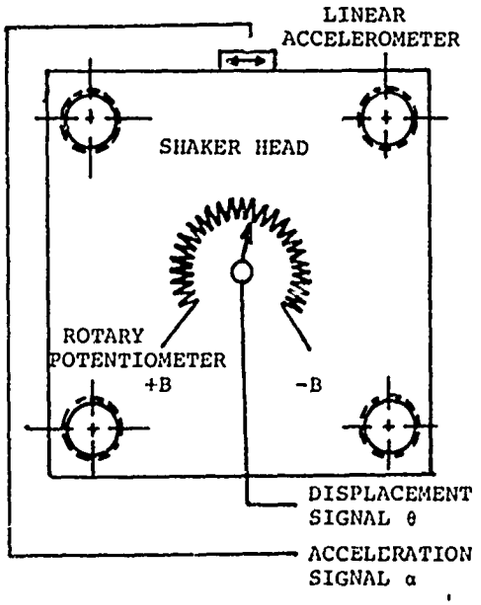

FIGURE 6
FEEDBACK SIGNALS

Several different size heads were evaluated on this machine. The largest head has a moment of inertia of 1.38 inch-pound-seconds^2. With an output shaft stiffness of 28 X 10^4 inch-pounds/radian, a first resonant frequency of 320 Hertz results. This resonance is at such a low frequency that it seriously contaminated the vibration wave shape. A smaller, 5-inch square head (shown in Figure 7) having a moment of inertia of 0.058 inch-pounds-seconds^2 resulted in a first resonant frequency of 460 Hertz.

FIGURE 7
ROTATIONAL SHAKER

This head greatly improved the wave shape. However, there still exist ranges of frequencies in which considerable contamination is present. The contamination exists at subharmonics where wave distortion excites the 460 Hertz resonance. The wave distortion arises primarily from bearing and brush noise.

The motor armature is supported by two ball bearings as shown in Figure 8. The table rests on a needle thrust bearing to resist overturning moments. Motor brushes transmit the armature current and shop air provides cooling.

The performance of this machine could be improved by the use on flexture mounting of the armature and flexible cables to carry armature current. However, this would restrict the angle through which the table may turn.

The machine's performance varies drastically as a function of frequency. At 500 Hertz, 6000 Radians/Second^2 is easily obtained. However, 400 Radian/Second^2 is a realistic rating over the design frequency range of 10 to 200 Hertz.

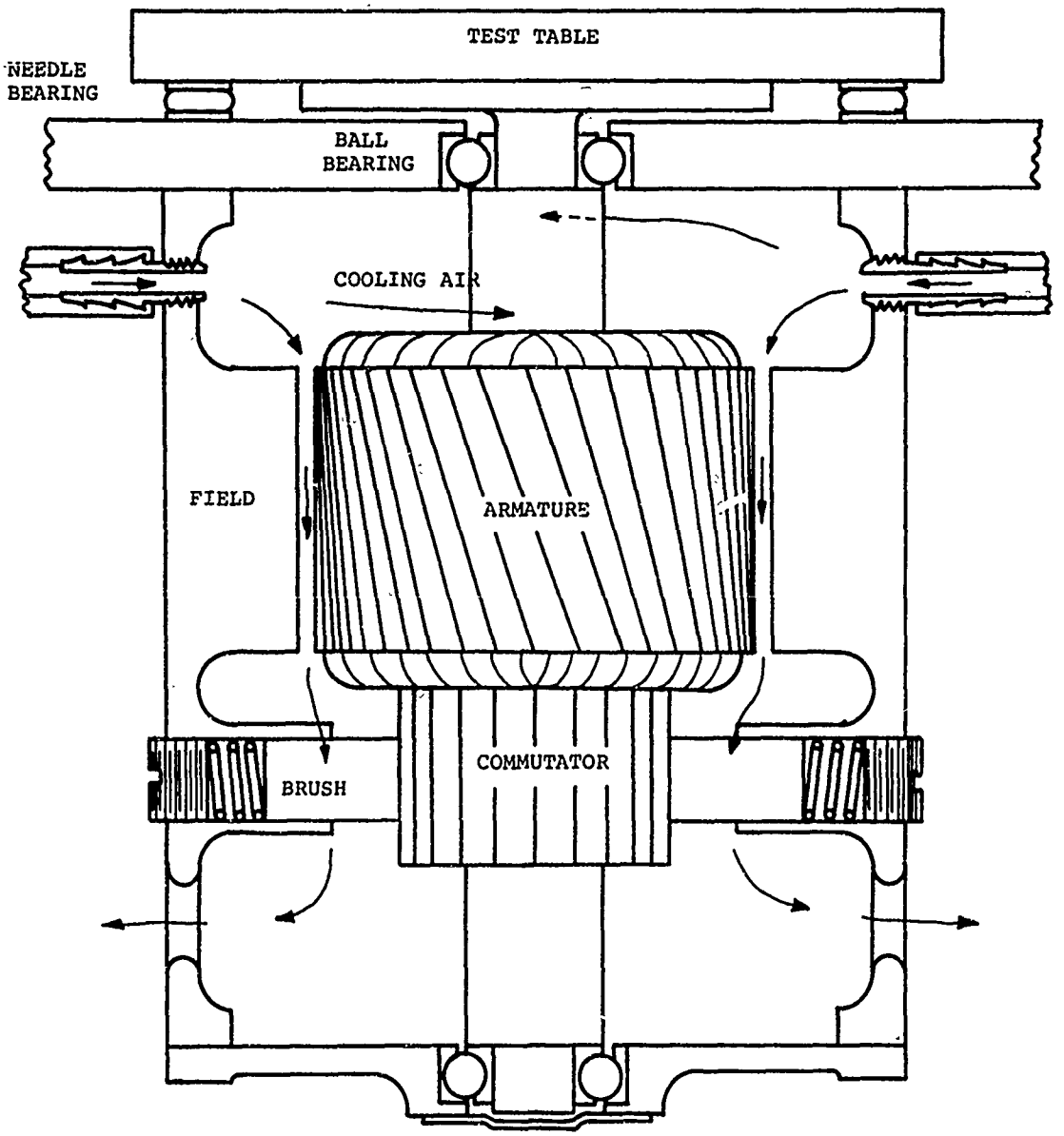

FIGURE 8

ROTATIONAL SHAKER CONSTRUCTION

CONCLUSIONS

The rotational shock and vibration facility described satisfactorily applies shocks to heavy, imbalanced loads and vibration to balanced loads. At present, square wave shocks, sinusoidal fatigue, random vibration and limited sinusoidal sweep testing is possible. A redesign of the armature mounting and motor brushes would allow more extensive sinusoidal testing.

THE EFFECTS OF VARIOUS PARAMETERS ON SPACECRAFT SEPARATION SHOCK

W. Brian Keegan and William F. Bangs
NASA, Goddard Space Flight Center
Greenbelt, Maryland

This paper presents the results of a series of 17 pyrotechnically actuated spacecraft separation tests conducted at the Goddard Space Flight Center. The prime objective of this test program was to evaluate the effects of varying the many parameters which might possibly influence the magnitudes of the induced transient responses.

The structure used was an exact replica of the IMP-I flight spacecraft hardware. The separation system components were also flight type. Transient acceleration response levels induced by the pyrotechnic firings were measured at the separation plane as well as at representative locations in the spacecraft. In all, 28 accelerometers were monitored during each of the 17 tests. Used as a baseline for all firings was the currently accepted Goddard method of performing pyrotechnic separation tests.

Parametric variations investigated included: Marmon clamp tension (50% to 150% of flight tension), attach fitting end condition (fixed or free), simulation of burned-out third stage (static with several weights, dynamic and none), number of squibs fired (one or two), and separation springs (with and without). Two test firings were made for most of the conditions investigated, so as to measure the variation in levels induced by identical tests.

All data reduction was performed using shock spectra techniques. Computations were made at one-fiftieth decade increments from 100 to 5,000 Hertz. The data analysis effort included a statistical analysis to determine the variance between multiple firings on identical configurations. This analysis is discussed in the paper along with an evaluation of the significance of each of the investigated parameters in influencing the induced shock transients.

INTRODUCTION

In recent years, the phenomenon of pyrotechnic shock has been studied with increasing interest. During this time the emphasis has shifted from considering a pyrotechnic firing as simply a functional test of a specific event to considering it as an environmental test of an entire system. With the adoption in 1969 of the GSFC General Environmental Test Specification, exposure to the worst-case pyrotechnic induced shock transient became an environmental test requirement for all Goddard managed spacecraft.

This specification defines the worst-case launch vehicle induced shock transient by enveloping the response to stage separation, shroud jettison, and other launch vehicle associated functions. The definition takes the form of a shock response spectrum at the

spacecraft/launch vehicle interface covering the bandwidth from 100 to 2,000 Hz for a specified damping coefficient. If it can be demonstrated that the shock spectrum due to the spacecraft separation transient envelopes the shock spectrum of launch vehicle inputs at all frequencies, then the spacecraft does not have to be exposed to a shock test for launch vehicle inputs since they are not the worst-case. When this is true, the shock test program of a spacecraft will consist of a live pyrotechnic separation test followed by firing the remainder of the spacecraft related pyrotechnic functions. If the spacecraft separation shock spectrum does not envelope the launch vehicle shock specification then the spacecraft test must include a launch vehicle shock test. Since live firings are impossible in these cases, a simulation on the electrodynamic shaker is required using the shock spectrum for controlling the input. Implementation of this shock test requirement has therefore resulted in two approaches: actual pyrotechnic firing and simulation of the transient on an electrodynamic shaker, with the former being the most usual method.

A number of questions have been raised since the inauguration of live pyrotechnic firings. Most of these have been directed toward the test configuration, i.e., the importance of attitude, method of support, simulation of the third stage weight, etc. In addition, there appeared to be a fairly basic shortcoming of the pyrotechnic test as an environmental simulation: there is no obvious way to increase levels by a predetermined increment or factor. At Goddard, where qualification testing is usually performed at levels 1.5 times those used for flight acceptance, this has caused serious concern. Thus when the opportunity arose to use representative spacecraft hardware to investigate some of the questions associated with pyrotechnic testing it was quickly decided to capitalize upon it.

A test program was then defined with the principal objectives of: (1) Establishing whether the present GSFC approach of conducting separation shock tests is satisfactory or whether perhaps some other method may be more desirable. The standard GSFC method of separation testing consists of suspending the spacecraft from above and pyrotechnically releasing the Marmon clamp, thereby allowing the attach fitting without separation springs and with no simulated launch vehicle stage to fall freely away from the spacecraft, and (2) Evaluating the relative importance of the explosive charge and the strain energy release in developing the measured transient response levels.

These objectives were accomplished by designing the test program to: (1) Measure the transient response induced at the spacecraft/attach fitting interface and throughout the test item structure by GSFC's presently accepted method of conducting separation shock tests, and (2) Measure the variations in the transient response levels induced by varying parameters such as the boundary conditions of the aft end of the attach fitting, the weight and dynamic characteristics of the simulated third stage, and the tension in the Marmon clamp.

TEST DESCRIPTION

The structure used for this test sequence was the Engineering Test Unit (ETU) for the Interplanetary Monitoring Platform (IMP)-I program. The IMP-I ETU had a structure identical to the IMP-I flight spacecraft and was equipped with a representative solar array and mass and inertia simulated components and experiments. It provided an ideal test item because of its similarity to most of the NASA Explorer class satellites. The separation system, including the spacecraft/launch vehicle attach fitting, separation springs, Marmon clamp, clamp bolts, and bolt cutters, were flight type hardware used with the standard Delta Launch Vehicle 18-inch diameter cylindrical attach fitting. The firing circuitry used was identical to that of the Delta Launch Vehicle. Both rigid and dynamic simulations of the burned-out Delta third-stage were used during the test program.

Transient acceleration response levels were measured at the spacecraft separation plane, at the base of the attach fitting, and at representative locations in the spacecraft, including the center tube (the primary structural element), the primary and secondary equipment mounting platforms, and the solar array. (See Figure 1)

During the course of the test program three different hardware configurations were employed. These were:

Configuration 1: Hard-Mounted Without Attach Fitting - For these tests the spacecraft was installed using the flight-type Marmon clamp on a rigid fixture which simulated the mounting flange of the forward end of the Delta attach fitting and the bolt cutters were installed. The base of the fixture was then tied to the lateral vibration table, essentially securing the

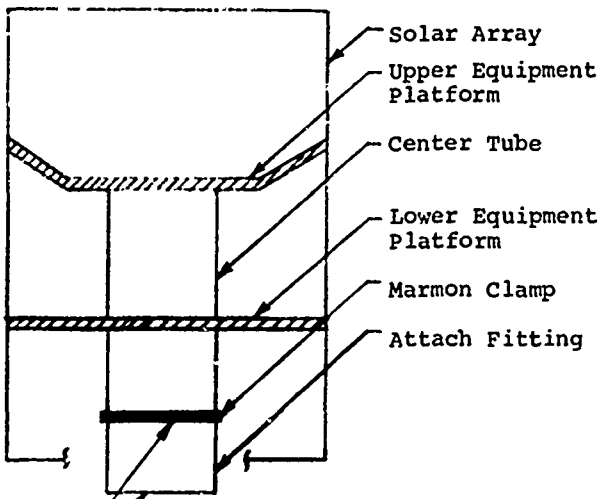

Lower Attach Fitting Plane: Spacecraft Hard Mounted Here for Configuration 2 Testing Simulated 3rd Stage (if any) attached here for Config. 3 testing

Separation Plane: Spacecraft Hard Mounted Here for Config. 1 Testing

(a) Elevation View of Spacecraft

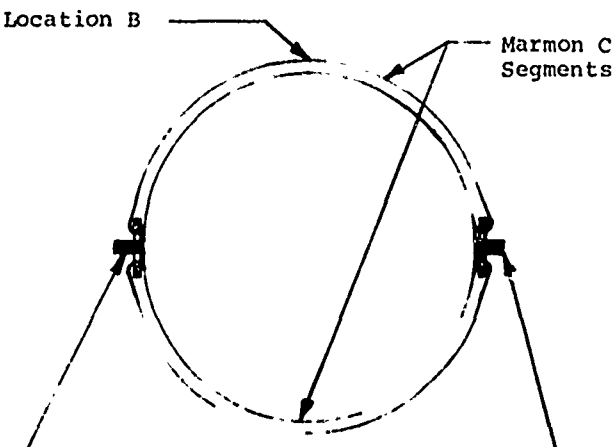

Location A: Bolt and Bolt Cutter #1

Location C: Bolt and Bolt Cutter #2

(b) Plan View of Separation Plane

Figure - tructural matic of Test Hard re

spacecraft to ground. For tests in this configuration the IMP-I lifting sling was attached to the spacecraft but did not support any weight.

Configuration 2: Hard-Mounted With Attach Fitting - For these tests the spacecraft was installed normally on the attach fitting with the bolt cutters installed. The base of the attach fitting was then tied to the lateral vibration table, thus essentially securing the attach fitting to ground. For tests in this configuration the IMP-I lifting sling was again attached to the spacecraft not supporting any weight.

Configuration 3: Suspended - For these tests the spacecraft was installed normally on the attach fitting with the bolt cutters installed. Attached to the bottom of the attach fitting was the desired simulation of the Delta third stage motor. This simulation consisted of either nothing at all, a rigid mass of varied weight, or a dynamic simulation. The entire assembly was then suspended from the IMP-I lifting sling over the center of a large platform. After detonation of the squibs, the attach fitting and simulated third stage was allowed to fall freely onto an aluminum honeycomb grid arrayed on the platform.

During the course of the test program it was sought to define the significance of each major parameter in contributing to the magnitude of the induced transient. Parameters such as the Marmon clamp tension, the attach fitting end condition, the burned-out third stage simulation, the number of squibs fired, and the separation springs were therefore varied over a range of practical conditions. Additionally, six conditions were performed twice in order to provide a measure of the variance of the induced shock levels for identical test conditions. In all, 17 separation tests were performed. Table I details each of the runs giving the magnitude or condition of each parameter.

For each, of the 17 firings, the hardware was arrayed in one of the three configurations described above, the parameters set to those defined in Table I, and the firing conducted while recording the output of all 28 accelerometers on magnetic tape with selected channels also displayed on high speed oscillograph.

Maximax shock spectra were computed for all channels for all runs over the frequency band from 100 to 5,000 Hz for a damping coefficient, c/c_c, equal to .05 (Q=10). In addition, all channels for two selected firings had shock response spectra computed for a damping coefficient, c/c_c, equal to 0.1 (Q=5) in order to permit assessment of the effects of damping. All data presented in this paper are in the form of shock response spectra computed for Q=10.

TEST RESULTS

Comparison of Test Data with Flight Data

The first action required during the data analysis was to determine the adequacy of the standard GSFC test configuration in duplicating the flight environment. Only limited data were available from flight on the separation system used in the test program, and the flight data which did exist were taken at the base of the attach fitting, ten inches below the shock source. The shock spectrum of this flight data was compared to the shock spectra obtained at the bottom of the attach fitting during the baseline firings, the baseline firings being those using the standard GSFC approach to shock separation testing (runs 5 and 6). These comparisons, presented in Figures 2a and 2b for the longitudinal and radial directions respectively, compare the one available flight data sample with the envelope of data obtained in the same location for the baseline firings. It can be seen that the flight data fall sufficiently well within the observed test envelope over the frequency range where comparison is possible. Above 2,000 Hz, comparison is prohibited because of limitations on the frequency response of the flight data. Data below 100 Hz are not considered in this report because it is obviously influenced by end conditions and is also sensitive to errors resulting from zero shift and noise.

Statistical Analysis

Having made the above determination, it was desired to evaluate the influence of the various parameters on the induced shock transient. A statistical treatment of the shock spectra was therefore undertaken to help quantify the scatter of the data and to identify the test parameters which produce statistically significant differences in the shock.

An examination of the data from the tests which were repeated indicated that scatter or random differences for identical test conditions was greater near the interface and on the adapter than on the spacecraft. This is probably due to the fact that the origin of the shock is not concentrated at a point

TABLE I

SHOCK SEPARATION TEST SCHEDULE

Firing No.	Configuration	No. of Squibs	Clamp Tension	3rd Stage Simulation	Separation Springs
1	1	2	2,000 pounds	None	No
2	1	2	2,000 pounds	None	No
3	2	2	2,000 pounds	None	No
4	2	2	2,000 pounds	None	No
5	3	2	2,000 pounds	None	No
6	3	2	2,000 pounds	None	No
7	3	2	2,000 pounds	Rigid (60 pound)	No
8	3	2	2,000 pounds	Rigid (130 pound)	No
9	3	2	2,000 pounds	Rigid (290 pound)	No
10	3	2	2,000 pounds	Dynamic (130 pound)	No
11	3	2	2,000 pounds	Dynamic (130 pound)	No
12	3	2	2,000 pounds	Rigid (130 pound)	Yes
13	3	2	1,000 pounds	None	No
14	3	2	3,000 pounds	None	No
15	3	1	2,000 pounds	None	No
16	3	1	2,000 pounds	None	No
17	3	2	3,000 pounds	None	No

NOTE: Firings 5 and 6 were the baseline firings.

but is distributed somewhat around the interface and at the bolts. This distribution is dependent on the strain energy and such things as frictional forces and the bolt tightening sequence which will vary from test to test even though controlled by procedural methods. Thus close to the sources, variations are expected while far away the levels are more a function of the average or integrated energy available.

Spacecraft accelerometer data were selected for statistical analysis because of the lower scatter and also because it is indeed more important, regarding the survival of the spacecraft, than levels near the interface. Four accelerometers, 10R, 12L, 13L and 14R, were chosen for detailed analysis. Two were radial and two were longitudinal. Two were on the equipment platform, one on the thrust tube, and one on the external shell structure.

The first task was to quantify the variability of the spectrum for the same test conditions. As shown in Table I, of the 17 separations only 6 test conditions were done more than once. Runs number 1, 3, 5, 10, 14 and 15 were repeated by number 2, 4, 6, 11, 17 and 16 respectively. No test condition was run more than twice. One set of data, from run 15, was not available at the time of this analysis. Thus to evaluate variability or repeatability, there were available data from only five pairs of tests, each different.

Ideally, repeatability could best be determined from a series of perhaps 10 identical tests. Because the determination of repeatability was not the primary purpose of this test program, the resulting experiment is less than ideal. Instead of a sample size of 10, we must be satisfied with 5 different samples of size 2. Since a sample size of 2 is of no practical value, it was necessary to effectively increase the sample size, even at the sacrifice of some rigor. The assumption was made that the variance of the spectral response, σ^2, at any frequency is a constant percentage of the true mean, μ, at that frequency. This assumption simply states that one expects the scatter of the data to be proportional to the average value of the data. This is reasonable for non-negative quantities such as shock response, since as

the mean approaches zero, the variance must also vanish.

The four accelerometers selected were studied for the five pairs of tests, at five frequencies 200, 500, 1,000, 2,000, and 5,000 Hz. For each test pair, at each frequency, the dimensionless deviation was calculated by dividing the usual deviation by the estimated mean:

$$\frac{| S_1 - \bar{S} |}{\bar{S}}$$

where S is the shock spectrum magnitude and $\bar{S}$ is the estimated mean. For a sample size of 2, this becomes

$$\frac{| S_1 - S_2 |}{S_1 + S_2}$$

where subscripts refer to the test number. Using the dimensionless deviation, and lumping the data from the five pairs of tests, we are able to extend the effective sample size from 2 to 5. This is done by calculating the estimated non-dimensional variance from

$$\sigma^2 = \frac{1}{n-1} \sum \left(\frac{S_a - S_b}{S_a + S_b} \right)^2$$

where n=5, the number of test pairs, and S_a and S_b are the spectral values for the two runs in a given pair.

The non-dimensional variance and its square root, the non-dimensional standard deviation, σ, were calculated for the four spacecraft locations and the five frequencies mentioned previously. The results are summarized in Table II.

The mean of these values is 0.138. Considering the uncertainties of the analysis and the lack of rigor, no attempt was made to test the σ values in Table II for frequency or location dependence. Based solely on intuitive judgment, it was decided to use the overall mean of σ for all data. Thus, the conclusion for this brief study may be stated as follows: The standard deviation for shock spectrum values for identical test conditions is approximately 13.8% of the spectrum value. This applies only to spacecraft locations and the frequency range of 200-5,000 Hz.

An assumption of normality was made to simplify the calculation of uncertainties and to make the hypothesis test stronger. This assumption was accepted based on the graphical comparison of the data with the Normal Distribution as shown in Figure 3.

When comparing two spectra from different test conditions, the value of the previous paragraphs may become evident. The question one asks when comparing spectra is are the differences statistically significant, implying a different population, or are they what one would reasonably expect from two elements of the same population. Since an estimate of the Standard Deviation is available and normality has been accepted, the concept of the "null hypothesis" can be applied in a straightforward manner.

When comparing two spectra, from different test conditions at some frequency, the null hypothesis states that there is no difference (other than random fluctuations) in the two spectra. A significance level, α, of 0.10 was

TABLE II

SHOCK SPECTRAL NON-DIMENSIONAL STANDARD DEVIATION (σ)

Location	Axis	Non-Dimensional Standard Deviation at 200 Hz	at 500 Hz	at 1,000 Hz	at 2,000 Hz	at 5,000 Hz
Center Tube	Radial	.118	.222	.146	.133	.121
Lower Equipt. Platform	Longitudinal	.129	.196	.126	.120	.193
Lower Equipt. Platform	Longitudinal	.117	.120	.064	.068	.069
Solar Array	Radial	.131	.119	.103	.399	.063

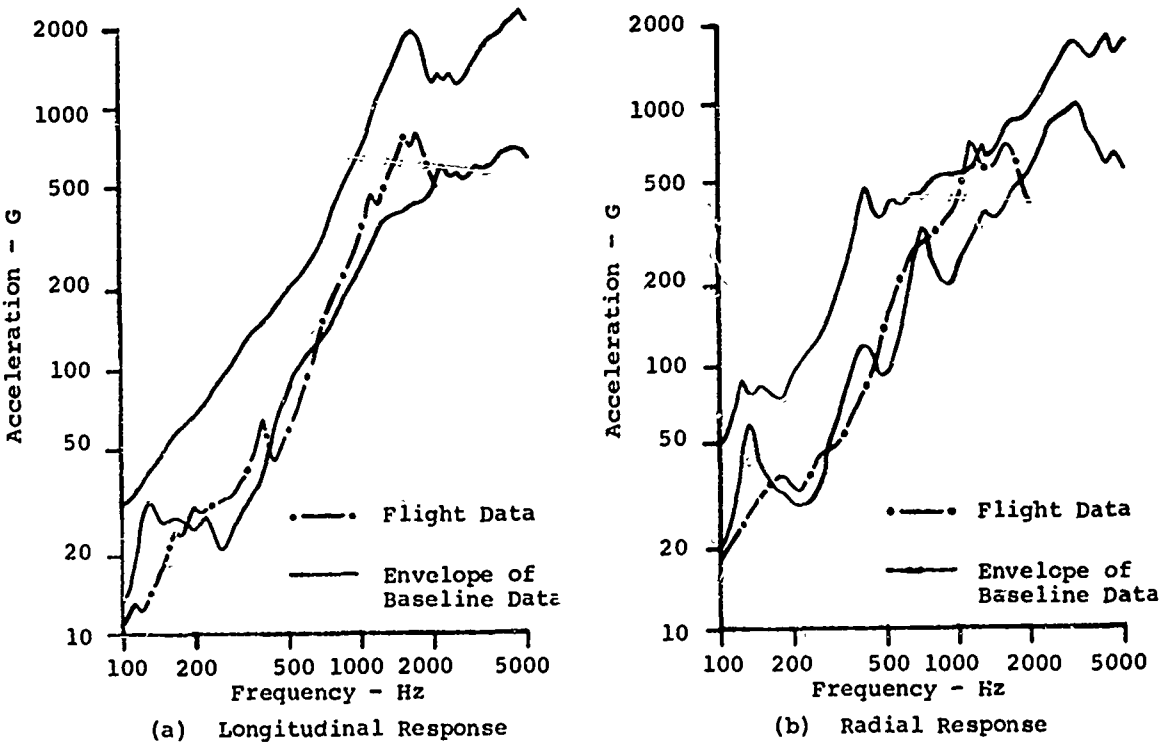

Figure 2 - Comparison of Flight and Test Data at Base of Attach Fitting

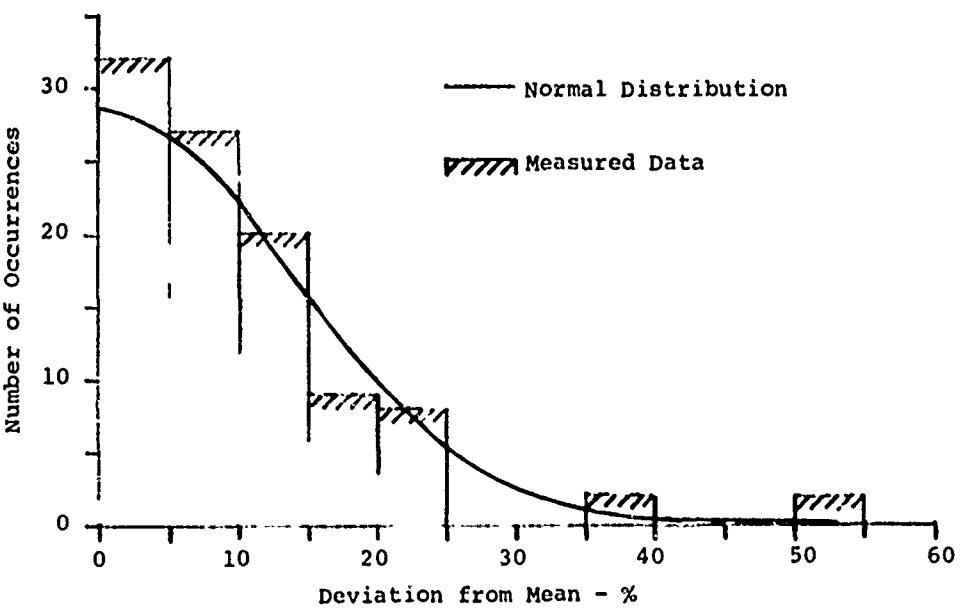

Figure 3 - Comparative Distribution of Measured Data and Normal Distribution

was selected since it seems appropriate not to adopt a "stiff" criteria for this data. As stated in Reference (1), α is a measure of one's reluctance to give up or "reject" the null hypothesis. It is, at the same time, a measure of the probability of rejecting the null hypothesis when it is true.

Spectra from the same population, when compared two at a time, will have differences which are normally distributed. The mean value of the differences will be zero and the Standard Deviation will be $\sqrt{2}$ times the Standard Deviation of each when they are approximately equal. This becomes 19.5 percent of the spectral value when the previous assumptions are considered. Using α = 0.10, we find from standard tables that a difference greater than 1.65 times 19.5 percent (that is, 32.2 percent) is cause for rejecting the null hypothesis when comparing two unique spectra, that is, when each spectrum is from firings whose configurations were not repeated.

When a pair of runs having the same configuration had been made, it was felt that the most meaningful evaluation would result from a comparison of the linearly averaged spectral value as a function of frequency. Two additional types of spectral comparison therefore arose: the comparison of two averaged spectra and the comparison of an averaged spectrum with a unique spectrum. For both of these, the rejection criteria is different from that above. Using α=.10 as above, in the case of the comparison of two averaged spectra the rejection value becomes 22.8 percent; and for the comparison of an averaged spectrum with a unique spectrum this rejection value becomes 27.6 percent. The phrase "outside the tolerance band" used throughout later sections of this report refers to the comparison spectrum being different from the baseline spectrum by more than the above percentages. The term refers only to the percentage difference between two spectra and the comparison spectrum may actually be greater than or less than the baseline spectrum.

These percentages were then used to determine if variation of the several parameters created a statistically significant variation in induced response. In order to produce a conclusion that a specific parameter had produced a change in the spectral response characteristics, the above percentages had to be equalled or exceeded over at least one-third of the spectral bandwidth for most of the spacecraft locations included in the comparison. Although data measured on the attach fitting is presented in this report and was considered in the evaluation of the effects of the parametric variations, it was the spacecraft locations on which emphasis was placed in drawing conclusions since there was more scatter in the data measured on the attach fitting and since it was principally the spacecraft locations where a measurement of the relative damage potential was desired.

Effects of Number of Squibs Fired

The standard Delta separation system uses two bolt cutters located 180 degrees apart (see Figure 1) to effect the release of the Marmon clamp and thereby permit separation. Satisfactory separation can be achieved if either one of the two squibs ignite. The effect of firing only one squib was evaluated during the test program by comparing the average spectrum of the two baseline firings (runs 5 & 6) with the spectrum from one of the two firings which used only one squib (run 16) but which was otherwise identical.

Comparisons from three channels at the separation plane are presented in Figure 4. Locations A and C (again see Figure 1) were at the squib locations, and Location B was 90 degress from each, approximately 15 inches from the two squib locations. For the firing using only one squib, Location A was at the squib location and Location C was 180 degrees away. An examination of Location A (see Figure 4a) shows a tendency for the single squib firing to shift the response spectrum so that you get higher magnitudes in the mid-frequency range (500 Hz to 2,000 Hz) and lower magnitudes in the high frequency range (above 2,000 Hz). Location B (see Figure 4b) does not show much difference between the baseline firings and the single-squib firings, whereas Location C (see Figure 4c) shows a definite trend toward lower spectral magnitudes over a large portion of the bandwidth. Accepting for the moment the assumption that the energy release of the squib itself only affects the response in the near field, then the data pattern seen at Locations A, B, and C can be rationally explained: Location A while experiencing a change in spectral distribution has nearly identical peak values and is not drastically affected by firing only one squib. It must be noted again that Location A was in the near field for both baseline and one squib firings. Location B meanwhile in the far field for both cases, is relatively unaffected by firing only one squib, and Location C shows a significant reduction since it has effectively been removed from the

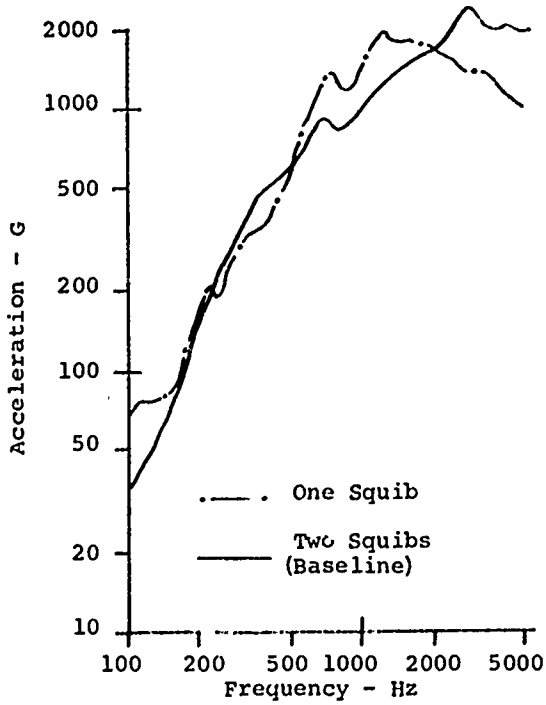

(a) Measurements at Location A

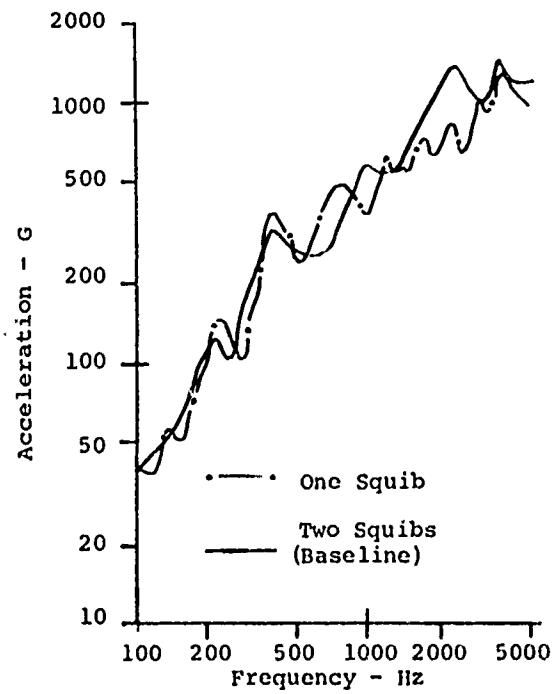

(b) Measurements at Location B

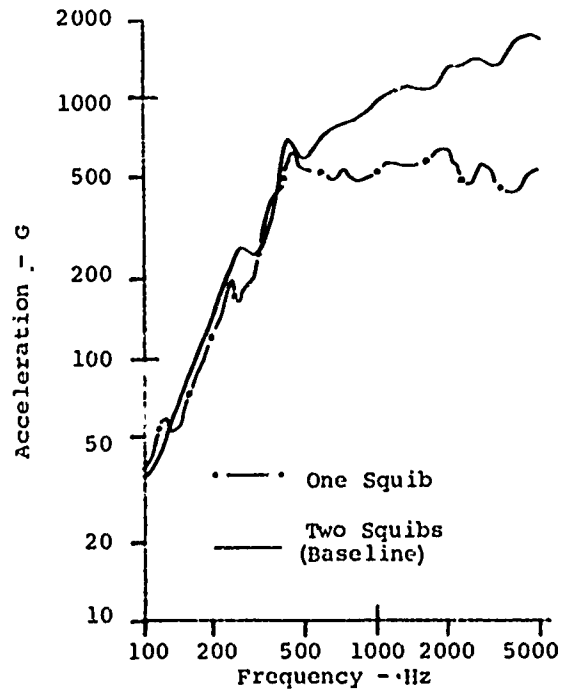

(c) Measurements at Location C

Figure 4 - Effect at Separation Plane of Firing One Squib

near field in the baseline firings to the far field during the single squib firings.

Comparisons from two representative spacecraft locations are presented in Figure 5. The data clearly show that firing only one squib has very little effect on the induced shock response spectrum throughout the spacecraft structure. On the average the spectrum from the one squib firing for six spacecraft locations is outside the tolerance band by only 27 percent of the bandwidth from 100 to 5,000 Hz, with this average being drastically influenced by one location which itself was outside the tolerance band for 83 percent of the bandwidth.

It is therefore concluded that firing only one of the two squibs has no significant effect on the induced response when the measured data are in the far field (approximately one foot or more from the source). Although no direct supportive data was taken during the test program, it is felt that the use of more explosive in the squibs (within some reasonable factor, such as two) would also not affect the induced far-field transient responses, although the area over which the near field effects are observed may be increased.

Effects of Marmon Clamp Tension

The standard Delta separation system uses 2,000 pounds tension in the Marmon clamp. The clamp, however, is designed for higher loads and higher tension could be used in test if for some reason it was desirable. The effects of Marmon clamp tension were evaluated during the test program by comparing the average spectrum of the two baseline firings with the spectra from two firings using 3,000 pounds tension in the Marmon clamp (runs 14 and 17) and the one firing using 1,000 pounds tension in the Marmon clamp (run 13).

Comparisons from two representative channels at the separation plane and two on the spacecraft structure are presented in Figures 6 and 7, respectively. Examination of this data, particularly that from the spacecraft locations, shows a definite trend towards increased shock spectral magnitudes at all frequencies with increased tension and decreased magnitudes with decreased tension. It will be noticed that the spectral shape remains very nearly the same, such that the effect of varying the tension merely shifts the entire spectrum up or down with the clamp tension. When compared to the baseline data, the spectra from six spacecraft locations for the high tension runs were outside the tolerance band for an average 61 percent of the total bandwidth. Similarly, data from the same six locations for the low tension run were outside the tolerance band for an average 82 percent of the bandwidth. It is therefore concluded that there is a definite relationship between Marmon clamp tension and induced transient response levels. Because of the limited data taken, no exact relationship can be determined as to the effect of tension on shock levels, but a best estimate from the available data shows the two to be directly proportional. It is recommended that further investigation be conducted into this specific aspect of the shock problem.

Effects of Mass Loading

In flight, at the time of spacecraft separation, the burned-out second or third stage of the Delta Launch Vehicle is attached to the aft end of the attach fitting; whereas, in the GSFC standard approach to shock separation tests, nothing is attached to the aft end of the attach fitting. The effects of various mass loadings were evaluated during the test program by comparing data from the baseline firings with a firing having a rigid plate equal to the burned-out weight of the TE-364-3 rocket motor attached to the aft end of the attach fitting (run 8) and two firings with a dynamic simulation (total weight and approximate modal density) of the TE-364-3 attached to the aft end of the attach fitting (runs 10 and 11).

Comparisons from two representative channels at the separation plane and two on the spacecraft structure are presented in Figures 8 and 9, respectively. Looking at the two separation plane locations, there appears to be a trend towards lower responses over a large percentage of the bandwidth when a third stage simulation is used, whether it be rigid or dynamic. When compared to the baseline data, data from four locations at the separation plane from the firing with the rigid mass is outside the tolerance band over an average 49 percent of the bandwidth while the dynamic mass data are outside the tolerance band over an average 40 percent of the bandwidth.

At the spacecraft locations, however, such a trend is not evident. Here data from six spacecraft locations showed that the firing with the rigid mass was outside the tolerance band over an average 22 percent of the bandwidth

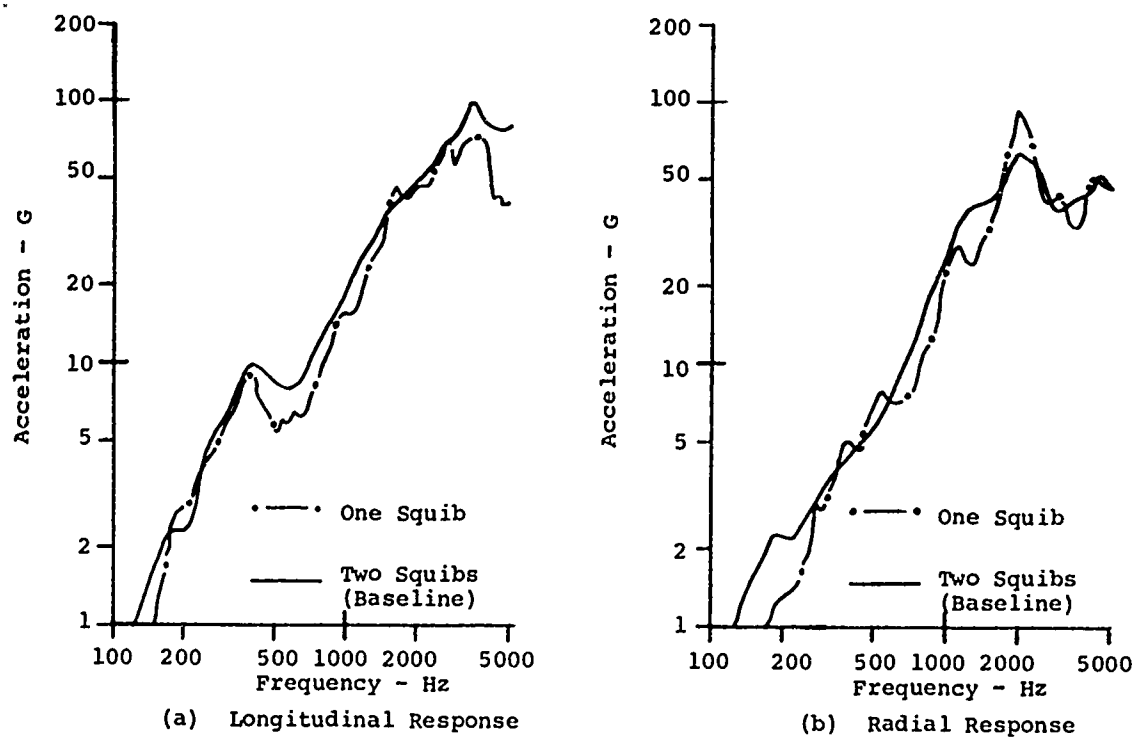

Figure 5 - Effect in Spacecraft of Firing One Squib

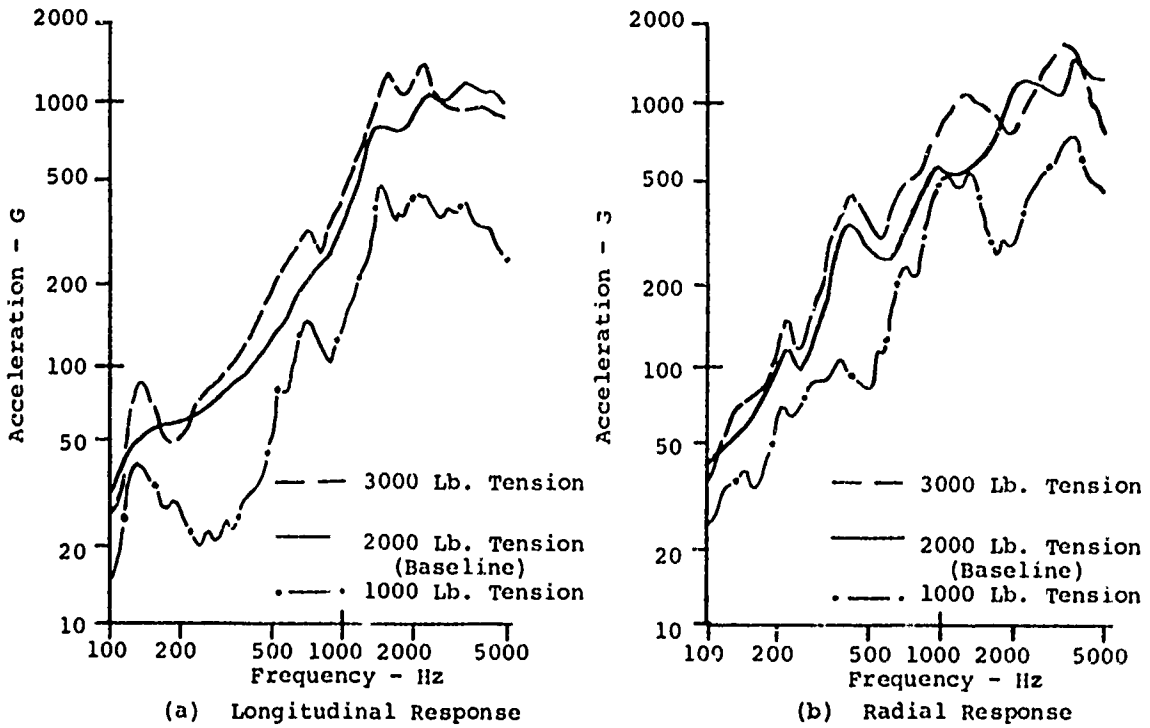

Figure 6 - Effect at Separation Plane of Marmon Clamp Tension

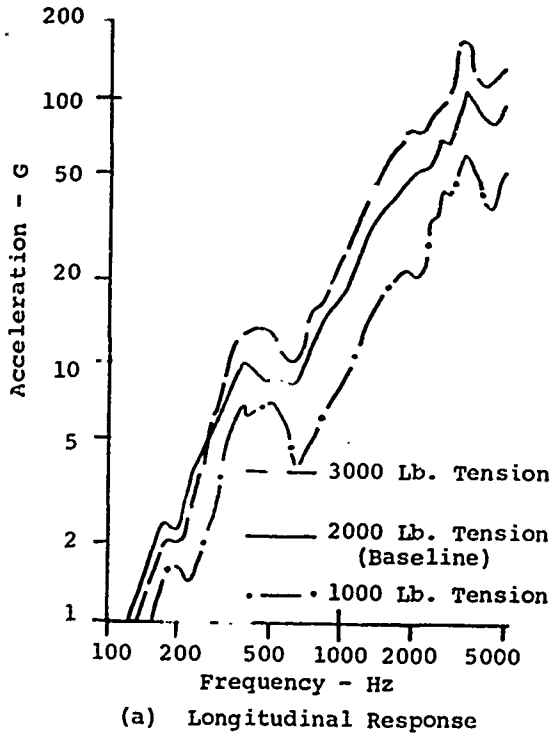

(a) Longitudinal Response

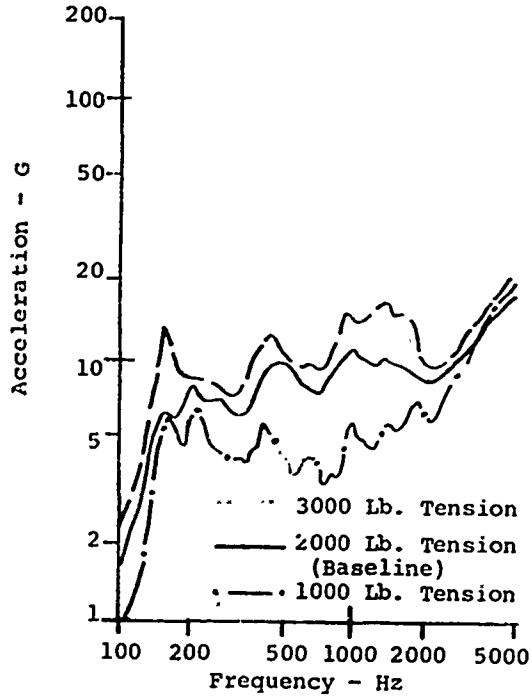

(b) Radial Response

Figure 7 - Effect in Spacecraft of Marmon Clamp Tension

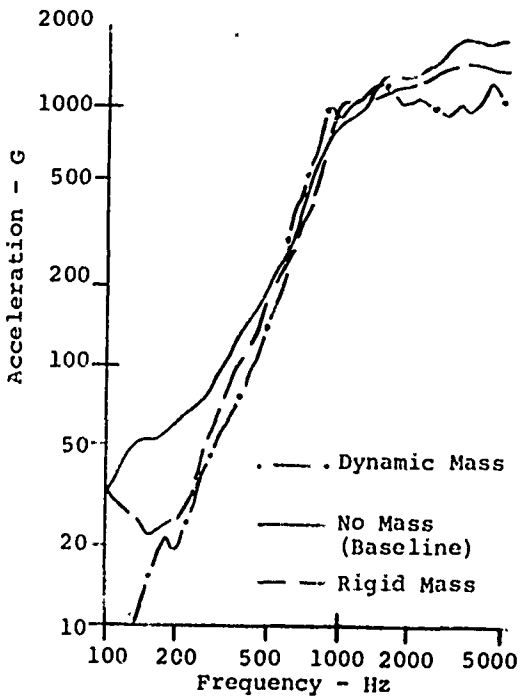

(a) Longitudinal Response

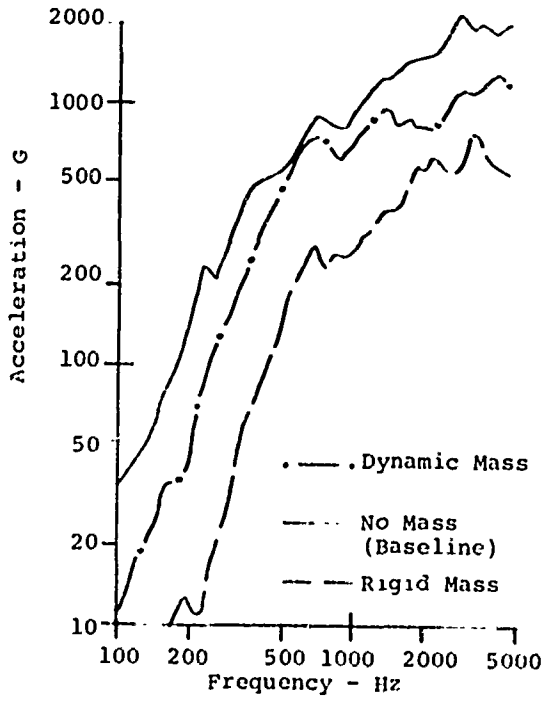

(b) Radial Response

Figure 8 - Effect at Separation Plane of Mass Loading

and the dynamic mass data were outside the tolerance band over an average 46 percent of the bandwidth. Here, though, the rigid and dynamic masses generate higher spectral levels at some frequencies and lower spectral levels at other frequencies; no preferred shift in spectral magnitude could be detected.

Since the spacecraft locations are of prime importance, it is therefore concluded that mass loading has no significant effect on the induced transient response.

It is felt, however, that if any other configuration is more representative for separation tests than that currently used, it would be one with some partial launch vehicle simulation, since it would be so much more like the flight configuration, but a positive recommendation cannot be made with the data available. A comparison of the data from the various mass loadings with flight data, particularly in the 2,000 to 5,000 Hz band would therefore be of great value; but unfortunately such a comparison cannot be made because of the limited flight data available.

Effects of End Conditions

As previously stated, the standard GSFC approach to shock separation testing involved suspending the spacecraft from above and allowing the attach fitting to fall freely away. From an operations standpoint, it would be easier to have the spacecraft attached to some base, thereby providing a more stable platform for the spacecraft and entirely eliminating the problem of catching the falling attach fitting. An evaluation of the effects of varying end conditions of the spacecraft was therefore made during the course of the program by comparing data from the baseline firings with data from two firings during which the spacecraft was mated directly to a rigid, mechanically grounded fixture by means of the Marmon clamp (runs 1 and 2), and two firings during which the attach fitting was bolted directly to a rigid mechanically grounded fixture (runs 3 and 4).

Comparison data for two representative separation plane locations are presented in Figure 10. Since data for the spacecraft rigid mount does not exist for these locations, the comparison is only between the baseline firings and the adapter rigid mount firings. Data from four separation plane locations for these runs with respect to the baseline runs were outside the tolerance band over an average 46 percent of the bandwidth and were characterized by a definite tendency to lower the spectral levels in the low and high frequency ranges while raising them in the middle frequency range (500 to 2,000 Hz).

Comparison data for two representative spacecraft locations are presented in Figure 11. The data from six spacecraft locations for the adapter rigid mount tests were outside the tolerance band with respect to the baseline firings over an average 36 percent of the bandwidth and again a definite trend can be observed towards higher spectral levels between 500 and 2,000 Hz, with lower levels at other frequencies. Data from the spacecraft rigid mount meanwhile were outside the tolerance band with respect to the baseline data over 73 percent of the bandwidth and showed a definite trend toward lower spectral levels at all frequencies.

It was therefore concluded that variation of the end conditions of the spacecraft have a definite effect on the induced transient response levels. It was further concluded that to change from the currently used free end condition during test would unrealistically lower the induced shock levels over a large portion of the frequency range and that the current test approach was correct.

Effects of Separation Springs

In flight the Delta separation system uses three springs to provide an initial separation velocity between the spacecraft and launch vehicle. The energy delivered by the springs after the Marmon clamp has been released is approximately 400 foot-pounds. If in test this energy were allowed to act on the attach fitting with no burned-out launch vehicle simulation the problem of catching the attach fitting without damage would be compounded immensely. Therefore, the separation tests at GSFC are conducted without the separation springs in place based on the assumption that they have no influence on the induced responses. The correctness of this assumption was evaluated during the test program by comparing data obtained during a firing using the separation springs (run 12) with data from an identical firing except for the fact that no separation springs were used (run 8). Neither of these firings were of the baseline configuration since both had a rigid weight equal to the burned-out Delta 3rd stage weight bolted to the base of the attach fitting.

Comparison data for two representative channels at the separation plane

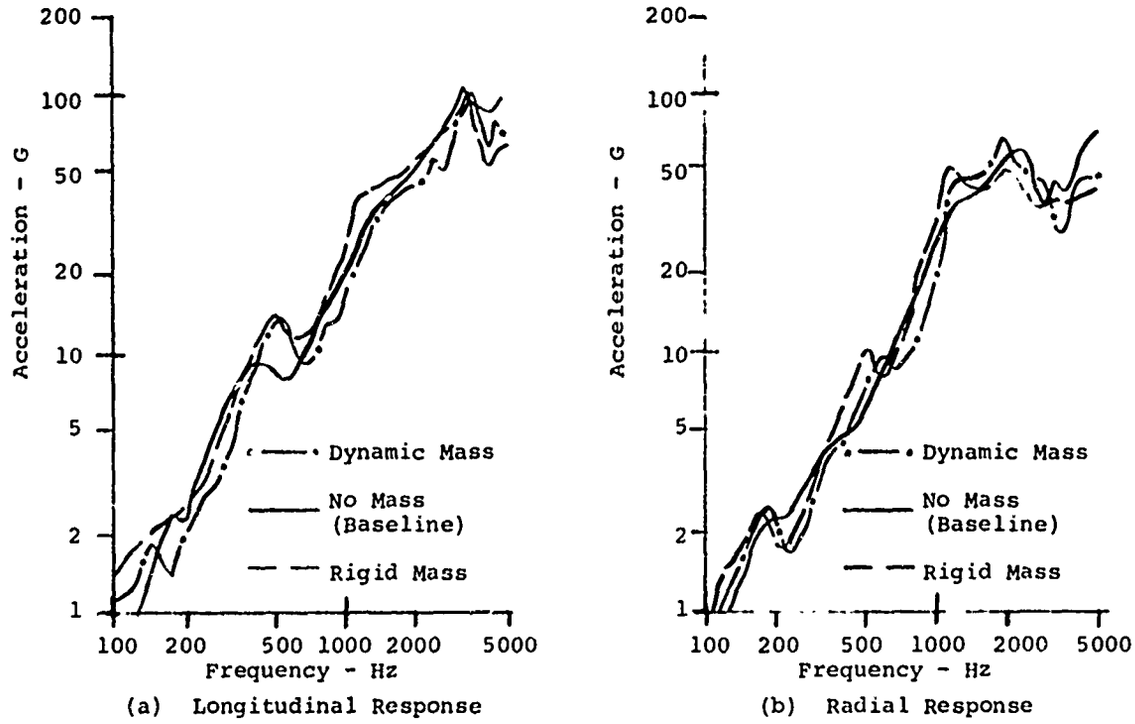

Figure 9 - Effect in Spacecraft of Mass Loading

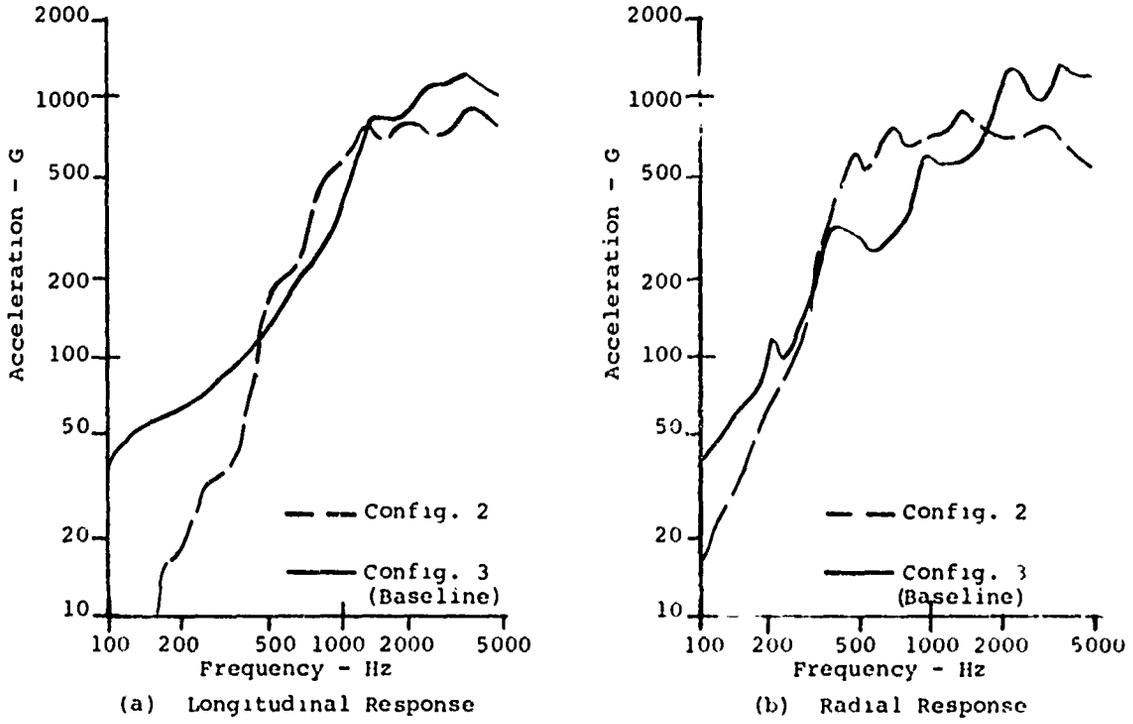

Figure 10 - Effect at Separation Plane of End Condition

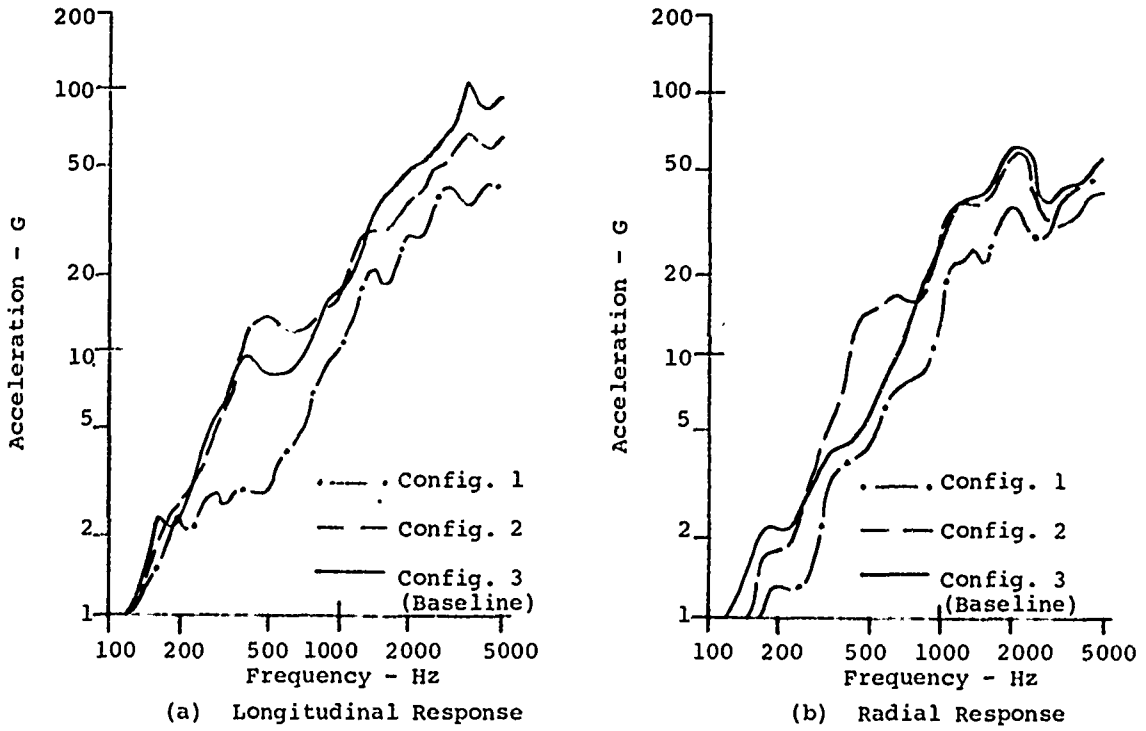

Figure 11 - Effect of spacecraft of End Condition

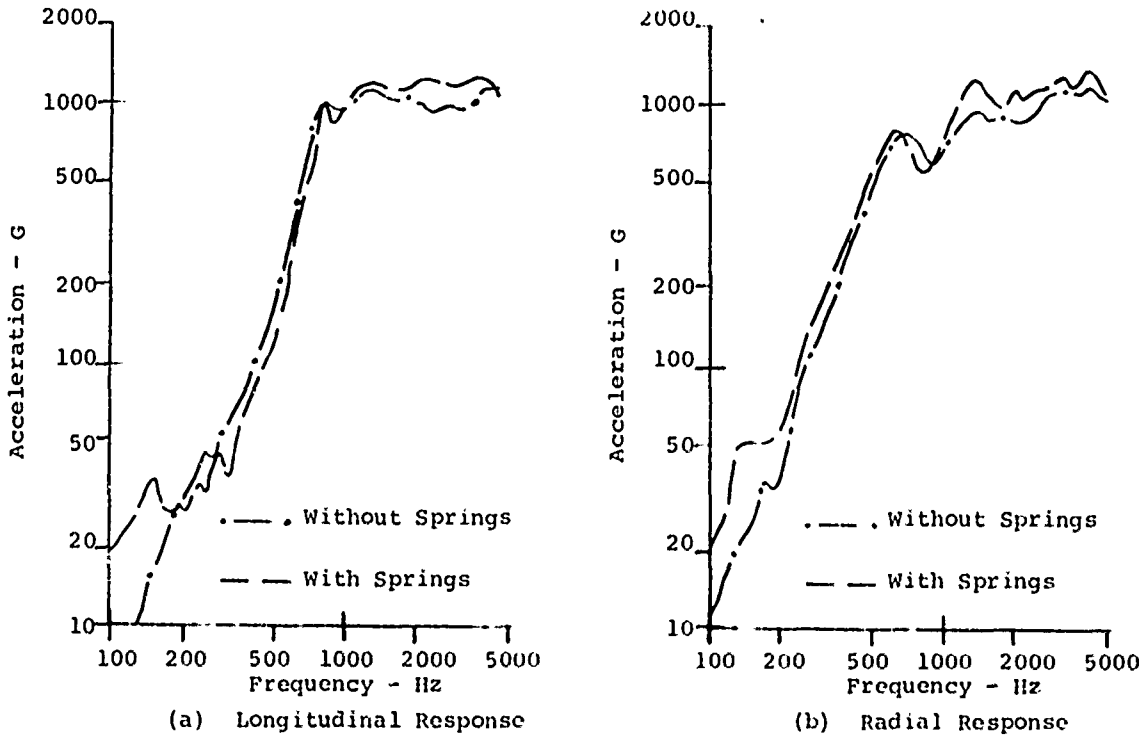

Figure 12 Effect of Separation of Separation Springs

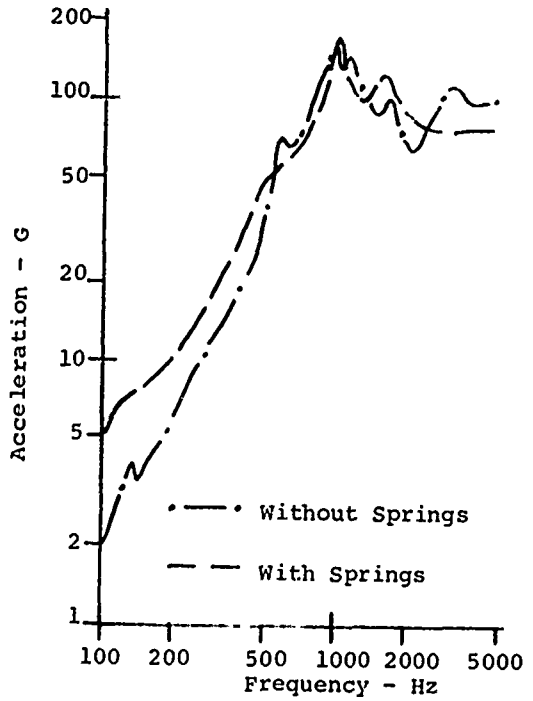

(a) Longitudinal Response

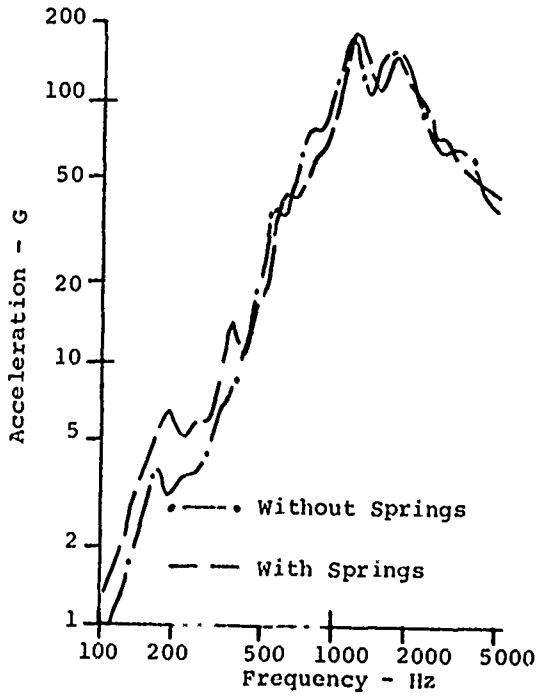

(b) Radial Response

Figure 13 - Effect in Spacecraft of Separation Springs

are presented in Figure 12. Data for four separation plane locations from the firing with separation springs were outside the tolerance band with respect to the data from the firing without the springs over an average of only 14 percent of the bandwidth with no trends being obvious as to shifts in the response magnitudes as a function of frequency.

Comparison data for two representative spacecraft channels is presented in Figure 13. Data from six spacecraft locations for the firing with springs were outside the tolerance band with respect to the data from the firing without the springs over an average of 34 percent of the bandwidth. No trends were obvious in this data either, with the increases and decreases in spectral magnitude randomly distributed from channel to channel and over the whole frequency range.

It was therefore concluded that the separation springs have little if any effect on the induced transient responses and that a shock separation test which does not use the separation springs is an acceptable simulation.

CONCLUSIONS AND RECOMMENDATIONS

Conclusions as to the effects of each parameter on the induced transient responses, although presented previously in separate sections of the paper, are repeated here. As a result of the parametric variation study it was concluded that:

1. Firing only one of the two squibs has no significant effect on the induced response when the measured data are in the far field (approximately one foot or more from the source). Although no direct supportive data were taken during the test program, it is felt that the use of more explosive in the squibs (within some reasonable factor, such as two) would also not affect the induced far-field transient responses, although the area over which the near field effects are observed may be increased,

2. There is a definite relationship between Marmon clamp tension and induced transient response levels. Because of the limited data taken, no exact relationship can be determined as to the effect of tension on shock levels, but a best estimate shows the two to be directly proportional,

3. The use of a third-stage simulation has no significant effect on the induced transient response,

4. Variation of the end conditions of the spacecraft has a definite effect on the induced transient response levels, and

5. The separation springs have little, if any, effect on the induced transient responses.

Consideration of the above in combination led to the following conclusions:

1. The GSFC standard method of shock separation testing as previously defined is an acceptable simulation and no changes are recommended as a result of data taken during this test program or as a result of comparisons with the limited flight data that are available, and

2. The principle source of induced transient responses throughout the spacecraft is the release of the strain energy in the Marmon clamp, with the explosive charge having an effect only in the near field.

Thus, the two principle objectives of the program have been satisfied.

As a result of this test program, it is recommended that future investigations into the shock problem consider that:

1. The need for flight data from pyrotechnic events in the 2,000 to 5,000 Hz band is evident and a program to increase the bank of flight data good to 5,000 Hz should be started, and

2. Increase of Marmon clamp tension seems to be the most promising area for investigation as to how to perform qualification level shock tests and a program to further investigate the specific aspects of this one parameter should prove fruitful.

REFERENCE

1. "Experimental Statistics" by M. G. Natrella, National Bureau of Standards Handbook 91, dated August 1, 1963.

DISCUSSION

Mr. Favour (Boeing Aerospace Group): On the last comparison, where you utilized the separation springs, it appeared that your overall shock spectrum level was lower by about an order of magnitude than on all previous tests. You showed peaks of around 200 g's response and all others were between one and 2,000 g's.

Mr. Keegan: No, the shock spectral data in this spacecraft were consistently matching at a little under 200 g's. The data taken at the separation plane characteristically peaked slightly below 2,000 g's; so the peak amplitude scale for spacecraft data on all of those slides was 200 g's, and for the separation plane data was 2,000 g's.

Mr. Favour: You talked about strain energy coupling into the structure. What about the acoustic coupling into the structure and the acoustic sensitivity of the accelerometers?

Mr. Keegan: To our knowledge there is an acoustic excitation of the accelerometer.

Mr. Favour: Did you have significant acoustic coupling into the structure?

Mr. Keegan: Perhaps that is true. What are you referring to? Wouldn't that be more of a comparison of flight data versus ground test data?

Mr. Favour: My main concern is, in connection with other possible simulation techniques, whether the acoustic coupling has to be accounted for so could it be assumed to be all mechanical?

Mr. Keegan: I am not sure. We only looked at the pyrotechnic method of testing in this study.

Mr. Trummel (Jet Propulsion Laboratory): Could you compare the effect of mounting the spacecraft on top of the lower adapter with suspending it? In other words, if there were no actual physical separation in the clamp fire? I ask because this is the way we run our tests.

Mr. Keegan: You mean just let the spacecraft sit and fire the clamp and allow the separation of cargo? We evaluated that and I must apologize though I do not remember the exact results.

Mr. Wada: (Jet Propulsion Laboratory): Why did you only go to 5,000 Hz on your shock spectrum curves?

Mr. Keegan: That was the highest frequency at which we could obtain reliable shock spectral computation at the digitizing rate that we had available to us.

Mr. Wada: Do you feel that the information above that frequency is pertinent in evaluating shock spectra or is it the limitation of the equipment?

Mr. Keegan: I am not really sure. I have seen shock spectrum data presented, some to 2,000 Hz, some to 5,000 Hz, and some to 10,000 Hz. The flight data which we have is good only to 2,000 Hz.

Mr. McClymonds (McDonnell Douglas Aeronautics Company): Why were the shock spectra measured during the test higher than those measured during flight? Did you introduce a factor of some sort?

Mr. Keegan: No, the only shock spectra that I showed from flight data were in the first data slide which compared the envelope of data that we took in the ground test with the flight sample that we had. I think that the flight data generally fell within the envelope of data observed in the ground test. Certainly the upper envelope of ground test data exceeded the flight data, but I think that the slide showed that the flight data fell within the envelope of the observed test data.

Mr. McClymonds: Do I also understand that at the Goddard Space Flight Center you do not introduce any 1.5 factor in your qual testing?

Mr. Keegan: Customarily we do not require it with live pyrotechnic firing simply because at the moment we have no known method of doing it.

NON-DESTRUCTIVE TESTING OF WEAPONS EFFECTS ON COMBAT AND LOGISTICAL VEHICLES

R. L. Johnson, J. H. Leete, J. D. O'Keefe
TRW Systems Group
Redondo Beach, California

and

A. N. Tedesco
Advanced Research Projects Agency, Department of Defense
Washington, D.C.

This paper gives an account of tests carried out to demonstrate the validity of a possible approach to simulating weapon secondary effects nondestructively. Secondary effects here refer to weapon induced shock and vibration, but excludes plastic deformation, penetration by shrapnel, etc. The technique employed is that of a sacrificial plate wherein sacrificial armor attached to combat vehicles is used to absorb the plastic deformation of a projectile at the same time permitting the application of the elastic secondary load to the vehicle structure. The first tests were carried out at TRW using small scale armor and 22 calibre projectiles. The second series was carried out by DOD personnel at the Aberdeen Proving Grounds using 20 mm and 57 mm projectiles impacting thick armor plate attached to a M60A1E1 turret. The results of both experiments indicate that the far field response due to direct impact on the vehicle armor can be reproduced by impact on the sacrificial plate.

INTRODUCTION

Combat and logistical vehicles, including tanks, armored personnel carriers, river patrol craft, self-propelled artillery, etc., suffer varying degrees of damage to their component parts as a result of enemy action using mines, artillery, and other heavy weapons. Not all such encounters result in a K kill. Frequently, the only damage incurred which degrades subsequent combat performance is the loss of function of mechanical, optical or electronic subsystems. These systems are particularly vulnerable to damage induced by weapon secondary effects, that is, the shock and vibration response of the vehicle induced by impact or blast. Today's combat vehicles rely more than ever on the performance of such subsystems.

Weapon secondary effects on combat and logistical vehicles can be determined by destructive testing, that is, tests whose integrated effect is to destroy the vehicle. The environment so determined can then be used to formulate specifications for the qualification testing of subsystems and their components. This approach is costly in terms of vehicles, and is not always practical because of schedule and availability of prototype test vehicles.

In many cases it might be possible to simulate weapon secondary effects (shock, vibration) nondestructively to obtain results at lower cost, with more safety, and more expeditiously. For example, the shock load on a tank component mounted at some distance from the impact point of an AP projectile is determined largely by the elastic response of the structure away from the impact site. Since the plastic stress waves generated by the impact are dissipated in the near field, one method of simulating this event is to reproduce the nonlinear near field effects exactly and transmit the linear far field effects using a piece of sacrificial armor to absorb the impact. Thus the same shock environment might be generated by a projectile impacting a plate of sacrificial armor attached to the vehicle armor at the same point. The plastic deformation is absorbed by the sacrificial plate which imparts elastic waves to the tank armor. In this way a shock loading equivalent to that experienced when a projectile impacts the armor might be generated.

The validity of this approach has been experimentally investigated, first at TRW using a 3 ft by 3 ft, .4-in. thick, hard steel plate and a .22 calibre projectile and later in an M60A1E1 turret at the Aberdeen Proving Grounds

using 20 mm and 57 mm projectiles and much thicker plate. An account of these experiments is given below.

ARMOR PLATE IMPACT TESTS USING SMALL CALIBRE PROJECTILES

The TRW laboratory test employed a three-foot square, hard steel plate (350 Brinell), .4 in. thick. The faces of the plate were ground smooth and parallel. For a sacrificial plate, a three-inch square, 3/8-in. thick, plate of softer steel was selected. The sacrificial plate was fastened with four screws to the test plate as shown in Figure 1. A thin layer of silicone grease was included between the plates to ensure good momentum transfer at their interface.

Fig. 1 - Sacrificial plate mounted on test plate prior to testing with a projectile impact

The projectile used to impact the plates was specially constructed. The projectile was composed of a solid steel cylinder .171 inches in diameter and 1.050 inches long, jacketed with copper to bring the total diameter to .222 in. and the total length to 1.100 inches. The steel core was machined from drill-rod stock. Although the geometry of this projectile is not similar to those commonly used, the relative weights of the copper jacket and the steel core are in the same proportion as that of the jacket and penetrator of a 50 calibre AP projectile. The bullet was fired from a modified AR-15 rifle loaded to produce a velocity at impact of approximately 2200 feet per second.

To measure the response of the test plate to the bullet impact, both accelerometer and strain gage instrumentation were employed. Figure 2 shows the positions on the plate of four accelerometers, four strain gages and the point of impact of the bullet. Endevco Model 2225 shock accelerometers, having nominal resonant frequencies of 80 KHz, provided linear response for frequencies up to 20 KHz and accelerations up to 20,000 g's. The signals from the accelerometers were conditioned and then displayed and photographed on CRT oscilloscopes. The oscilloscope sweeps of these traces were delayed to allow for the time interval between the time the projectile broke a current carrying trigger wire and the time the stress waves caused by the impact first reached the accelerometers.

For strain gage instrumentation two sets of semiconductor gages were used. The foil gages were employed at Stations 1 and 3 while the semiconductor gages were located at Stations 2 and 4. Stations 2 and 3 were the same distance from the bullet impact to provide a means for comparison of the response of the two types of gages. The foil gages were less sensitive than the semiconductor gages. However, the foil gages were mounted on a thin epoxy base while the semiconductor gages were mounted on a thicker phenolic base. The foil gages seemed to provide a higher frequency response than the semiconductor gages, possibly due to their more intimate contact with the test plate surface. At each station identical gages were mounted on both sides of the plate, at opposing points, and connected in a bridge circuit in an anti-symmetric manner, so that each station measured essentially the bending strains of the plate.

The signals from the strain gage stations were amplified by broad band amplifiers and displayed and photographed on CRT oscilloscopes. The sweeps of the oscilloscope traces were delayed an appropriate amount of time after the interruption of current in the break wire trigger.

The velocity of the projectile prior to impact was measured for each test by interrupting current in two additional breakwires spaced 10 inches apart. The time interval between the signals from the breakwires was measured on an electronic counter, providing a time interval resolution of about 1 part in 300. Figure 3 is a photograph showing the experimental setup ready for a test. The breakwires are mounted at the ends of the 10-inch plexiglas cylinder. The AR-15 rifle was mounted 40 inches above the test plate. The test plate itself was placed in a wooden enclosure, spaced a short distance from the plate, made of four layers of 3/4-inch plywood. The bullets passed through a small hole in the enclosure. Fragments from the bullet after impact were absorbed in the layers of wood surrounding the plate.

After preliminary shots to scale the instrumentation, two impacts were performed to obtain data. The first was with the sacrificial plate mounted in place and the second without the sacrificial plate. Figures 4 and 5 show close-up photographs of the impacted areas after each test.

The initial portion of the accelerometer signals have been plotted so that they appear on the same time and amplitude scale in Figure 6.

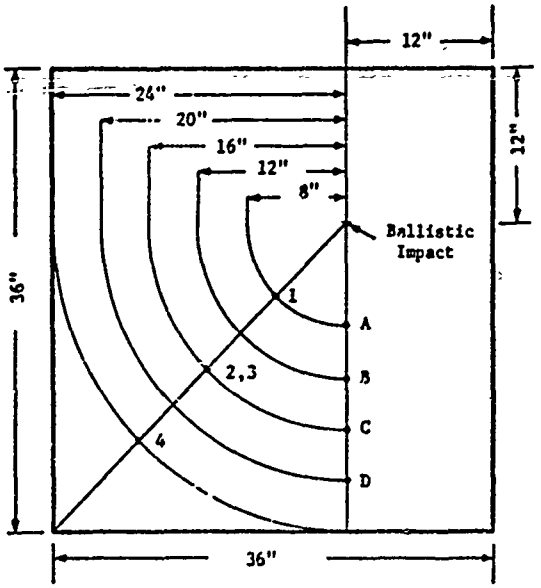

Fig. 2 - Diagram of instrumented test plate showing the point of impact of the bullet and the positions of the accelerometer stations (letters) and the strain gage stations (numbers)

Fig. 4 - Close-up photograph of the sacrificial plate after the first test

Fig. 3 - View of the experimental setup showing the AR-15 Rifle (top, center), the foil breakwires, the electronic timer and the enclosure surrounding the test plate

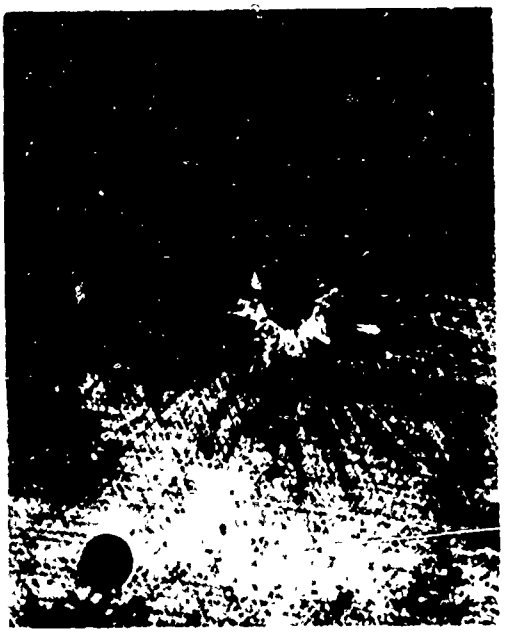

Fig. 5 - Close-up photograph of the test plate after direct impact by the bullet in the second test. The four holes surrounding the impact point are those used to mount the sacrificial plate for the first test.

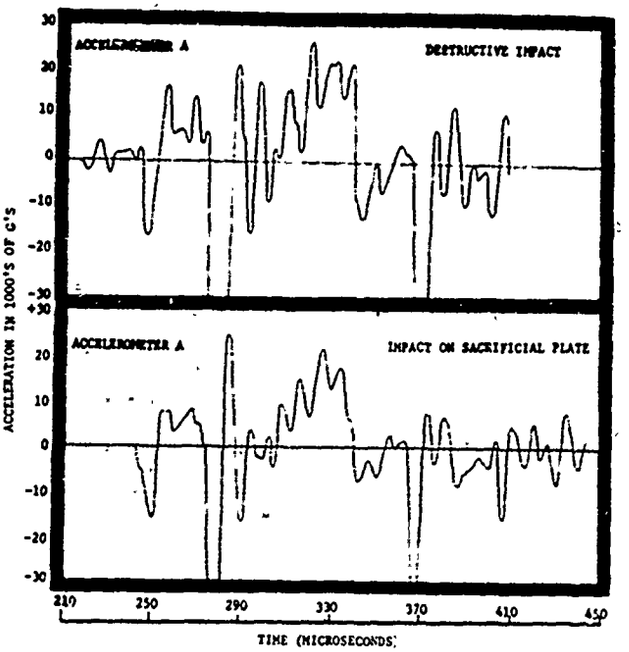

Fig. 6 - Ballistic Impact Experiment Accelerometer Traces

Two traces are shown. The first trace is the signal from accelerometer A (see Figure 2) when the plate was impacted without a sacrificial plate (impact No. 2). The second trace is the signal from the same accelerometer for the impact with a sacrificial plate (impact No. 1). Comparison of these traces demonstrates that the response of the plate to the two impacts is identical except in small detail, thus demonstrating the feasibility of the sacrificial plate approach for nondestructive loading of a structure. The acceleration histories contain information only in a relative sense because resonant response has been excited in each accelerometer. Their resonant frequencies vary from about 91 KHz (accelerometer B) to 120 KHz (accelerometer C). The fundamental period of response, measured where the first two traces go off scale, is 0.108 milliseconds, corresponding to a frequency of 9.260 KHz. The acceleration histories continue in the same manner beyond the 0.2 millisecond time duration shown in Figure 6, decaying to zero in approximately 10 milliseconds. The only comment that can be made about the acceleration signals in an absolute sense is that the accelerations are severe. The oscilloscope traces for accelerometer A went off scale at 60,000 g's for both impacts, well beyond the 20,000 g linear response range of these transducers. It is apparent that even state-of-the-art shock accelerometers would be inadequate for measuring accelerations in the vicinity of the impact point because their fundamental resonance would be excited. Since the output signal of a resonating accelerometer is a nonlinear function of the actual accelerations, the accelerometer output is not a unique function of the acceleration input and information about the environment is lost.

Photographs of the recorded strain gage signals are shown in Figures 7 and 8. Results are shown for strain gage Stations 2 and 3 for both tests. The signal from Station 1 was lost for Test No. 2; hence neither is shown. The difference in appearance of the signals between Stations 2 and 3 is due to the type of gage employed there. Station 3 employed foil strain gages while Station 2 employed semiconductor strain gages. It is thought that the greater high frequency content of the signals for Station 3 is the result of a more intimate contact of the gage with the test plate than that for the semiconductor gages at Station 2.

The signals from Station 2 (Figures 7 and 8) for both shots may be compared directly. Except for a broader line width caused by the higher amplitude high frequency content for Test No. 2, the two signals appear almost exactly equivalent. Comparison of the signals from Station 3 reveals a greater high frequency content (above 150 KHz) by about a factor of two for the direct impact (Test No. 2). The same relation is also approximately indicated by the relative line widths of the traces from Station 2 for the two tests.

In summary, the above comparison (between Test No. 1 to Test No. 2) of the strain gage measurements show the validity of the sacrificial plate nondestructive loading method, as did the accelerometer measurements, for response

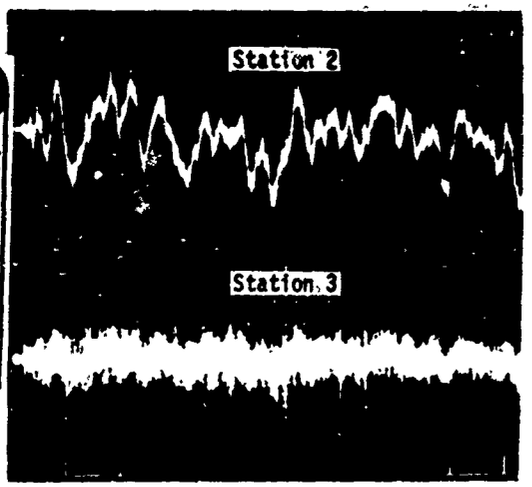

Fig. 7 - Strain gage signals from Stations 2 and 3 for Test No. 1 (sacrificial plate impact). Both sweeps were at 200 microseconds per division and were delayed 240 microseconds from the breakwire trigger. The vertical scales were 240 microstrain per division for Station 2 and 1500 microstrain per division for Station 3.

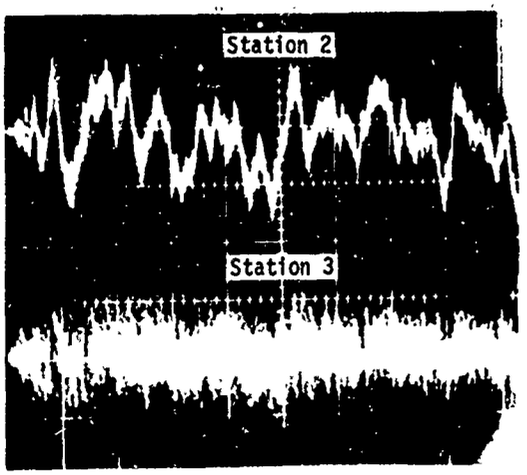

Fig. 8 - Strain gage signals from Stations 2 and 3 for Test No. 2 (direct impact). Sweep rates, delays and vertical scales remained the same as for Figure 7.

frequencies below about 100 KHz. These frequencies correspond to the flexural modes of the plate. The importance of this result is evident; it provides the basis for a nondestructive testing technique utilizing the vehicle as the test bed.

IMPACT ON THE M60A1E1 TURRET USING HIGH ENERGY PROJECTILES

Although the results of the above experiments indicate that the far field (well away from the impact point) response is very similar with and without the sacrificial plate, the tests were with low energy projectiles and light armor. Additional tests using large scale armor and projectiles were clearly necessary. These tests were performed at the Army's Aberdeen Proving Grounds by DOD personnel.

An M60A1E1 turret, in undamaged condition, was selected for the tests. This type of turret has several advantages as a test object for this program. The sides of the turret have a large area of plane, nearly vertical surface, making it easy to obtain close to normal impact. The armor at this point is several inches thick. Finally, the armor is of the homogenous type, eliminating complexities which would be associated with composite plates.

Projectiles selected for impact were 20 mm and 57 mm AP. The selection of these two projectiles was made to obtain a large range in the projectile energy; at the same time the calibre was small enough to permit accurate control and care and economy of testing.

Figure 9 is a photograph of the test setup prior to firing taken from behind the gun. The M60A1E1 turret was mounted on the chassis for convenience. The sacrificial armor plates can be seen attached to the turret. Velocity rings were for measuring the projectile velocity. The sacrificial plates were attached to the turret by welding along the edge. The turret was ground fairly flat so that the plates would fit flush. A silicon compound was applied to the turret before applying the plates to insure uniform momentum coupling.

Figure 10 is a schematic of the M60A1E1 turret as seen from the top. The figure shows the position of the instrumentation mounts relative to the sacrificial plates. Instrumentation consisted of 6 accelerometers mounted on brackets in the interior of the far side of the turret, 6 accelerometers mounted on the interior of the roof, and 6 accelerometers and 4 strain gages mounted on the turret wall in the vicinity of the target plate. Two additional strain gages were mounted on the bracket mounts on the opposite side of the turret. Figure 11 is a photograph of the rear bracket strain gage mount with 3 Endevco gages attached to measure the longitudinal, vertical and transverse components of acceleration.

A total of 12 (20 mm) and 16 (57 mm) rounds were fired. Of these 6 (20 mm) and 8 (57 mm)

Fig. 9 - Test setup - Aberdeen Proving Grounds showing sacrificial plates on M60A1E1 turret

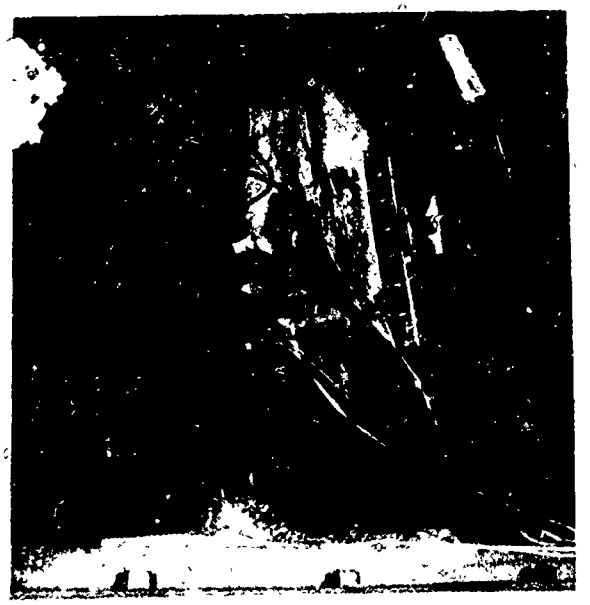

Fig. 11 - Rear bracket accelerometer mount and accelerometers

rounds were data rounds fired either into the sacrificial plate or the turret wall. The remainder of the shots were warmers. There is insufficient space here to present all the data; instead we present selected results of one round with the 57 mm into the plate and the identical round fired into the turret and a similar record of 2 (20 mm) rounds.

Figure 12 shows plate A after impacting with 2 (57 mm) and 2 (20 mm) rounds. Figure 13 shows the turret after the removal of plate C and impact by 2 (57 mm) rounds.

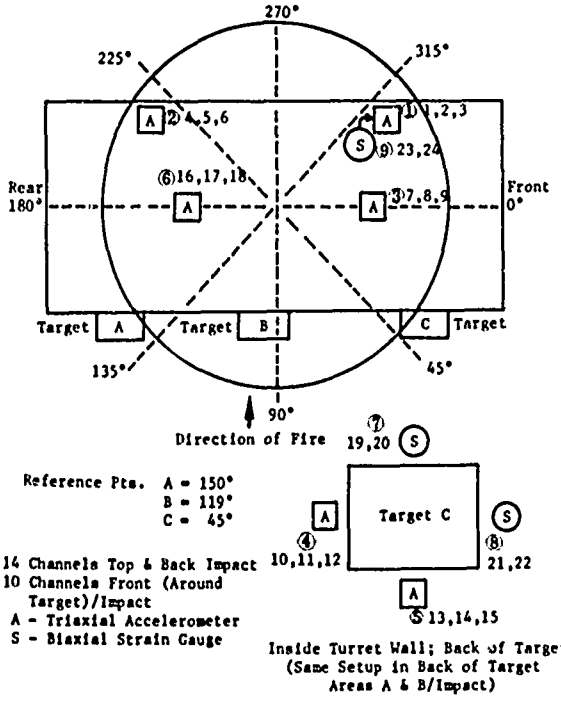

Fig. 10 - M60A1E1 turret schematic showing position of instrumentation relative to the sacrificial plates

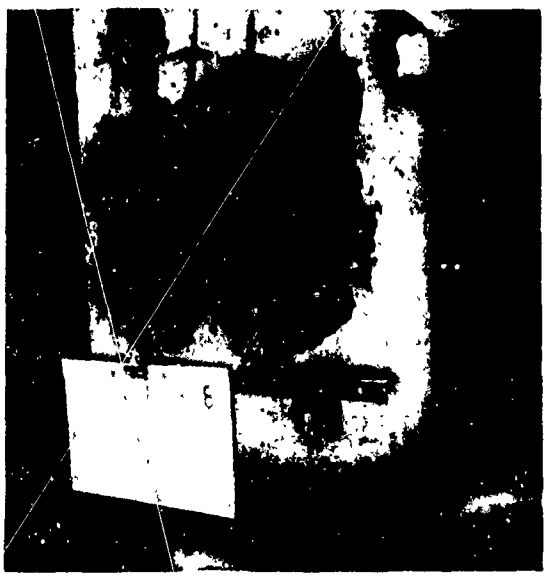

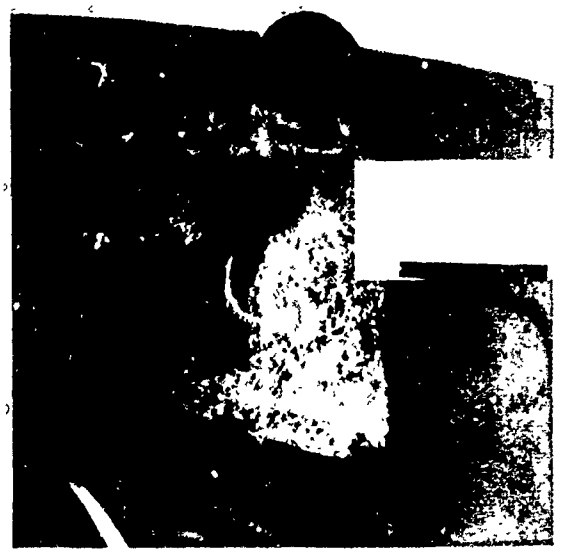

Fig. 13 - Area after removal of Plate C and impact by 2 (57 mm) rounds

Data from each impact consists of accelerometer traces from each of 24 channels. The data was reduced to form shock spectra and Fourier spectra of the response.

The resulting Fourier spectra for three data channels are compared in Figure 14 which gives the data reduced from three accelerometer traces for round 11, plate on, and round 14, plate off. The accelerometer traces used were from channels 1-3 located on the front bracket, far side of the turret from impact. The left column shows the results for round 11, the right - those for round 14. As can be seen, there is a general, if not precise, similarity between the spectra for impact on the plate with those of impact on the turret. The peak amplitudes are nearly identical except for the case of longitudinal acceleration where those for plate impact are somewhat lower. The behavior of the curves on the high frequency end of the spectrum is quite similar in all cases. In this regard note the general increase in transverse amplitude beyond 1000 Hz for both traces.

Strain gage traces for two 20 mm rounds are shown in Figure 15 along with their Fourier spectrum amplitudes. This particular gage was positioned on the interior turret wall just below the target plate and was mounted to measure the horizontal component of strain. The strain gage position was about one foot removed from the impact point in the transverse direction. Again, the Fourier amplitudes show a general similarity of form if not exact numerical agreement. The results for this data channel are typical of most of the 24 channels used. Several channels, however, showed instrumentation malfunction (amplifier saturation and d.c. drift) possibly due to the rather long (several days) delay between the 20 mm rounds into the sacrificial plates and those into the turret. Round 1 data was into plate B, round 15 data was with plate B removed. The impact location was nearly identical for the two rounds. No pronounced difference in response amplitude appears although one round was fired into a sacrificial plate of nearly 12 inch thickness; the other directly into the turret wall.

CONCLUSION

The results cited above indicate that the response obtained when impact loading through a sacrificial plate is similar to that obtained by direct impact. The differences in response, that is, the failure to give precisely the same amplitude at a given frequency is probably due to instrumentation limitations such as the accelerometer resonance problem mentioned earlier. A statistical approach to the data has not yet been attempted but is clearly needed. Further, the expected result is based entirely on the intuitive notion that the far field response should be the same in the two cases, and, as shown, the experimental results indicate that this is so. The deviation to be expected due to the presence of the plate has not been analyzed although one would expect that for a given projectile energy the far field response should be somewhat less when the plate is present. These aspects hopefully will be the subject of future experiments and analyses.

Several potential applications of this technique are apparent. If the proper scaling factors were known, a plate could be attached to a combat vehicle after assembly and a predetermined impact administered. In this way the subsystems could be subjected to a known combat equivalent shock while in place and operating. Subsystems which malfunction could be replaced immediately and the test repeated. Another possible application is a definition of the weapon secondary effects environment. Tests could be performed without damage to the vehicle and repeated any number of times. This would permit obtaining sufficient data to accurately define the shock environments under which subsystems would be expected to remain functional. The sacrificial plate technique, therefore, offers several potential solutions to hardness problems of interest to the combat vehicle designer and the quality control engineer.

We are indeed indebted to the following Army personnel who were responsible for conducting the M60A1E1 turret impact tests at the Aberdeen Proving Grounds, including instrumentation, data reduction and analysis:

W. C. Pless, Chief, Armor Branch, MTD, Automotive Division
I. W. Teichman, Chief Vehicle Structure Sec., MTD, Automotive Division
J. Coryell, Project Test Engineer, Armor Branch, Automotive Division

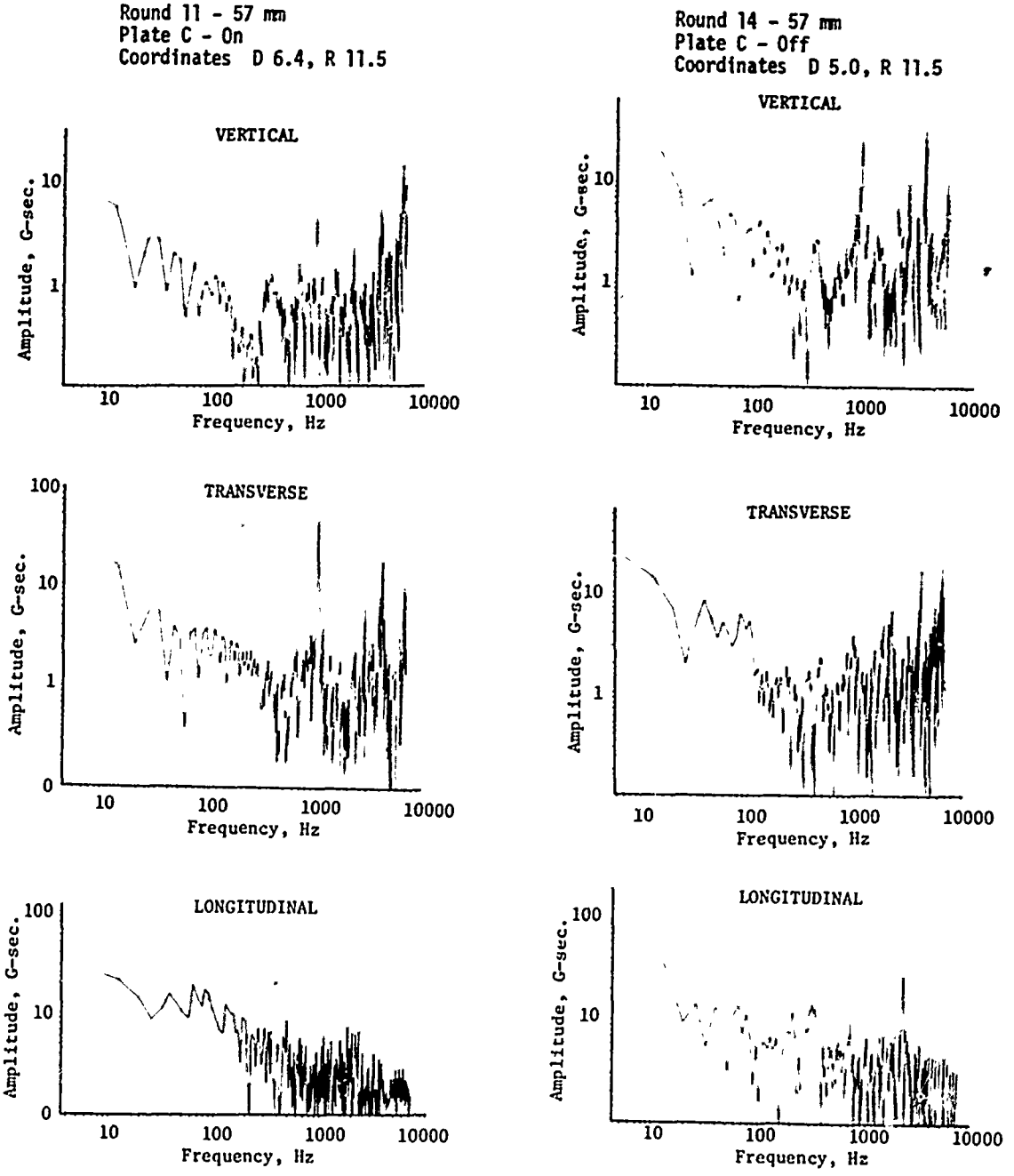

Fig. 14 - Fourier spectra from six accelerometer traces

J. K. Whallon, Chief, Mathematical Unit, Analytical Section, MTD
H. F. King, Mathematician, Analytical Section, MTD
W. Connolly, Mechanical Engineer, Instrument Development Sec., MTD

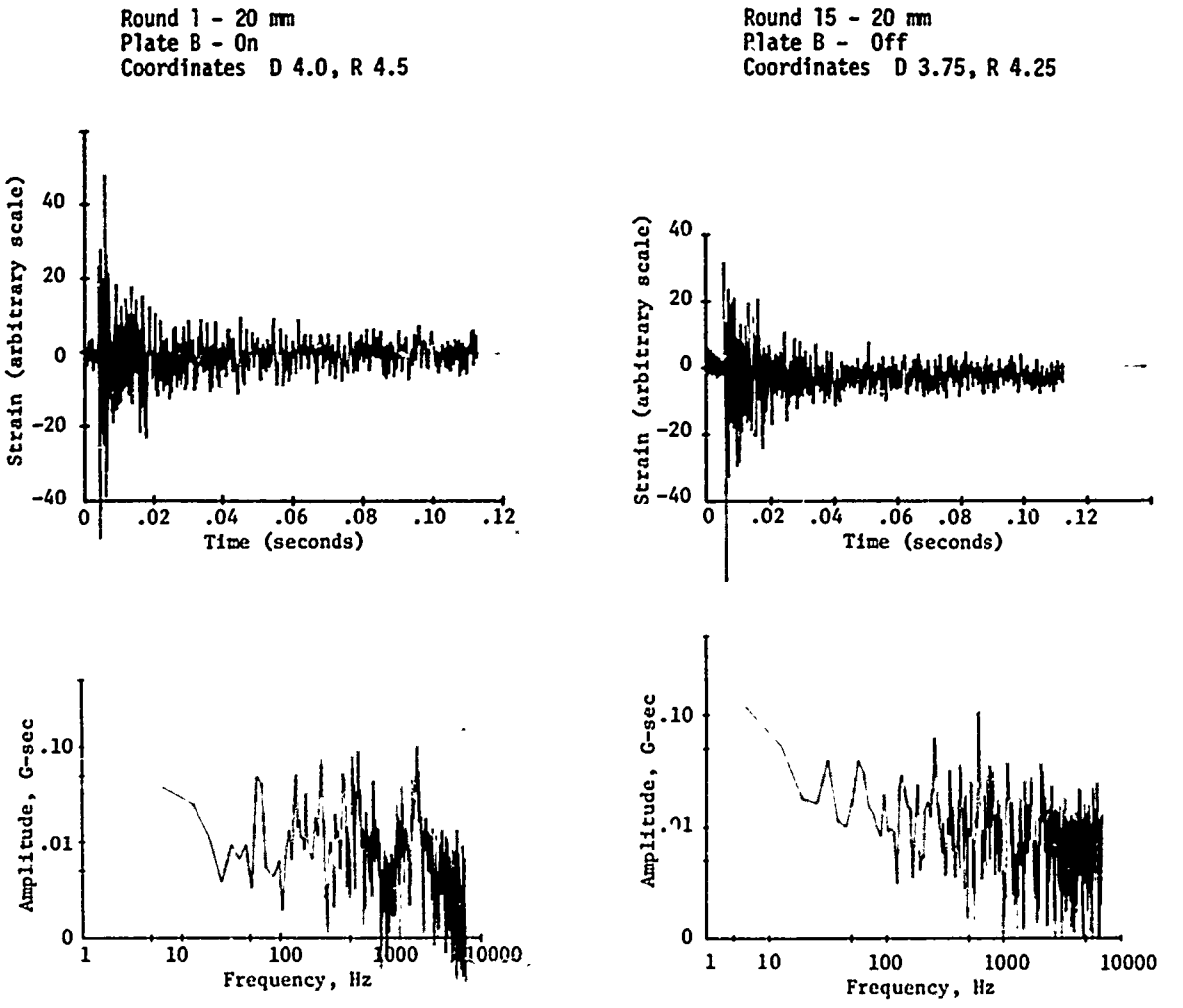

Fig. 15 - Strain gage traces and Fourier amplitude

THE EFFECT OF THE FIN-OPENING SHOCK ENVIRONMENT ON GUIDED MODULAR DISPENSER WEAPONS

K. D. Denton, K. A. Herzing
Honeywell Inc., Government and Aeronautical Products Division
Hopkins, Minnesota

Recent laboratory studies of a first-generation aircraft modular dispenser weapon have shown that modularity, while increasing the efficiency and effectiveness of the inventory, may result in subjecting weapon components to significant self-generated system operational environments for which the component was not originally designed or was not expected to experience in its normal manufacture-to-target logistic flow. For example, the shock environment produced by tail-fin opening of a weapon in free flight was found to be a significant factor that should be considered when designing and developing future modular weapon systems employing folded fins. This paper presents the results of the fin-opening shock study and shows the fin-opening shock environment levels to be higher than those allowed by conventional MIL-STD requirements. A procedure for developing a shock spectrum test criterion for modular fuze and guidance electronic components is also included.

INTRODUCTION

The development of future externally carried aircraft weapon systems will emphasize the modular design concept, which allows various weapons or weapon components in the inventory to be combined in the field to form a system optimally suited for a particular mission requirement. However, recent laboratory studies of a first-generation aircraft modular dispenser weapon have shown that modularity, while increasing the efficiency and effectiveness of the inventory, may result in subjecting weapon components to significant self-generated system operational environments for which the component was not originally designed or was not expected to experience in its normal manufacture-to-target logistic flow.

By combining components from different weapon systems, a new system is formed which has unique dynamic characteristics. Consideration normally would be given to the response of this new system to the commonly recognized dynamic environments which produce vibration or shock transients through external excitation, such as fluctuating aerodynamic pressures or abrupt aircraft decelerations produced by hard landing. Often, however, the effects of significant self-generated environments are ignored or overlooked. [1]

A component in the newly created modular system may not be compatible with an environment induced into the system by one of the other components. For example, a component designed for use in a 500-pound bomb may work satisfactorily in a system which is deployed in a ballistic trajectory from the aircraft, but may fail to operate when subjected to the high setback forces of a weapon system which utilizes a rocket motor.

The Guided Rockeye Munition (GRM), a first-generation modular weapon made up of weapon components which previously existed in the inventory, was used in the laboratory

test program described in this paper. The GRM system is composed of a laser guidance kit, a proximity fuze, a cylindrical dispenser, and a cluster bomblet warhead. The guidance kit and fuze were previously used in systems employing fixed stabilizing tail fins. The GRM application employs spring-loaded folding tail fins, which open after release from the aircraft.

Because the dispenser structure transmits shock energy from one end of the dispenser to the other with little or no attenuation, it was suspected that the self-generated fin-opening shock environment could significantly affect the nose-mounted modular electronic components. This suspicion was supported by field reports of failures of various types of dispenser fuzes. These failures could not be attributed to any cause other than fin opening.

The following sections describe the laboratory test program conducted to experimentally determine the shock environment associated with fin opening, which was measured throughout the dispenser and at the nose-mounted modular components. The purposes of this paper are to show that the self-generated shock associated with the tail fin opening contributes significantly to the service shock environment of a store, and to present fin-opening shock-spectrum criteria for component qualification testing.

SYSTEM DESCRIPTION

The Guided Rockeye Modular Weapon (GRM) is shown in Fig. 1 and is composed of the basic Rockeye dispenser, a laser guidance kit which is attached to the dispenser by means of an adapter section, and a proximity fuze which is mounted in the adapter section. The system weight is 570 pounds and the overall length is 12 feet. The GRM weapon includes canard control surfaces attached to the guidance nose section and stabilizing tail fins attached to the aft end. The Rockeye dispenser utilizes folding tail fins to insure adequate clearances for multiple carriage. During captive carriage, the fins are retained in the preloaded folded position by a metal band which is mechanically released when a lanyard is pulled during separation from the aircraft. When the metal retaining band is released by the lanyard, the fins are forced open by steel torsion springs. As the fins rotate back and reach their fully open position, rubber snubbers mounted in the base of each fin are compressed to cushion the impact between the fin and the base of the fin housing. When each fin is in the fully open position, a spring-loaded pin engages a detent to lock it in that position and restrain further motion. The dispenser may be released at pitch angles up to 15 degrees which will induce side loads as high as 480 pounds normal to each fin at its center of pressure. The moment resulting from this side-load condition is reacted by needle thrust bearings at either side of the fin root, to provide low dynamic friction during opening. The time required for fin opening is approximately 90 milliseconds.

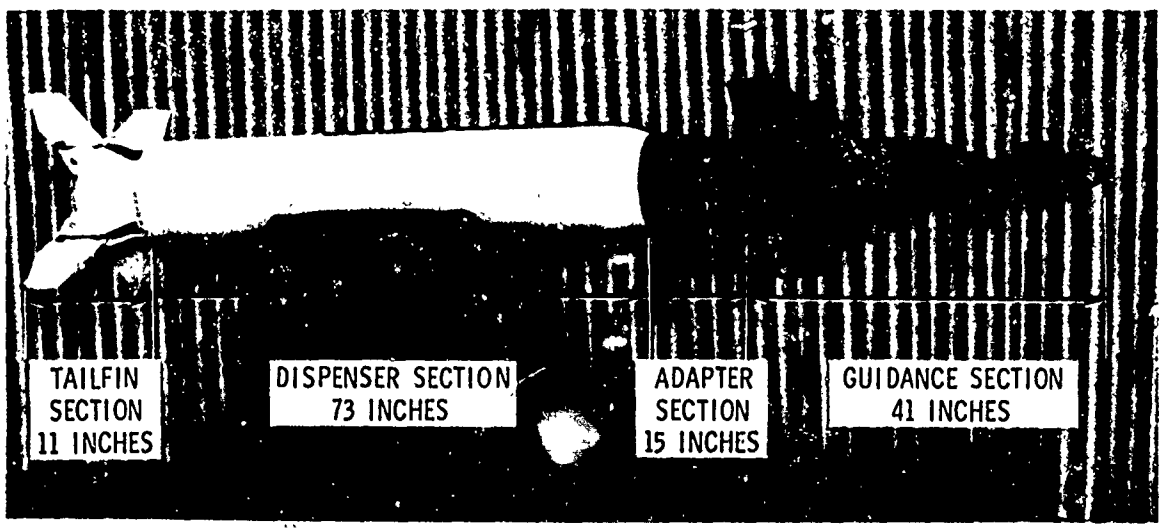

FIG. 1. Guided Rockeye Modular Dispenser Weapon (GRM)

TEST PROCEDURE

A laboratory test was performed to measure the shock environment produced by the tail fin opening. A full-scale GRM weapon was suspended from bungee in an environmental laboratory (Fig. 2). The suspension arrangement simulates the store configuration when it is in free flight following release from the aircraft.

The suspended weapon was instrumented with twelve piezoelectric accelerometers (see Fig. 3). The accelerometers were attached using dental cement. Transducer outputs were signal-conditioned by charge amplifiers, and the data were recorded on magnetic tape at a speed of 120 ips (standard IRIG mode, ±40 percent deviation, 0 to 20 kHz frequency response). Along with the twelve data channels, a constant 10-kHz time base and an event pulse signaling the start of fin motion (obtained by the fin breaking a pencil lead) were recorded on the 1-inch magnetic tape.

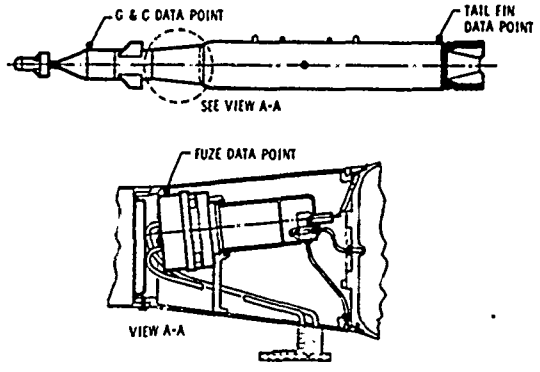

FIG. 3. Accelerometer Locations

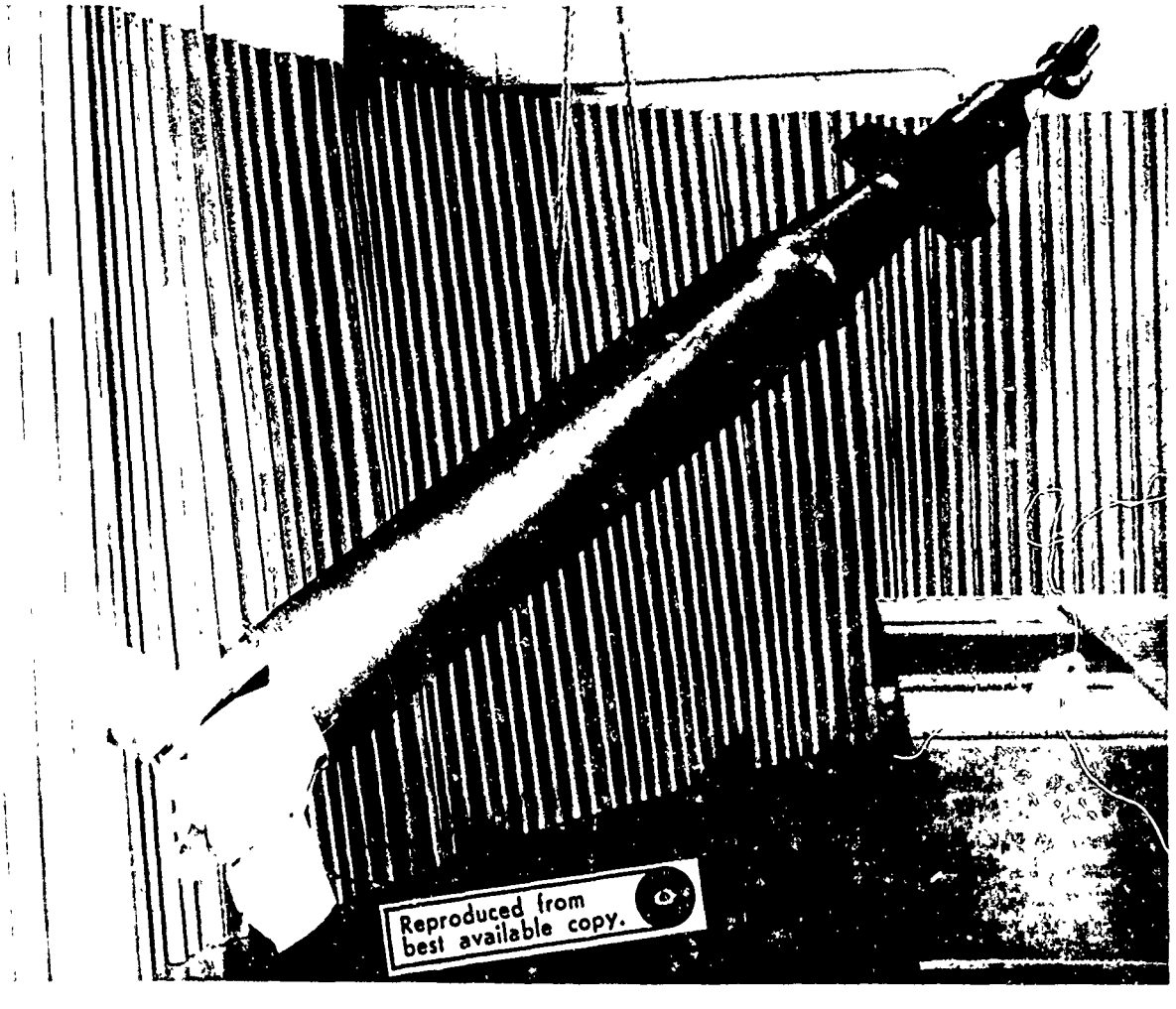

FIG. 2. GRM Suspended for Laboratory Test

The test sequence consisted of opening the same set of fins eight times. After each opening, the fins were refolded, the metal retainer band was replaced, and the lanyard was installed in the mechanical lock.

DATA ANALYSIS

Preliminary review of the tape-recorded data was performed by examining expanded oscillograms of the acceleration time histories. Even though the data acquisition and recording system bandwidths were on the order of 20 KHz, all the data were low-pass filtered at 5 KHz during playback. The low-pass cutoff frequency corresponds to 20 percent of the natural frequency of the test accelerometers.

The band-limited time history records were digitized at a rate of 10,000 samples/second. The record length utilized was nominally 50 milliseconds, with the record starting at the time the fin contacted the snubber. The digitized time history was processed by digital computer to calculate the undamped maximax shock spectrum for each record. The calculation involves a recursive solving of the response equations for an undamped single-degree-of-freedom system to which the time history record is applied as a base-forcing function. The maximum absolute response of the inertial element of the system is tabulated for each arbitrarily assigned natural frequency, and this response, converted to an equivalent static g, constitutes the shock spectrum. The assigned natural frequencies are designed to yield maximum spectral resolution while optimizing compute time. The frequency ranges and analysis resolution used for these analyses were:

10 to 100 Hz Δf = 10 Hz

100 to 500 Hz Δf = 50 Hz

500 to 1,000 Hz Δf = 100 Hz

1,000 to 5,000 Hz Δf = 250 Hz.

A typical shock time history is shown in Fig. 4 and its corresponding undamped shock spectrum in Fig. 5. The complex nature of the shock time history dictated the use of a spectrum analysis approach, to define predominant frequency characteristics and to correlate the shock data with previously obtained mode study and vibration transmissibility test results. [2]

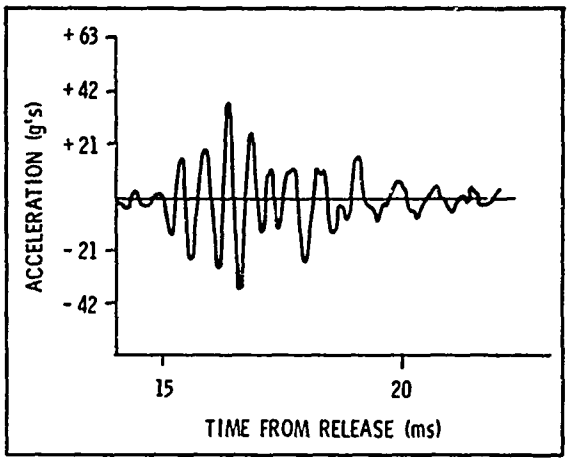

FIG. 4. Typical Acceleration Time History, (Run 1, Tail Vertical)

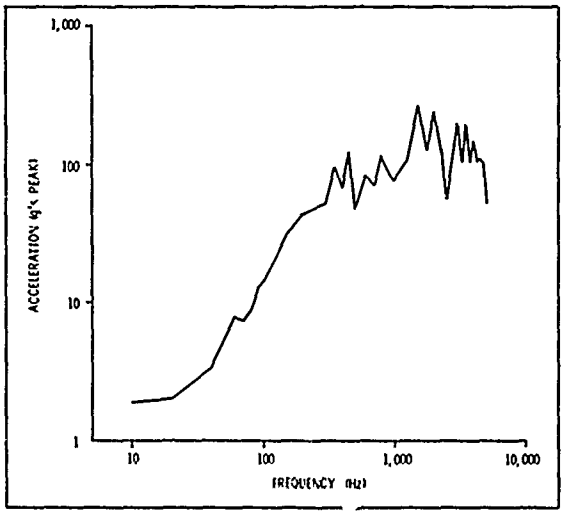

Fig. 5. Typical Undamped Shock Spectrum, (Run 1, Tail Vertical)

The preliminary review of the data revealed that significant shock levels were being generated by the fin opening, and were being transmitted with slight attenuation to the adapter-mounted components. The fin-opening environment was found to be very repeatable, with peak acceleration amplitudes occurring at the tail on the order of 30g.

THE DISPENSER FUZE ENVIRONMENT

Because of the previously noted susceptibility of dispenser fuzes to the fin-opening shock environment, special attention was given to the measurements made at the Dispenser Fuze Location (Fig. 3). The shock spectrum

envelope from this location, and for the 20g (peak), 11-millisecond sawtooth waveform shock used for fuze qualification, are compared in Fig. 6.

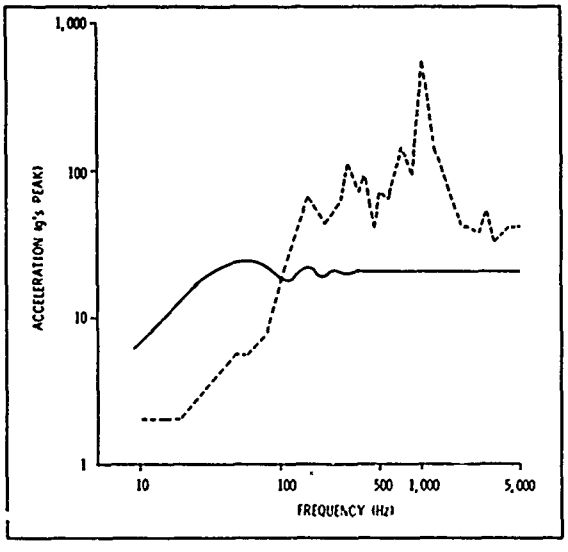

FIG. 6. Undamped Shock Spectrum Comparisons, MIL-STD-810, Operational Shock Response (——) and Maximum Envelope of Fuze Response From Fin Opening (-----)

The reduced data spectrums point out the extreme spectral differences in the two environments. The differences are very significant with respect to the fuze since its critical frequencies fall above 100 Hz, a range in which the fin-opening environment is highly dominant.

CRITERIA DEVELOPMENT

Because the measured fin-opening shock levels exceeded the existing shock test criteria for at least one of the GRM components, it was decided that the qualification test program should include a fin-opening shock test on all components. The most straightforward method of conducting this test is to assemble the components into a system and open the fins; the qualification test was performed in this manner. Prior to qualification, however, a more thorough examination of component response to the fin-opening environment was desired. Since the major components of the GRM system are manufactured by different contractors, and because of a shortage of available hardware which could be assembled into systems and shipped to each of the contractors for use as test vehicles, a repeatable equivalent damage test criterion was required which could easily be applied to a component in the laboratory. This criterion was also required to enable components to be tested while operating near special test-monitoring equipment installed in limited-size facilities.

It was felt that the most suitable equivalent damage test criterion could be defined in terms of shock spectra. This criterion could then be used to simulate the measured responses during laboratory tests on an electrodynamic vibration exciter.

A separate test criterion was desired for each of the three primary locations considered for mounting the electronic components in the modular system. A shock spectrum criterion was required for tail-mounted fuze components, adapter-mounted fuze components, and nose-mounted guidance components.

A review of the individual shock spectra from these respective locations revealed a very small dispersion between the maximum and minimum spectrum levels observed at any particular measurement location, substantiating the repeatability of the fin-opening environment. An example of the range in the maximum and minimum shock spectrum levels is shown in Fig. 7 for the tail vertical response.

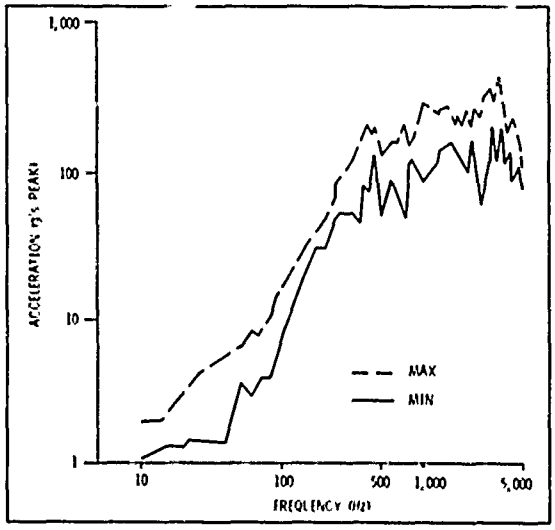

FIG. 7. Typical Range of Maximum and Minimum Undamped Shock Spectra (Tail Vertical)

The shock spectrum test criterion for each location of interest was generated by enveloping the undamped shock spectra of the measurements taken at that location, as illustrated in Figs. 8, 9, and 10.

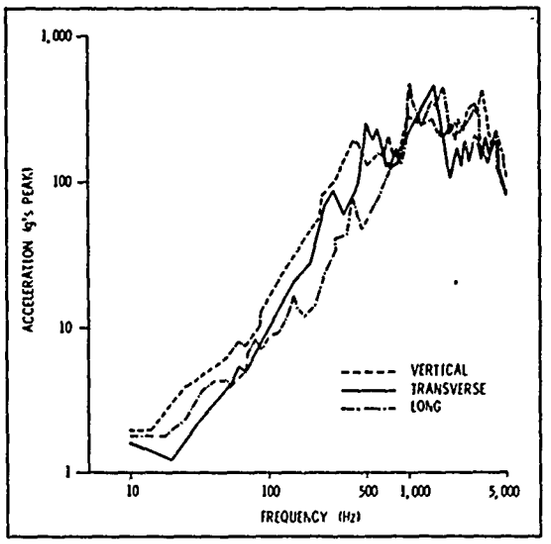

FIG. 8. Maximum Envelope of Tail Shock Spectrum

While the dispenser had little effect on attenuating the time history peak responses observed across the length of the system, the transmissibility of the structure did narrow the frequency band of the responses as the distance forward from the fins was increased.

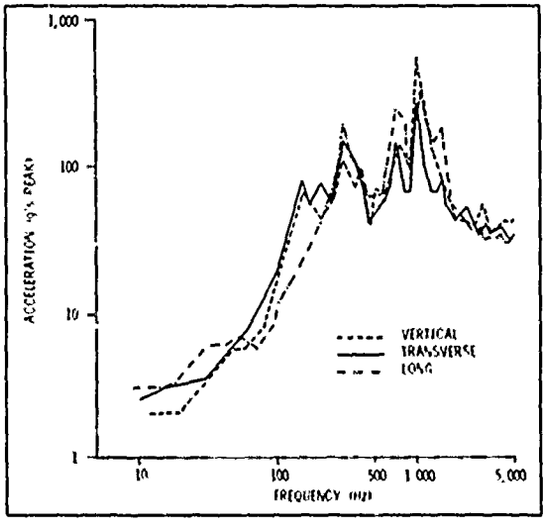

FIG. 9. Maximum Envelope of Fuze Shock Spectrum

The shock spectra revealed a wide-band response at the tail-fin source and a narrow-band response at the nose-mounted guidance section. This narrowing effect resulted in significant energy in a spectral band slightly above the frequencies considered critical to the guidance section equipment, and in a band coincident with the adapter-mounted fuze critical frequencies. The shock spectra revealed the tail-fin-opening shock to be a very significant self-generated environment with respect to adapter- and tail-mounted fuze electronic components.

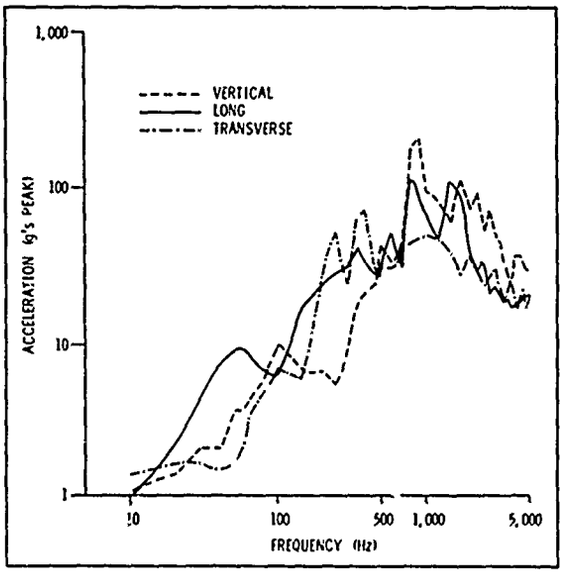

FIG. 10. Maximum Envelope of Guidance Shock Spectrum

SUMMARY

The structure of the Guided Modular Weapon was found to transmit fin-opening shock with little or no attenuation. The structure did, however, cause a narrowing of the frequency bandwidth of the response as the transient pulse moved through the weapon. Of prime importance, the shock resulting from tail-fin opening was found to be a significant environment which should be considered during the design and development of future modular weapon systems which employ folded fins. By comparison, the MIL-STD-810 operational shock test levels for the fuze electronics were found to contain little energy in the fuze critical frequency range relative to the fin-opening environment.

Self-generated environments are unique to the system in which they occur. Different fin-opening mechanisms on future modular dispenser weapons will have certain unique features which could be expected to generate a distinct fin-opening shock spectrum. The transmissibility of the different system structures would also affect the shock which is transmitted to the modular components. The fin-opening data presented in this paper may not be directly applicable to other modular weapons, but they do present an estimate of the magnitude of the shock which could be expected for a similar system. Of particular importance, these data reveal the fin-opening shock to be a significant environment which should not be overlooked in the design process.

REFERENCES

1. Denton, K., Herzing, K., Schwantes, S., "The Development of Shock Test Criteria for Aircraft Dispenser Weapon Ejection Mechanisms," The Shock and Vibration Bulletin 41, Part 5, December 1970.

2. Herzing, K., "GRM Qualification Vibration Test Report," Honeywell Ordnance Evaluation Report OEXM 22, 866, May 1971.

DISCUSSION

Mr. Wrenn (Lockheed Missiles and Space Company): The time history plot of the fin opening appeared to be a rather narrow-band signal with a predominant single frequency. Yet your shock spectrum showed a rather broad response. What is the explanation for that?

Mr. Denton: I do not know. I noticed the same thing when we were analyzing it. The responses were pretty much the same.

Mr. Wrenn: I noticed that the end of your time history had a couple of little jiggles which one might say would be a little bit of a frequency dispersion. But it was predominately narrow band, so that one might expect the spectrum to be rather narrowly peaked around that band, and yet there was quite a wide distribution.

Mr. Witt (Bell Telephone Laboratories): I was lead to believe that the data in your paper were obtained in still air. If that was the case would you not expect the shock levels to be somewhat different if these fins opened while the missile was in flight?

Mr. Denton: No, we considered that, but the fins are designed to eliminate that problem. That is the reason for the thrust bearings at the root of the fin. The weapon can be delivered at pitch angles up to about 20 degrees which causes normal air loads of about 450 lbs, and we have run tests in the lab to show that it does not affect the fin opening shock.

Mr. Schell (Naval Research Laboratory): You ran a 20 g sawtooth shock test. Was this in the original specification that was called out in the contract?

Mr. Denton: Yes, it was. That was the specification for the dispenser fuse which was used in other systems in a different kind of application. We used it in this system, many people thought just because it was qualified and in use that it would be suitable for this system. However, because of the fin opening shock that assumption was questionable.

DEVELOPMENT OF A FLUIDIC HIGH-INTENSITY SOUND GENERATOR

Howard F. Wolfe
Air Force Flight Dynamics Laboratory
Wright-Patterson Air Force Base, Ohio

An experimental investigation was conducted to determine the performance characteristics of a prototype fluidic high intensity sound generator. Acoustic and steady-state flow tests of a two stage annular slot configuration were performed to establish the primary performance parameters. The acoustic performance for a sine sweep input indicated a relatively flat output between 600 and 1800 Hz. The steady-state results indicated that the load on the receiver altered considerably the nozzle pressure profiles and amplifier characteristics. A method of evaluating changes in geometry from steady-state measurements is presented. The configuration tested indicated that a greater modulation of the supply nozzle jet is needed to improve the performance. The possibility of modulating the sound output to almost any arbitrary input waveform without the limitations imposed by mechanical parts represents a significant advantage in high intensity sound generation.

INTRODUCTION

High intensity noise associated with rocket and turbojet engine operation has long been recognized as an environment which can be detrimental to lightweight structures, equipment and personnel. Sound generators are used in the laboratory to simulate acoustic environments produced by high performance aerospace vehicles.

Present high intensity sound generators operate on the principle of modulating an air flow by mechanical means. Some examples are pure tone sirens, wide band sirens, and electropneumatic transducers. The primary disadvantages of these sound generators are low reliability and limited control. Sirens have close tolerances between rotors or between rotor and stator which are difficult to maintain with the speeds and loads involved in their operation. Also the output spectra produced are somewhat limited. An electropneumatic valve or air modulator has a reciprocating valve with a limited fatigue life. Its frequency output is limited due to the high acceleration involved with a reciprocating mass. Also wear between the armature and stator of the valve reduces efficiency which requires replacement of the valve assembly to restore performance.

The application of fluid state techniques to high intensity sound generation offers many potential advantages over current sound generators. The reliability problem can be virtually eliminated since no moving parts are required in the amplifier. Control is limited by the mechanics of the fluid and not by the inertia effects of a rotating mass or reciprocating parts. Thus the possibility exists of modulating the sound output to almost any arbitrary input waveform without the limitations imposed by mechanical parts.

Since 1966 the Air Force Flight Dynamics Laboratory has been investigating high intensity sound generation using fluidic technology. This paper presents the results of a study of the performance characteristics for a prototype model fluidic sound generator. The purpose of the study was to determine how to optimize the acoustic performance of the device.

BACKGROUND

Fluidics [1] refers to that field of technology that deals with the use of fluids in motion, either gaseous or liquid, to perform functions such as signal or power amplification, temperature or rate sensing, logic or computation, and control. Inherent is the

concept of achieving amplification or gain, often with no moving parts.

The fluidic approach to high intensity sound generation has been investigated previously. The first phase effort as reported in Ref. [2] included a feasibility study of the application of fluid state technology to high intensity sound generation, the fabrication of a breadboard sound generator, and an experimental investigation. The generator consisted basically of a jet-deflection-type fluid amplifier [3] with a rectangular nozzle configuration shown in Fig. 1. The momentum flux of the power jet and the forces exerted on it by the control jet determine the direction the fluid will assume after it leaves the interaction region as depicted in the next two figures. Fig. 2 shows the instantaneous flow for a positive peak of an input cycle and Fig. 3 shows the instantaneous flow for a negative peak or valley of an input cycle. The time modulated flow from the control jet results in a time modulated flow entering the receiver-horn, thus generating sound. The control flow source was an electromagnetically driven valve which provided a constant frequency sinusoidal control jet. Sound pressure levels as high as 150 dB (re: 2×10^{-5} Newtons/Meter^2) were obtained at the exit of the horn (17.25 inches x 17.25 inches), thus demonstrating the feasibility of fluid state sound generation. Since the main power flow was deflected rather than throttled, the theoretical maximum sound power radiated per unit of jet flow power was less than the sound power produced by other types of sound generators which throttle the flow.

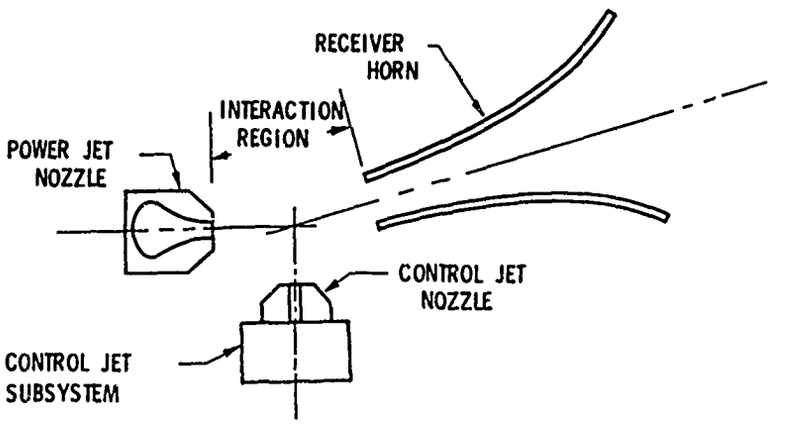

Fig. 1 - Basic Configuration of Fluidic Amplifier - Rectangular Nozzle

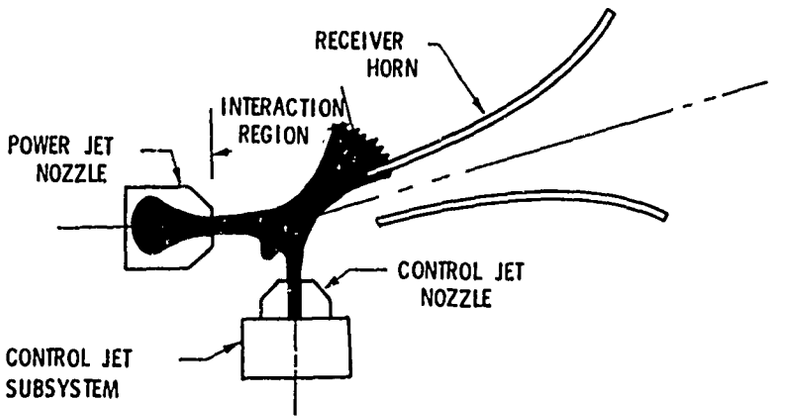

Fig. 2 - Positive Peak of an Input Cycle - Rectangular Nozzle

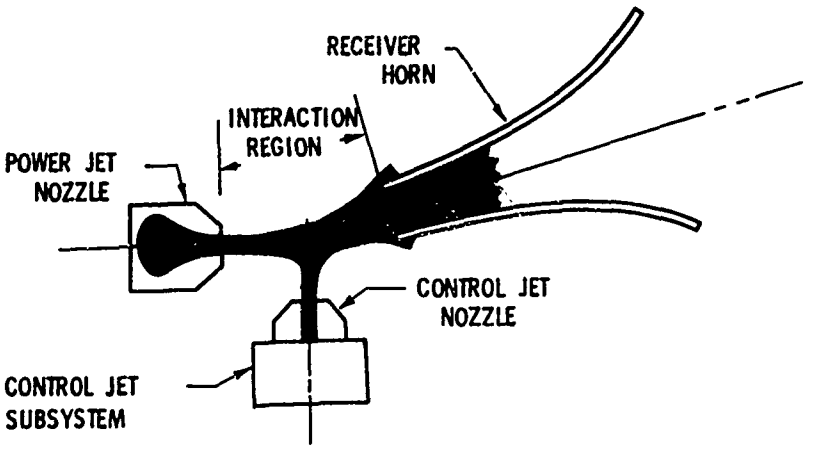

Fig. 3 - Negative Peak of an Input Cycle - Rectangular Nozzle

The second phase effort as reported in Ref. [4] investigated an annular slot fluidic jet-deflection proportional amplifier. The annular slot geometry is shown in Fig. 4. This geometry lends itself well to the symmetric interconnection of the components. The supply jet nozzle and receiver annular slots are concentric. Control flow is injected through a circular port inside the supply jet nozzle. The device works on the same principle as the rectangular configuration described previously. Fig. 5 shows the instantaneous flow for a positive peak of an input cycle. Fig. 6 shows the instantaneous flow for a negative peak or valley of an input cycle. The time modulated flow from the control port results in a time modulated flow entering into the receiver, thus generating sound at the entrance to the receiver.

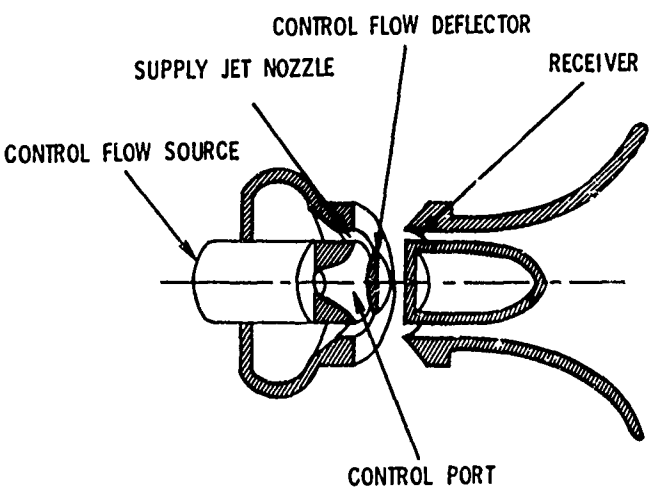

Fig. 4 - Annular Slot Jet Amplifier

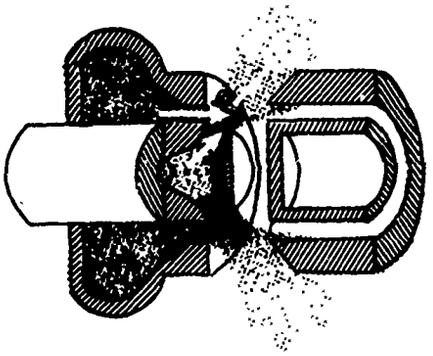

Fig. 5 - Positive Peak of an Input Cycle - Annular Slot Nozzle

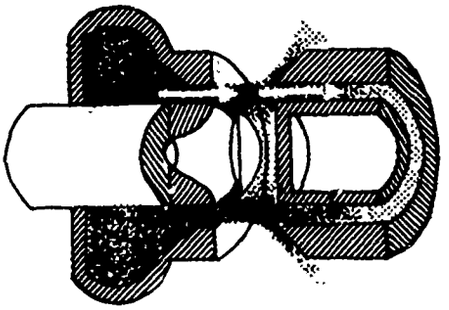

Fig. 6 - Negative Peak of an Input Cycle - Annular Slot Nozzle

A two stage prototype model of an annular slot fluidic sound generator was designed and fabricated as shown in Fig. 7. The control source selected for the first stage was an electrodynamic driver which transforms an arbitrary input electrical waveform to an acoustic output. The output of the first stage was the control source for the second stage. The second stage was scaled from the first stage such that the flow passage areas were increased by a factor of ten. The dimensions of the device are given in Table I. The vent regions of both stages were open to the atmosphere.

The construction details of the annular slot geometry are shown in Fig. 8. The distance between the nozzle exit and the receiver entrance was adjustable. The axial position of the deflector was also adjustable.

The results of the study [4] indicated that the average static pressure gain for the first stage was higher than the rectangular jet amplifier; however, the sound pressure levels at the output of the second stage were not as high as expected. It was concluded that a better understanding of the annular slot amplification mechanism is needed to improve performance.

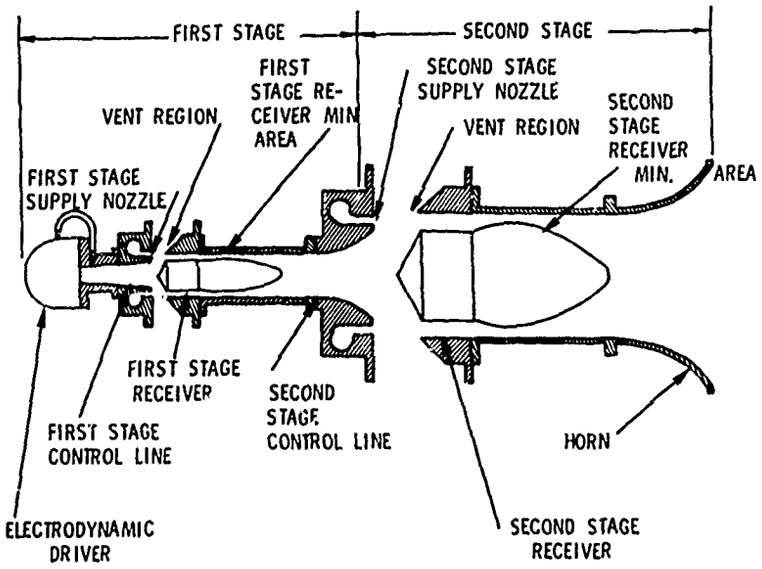

Fig. 7 - Original Configuration of Two Stage Annular Slot Amplifier

TABLE I
Two Stage Annular Slot Amplifier Dimensions

	Dimensions - Inches	
	First Stage	Second Stage
Control Line Dia.	1.4 - 1.95	6.16
Supply Nozzle I.D.	2.60	8.22
Supply Nozzle O.D.	2.74	8.57
Receiver I.D.	2.58	8.17
Receiver O.D.	2.83	8.96
Overall Length	112	
Horn Exit Dia.	42	

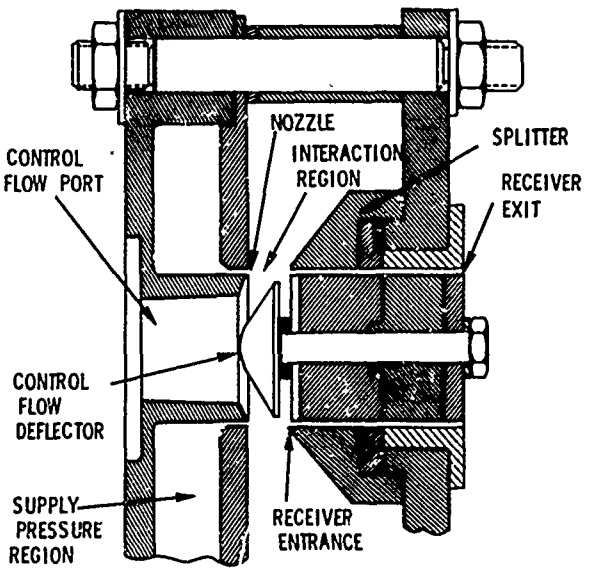

Fig. 8 - Drawing of Annular Slot Model

EXPERIMENTAL APPROACH

The investigation covered in this paper evaluated the performance characteristics of the annular slot model fluidic sound generator. The primary performance characteristic desired is a constant high acoustic output over a broad frequency range. To achieve this objective and to determine the primary functional parameters that govern the acoustic performance, several approaches were considered.

One approach was to measure the acoustic output at various locations in the system. These outputs result from a complex multitude of acoustic and fluid flow effects, but they do not reveal the basic operational parameters of the device. The overall system performance was determined by this approach.

The second approach considered was to study the fluid flow characteristics, since the acoustic generator is also a fluidic device. In general, the flow characteristics of fluidic devices are strongly nonlinear [3]. The formulation of an analytical model is complicated by the fact that the fluid flow phenomena are very sensitive to virtually every possible variable. Consequently, the models usually involve a number of simplifying assumptions such as two dimensional flow, incompressible fluid and a linear pressure-flow relationship which heavily restrict the validity of the model.

The third approach considered some of the analogies [5] between electrical networks and fluid circuits. These analogies yield rapid approximate solutions to fluid circuit problems; however, the inherent restrictions severely limit their applications. In view of the difficulties of adequate treatment, the development of fluidic devices has been heavily dependent upon empirical investigations to determine critical design parameters.

The last approach considered was the study of the steady-state fluid flow performance parameters which are related to the acoustic performance. Maximum acoustic efficiency is achieved when all of the flow is vented at the positive peak of the input cycle and all of the flow is recovered in the receiver at the negative peak of the input cycle. The steady-state operating points were considered as instantaneous amplitudes during part of a dynamic cycle. This approach was selected to optimize the steady-state flow parameters.

TEST PROCEDURE

The annular slot device shown in Fig. 7 was set up in the large test chamber of the AFFDL Sonic Fatigue Facility. A typical test set-up is shown in Fig. 9. An acoustic test was performed with air supplied at 10 psig to determine the overall performance of the system. A constant amplitude sinusoidal input was supplied to the driver and the frequency was swept slowly from 200-2500 Hz. Steady-state tests were also performed by replacing the dynamic driver with a constant flow air supply. Steady-state pressure measurements were taken in the vent and nozzle region of the first stage of the original configuration with probes and manometers. Stagnation pressure, static pressure and stagnation temperature measurements were taken in the first stage control line and both receivers.

The second model tested was the minimum load configuration as shown in Fig. 10. The load on each receiver was reduced to a minimum by removing the restriction and installing a constant diameter cylinder. Static pressure measurements in the first stage control line and stagnation pressure measurements in the first stage receiver were taken for various nozzle-to-receiver distances. The steady-state pressure measurements in the vent and nozzle region of the first stage and the pressure and temperature measurements in the control line and the receiver were repeated for the minimum load configuration. Also changes in the deflector position for the minimum load configuration were investigated. More detailed information about the test may be found in Ref. [6].

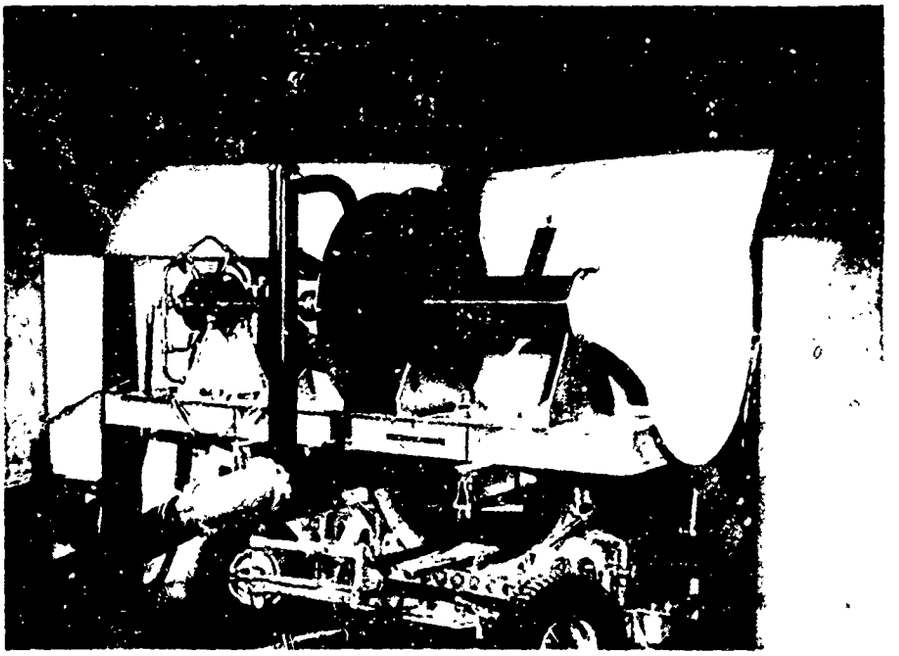

Fig. 9 - Typical Test Set Up

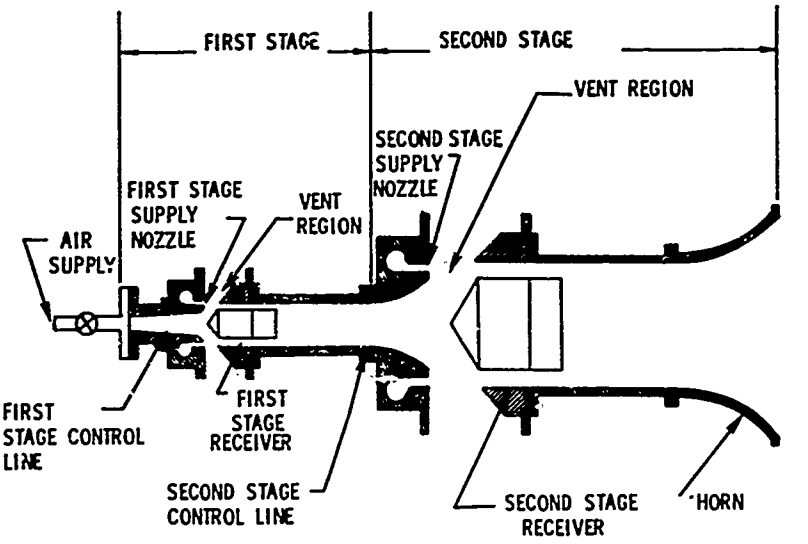

Fig. 10 - Minimum Load Configuration of Two Stage Annular Slot Amplifier

ANALYSIS OF TEST DATA

An estimate of the acoustic power [7] of the device can be made from the steady-state test data. Sound is defined on the basis of a fluctuating pressure above and below a reference level. Consider the acoustic input operating above and below an arbitrary reference level or bias level. For a sinusoidal input the maximum acoustic efficiency is achieved when all of the flow is vented at the positive peak of the input cycle and all of the flow is recovered in the receiver at the negative peak of the input cycle. This represents the maximum modulation available. The experimental steady-state operating points were considered as instantaneous amplitudes on a sine wave oscillation about some mean reference pressure. The difference between two points was viewed as a measure of the peak-to-peak amplitude of the sine wave. The acoustic amplitude parameter selected to estimate an equivalent acoustic power was the particle velocity as defined in Ref. [7]. This choice was based upon a direct relationship assumed between the particle velocity and the steady-state flow velocity. The difference in two steady-state fluid flow velocities divided by two was assumed equivalent to the peak particle velocity. Assuming free plane progressive wave propagation and no losses, the acoustic power is given by:

$$W = A\bar{I} = AP_o^2/2\,\rho_o c \quad \text{(Ref. [7])} \qquad (1)$$

where A = area

$\bar{I}$ = average intensity

P_o = the peak sound pressure

ρ_o = density

c = speed of sound

The pressure can be written in terms of velocity assuming no reflections:

$$P_o = U_o \rho_o c \qquad (2)$$

where U_o = peak particle velocity

$$\text{then: } W = A\rho_o\, cU_o^2/2 \qquad (3)$$

From the perfect gas law ($P/\rho = RT$) and $c = (\gamma g_c RT)^{\frac{1}{2}}$

where R = gas constant

T = absolute temperature

γ = ratio of specific heats

g_c = gravitational force per unit mass

the equation can be written as follows:

$$W = U_o^2 A\, P_s\, (\gamma/4g_c RT_s)^{\frac{1}{2}} \qquad (4)$$

P_s = static pressure

T_s = static temperature

The peak particle velocity was determined by taking the difference between two steady-state velocities and dividing by two. The steady-state velocity was computed from the total temperature, total pressure, and static pressure measurements. The equation for velocity for a perfect gas in an isentropic process is given by:

$$V = \left\{2\, g_c c_p JT_t \left[1-(P_s/P_t)^{(\gamma-1)/\gamma}\right]\right\}^{\frac{1}{2}} \qquad (5)$$

Ref. [8]

where: J = Joule's constant

c_p = specific heat at constant pressure

T_t = total or stagnation temperature

The above equations were used to estimate the acoustic power. The mass rate of flow was computed from the continuity equation and the perfect gas law. The equation is given by:

$$\dot{m} = P_s A \bar{V}/R T_s \qquad (6)$$

where $\bar{V}$ = average velocity

The average velocity was determined from data taken at five locations across the duct.

TEST RESULTS

A 50 Hz bandwidth analysis of the overall acoustic test of the two stage annular slot configuration is shown in Fig. 11. The response was approximately flat between 600 and 1800 Hz for a sine sweep input. The output of the electrodynamic driver has a resonant peak around 500 Hz and a relatively flat output between 800 and 2500 Hz. The output levels indicated that some gain was achieved.

The pressure distribution and pressure profiles were obtained from the steady-state pressure measurements in the nozzle and vent region of the first stage of the original configuration. Fig. 12 shows the pressure distribution in the nozzle-vent region. The pressures measured in the vent region were slightly below atmospheric pressure except for the thin layer along the splitter and in the nozzle flow. An increase in the mass rate of flow in the control line deflects more of the power nozzle mass rate of flow, thereby reducing the flow in the receiver. Typical pressure profiles for the original configuration are shown in Fig. 13. The shape of the profiles was affected by a feedback and an entrainment effect. The flow issuing out of the nozzle entrains part of the surrounding air due to viscosity effects [3] which results in a low pressure in the vent region. The center of an annular slot nozzle is isolated from the surrounding medium. The entrainment in this region generally causes a low pressure that results in the convergence of the annular flow; however, the load on the receiver and the proximity of the deflector forces some of the flow back along the deflector into the control line resulting in a feedback. The feedback effect predominated over the entrainment effect in the center of the annular slot nozzle resulting in a slightly higher than atmospheric pressure on the control line with no input to the control line.

The input-output pressure, velocity and mass rate of flow characteristics were obtained from the steady-state pressure and temperature measurements in the control line and receiver. The pressures measured in the first stage control line of the original configuration were unstable and therefore unsatisfactory for evaluation. The velocity profile across the duct indicated large changes in velocity with distance across the duct. The control line flow was nonuniform thus resulting in unreliable flow data. The input mass rate of flow was obtained from pressure and temperature measurements taken from a metering tube installed in the air supply to the control line.

The mass rate of flow was selected as the parameter for evaluating the fluidic sound generator. The input-output mass rate of flow characteristics of the original configuration are shown in Fig. 14. The two configurations are compared in Table II. The maximum mass rate of flow recovered by the receiver from the power nozzle was small. The estimated acoustic power output for the first stage was also small. The output of the first stage was insufficient to evaluate the second stage.

The minimum load configuration required a change in the nozzle-to-receiver distance with the deflector position remaining fixed at the receiver entrance. A small nozzle-to-receiver distance was selected.

The steady-state measurements in the nozzle and vent region for the minimum load configuration were similar to those obtained for the original configuration. They indicated a slightly lower than atmospheric pressure in the vent region except the thin layer along the splitter. Typical pressure profiles for the minimum load configuration are shown in Fig. 15. The receiver load affects the shape of the pressure profiles. In this case the flow along the splitter was smaller and a higher total pressure at the entrance of the receiver was achieved. Less feedback was also apparent.

The input-output mass rate of flow characteristics for the minimum load configuration are shown in Fig. 16 and Table II. The maximum mass rate of flow recovered by the receiver from the power nozzle increased considerably. The estimated acoustic power output remained small for the minimum load configuration. The peak of the input control signal must deflect more of the supply jet flow out of the receiver to increase the acoustic power output. The output of the first stage was insufficient to evaluate the second stage.

Changes in the deflector position along with various nozzle-to-receiver positions for the minimum load configuration resulted in some improvement in the amplifier characteristics. The feedback into the control line was eliminated by moving the deflector closer to the nozzle while retaining the same nozzle-to-receiver distance. A small increase in mass flow gain was obtained.

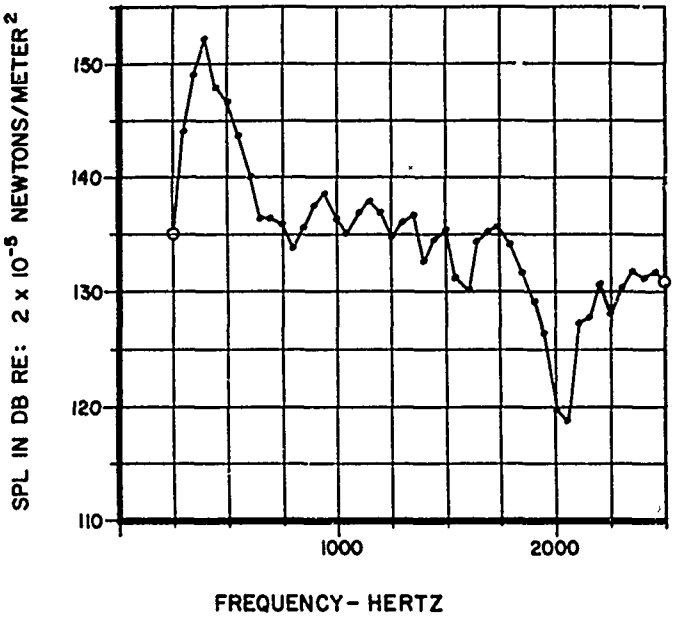

Fig. 11 - 50 Hz Analysis, Sine Sweep Test, Microphone Located at Horn Exit, Original Configuration

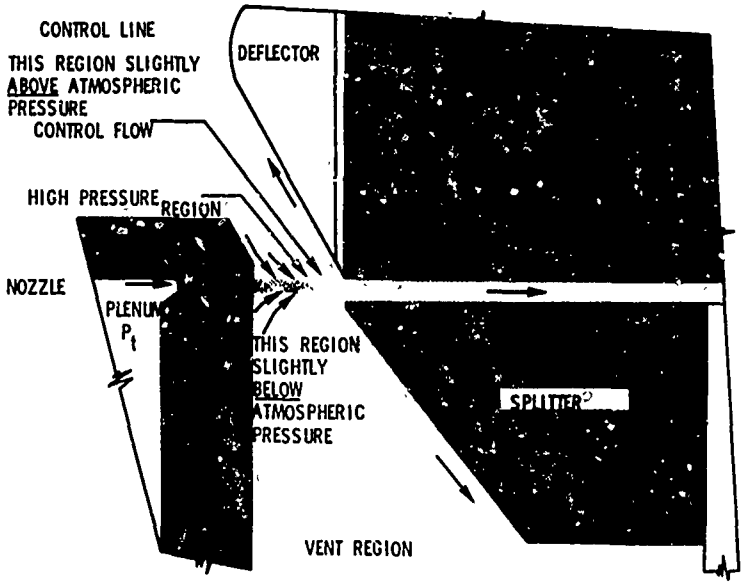

Fig. 12 - Nozzle-Vent Region Pressure Distribution, Original Configuration, No Input

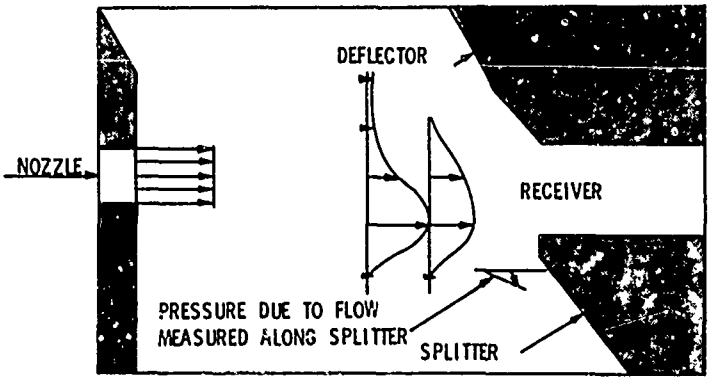

Fig. 13 - Pressure Profiles, First Stage Nozzle, Control Input = 0.034 lbm/sec, Nozzle Supply = 10 psig Original Configuration

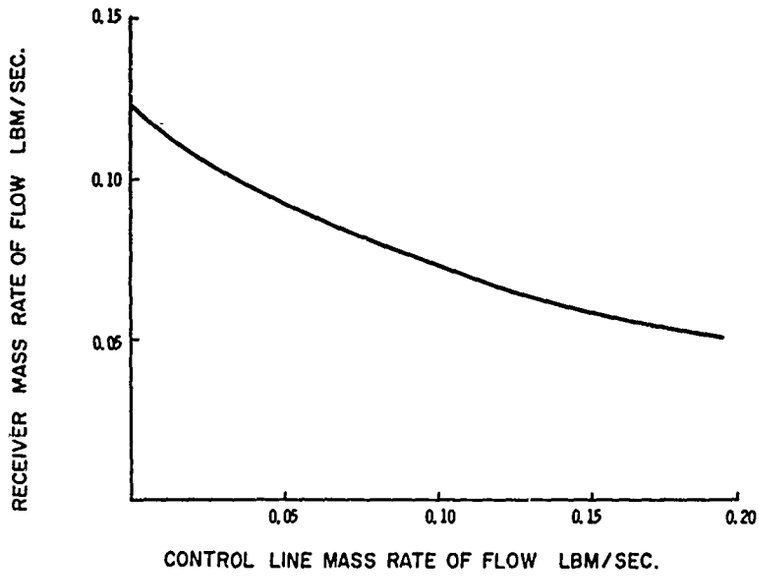

Fig. 14 - Mass Rate of Flow Characteristics, First Stage, 10 psig Supply, Original Configuration

Fig. 15 - Pressure Profiles, First Stage Nozzle, Control Unit = 0.062 lbm/sec, Nozzle Supply = 10 psig, Minimum Load Configuration

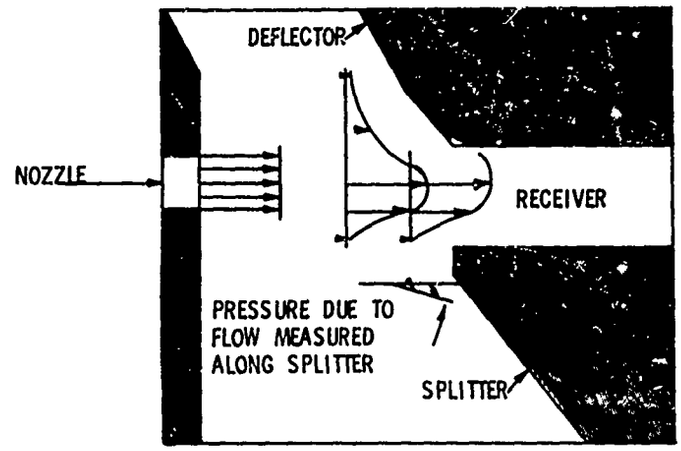

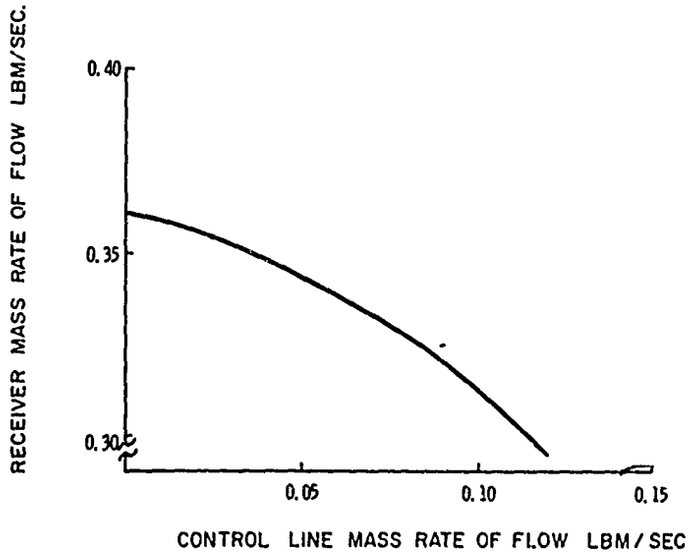

Fig. 16 - Mass Rate of Flow Characteristics, First Stage, 10 psig Supply Minimum Load Configuration

TABLE II
Mass Rate of Flow Characteristics

	FIRST STAGE			SECOND STAGE	
ORIGINAL CONFIGURATION					
Receiver min. area ($inch^2$)	0.403			3.80	
Nozzle-to-receiver distance (inches)	0.536			1.68	
Mass rate of flow (lbm/sec)	Nozzle	Control Line	Receiver	Nozzle	Receiver
No input	0.326	0	0.121	3.24	1.23
Max input	0.326	0.120	0.054	3.24	1.23
MINIMUM LOAD CONFIGURATION					
Receiver min. area ($inches^2$)	1.06			10.7	
Nozzle-to-receiver distance (inches)	0.306			1.86	
Mass rate of flow (lbm/sec)	Nozzle	Control Line	Receiver	Nozzle	Receiver
No input	0.324	0	0.359	3.21	3.51
Max input	0.324	0.124	0.292	3.21	3.51

CONCLUSIONS

Sound generators capable of producing high levels over a wide frequency range for long periods of time are required for many acoustic investigations. Projected requirements for increased capabilities have resulted in a search for better methods of generating high intensity sound. The fluidic approach to high intensity sound generation appears promising, since the amplification is not dependent upon mechanical parts. Progress so far demonstrates the feasibility of sound amplification with a fluidic device and represents the first step in the development of such a device. Tests with the two stage annular slot configuration indicate that the performance of the device is primarily a function of geometry and that the full potential capabilities have not been achieved. The successful development of the fluidic sound generator will depend upon the improvements in design geometry. With further development the fluidic approach has the potential capability of meeting the need for more versatile and reliable high intensity sound generating systems.

REFERENCES

1. MIL-STD-1306, Military Standard Fluerics Terminology and Symbols, July 1968.

2. B.R. Teitelbaum, A.A. Seleno, "Fluid State High-Intensity Sound Generator", Bendix Research Laboratories, Technical Report AFFDL-TR-67-112 (AD 831 444), Air Force Flight Dynamics Laboratory, Wright-Patterson Air Force Base, Ohio, June 1967.

3. Joseph M. Kirschner, Fluid Amplifiers, McGraw-Hill Book Company, New York, 1966.

4. B.R. Teitelbaum, L.B. Taplin, "Investigation of Fluidic High Intensity Sound Generator", Bendix Research Laboratories, Technical Report AFFDL-TR-70-98, Air Force Flight Dynamics Laboratory, Wright-Patterson Air Force Base, Ohio, May 1971

5. Charles A. Belsterling, "Fluidic Systems Design Manual", USAAVLABS Technical Report 67-32 (AD 659 415), July 1967.

6. H.F. Wolfe, "Experimental Investigation of the Interaction Region of an Annular Slot Fluidic Noise Generator", Masters Thesis, Ohio State University, December 1970.

7. Leo L. Beranek, Acoustics, McGraw-Hill Book Company, Inc., New York, 1954.

8. Victor L. Streeter, Fluid Mechanics, Third Edition, McGraw-Hill Book Company, Inc., New York, 1962.

DEVELOPMENT OF A LIGHTWEIGHT, LINEAR MECHANICAL SPRING ELEMENT*

R. E. Keeffe
Kaman Sciences Corporation
Colorado Springs, Colorado

The analytic and experimental development of an annular plate spring element suitable for pulse shaping studies is presented. This element has the desirable characteristics of linearity and low-weight combined with the capability for obtaining the wide range spring rates necessary for transient shock pulse shaping experiments.

INTRODUCTION

At the December 1970 Shock and Vibration Symposium an analytic technique [1] was described for designing a drop test experiment for simulation of transient acceleration-time histories. The method, simply described, involves the use of standard drop test apparatus in conjunction with a receiver assembly consisting of alternating layers of linear springs and rigid masses, designed so as to shape a desired pulse experienced by the drop table.

Obviously, the critical components in a system of this type are the linear spring elements, which in addition to having the required characteristics of linearity and low weight should be readily designable to any desired rate. For the applications of interest, spring rates on the order of 10^5 to 10^7 lb/in were required. Initial experimental attempts to obtain these spring rates involving use of polyethylene rod spring elements were not completely successful due to nonlinearities and strain rate sensitive behavior inherent to this class of materials. Additional studies into the design of suitable spring elements have been initiated; partial results of these studies are presented below.

*This work was accomplished under Army Contract DAAH01-69-C-1809 in cooperation with the U. S. Army Missile Command and the Defense Nuclear Agency.

DISCUSSION

The basic spring element to be discussed consists of a plate-spring design incorporating a series of thin, metallic circular plates connected in series by bolted joints. Details of the analytic design procedures required for this spring design, followed by the results of a series of plate-spring calibration tests, are presented in the following subsections.

Analytic Design Procedures

The spring element consists of a thin circular plate annulus with local areas of slightly increased plate thickness at the inner and outer edges (see Figure 1).

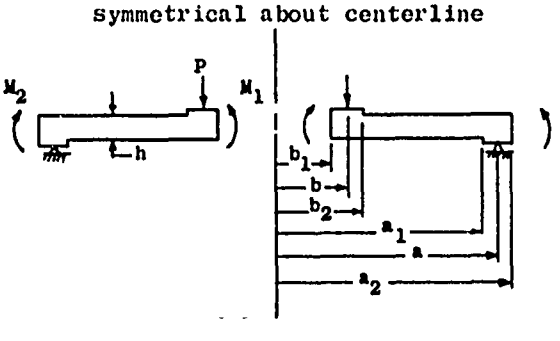

FIGURE 1

BASIC PLATE ELEMENT

In practice, an assemblage (even number) of these plate elements is bolted together at the bolt circles b and a to arrive at a composite element stiffness compatible with test design objectives. The stiffness of the basic plate element is dependent upon the flexibility of the circular plate (approximated by the inner radius b, outer radius a, and thickness h) and the flexibilities offered by the stretching of the bolts holding the edges of the plates together. The bolt forces are effectively reacted by uniformly distributed edge moments M_1 and M_2.

Three equations are necessary to relate the deflection of the plate (ω_b) and the rotations of the edges of the plates (θ_a and θ_b) to the applied loading P and the reactive edge moments M_1 and M_2. Required expressions, derived from thin plate theory [2] (with a shear correction term), are given in Equations (1), (2), and (3).

$$\omega_b = P\beta_1 + M_2\beta_2 - M_1\beta_3 \qquad (1)$$

$$\theta_b = -P\alpha_1 + M_1\alpha_2 - M_2\alpha_3 \qquad (2)$$

$$\theta_a = -P\alpha_4 - M_2\alpha_5 + M_1\alpha_6 \qquad (3)$$

where:

$$\beta_1 = \frac{1}{16\pi D}\left\{\frac{(3+\nu)(a^2-b^2)}{(1-\nu)} + \frac{2h^2}{(1-\nu)}\ln\frac{a}{b} + \frac{4a^2b^2(1+\nu)}{(a^2-b^2)(1-\nu)}\left(\ln\frac{a}{b}\right)^2\right\}$$

$$\beta_2 = \frac{a^2}{2D(1+\nu)}\left\{1 + \frac{2b^2(1+\nu)\ln\frac{a}{b}}{(a^2-b^2)(1-\nu)}\right\}$$

$$\beta_3 = \frac{b^2}{2D(1+\nu)}\left\{1 + \frac{2a^2(1+\nu)\ln\frac{a}{b}}{(a^2-b^2)(1-\nu)}\right\}$$

$$\alpha_1 = \frac{\beta_3}{2\pi b}$$

$$\alpha_2 = \frac{b}{D(a^2-b^2)(1-\nu^2)}\left\{a^2(1+\nu) + b^2(1-\nu)\right\}$$

$$\alpha_3 = \frac{2a^2b}{D(a^2-b^2)(1-\nu^2)}$$

$$\alpha_4 = \frac{\beta_2}{2\pi a}$$

$$\alpha_5 = \frac{a}{D(a^2-b^2)(1-\nu^2)}\left\{a^2(1-\nu) + b^2(1+\nu)\right\}$$

$$\alpha_6 = \frac{b}{a}\alpha_3$$

$$D = \frac{E\,h^3}{12(1-\nu^2)}$$

In order to relate the flexibility of the bolts to the edge moments, M_1 and M_2, the assumption is made that the local bolt reaction can be represented by uniformly distributed spring forces φ_1 and φ_2, acting at radii b and a respectively.

$$\varphi_1 = \frac{N_1 A_1 E_1}{2\pi b\, \ell_1} \qquad (4)$$

$$\varphi_2 = \frac{N_2 A_2 E_2}{2\pi a\, \ell_2} \qquad (5)$$

where: N = Number of bolts
A = Area of each bolt
E = Modulus of bolt material
ℓ = Length of each bolt.

The distributed spring forces acting over the moment arms defined by $(b-b_1)$ $(a-a_1)$ cause the edges of the plate to rotate. The relations between the edge moments and rotations are then:

$$M_1 = -\varphi_1(b-b_1)^2 \quad \theta_b = -\frac{\theta_b}{\gamma_1} \qquad (6)$$

$$M_2 = \varphi_2(a-a_1)^2 \quad \theta_a = \frac{\theta_a}{\gamma_2} \qquad (7)$$

where: $\gamma_1 = \dfrac{1}{\varphi_1(b-b_1)^2}$

$$\gamma_2 = \frac{1}{\varphi_2(a-a_1)^2}$$

Substituting Equations (6) and (7) into Equations (2) and (3), the relationships between the applied load and the edge moments and total deflection are obtained.

$$M_1 = P\,\epsilon_1 \qquad (8)$$

$$M_2 = P\,\epsilon_2 \qquad (9)$$

$$w_b = P(\beta_1+\beta_2\ \epsilon_2-\beta_3\ \epsilon_1) \qquad (10)$$

where:

$$-\epsilon_2 = \frac{\left[(\alpha_2+\gamma_1)\,\alpha_4 - \alpha_1\alpha_6\right]}{\left[(\alpha_5+\gamma_2)(\alpha_2+\gamma_1)-\alpha_3\alpha_6\right]}$$

$$\epsilon_1 = \frac{\left[\alpha_4+\epsilon_2(\alpha_5+\gamma_2)\right]}{\alpha_6}$$

The stiffness (k_i) of the plate element is then:

$$k_i = \frac{P}{w_b} = \frac{1}{\beta_1+\beta_2\ \epsilon_2-\beta_3\ \epsilon_1} \qquad (11)$$

The stiffness of plate elements combined in series can be readily computed using the standard relations for effective rates of series-joined springs.

Care must be exercised for a given spring design that the induced bending stresses in the plate do not exceed the material yield strength. The equation for radial stress (σ_r) as a function of plate radius can be derived and cast in the following form:

$$\sigma_r = \frac{6P}{h^2}\left\{\frac{\epsilon_1 a^2\left(1-\frac{b^2}{r^2}\right) - \epsilon_2 b^2\left(1-\frac{a^2}{r^2}\right)}{(a^2-b^2)}\right. \qquad (12)$$

$$\left. - \frac{(1+\nu)}{4\pi}\left(\ell n\,\frac{r}{a} + \frac{b^2}{a^2-b^2}\left[1-\frac{a^2}{r^2}\right]\ell n\,\frac{b}{a}\right)\right\}$$

For a given configuration of plate geometry and bolt distributions, this stress must be computed at various stations over the plate radius (from b to a) to find the point where the maximum stresses occur. If these stresses exceed the plate material yield stress, design iterations are required (usually resulting in an increase in the number of plates - N) until an acceptable configuration results.

Plate Calibration Tests

During the course of these studies a short series of calibration drop tests was performed to establish the validity of the plate-spring concept. Essentially there were three basic 7075-T6 aluminum plate elements used in these tests. Table I summarizes the dimensions of the plate-spring configurations, identified as k_{1B}, k_{2B} and k_{3B}. Various combinations of these plate elements were joined in series (using uniform bolt patterns at the outer and inner bolt circles) and tested to a velocity shock input at two different impact velocities. Table II summarizes the six different calibration configurations tested along with the two impact velocities for each; the resultant durations and amplitudes of the acceleration pulses are also included in the table.

Typical results for configurations involving two, four, and six plate elements are shown in Figures 2 through 4 (these figures were plotted from digitized acceleration data obtained after filtering at 8 kHz). It is seen that some deviation from a true half-sine pulse occurs as more plate elements are used. The induced high frequency content in the acceleration records is attributed to local mass and stiffness effects in the more complex plate configurations.

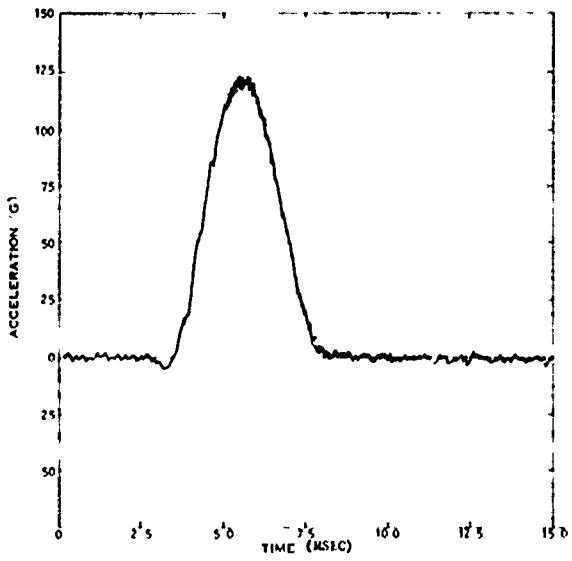

FIGURE 2

2-k_{2B} METALLIC PLATES

CALIBRATION TEST 3

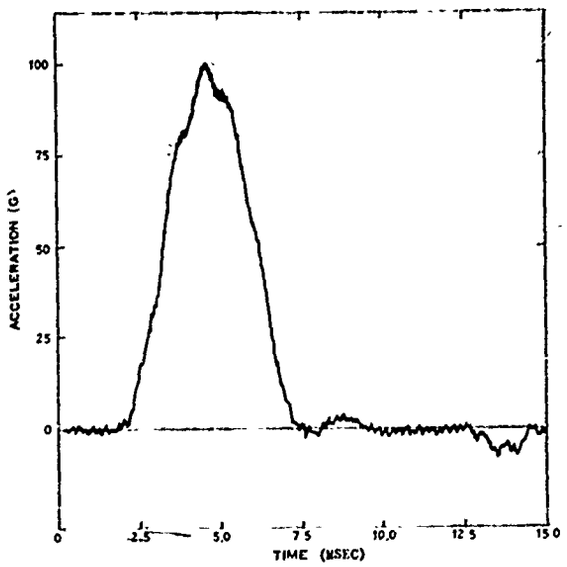

FIGURE 3

4-k_{2B} METALLIC PLATES

CALIBRATION TEST 5

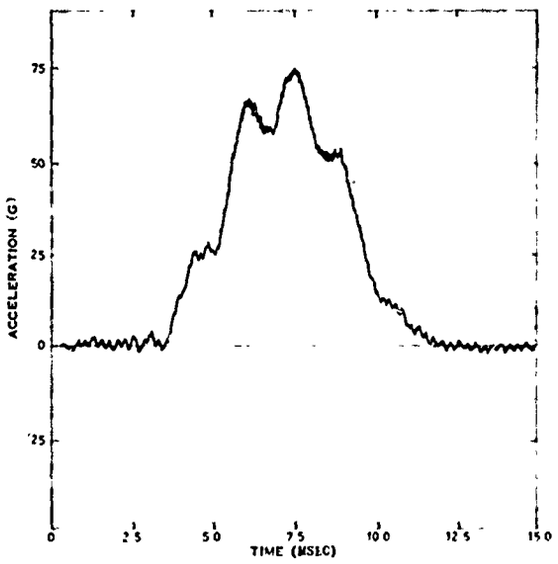

FIGURE 4

6-k_{3B} METALLIC PLATES

CALIBRATION TEST 11

Changing the impact velocity imparted to any given configuration had little effect on the duration or general shape of the measured acceleration pulse, but the amplitude of the pulse did change as expected. Figure 5 shows a comparison of the two separate pulses obtained by using different impact velocities on the same test configuration. System linearity was good, as can be seen by ratioing pulse amplitudes to corresponding impact velocities for the tests on the same configuration.

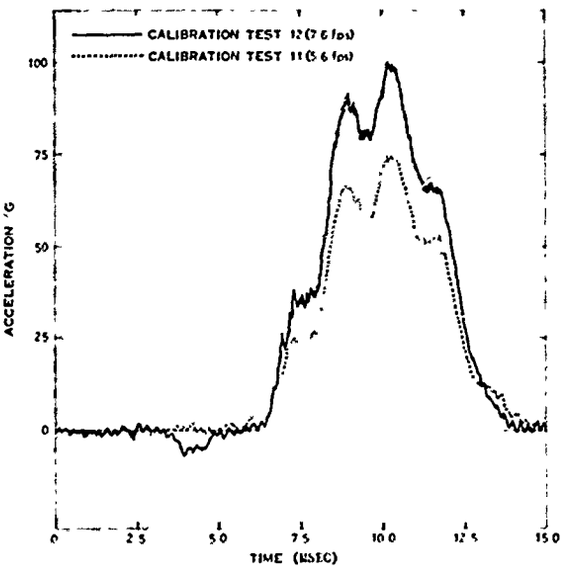

FIGURE 5

6-k_{3B} METALLIC PLATE CONFIGURATION;

EFFECT OF CHANGING IMPACT VELOCITY

The duration of the calibration pulses given in Table II along with the test mass (drop table tare weight) can be used to compute an equivalent stiffness for each plate-spring configuration tested. The analytic stiffness for each configuration was also computed using the procedures described in the analytic design procedures. Table III summarizes both the empirical and analytic stiffnesses for each calibration test configuration.

In general, the test and analytic stiffness results compare reasonably well, indicating that the developed analytic procedures are valid. As might be expected the largest deviation between experiment and theory occurs for the more complex 4- and 6-plate configurations. For these cases,

differences between test and analysis vary from 7% to 10%. However, the analytic methods may be considerably more accurate than indicated by these differences. This accuracy can be better evaluated by using the analytic stiffnesses derived for a given plate calibration test and accounting for the effect of the plate masses upon the response of the system. For example, consider the 6-k_{3B} plate configuration used in calibration Tests #11 and #12; a lumped parameter approximation including the effects of the plate masses is shown in Figure 6.

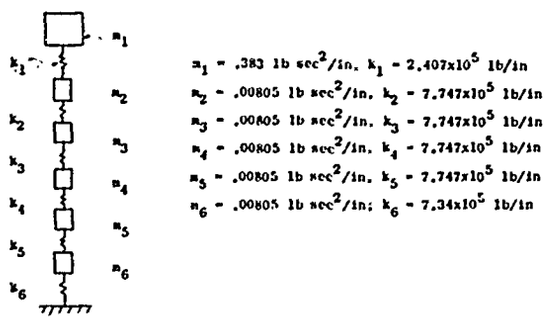

FIGURE 6

DETAILED MODEL OF 6-k_{3B}

CALIBRATION TEST

In Figure 6, m_1 represents the table tare weight and m_2 through m_6 represent the total distributed plate-spring mass. The values of k_1 through k_6 are the analytically computed values of individual plate stiffnesses. The k_1 and k_6 values are less than the other plate stiffness values due to variations in bolted joint configurations; that is, the k_1 plate is free at its outer bolt circle, and the k_6 plate has only 4 bolts at its outer bolt circle holding it to the drop table anvil.

Using the standard approximation for springs in series, the equivalent stiffness for this configuration would be k = .0935x10^6 lb/in, the number indicated in Table III. If the mass of the springs is neglected, a half-sine calibration pulse duration of T = 6.36 msec should result using this equivalent stiffness along with the mass of the table. As seen from the test data in Table II, this analytic value is approximately .3 msec less than the duration actually measured. However, if the local mass of the plates is included in the response calculation for this calibration test, the pulse shown in Figure 7 results (calculated using 2% critical damping and an impact velocity of 5 fps). Note that this pulse duration and shape compares extremely well with the recorded pulse shape shown by the solid line.

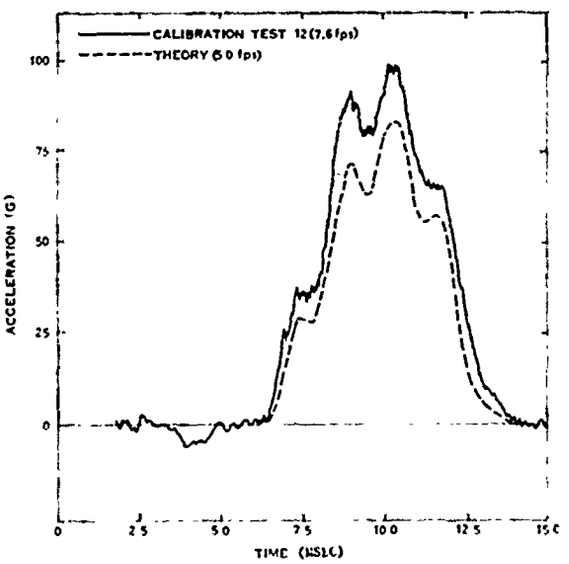

FIGURE 7

COMPARISON OF 6-k_{3B} METALLIC PLATE

WITH THEORY

(PLATE MASS INCLUDED)

CONCLUSIONS

Based upon these calibration results, it is concluded that the plate-spring concept is a feasible method for designing spring elements for use in shock pulse shaping experiments. The analytic methods correlate reasonably well with test results, particularly when the effects of local plate mass are taken into consideration. Even when the plate mass is neglected, application of analytic approximations for springs in series results in reasonable values of assembled plate configuration stiffness. It appears desirable to use as few plates as possible in arriving at a required element design based upon optimum simulation and cost considerations.

TABLE I

PLATE GEOMETRIES

Basic Configuration	a (ins.)	b (ins.)	a_1 (ins.)	b_1 (ins.)	h (ins.)	E (psi)	ν
k_{1B}	4.5	2.21	4.0	1.96	.458	$1x10^7$	.3
k_{2B}	4.5	2.46	4.0	2.21	.368	$1x10^7$	.3
k_{3B}	4.5	2.14	4.0	1.89	.386	$1x10^7$	.3

TABLE II

METALLIC-PLATE SPRINGS

CALIBRATION TESTS				
Calib. Test	Configuration	Impact Vel.(fps)	Pulse Amp. (G)	Pulse Duration (msec)
1	2-k_{1B} plates	5.9	132	3.50
2	2-k_{1B} plates	6.9	170	3.50
3	2-k_{2B} plates	5.6	115	4.00
4	2-k_{2B} plates	7.6	145	3.90
5	4-k_{2B} plates	5.6	100	4.60
6	4-k_{2B} plates	7.3	126	4.50
7	2-k_{3B} plates	5.2	95	4.40
8	2-k_{3B} plates	6.9	130	4.40
9	4-k_{3B} plates	5.4	80	6.00
10	4-k_{3B} plates	7.3	105	5.70
11	6-k_{3B} plates	5.6	72	6.65
12	6-k_{3B} plates	7.6	98	6.70

TABLE III

PLATE SPRING CALIBRATION STIFFNESS			
Calib. Test	Configuration	Experimental Stiffness (lb/in)	Analytic Stiffness (lb/in)
1	2-k_{1B} plates	$.309 \times 10^6$	$.302 \times 10^6$
2	2-k_{1B} plates	$.309 \times 10^6$	$.302 \times 10^6$
3	2-k_{2B} plates	$.237 \times 10^6$	$.250 \times 10^6$
4	2-k_{2B} plates	$.249 \times 10^6$	$.250 \times 10^6$
5	4-k_{2B} plates	$.179 \times 10^6$	$.171 \times 10^6$
6	4-k_{2B} plates	$.188 \times 10^6$	$.171 \times 10^6$
7	2-k_{3B} plates	$.195 \times 10^6$	$.182 \times 10^6$
8	2-k_{3B} plates	$.195 \times 10^6$	$.182 \times 10^6$
9	4-k_{3B} plates	$.105 \times 10^6$	$.123 \times 10^6$
10	4-k_{3B} plates	$.110 \times 10^6$	$.123 \times 10^6$
11	6-k_{3B} plates	$.0855 \times 10^6$	$.0935 \times 10^6$
12	6-k_{3B} plates	$.0845 \times 10^6$	$.0935 \times 10^6$

ACKNOWLEDGMENT

The calibration test program discussed above was performed at the Sandia Corporation (Albuquerque, New Mexico) Component Shock Testing Laboratory. The assistance provided by Mr. C. Endres, Mr. J. Cannon and Mr. K. Campbell of the Sandia Corporation is gratefully acknowledged.

REFERENCES

1. Keeffe, R. E. and E. A. Bathke, "Shock Pulse Shaping Using Drop Test Techniques," Shock and Vibration Symposium, December 1970.

2. Timoshenko, S., Theory of Plates and Shells, McGraw Hill, New York 1940.

TECHNIQUES FOR IMPULSE AND SHOCK TUBE TESTING OF SIMULATED REENTRY VEHICLES

N. K. Jamison
McDonnell Douglas Astronautics Company
Huntington Beach, California

The test techniques and procedures used in instrumenting and testing 12 simulated reentry vehicles to impulse and blast loadings are described herein. These tests were designed to supply data for structural hardening analyses, but were not designed to simulate any specific nuclear effects loading. The vehicles were of the same gross weight, but contained different heat shield and substructure materials. The vehicles were subjected to both short duration impulse tests using contact sheet explosive and long duration blast tests using an explosively driven shock tube. The overall objectives of this dynamic structural response test program were to determine experimentally the structural behavior and failure of each vehicle, rank the vehicle configurations as to their capability in resisting dynamic loading, and obtain strain data at selected locations for correlation with and verification of structural response computer codes. To meet the objectives, test techniques were developed for instrumenting, supporting, and retrieving, and loading the vehicles in a manner that would simulate, as nearly as possible, free flight environmental conditions and that would obtain high quality strain data in a dynamic test environment. The test techniques were very successful and for the first time large quantities of good quality structural response (strain) data were obtained that compared favorably with structural response computer codes.

INTRODUCTION

During the past 10 years, dynamic response of structures has received a significant amount of attention by various investigators in loading regimes where the duration of the loads covered a wide spectrum of conditions from nanoseconds to milliseconds (see Bibliography). The Air Force SPINE and HARTS Programs [1-7] produced extensive information about vehicle structures subjected to impulsive and blast-loading conditions, and provided the background work for this investigation. During this period, McDonnell Douglas Astronautics Company (MDAC) conducted mid-duration and long duration blasts tests of the SPINE structures, conical frustrums with different heat shield and substructure materials. The rigid end supports used seemed to influence the failures, the models failing at the ends rather than at midspan. For the SPARTAN program, contact sheet explosive tests were conducted to determine the relative vulnerability of a large number of multilayered shell structures employing different materials and design concepts. Following these tests, contact explosive loading tests (CELT) of a full size SPARTAN nose fairing/actuator section, were conducted.

The Air Forces (SAMSO) Dynamic Response Investigation of Simulated Reentry Structures (DRIS) program followed the SPINE, HARTS, and SPARTAN (Army) programs. The overall objectives of the DRIS program were to determine experimentally the structural behavior and failure of each vehicle, rank the vehicle configurations as to their capability in resisting dynamic loading, and obtain strain data at selected locations for correlation with and verification of structural response computer codes. These vehicles, of the same gross weight but containing different heat shield and substructure materials, were subjected to both short duration impulse tests using contact sheet explosives and long duration blast tests using an explosively driven shock tube. To accomplish these objectives, techniques were developed to explosively load, instrument, support, and retrieve the vehicles in a manner that would simulate, as nearly as possible, free flight environmental conditions and that would obtain high quality strain data in a dynamic test environment. These test techniques are described in subsequent paragraphs.

Whereas previous strain gage installations were limited by the strain gages inability to withstand small amounts of shock loading, new techniques were developed for this investigation which greatly increased the shock resistant range of the strain gage. Data acquisition systems continually were being improved such that complete systems with 80 KHz frequency responses were readily available for remote test site use. An innovative vehicle free flight support and retrieval system was developed which allowed the vehicle to

move freely during the time of loading and data acquisition yet would bring the vehicle to rest without post-test damage. In addition, structures, more representative of the reentry vehicles, were provided for these tests that were not available to past investigators.

The SABOR/DRASTIC system of computer codes was used in this investigation to correlate the strain histories of the tests at low load levels. These codes use finite element and finite difference techniques to determine the dynamic response of linear-elastic, branch, orthotropic shells. The complete reentry vehicle was modeled (including the internal structure and the foam used to support the equipment) as was the mass of all components. Boundary conditions were applied where required to improve the modeling, but care was taken not to restrict the rigid body motion in the computer code model. The computer model thus simulated the free spatial boundary conditions of the test setup.

Selected strain data are presented in this paper to show how well the structural response (strain) test data correlate with the responses predicted by the SABOR3A/DRASTIC11 computer code. Strain comparisons are given to show the differences between data recorded on the 20 KHz system and data recorded on the 80 KHz data acquisition system. There was some question whether the frequency response of the strain gage installation or the data acquisition system was adequate to pick up the high frequency peaks. Test results showed that the strain gage installations are more than adequate, but that 20 KHz data acquisitions systems could be losing some significant high frequency (30 to 40 KHz) vehicle responses.

LOADING PLAN

Before proceeding with any test investigation, a loading plan or load schedule is prepared indicating for each vehicle (1) the type of explosive load (impulsive using contact sheet explosive or long duration blast load using the explosively driven shock tube) and (2) the magnitude and duration of the explosive load (impulsive load in terms of taps* or the long duration blast load in terms of side-on reflected pressure in psi on the vehicle).

The plan for this investigation consisted of determining a number of selected loads for each vehicle, starting with the smallest load, that would give measurable vehicle elastic response and increasing in certain prescribed load increments until significant damage would occur in each vehicle. The rotation of explosive from the previously loaded half of the vehicle to the unloaded half would be sequenced with the predicted damage levels to obtain the maximum information with a minimum of loadings and test specimens. Elastic response and first damage load predictions for each vehicle were obtained using the structural response computer codes [8-11]. With these load predictions and test data from previous investigations [2-7], a pressure versus impulse isodamage (equal damage) curve shown in Fig. 1 was constructed. Using this curve as a guide, a buffer was selected that would give the best load duration for the impulse tests (load durations short compared to vehicle structural response times) and load durations were selected for the blast load levels (load durations long compared to response times of the vehicle).

*1 tap = 1 dyne-sec/cm^2 = 1 bar μsec = 14.5 x 10^{-4} psi-sec.

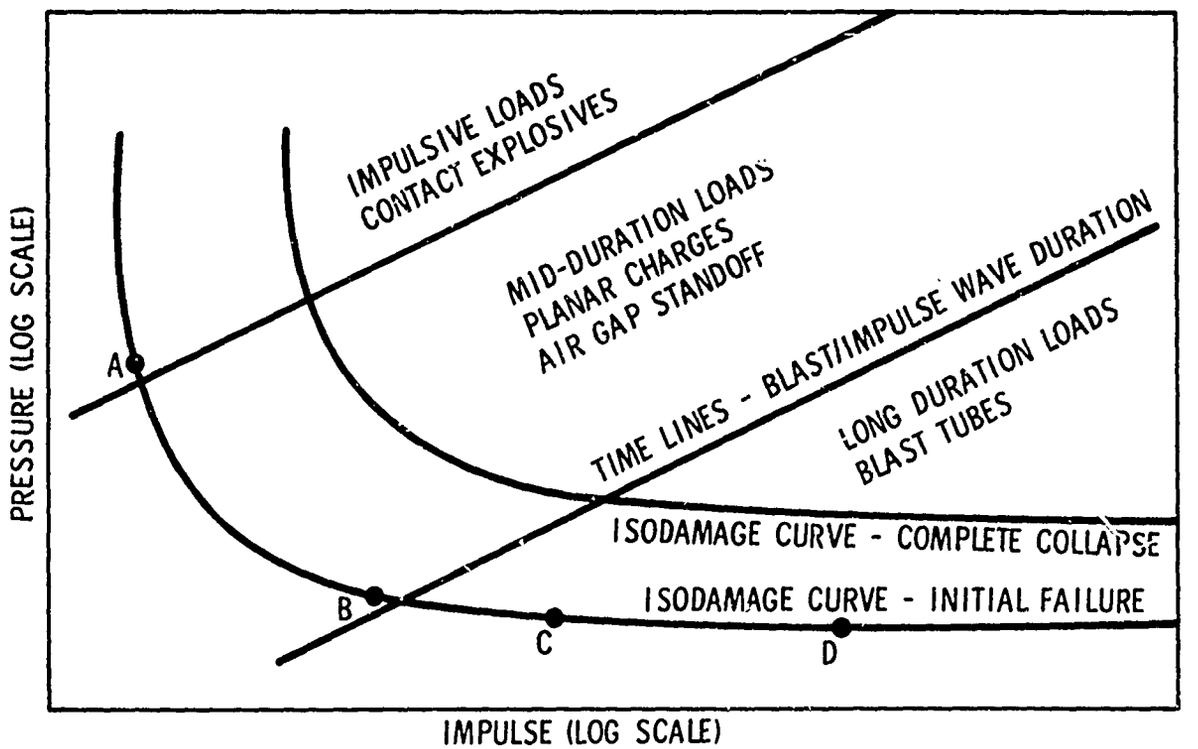

Fig. 1 Isodamage curve

Loading point A (Fig. 1) was chosen for the impulsive load level because the load duration was sufficiently long to minimize material damage yet short enough to ensure impulsive structural response. Loading point D was desired for blast loading, but for these longer durations, the explosive weight increases, the blast tube wall stresses increase and, in addition, the free vehicle retrieval system requirements increase very rapidly. Consideration of the desirability between mid-duration (point C) and long duration (point D) led to the selection of point C because the shock tube and vehicle retrieval system to supply point D were considered more costly. Loading point C was considered a satisfactory compromise of cost and length of time duration. Loading point B was also desired but was not used.

After establishing the initial loads for each vehicle, the loading plan was then varied during the tests (the next loading level would be adjusted up or down) according to the previous test results.

LOADING TECHNIQUES

Impulse Loading Techniques

Two different impulse loading techniques were used. In the first loading technique, the sheet explosive was applied directly to the buffer which had been lashed to the vehicle (Fig. 2). In the second technique, a 4-in. air gap standoff was provided between the explosive and the buffer (Fig. 3). In both techniques, the buffer, or the buffer and air gap, provided the desired pressure-time loading history and spatially distributed the explosive strip loads at the structural surface. In selecting a buffer material, it should be recognized that a buffer absorbs impulse; the heavier the buffer, the more impulse it will absorb. Also, the heavier the buffer the better it spatially distributes the explosive strip loads. The choice of buffer weight depends on the investigators evaluation of the importance of the above factors to his test. In this investigation a 0.5-in. thick neoprene foam rubber buffer (0.6 gm/cc) was chosen.

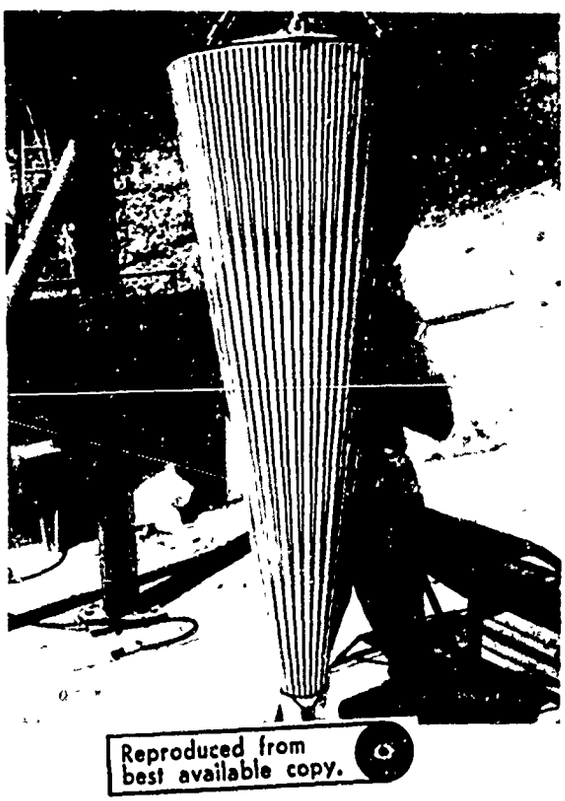

Fig. 2 Sheet explosive on vehicle

DuPont Detasheet D, whose explosive ingredient is PETN the same as in DuPont Primacord, was used to provide the impulsive loads. A solid sheet of 15 mil Detasheet D, if placed directly on a surface, will deliver an impulse of 10,000 taps. Since the output is proportional to thickness, the explosive output rating is 667 taps/mil. Therefore, to obtain a cosinusoidal pressure loading below 10,000 taps, it was necessary to use strips of explosive. The ratio of strip width to strip spacing is equal to the ratio of the desired impulse to the explosive output rating. The strip width, spacing, and thickness can all vary to achieve the required explosive patterns. The first step in this explosive pattern making process was to select an appropriate explosive thickness for the desired impulse load. Then, for three or four key vehicle station locations, the required strip widths were determined as a function of the angular position on the structure and angular strip spacing. Calculations were then iterated to achieve the desirable explosive strip widths and spacing geometry. For both loading techniques, the stripped sheet explosive was first bonded to a full size paper pattern before installation. Guidelines used in making the explosive patterns were (1) to keep the gaps between the strips as small as possible to minimize the pressure distribution variations at the structural surface and (2) to ensure proper detonation by maintaining an explosive width of at least 50 mils. Examples of explosive patterns used in both impulse loading techniques are shown in Figs. 2 and 3.

For the air gap standoff technique, the explosive pattern was mounted on a plywood holding fixture which was a constant 4 in. from the test vehicle surface over 180 deg of the cone frustrum. The loaded surface of the test vehicle was covered with a 0.25-in. thick, light (1.5 pcf), flexible polyurethane foam buffer. The buffers were lashed to the vehicle with bungee cords so that the buffer remained bound to the vehicle throughout the test (Figs. 2 and 3).

Shock Tube Loading Techniques

For the explosively driven shock tube tests, a thin walled (1-in. thick), 7-ft diameter by 20-ft long, horizontal steel shock tube open at both ends was used (Fig. 4). Primacord explosive was spirally wound on a polyurethane disk to form a planar charge (Fig. 5) and installed in the shock tube with a 16-ft standoff, to provide the explosive power for the blast loading. Primacord fuses were run to

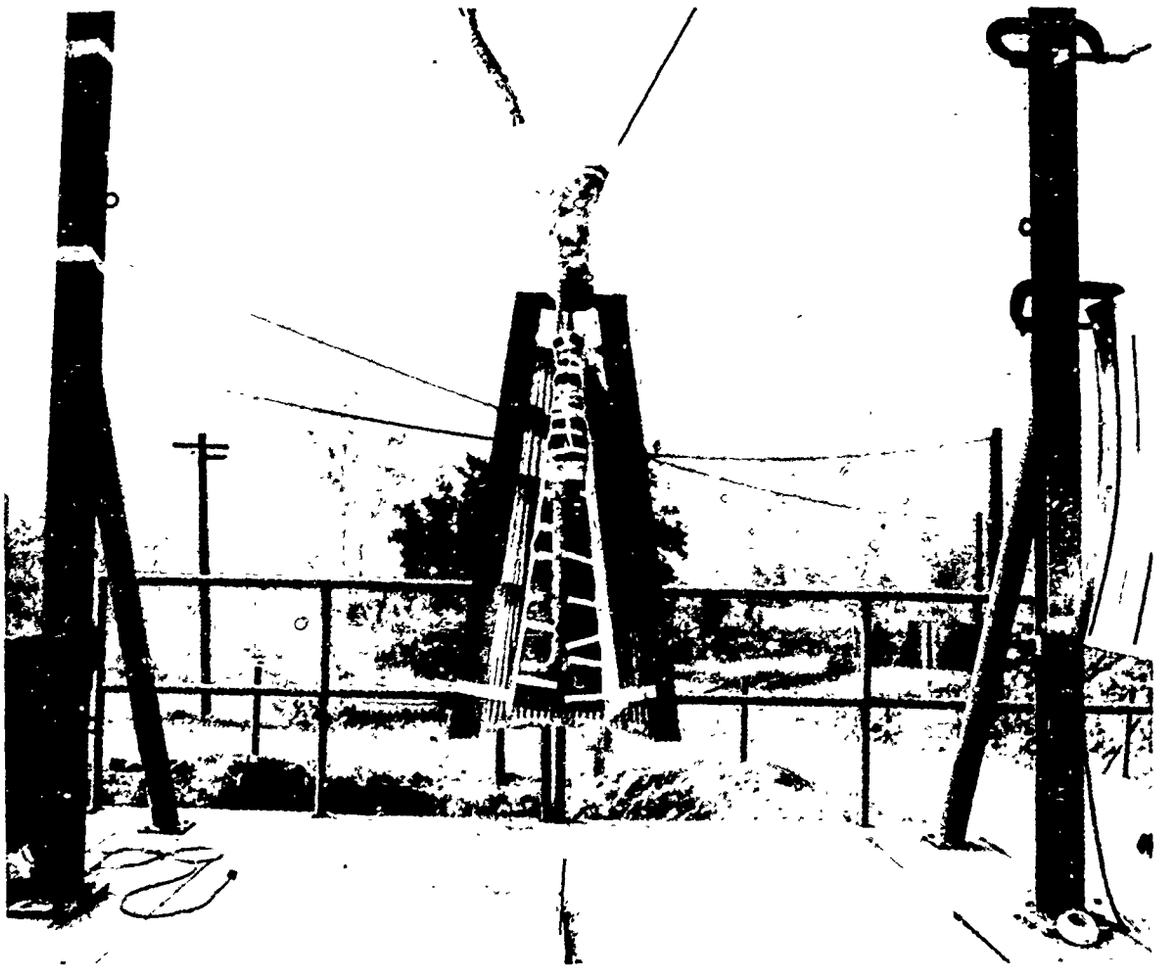

Fig. 3 – Air gap standoff loading technique

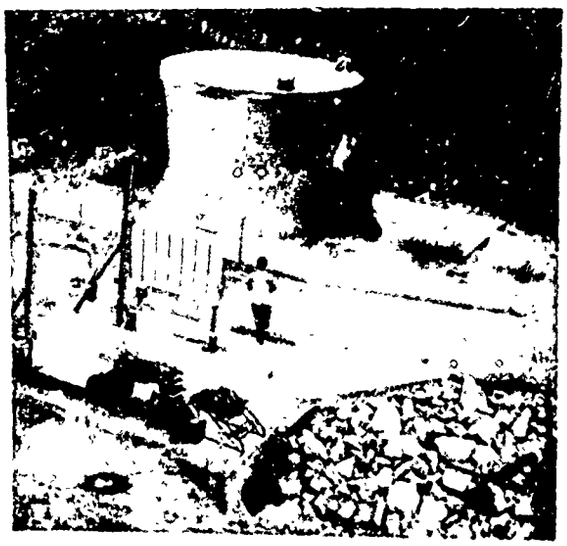

Fig. 4 Shock tube

several points on the charge for multiple point initiation which gives good shock-front planarity. The shock tube was instrumented with strain gages at select locations along the tube to measure the hoop and meridional strains in the tube during the calibration test firings. As the explosive loadings were successively increased, the maximum dynamic stresses induced in the tube were carefully monitored to ensure that the ultimate strength of the tube would not be reached and fail the tube.

To help extend the range and useful life of the shock tube, a stress damping technique was used. This technique consisted of completely surrounding the tube with 3 ft of wet compacted sand all along its length except for about 2 ft at each end. This technique effectively increased the mass of the tube without increasing its stiffness. During firings, the dynamic stress responses of the tube were reduced and rapidly damped out by the wet sand acting against the shock tube walls so that peak stresses would not combine into higher stresses and fail the tube.

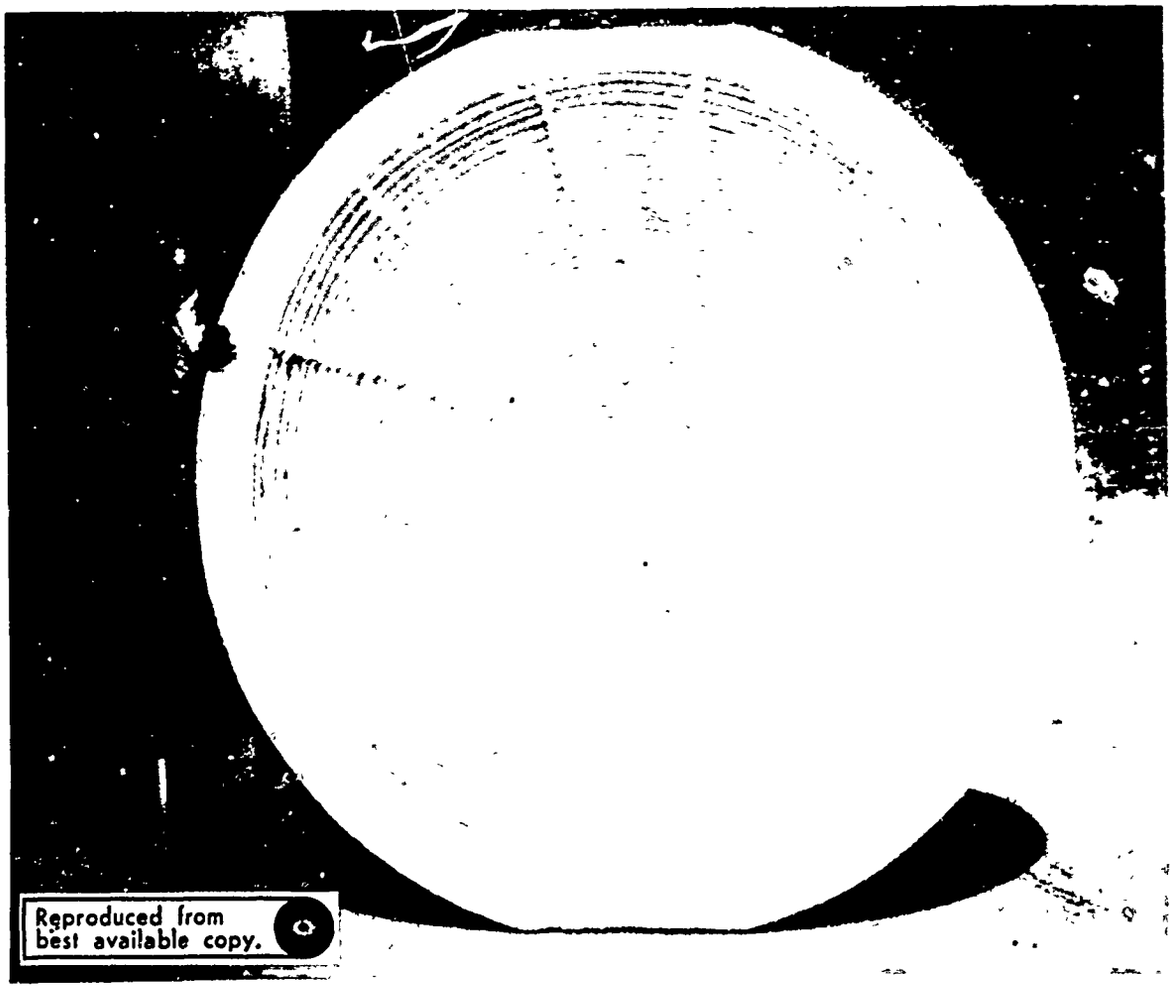

Fig. 5 – Shock tube planar explosive charge

Each new shock tube test must be individually calibrated to the kind of explosive used, to the type of charge used (planar or volume), to the standoff distance of the explosive from the vehicle, and to the placement of the vehicle in relation to the shock tube. For this investigation, a series of 15 calibration tests were conducted using a full-scale aluminum calbiration model (Fig. 6) with 12 Kistler pressure transducers (Models 603A, H, L) mounted in the model surface to measure the pressure distributions. Three tests were conducted at each of the selected planar charge loadings, starting with the lowest charge loading, and the resulting peak pressures and blast duration measured on the calibration model. This data plotted as a curve of peak pressure versus charge loading provided the initial calibration curve of the shock tube. Additional charge loadings were fired at the desired vehicle pressure loadings, using the calibration curve as a guide, to check on the validity of the calibration curve. Two key pressure transducers at identical locations in both the calibration model and the test vehicles provided a method of correlating test pressure measurements with the calibration tests pressure measurements.

VEHICLE SUPPORTING AND RETRIEVING TECHNIQUES

The main objective of the vehicle supporting technique was to provide boundary conditions that would simulate free flight. However, free flight vehicle supporting conditions have the additional requirement of catching or retrieving the vehicle after it has been set in motion by the explosive. The vehicle supporting and retrieving techniques used in both the shock tube and impulse tests simulated very closely free flight conditions and were successful in permitting the determination of valid dynamic structural responses. Measurements of the vehicles rigid-body motion, obtained from motion pictures taken during the tests, permitted the determination of the impulse imparted to the vehicles.

Shock Tube

In the shock tube tests, each vehicle was supported in front of the shock tube by the innovative cable-trolley vehicle support and retrieval system shown in Fig. 7. Each

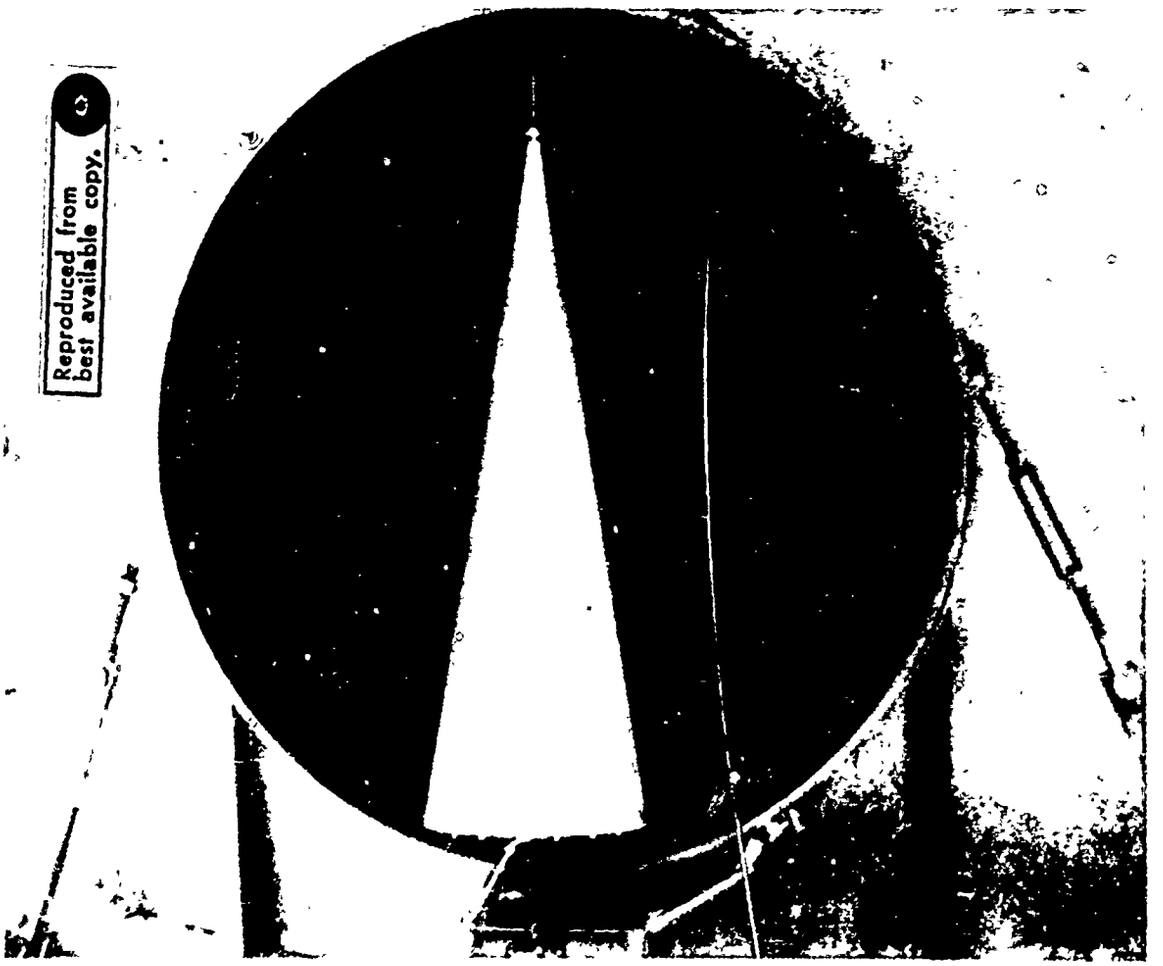

Fig. 6 – Calibration model in front of shock tube

test vehicle was attached through a short cable to a trolley which rode on the suspension cable. The length of the short cable was selected so that the blast pressure center would be at the center of percussion of the test vehicle support cable system. When the center of pressure is at the percussion center of the system, the vehicle will rotate pendulum fashion about its pivot point until it overcomes the friction between the trolley pulley wheels and the suspension cable, then it will travel up the suspension cable.

To minimize the initial downward deflection of the vehicle and the corresponding high tension load generated in the suspension cable due to the blast pressure acting on the sloping sides of the vehicle, the vertical axis of the vehicle was titled (Fig. 8) so that the resultant velocity imparted to the vehicle would be nearly horizontal. Two light lines held the vehicle in this cocked position. The lines broke easily during the blast loading and did not interfer with the vehicle travel.

The suspension cable, a 5/8-in. diameter steel cable strung between 2 steel towers 160 ft apart with a 30-ft difference in elevation, provided the guided path of travel for the vehicle. The 30 ft rise in height, combined with the frictional drag of the trolley, the aerodynamic drag of the vehicle, and final rope stop, were sufficient to retrieve all of the vehicles without any post-test damage. A one-way cam actuated mechanical stop attached to the trolley prevented the vehicles from backtracking, i.e., rolling back down the suspension cable and impacting the shock tube.

The trolley had two 5-in. diameter steel pulleys riding on top of the suspension cable and a single 5-in. diameter steel pulley riding the bottom of the suspension cable, the lower pulley positioned between the upper pulleys (Fig. 9). With the trolley constructed in this manner, the cable was completely enclosed in the pulley grooves, so that the cable could not jump out of the trolley pulleys, bind up on the trolley side plates, and wreck the vehicles.

Impulse Tests

For most of the impulse tests, the vehicles were suspended from the aft end by a 6-cable harness attached at 6

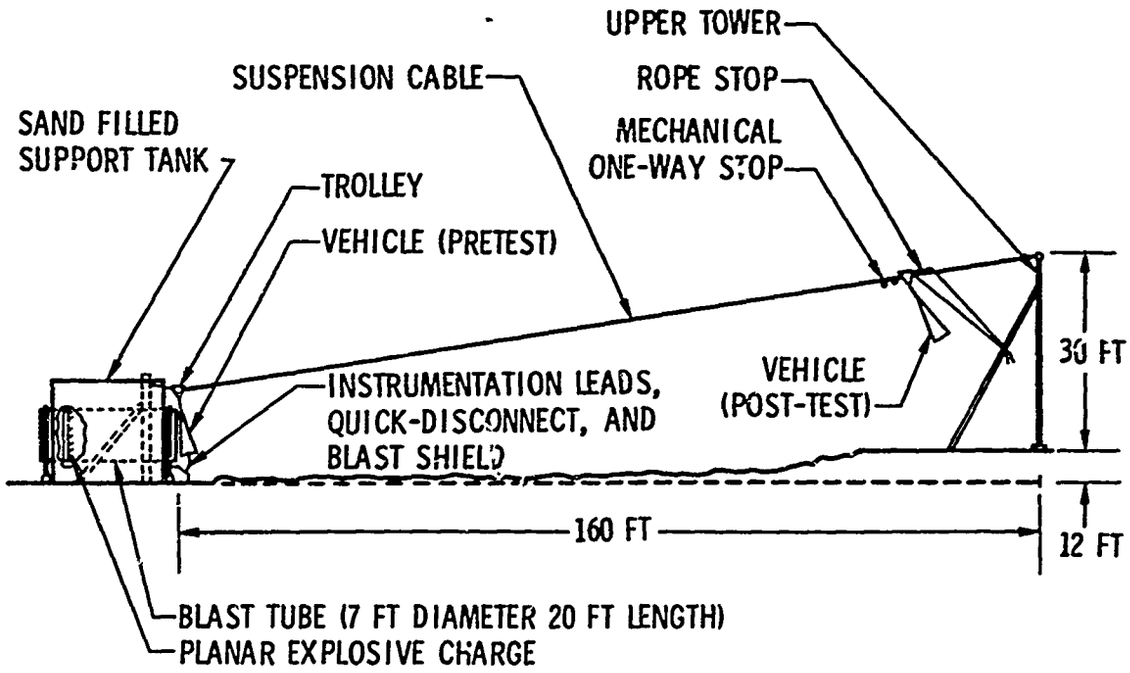

Fig. 7 – Seven foot diameter shock tube and vehicle support and retrieval system

Fig. 8 Shock tube test setup

aft-dome fasteners. This harness was supported from a steel frame cross-member by two support cables as shown in Fig. 10. For four of the impulse tests, the vehicle was suspended from the nose by a single cable attached to the two support cables as shown in Fig. 3. In both methods, the impulsive loads were principally horizontal and normal to the plane of support, causing the vehicle to swing up in pendulum fashion and gradually come to rest after several oscillations, without damaging the vehicles because of the support conditions.

INSTRUMENTATION TECHNIQUES

Strain Gages

The difficulty of preventing entirely or delaying strain gage failures long enough for the structural response to be obtained (3 to 4 milliseconds) of most structures increases very rapidly as the shock load levels reach the inelastic range of the structures, particularly if the rise times of the impulsive loads are in the low microsecond range (2 to 25 μsec). Previous MDAC impulsive tests of strain gage installations plus test results of other investigators showed that damage to strain gage installations occurred where the wire lead connections were made to the strain gage tabs. The strain gages and gage backing materials are inherently thin (< 3 mils) and continuous, and, with care, the adhesive can be kept thin during the installation. However, the solder connections of large wire leads are neither thin nor continuous, but are the more massive and discontinuous elements of the installation, so past failures would occur at the junction of the soldered leads to the gage tabs. The

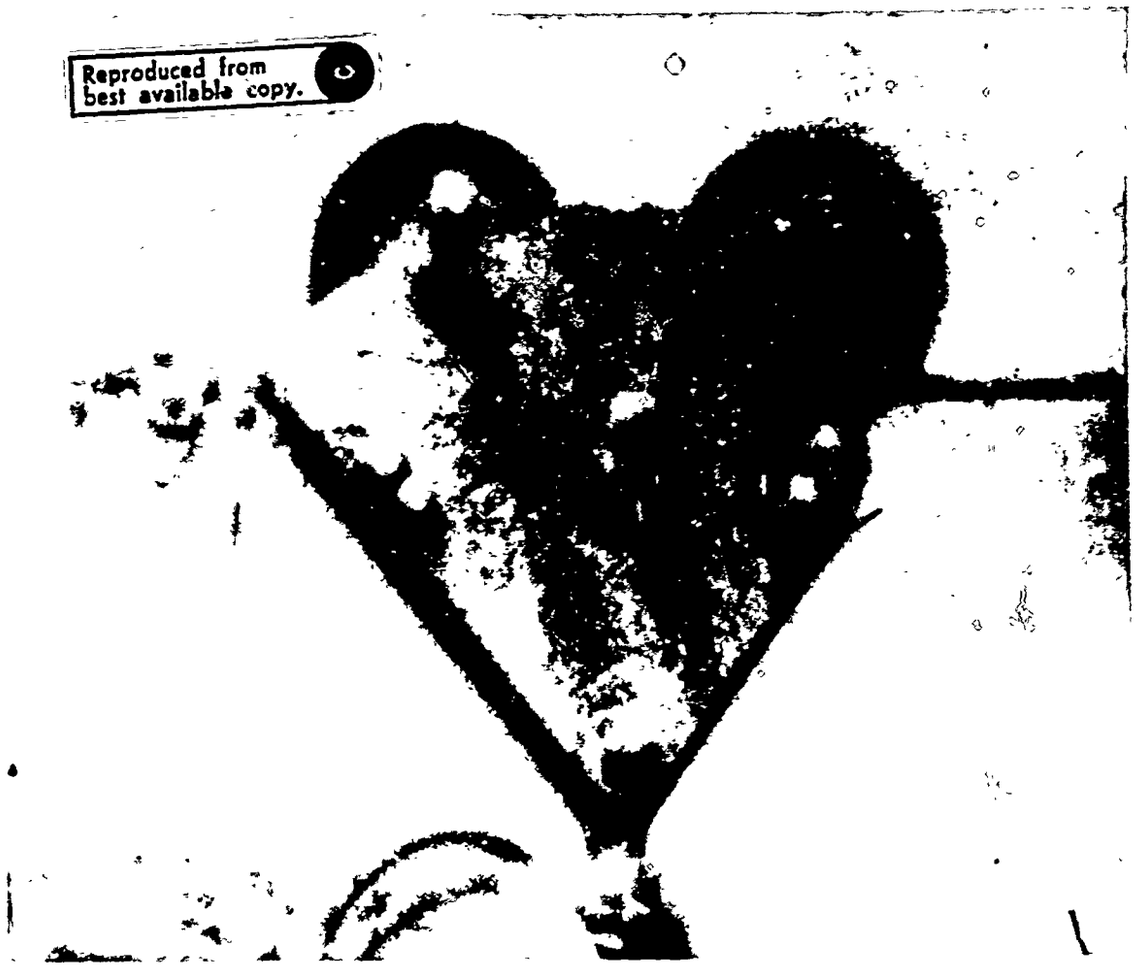

Fig. 9 Trolley

successful techniques used in this investigation to minimize these failures were (1) to use foil gages with thin, strong, flexible polyimide backing, (2) to reduce the gage of lead wires (No. 30 gage) and route them in strain-relieved wavy patterns a short distance around the vehicle to a less severly loaded point where the cable solder connections were made, (3) to minimize the size of the solder dots, and (4) to cover the entire gage assembly with glass cloth impregnated with RTV-118 bonded to the surface (Fig. 11). These installation techniques minimized the loss of strain gages due to stress-wave spallation even at load levels that produced significant yielding and cracking of the structure.

Micro-measurements EA series foil strain gages were selected for use because of their extended range (30,000 to 50,000 microstrain), good temperature compensation, good overall performance characteristics, and their thin (1 mil) strong, flexible polyimide backing. This gage backing material also has the relatively low acoustic impedance and good high strength properties that are desirable for high impulse resistant installations.

For all but 4 of the impulse tests, 24 strain gages were installed to measure the substructure and heat shield strains. For the shock tube tests, 22 strain gages plus 2 pressure transducers were installed. The 2 pressure transducers were located at 0 and 180 deg in the forward section of the vehicle. For 4 impulsive tests, 22 strain gages and 1 Kaman Nuclear noncontracting displacement gage were installed to measure the vehicle's structural response. The displacement gage was internally supported from a center frame by a cantilever type bracket. The displacement traces were clean and sharp, almost completely free of noise, one of the first times successful displacement measurements were made in this type of impulsive environment (Fig. 12).

Further improvements in both the strain gage and installation techniques have resulted in the development of a long lead strain gage and an installation where the long leads arch away from the surface, and the cable solder connections are made off the surface and are supported by shock attenuating foam. Care should be taken to ensure that no part of the unbonded long leads rests on the surface, since this portion of the lead could act like a flyer (during the

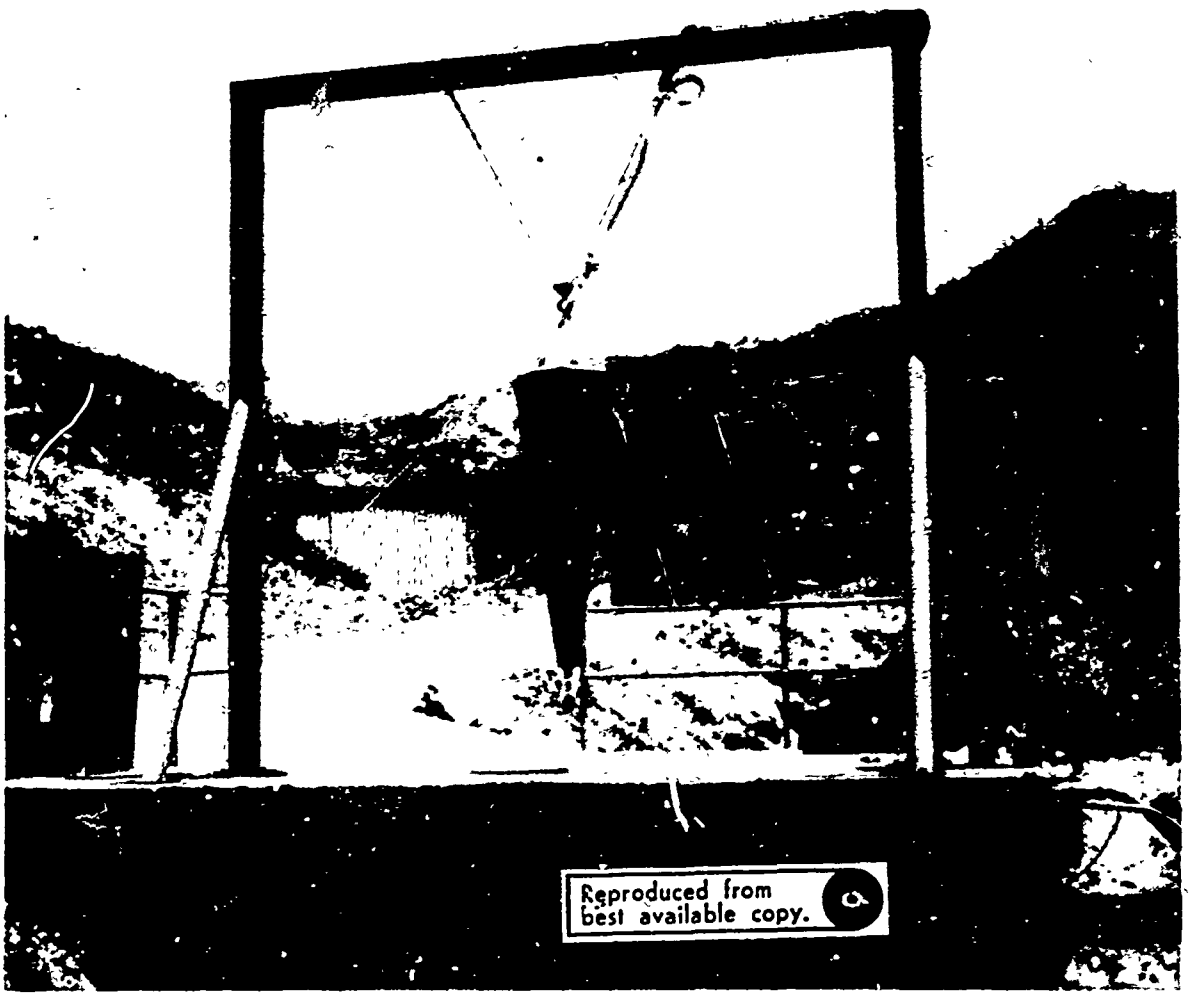

Fig. 10 – Impulse test setup

stress wave response) and tear the leads from the gage. These long lead strain gages are ideal in that they are a continuous thin mass that can be installed on the structure without the relatively massive discontinuity caused by soldering the lead wires to the gage tabs on the loaded vehicle surface. Additional details for the long lead strain gages are contained in Ref. [12].

Pressure Transducers

The Kistler pressure transducers were used to measure the blast pressures. These piezoelectric type transducers were the best available for the required fast response required of pressure measurements. The limitations of this type of pressure gage are its sensitivity to mechanical shock and ringing frequency (resonance-350 KHz). In addition, the connecting coaxial cables and associated quick-disconnect plug system are susceptible to effects from blast-wave impingement. These combined effects on the signal output caused distortions to the total pressure signal making it difficult to interpret the peak pressure and the pressure decay in the data taken during the early calibration tests. The four types of modifications made to minimize this signal distortion included (1) coaxial cables, (2) cable connectors, (3) quick-disconnect mounting panel, and (4) protective shields for the cable exiting from the base of the vehicle. The coaxial cable modifications consisted of the use of Kistler 131A oil-filled coaxial cable near the blast-wave exit area (junction box to disconnect panel, Fig. 13) and the use of microdot coaxial cable in the vehicle. The modifications to the cable connectors consisted of shock mounting of the disconnect plug panel, and a change of the disconnect plugs to standard BNC-type modified for automatic pullout. This latter modification provided the greatest improvement in noise reduction.

Data Acquisition System

The strain and pressure measurements from all of the vehicle instrumentation were recorded on magnetic tape by two 14-channel tape recorders. For all but 4 of the impulse tests, strain measurements for 12 channels were recorded on an 80 KHz Minneapolis-Honeywell Model 7600, and 12

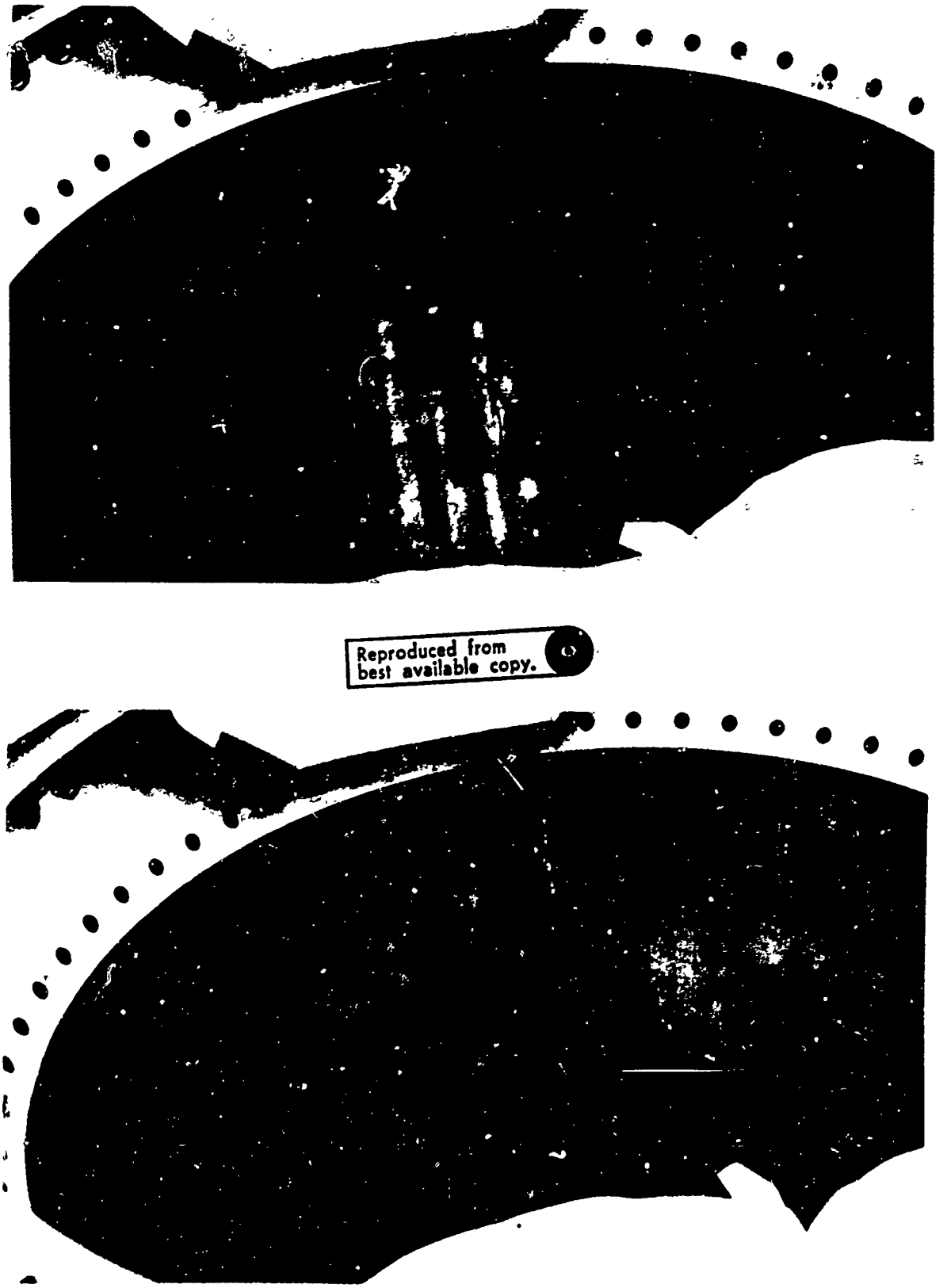

Fig. 11 – Strain gage installation

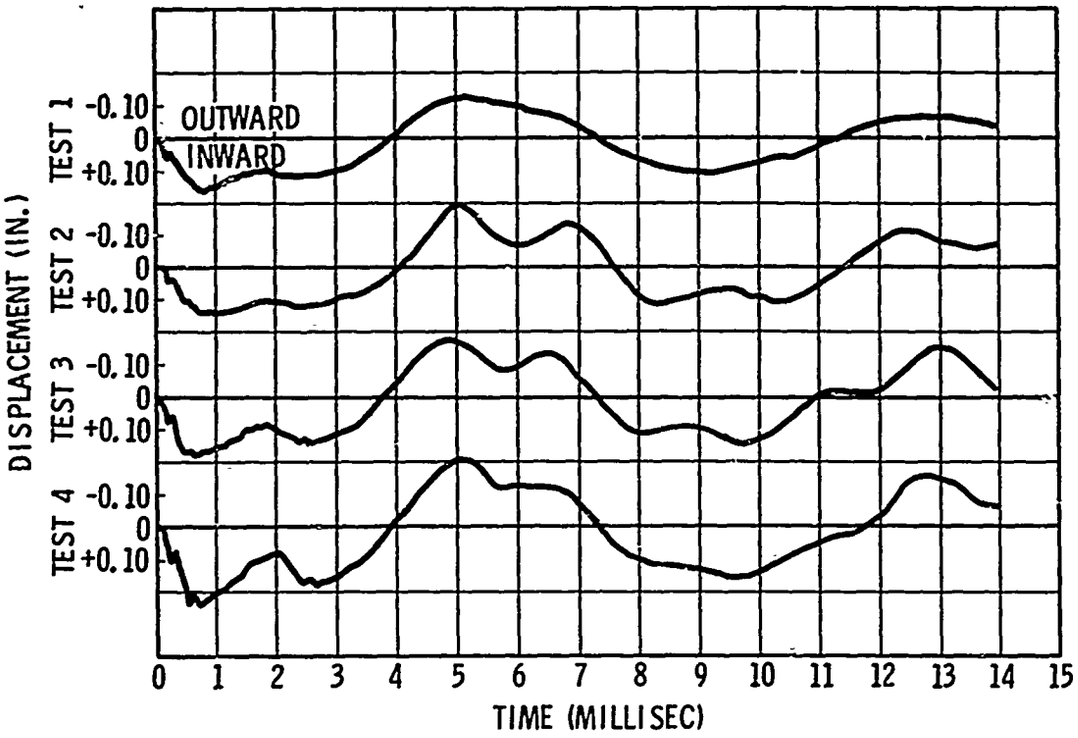

Fig. 12 – Displacement time curves

Fig. 13 Quick-disconnect panel and connector, blast tube calibration tests

channels on a 20 KHz Ampex Model FR1300 tape recorder. For 4 of the impulse tests, one displacement measurement also was measured on the Model 7600 tape recorder. For the shock tube tests, 11 channels of strain and 2 pressure measurements were recorded on the Model 7600 tape recorder and 11 channels of strain and 2 pressure measurements were recorded on the Model FR1300 tape recorder.

The strain signal measured by each strain gage passed through a signal conditioner and a differential amplifier before being recorded in FM mode on magnetic tape. The pressure signal measured by the transducer passed through a charge amplifier before being recorded in FM mode on magnetic tape. The displacement signal measured by the transducer passed through an impedance matching network and an oscillator-demodulator before being recorded in FM mode on magnetic tape. The data recorded on the Model FR1300 tape recorder system were limited by the 20 KHz response of the tape recorder. All of the other components in the systems had frequency responses greater than 80 KHz. Additional technical details concerning the data acquisition system components are presented in Refs.[8 and 10].

DISCUSSION

Selected vehicle structural responses (strain histories) will be presented in subsequent paragraphs as examples of the good quality strain data obtained and to substantiate the claim that good strain measuring techniques were used in this investigation. The theory designation on Figs 14 through 20

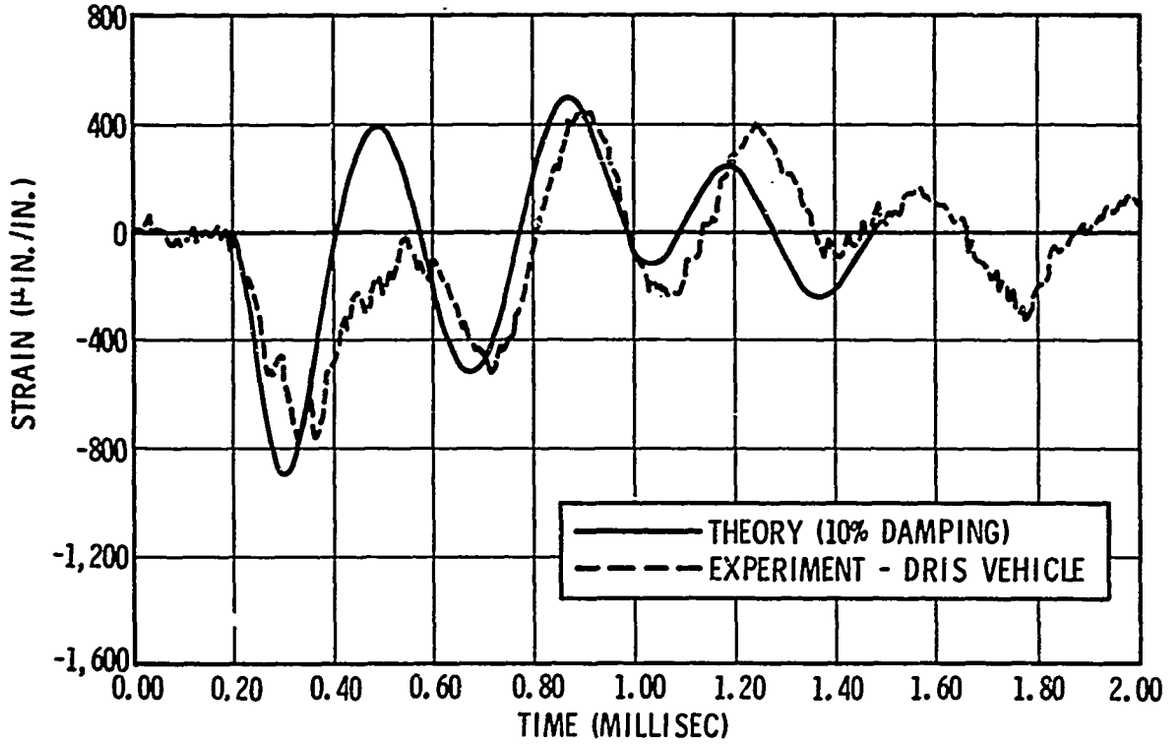

Fig. 14 – Correlation of SABOR3A/DRASTICII with DRIS vehicle test data substructure circumferential strain

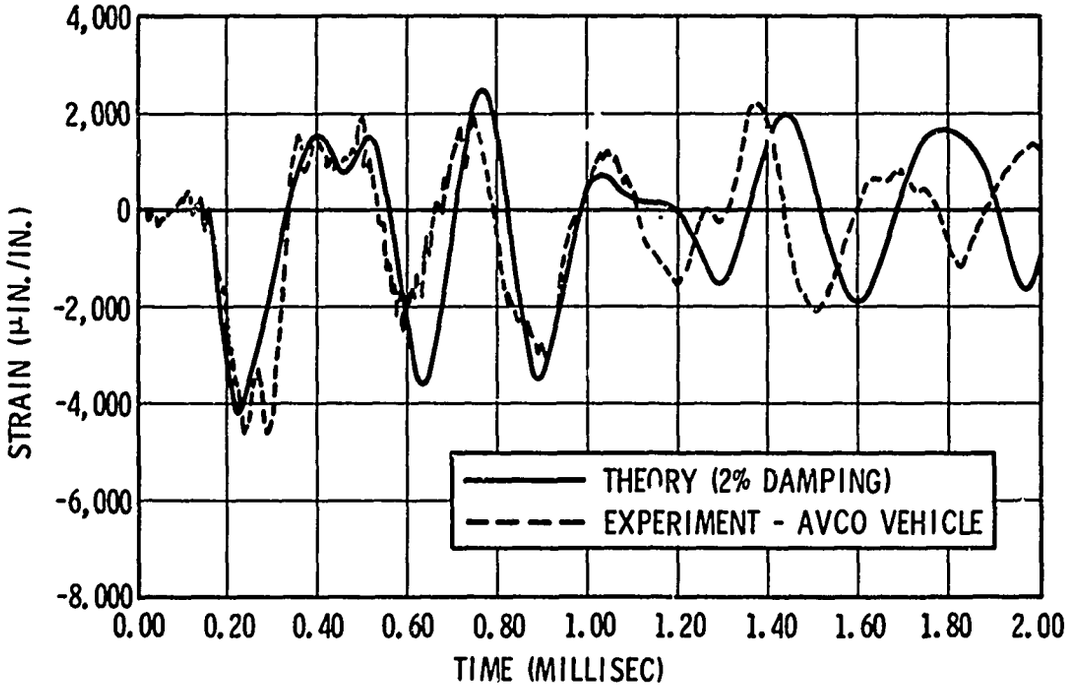

Fig. 15 – Correlation of SABOR3A/DRASTICII with Avco vehicle test data – outer fiber circumferential strain

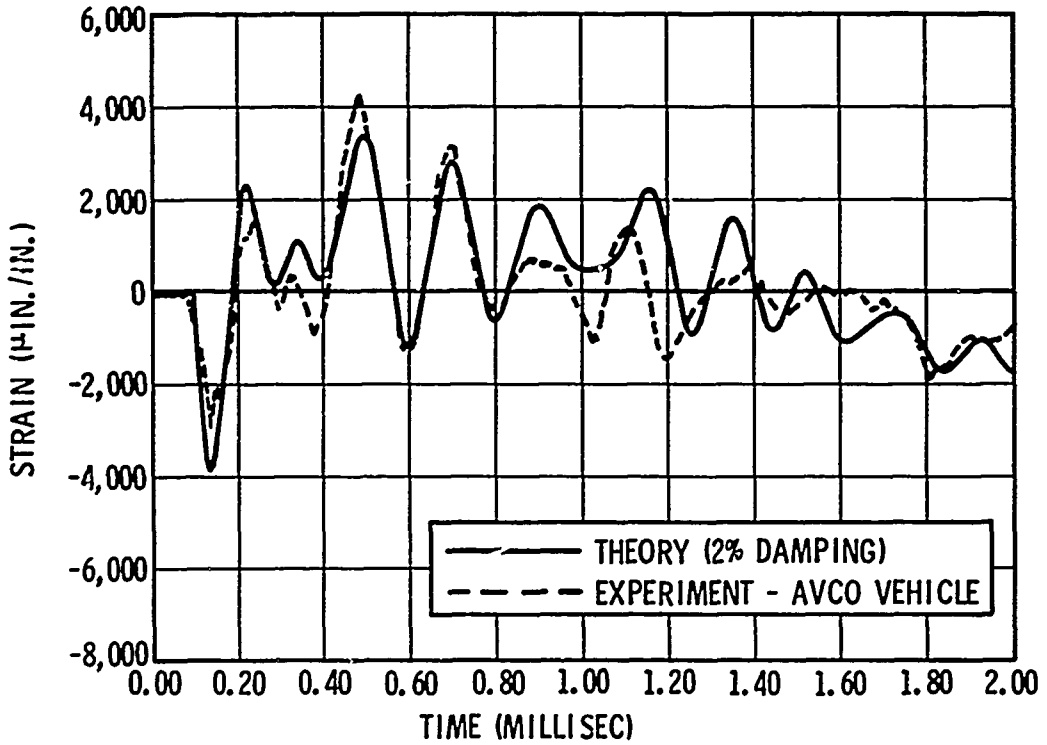

Fig. 16 – Correlation of SABOR3A/DRASTICII with Avco vehicle test data – inner fiber circumferential strain

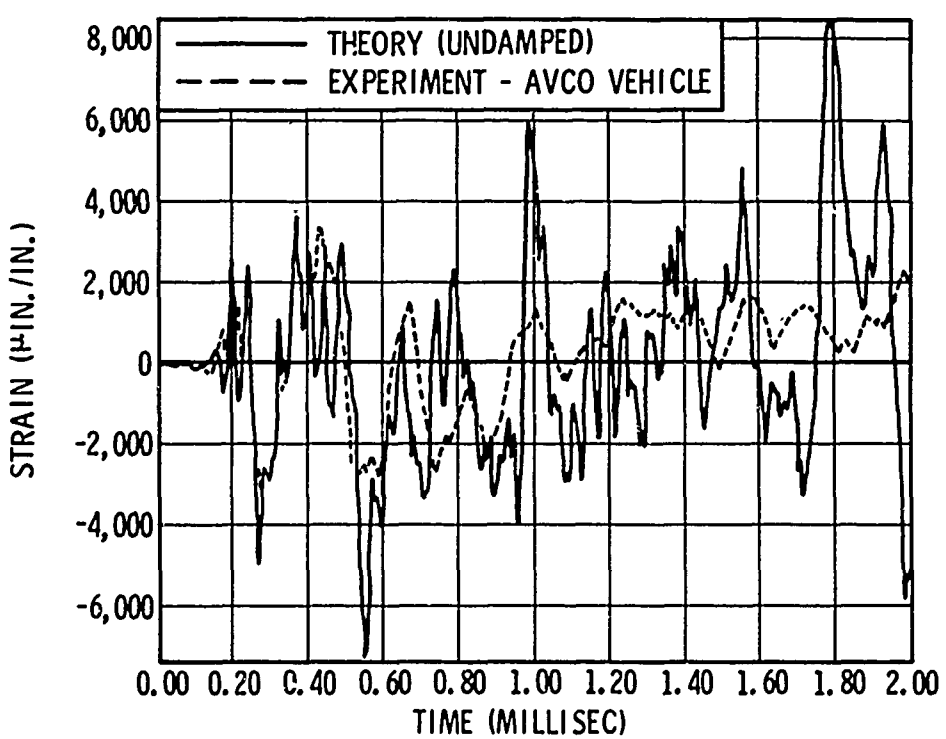

Fig. 17 Correlation of SABOR3A/DRASTICII undamped analysis with Avco vehicle test data - outer fiber meriodional strain

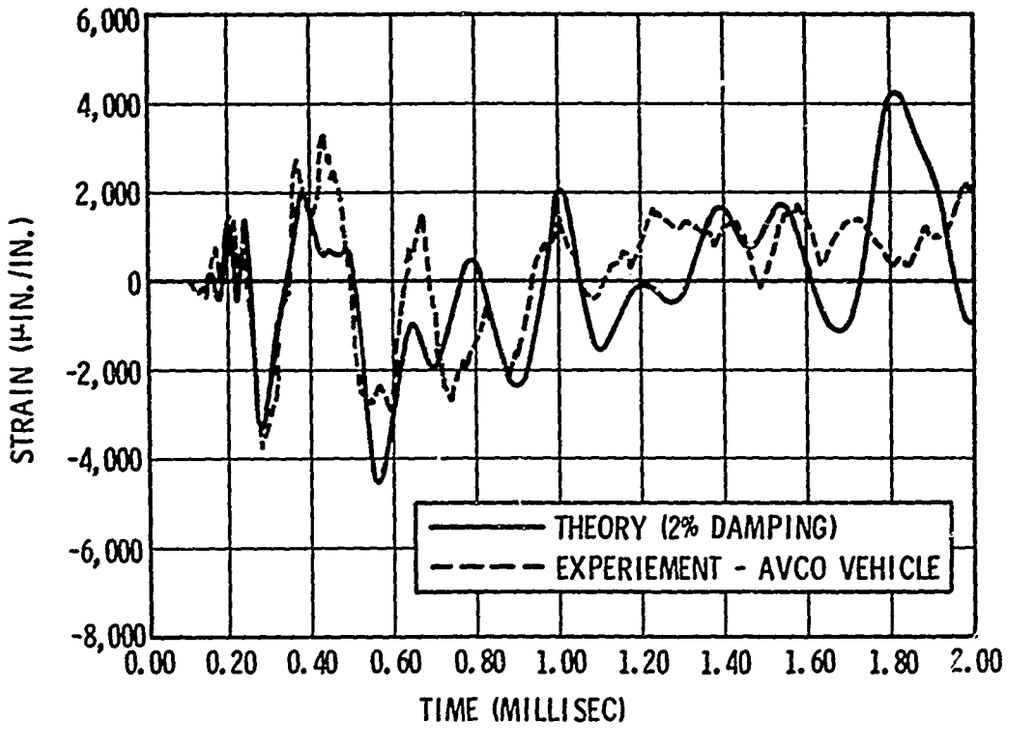

Fig. 18 – Correlation of SABOR3A/DRASTICII with Avco vehicle test data – outer fiber meridional strain

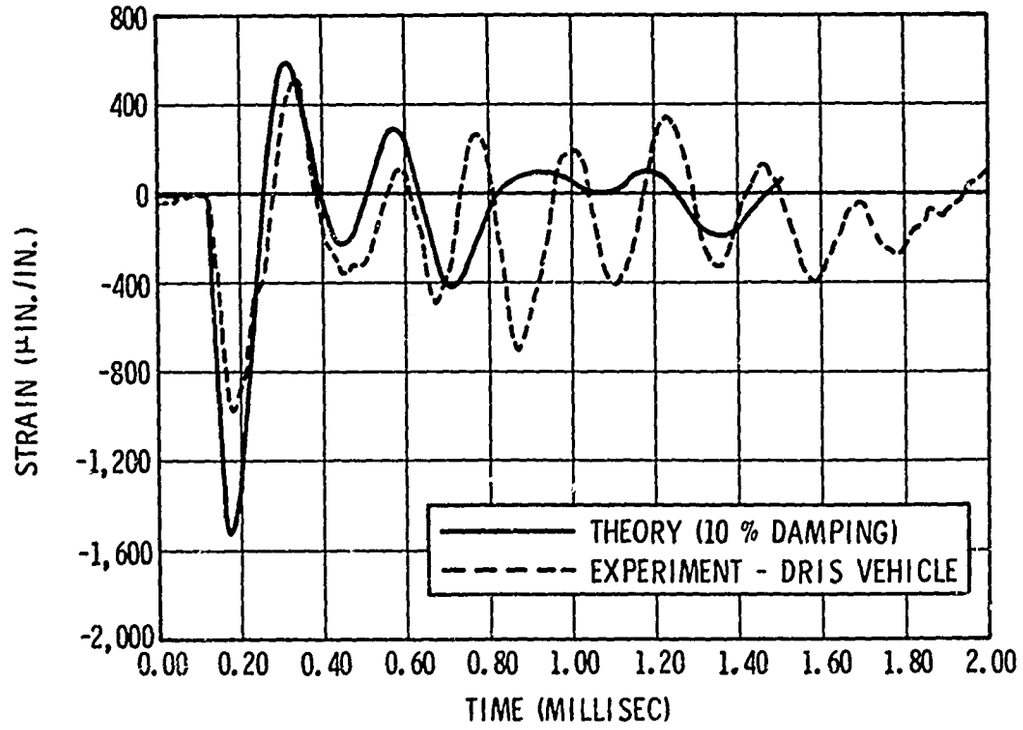

Fig. 19 Correlation of SABOR3A/DRASTICII with DRIS vehicle test data substructure circumferential strain

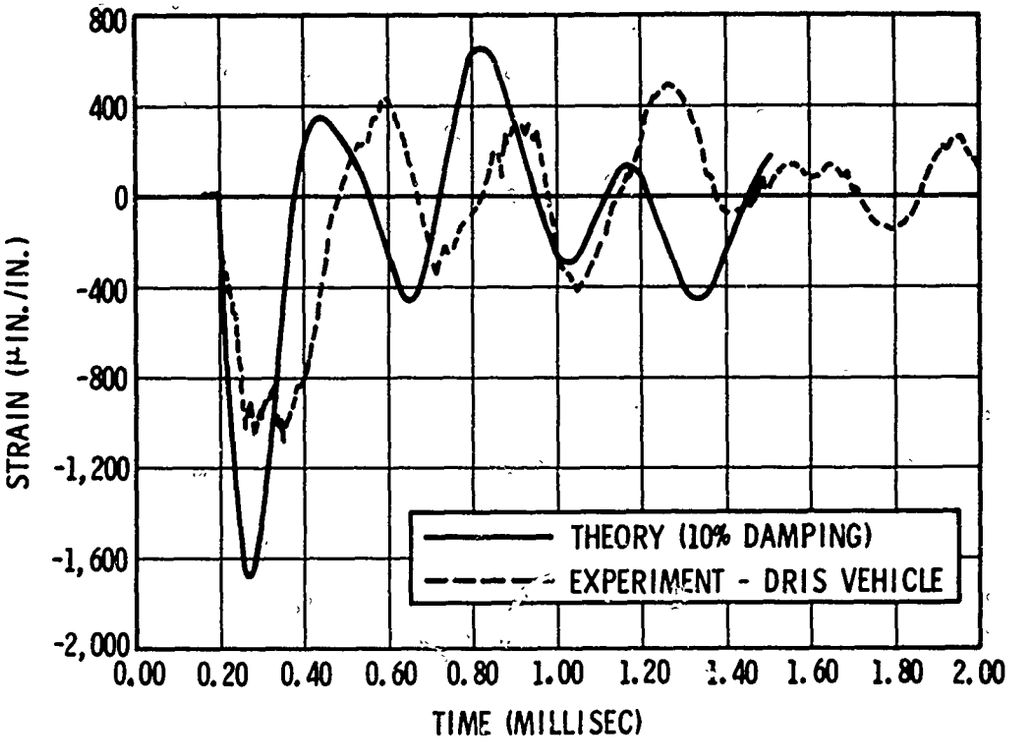

Fig. 20 – Correlation of SABOR3A/DRASTICII with DRIS vehicle test data – substructure circumferential strain

refers to SABOR3A/DRASTIC11 structural response computer code. In these strain comparison plots, the strain in microin is plotted against time in millisec. The angle designation, θ, refers to the strain gage angle location measured from $\theta = 0$ deg, the leading edge element line centered under the explosive load.

Three examples of the good agreement obtained between analysis and experiment are shown in Figs. 14, 15 and 16. Fig. 14 is for the DRIS vehicle substructure circumferential strain at vehicle station 59.6 and $\theta = 90$ deg. Fig. 15 illustrates the AVCO vehicle outer fiber circumferential strain at station 51.63 and $\theta = 0$ deg and Fig. 16 shows the AVCO vehicle inner fiber circumferential strain at station 34.02 and $\theta = 0$ deg. In each of the strain comparisons, the agreement in frequency response is very good, the agreement in magnitudes of peak strains is fair to good. The agreement of strain frequencies and magnitudes are especially good during the first millisec of vehicle response.

The effect of using damping in the computer code on the correlation can be seen by comparing Figs. 17 and 18. A very significant improvement in the meridional strain correlation can be noted when two percent damping is used (Fig. 18) as compared to Fig. 17, without damping. The analytical codes must have damping if they are to obtain favorable comparisons to test data.

The data acquisition systems frequency response was 80 KHz for all of the strain histories shown except the strain histories in Fig. 19, which was recorded on a 20 KHz response system. The experimental strain history in Fig. 19 is much smoother than any of the other experimental strain histories, the reason being that any frequency above 20 KHz has been damped out. In contrast to this, the significant strain amplitudes. (at about 40 KHz frequency) for several cycles on the first compression peaks of Figs. 20 and 21 were recorded on the 80 KHz response system. These high frequency responses would have been lost on the 20 KHz response system. The character of this high frequency strain signal, its location on the first compression peaks of many strain histories, and the significant amplitude at these high frequencies were strong evidences that these signals were strain, not extraneous noise. To ensure that these types of significant high frequency strain responses are not lost in future tests, a recording capability four to eight times the expected principal response modes would be advisable.

An excellent check on the validity of the strain measuring techniques would be a comparison of strains measured at the same location in different vehicles at the same impulse load. Such a comparison, shown in Fig. 21 shows the very good agreement between the substructure circumferential strains for the two vehicles. The minor differences are attributed to the differences in material properties and internal configurations and the usual experimental inaccuracies.

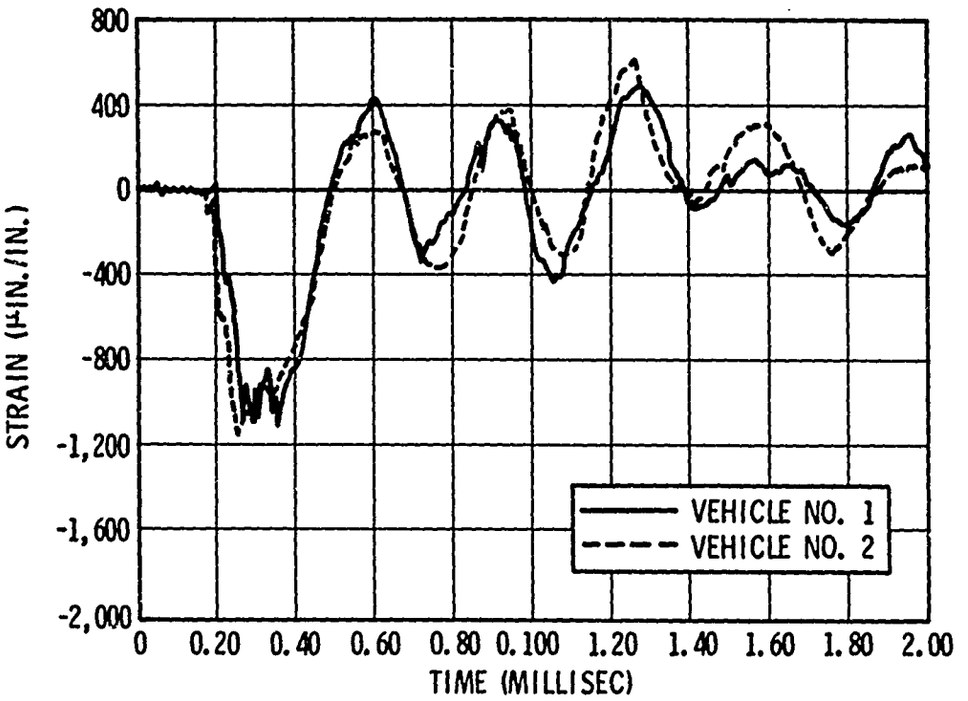

Fig. 21 - Comparison of experimental strain for two vehicles substructure circumferential strain

CONCLUSIONS AND RECOMMENDATIONS

The test techniques described herein were very successful and for the first time large quantities of good quality structural response (strain) data were obtained under severe shock environment that compared well with structural response computer codes (SABOR3A/DRASTIC11).

Data acquisition systems with frequency response capabilities of at least 80 KHz should be used for dynamic structural responses (strain) measurements so that significant high frequency strain responses are not lost. A recording capability of four to eight times the expected principal response modes would be advisable.

For blast tests using a free flight support and retrieval system, a better solution than using the quick-disconnect plug system to disconnect the instrumentation cables would be to loop about 10 ft of signal cable ahead of the vehicle then back to the blast shield and use the standard individual plugs (modified for automatic pullout) for each strain channel. This way the blast wave induced shock and vibration would be acting on tight fitting (standard) plug pins (instead of the looser quick-disconnect pins) for the time required for the vehicle to travel 20 ft when plug separation would occur. All of the structural response data would have been recorded long before plug separation so that the resulting plug separation noise would not affect the recording of the test data.

New test techniques of utilizing explosively driven shock tubes, to simulate the high aerodynamic/inertia or nuclear effects induced in the components of high performance defensive and maneuvering vehicles should be considered. Structural loading techniques to date have consisted of applying static loads to structures to simulate the aerodynamic and inertia loads with conventional loading straps, cables, and load linkages. This technique fails to give the proper load distribution because (1) the quasi-static inertia loads of skin frames, bulkheads, fittings, electronic black boxes, etc., cannot be simulated accurately by these conventional methods and (2) the size and configuration of these vehicles limit the access to internal systems and structure for load attachment points. In addition, current standard shock and vibration equipment cannot duplicate this severe internal load distribution because of the high impulse short duration loading environment applied to concentrated areas of these vehicles.

ACKNOWLEDGEMENTS

The DRIS investigation was funded by the Defense Atomic Support Agency (DASA) and was administered under the direction of the Air Force Space and Missile Systems Organization with Major N. J. Azzarita as technical administrator. R. A. Needham of the Aerospace Corporation served as principal technical monitor for the Air Force. This technical effort was performed by the Advance Structures and Mechanical Department, Research and Development,and the Structures Department, Development Engineering, McDonnell Douglas Astronautics Company. The author wishes to express his thanks to E. A. Fitzgerald R. J. Murphy, H. S. Parechanian, M. H. Schneider, Jr., G. C. Shanks, R. V. Smith, T. E. Strickland, and J. C. Telinde for their helpful suggestions in preparing this paper.

BIBLIOGRAPHY

1. G. R. Abrahamson, "Techniques for Simulating X-Ray Impulses on Re-Entry Vehicles (U)," Stanford Research Institute Final Report, Contract AF29-(601)-2592, AFSWC-TR-61-26, Mar.1961 (SRD)

2. G. R. Abrahamson, "Structural Response of Re-Entry Vehicles to Impulsive Loads (U)," Stanford Research Institute Final Report, AFSWC-TR-61-44, Contract AF29 (601)-2791, June 9, 1961, (SRD)

3. H. E. Lindberg, "Impulse Response of an Early A3X Polaris Re-Entry Structure (U)," Stanford Research Institute Final Report, Contract LMSC PO 18-10338 Under NOrd-17017, Nov.1, 1962, (SRD)

4. W. J. Schuman, Jr., "The Response of Cylindrical Shells to External Blast Loading, Part II," BRL Memorandum Report No. 1560, Aberdeen Proving Ground, Maryland, May 1964

5. A. L. Florence, "Structural Response of the Mark 6 Re-Entry Vehicle to Impulsive Loads (U)," Stanford Research Institute Final Report, TRD 63-3117, Contract AF29 (601)-5858, Nov.29, 1963, (SRD)

6. A. L. Florence, "Development of Long-Duration Explosive Loading Techniques (U)," Stanford Research Institute Semiannual Technical Summary Report No. 1, Contract AF29 (601)-6364, July 14, 1964 (C)

REFERENCES

1. D. W. Grand and A. M. C. Holmes, "Experimental Verification of Structural Response (U)," LMSC-B130200, Vol IVB, Sept.1965 (C)

2. H. E. Lindberg, D. L. Anderson, R. D. Firth, and L. V. Parker, "Response of Re-Entry Vehicle Type Shells to Blast Loads," Vol IV-C, Final Report LMSC 24-14517, Stanford Research Institute, Contract AF04 (694)-655, LMSC-B130200, Sept.30, 1965

3. H. E. Lindberg and R. D. Firth, "Simulation of Transient Surface Loads by Explosive Blast Waves," Vol II, Final Report AFWL-TR-66-163, Stanford Research Institute, Contract AF29 (601)-7129, 1967

4. R. J. Reck and P. L. Benson, "Structural Response of SPINE Conceptual Re-Entry Vehicle Models Under Blast Type Loads (U)," AFWL-TR-66-125, Douglas Aircraft Company, Santa Monica, Sept.1966, (S)

5. D. L. Anderson and H. E. Lindberg, "Impulsive Structural Response of SPINE Conceptual Re-Entry Vehicle Models (U)," AFWL-TR-66-163, Stanford Research Institute, Palo Alto, Dec.1966, (S)

6. R. J. Reck and T. E. Strickland, "Structural Response of SPINE Conceptual Re-Entry Vehicle Models Subjected to Mid-Duration Loads (U)," AFWL-TR-67-119, Douglas Aircraft Company, Santa Monica, Nov.1967, (S)

7. R. J. Reck and H. E. Lindberg, "Structural Response of the SPINE Re-Entry Vehicle Models to Blast and Impulsive Loads (U)," AFWL-TR-67-118, Douglas Aircraft Company, Santa Monica, Jan.1968, (S)

8. H. S. Parechanian, G. E. Wightman, N. K. Jamison, et al, "Dynamic Response Investigation of Simulated RV Structures - Vol II Impulse and Blast Tests (U)." SAMSO-TR-69-144, Vol II, McDonnell Douglas Corporation Report 63305, Sept.1969, (SRD)

9. M. H. Schneider, Jr., "Dynamic Response Investigation of Simulated RV Structures - Vol III Dynamic Analyses and Correlation to Test Results (U)," SAMSO-TR-69-144 Vol III, McDonnell Douglas Corporation Report 63306, Sept.1969, (SRD)

10. G. E. Wightman, B. A. Anderson, N. K. Jamison, et al, "Dynamic Response Invesitgation of Simulated RV Structures, Vol IV Elastic Response Tests of an Integrated (AVCO) Structure Under Impulsive Loads (U)," SAMSO-TR-69-144, Vol IV, McDonnell Douglas Corporation Report 63707, Sept.1969, (S)

11. M. H. Schneider, Jr., A. J. Cwiertney, Jr., H. L. Chane and J. S. Kirby, "STRECOS I - Structural Response Correlation Studies, Static and Dynamic Parametric Studies and Correlation of Dynamic Response Data (U)," SAMSO-TR-70-66, McDonnell Douglas Corporation Report, Jan.1970, (CNWDI)

12. J. C. Telinde, "Strain Gage Instrumentation for Magnetically Driven Flyer Plate Facility," McDonnell Douglas Astronautics Company Paper WD 1700, Presented at SESA Annual Meeting, Oct.1971

VIBRATION FIXTURING – NEW CELLULAR DESIGN, SATURN AND ORBITAL WORKSHOP PROGRAMS

Russell L. Stafford
McDonnell Douglas Astronautics Company
Huntington Beach, California

During the test programs for the Saturn S-IVB/V, IB, and Orbital Workshop, most of the vibration items were tested by mounting them on sections of vehicle structure representing actual vehicle installation. Some vehicle sections were as large as 5-1/2 by 10 ft. Fixtures, for mounting and holding these structures during vibration, having the capability of transmitting vibration up to 2,000 Hz to the extreme edges of the structure and, subsequently, to the test items, presented special design problems. Most large vibration fixtures used for these programs were of welded tubular construction. The welded tubular concept proved successful, complex, heavy, and costly. Therefore, a new cellular structure fixture design concept was used for some items of the Orbital Workshop. The cellular structure concept discussed herein has a higher stiffness-to-weight ratio and is less costly than previous tubular designs.

INTRODUCTION

Among the most important factors influencing the effectiveness of vibration tests is the vibration fixture. Vibration fixtures, particularly the very large fixtures to be discussed herein, present special design and manufacturing problems and represent a significant cost to a test program

This paper presents a brief history of the vibration fixturing for the Saturn S-IVB/V and IB Programs and places particular emphasis on a new cellular fixture concept used for some items of the Orbital Workshop Program. On all of these programs, McDonnell Douglas Astronautics Company is prime contractor to the National Aeronautics and Space Administration (NASA/MSFC).

During the test programs for the Saturn and Orbital Workshop, approximately 475 of the vibration items were mounted on portions of vehicle structure representing the actual vehicle installation so that the response of the item under test would more closely simulate the actual response. The response is primarily induced by rocket and boundary layer noise and is of a random nature with frequencies from 0 to 2,000 Hz. The portion of vehicle structure to which the test item was attached, referred to as the back-up structure, was in turn fastened to a stiff and often very large fixture which provided the mechanical linkage between the vibration generator (shaker) and the vehicle structure. This type of setup is generally defined as "soft mount." The remaining approximately 130 items were "hard mounted" directly to a rigid vibration fixture for testing. This paper will be concerned only with the fixturing for the soft mount tests. These tests require the large, complex, and more costly fixtures.

GENERAL FIXTURE REQUIREMENTS

The fixture must be designed to transmit vibration up to 2,000 Hz to the extreme edges of the back-up structure and, subsequently, to the item being tested. Fixtures for soft mount tests are often very large. Some weighing 1,250 lb and holding portions of the vehicle structure 5-1/2 by 10 ft have been made. These fixtures are difficult to design, manufacture, and are costly. Ideally, a perfect vibration fixture would have no resonances below 2,000 Hz, but realistically this is impossible when testing large specimens So, the trade-off is to make them as stiff as possible within a weight that the vibration shaker can handle. In the design of fixtures, it is necessary that they be stiff laterally as well as in the direction of excitation so that the lateral resonances of the members do not affect the test specimen. These resonances can cause an over or under test of the specimen.

LARGE TUBULAR VIBRATION FIXTURES FOR SATURN AND ORBITAL WORKSHOP PROGRAMS

Large vibration fixtures for the Saturn S-IVB/V and IB, and for some items of the Orbital Workshop Programs have a trussed structure of 4-in. diameter by 1/4-in. wall standard magnesium tubing for the basic structural members. Spans of less than 20 in. of these tubes have first bending mode and ring mode frequencies above 2,000 Hz. Also, the tubes are foamed to provide damping. Magnesium is the most commonly used material for the fixtures because (1) it is 37 percent lighter than aluminum, (2) has a stiffness-to-weight ratio greater than aluminum, and (3) has high internal

damping characteristics. When bolts are used (i.e., attachment of the fixture to the shaker and of the adaptors to the basic fixture), the joints are designed with properly sized and preloaded bolts so that resonance, and thus dynamic decoupling in the joint, does not occur within the test frequency range [1]. Examples of large tubular fixturing are shown in Figs. 1 and 2. Details of the general design criteria for these fixtures are contained in Ref. [2].

VIBRATION FIXTURES OF CELLULAR DESIGN

Recently, for some items of the Orbital Workshop Program, a new fixture design concept has been used. The basic structure is cellular with the cells made of thin flat magnesium plates with a hole in each face of each cell to (1) lighten the structure and (2) raise the first mode frequency. This design, for some configurations of fixturing, provides maximum stiffness in the direction of excitation and keeps the undesirable lateral response to a minimum. The final step in the manufacture of this fixture, after completion of welding, is to fill all cavities completely with low density foam to provide high internal damping. High damping is a desirable characteristic for vibration fixtures because dynamic isolation is less severe when the most damping is present. The overall purpose of the new design is to make a fixture with a greater stiffness-to-weight ratio and at a lower cost than previous designs. In addition to being lighter and somewhat less costly, it is expected that fixtures of this construction will have a greater fatigue life than the tubular type because of less residual stress as evidenced by less warpage during fabrication.

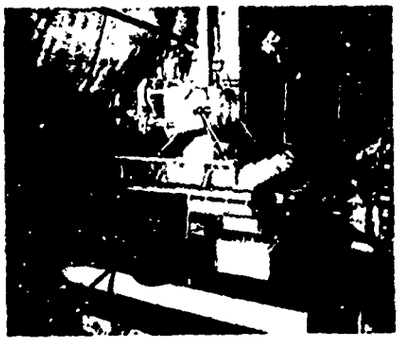

THRUST AND TANGENTIAL AXES

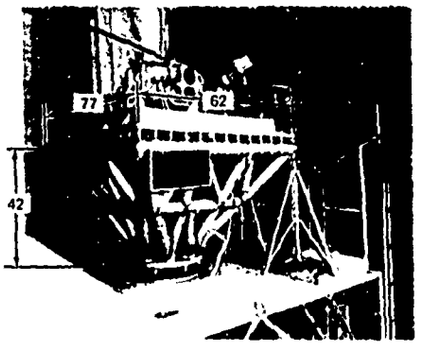

RADIAL AXIS

Fig. 1 Vibration fixturing and setup for Orbital Workshop fan cluster

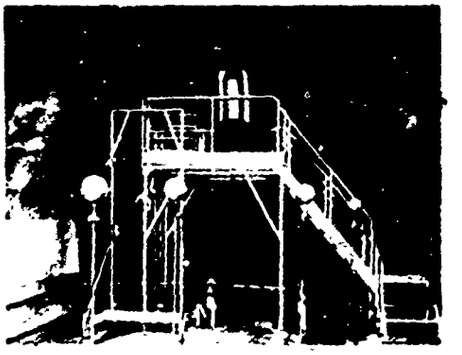

THRUST AXIS

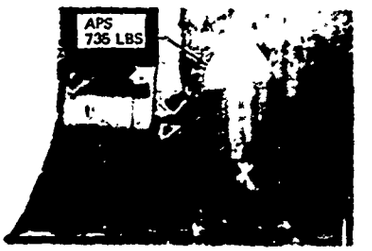

TANGENTIAL AXIS

RADIAL AXIS

Fig. 2 Vibration fixturing and setup for Saturn S-IVB/V auxiliary propulsion system (APS)

A fixture of cellular design in various stages of fabrication is shown in Fig. 3. The cells are sized so that the first mode frequency of the individual members is high, i.e., approximately 2,000 Hz for the members on the external surface and approximately 800 Hz for the inner members which will be buried in 2 pcf density, closed cell polyurethane foam when the fixture is completed

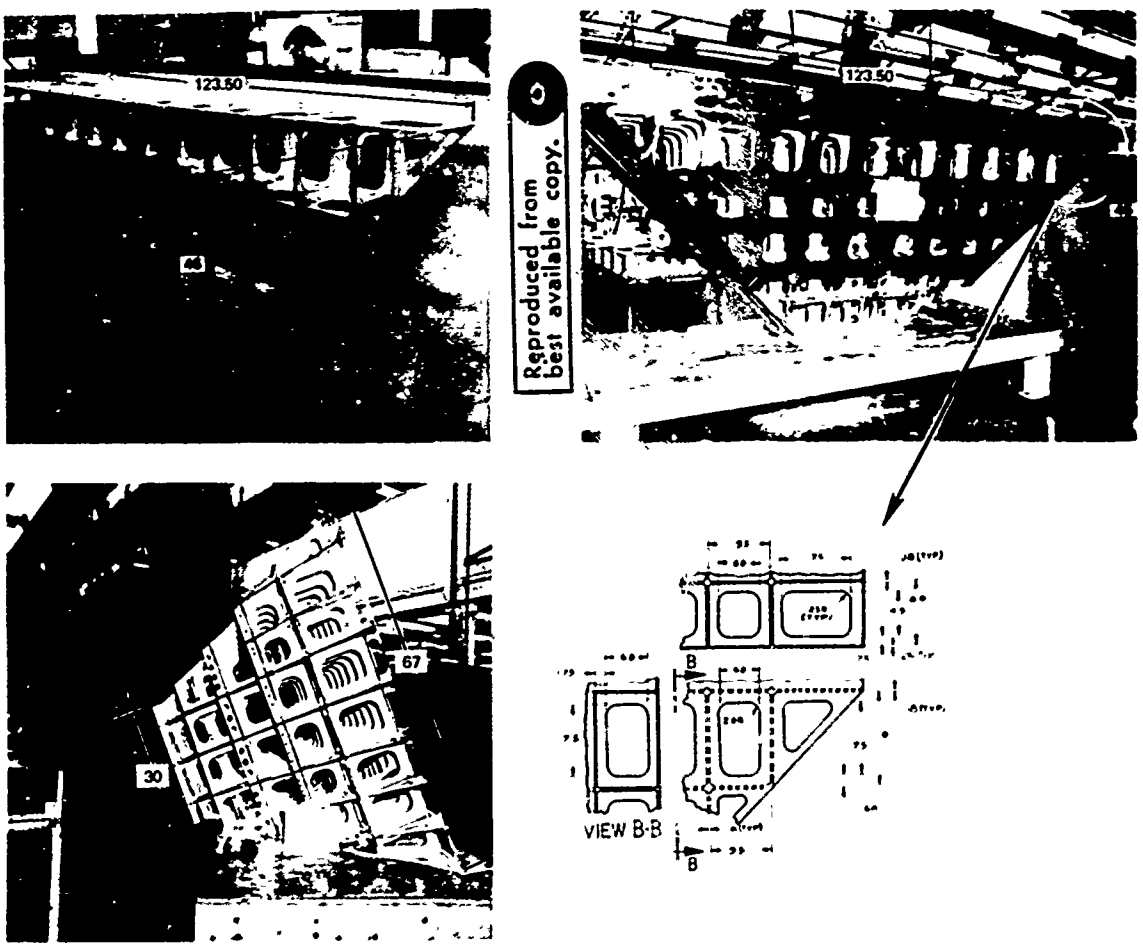

Fig. 3 Cellular fixture in various stages of fabrication

For the fixture shown in Fig. 3, the cells were sized using continuous plate natural frequency data which are available in literature with a wide variety of boundary conditions [3], with corrections for the increase in frequency because of the central holes in the face of each cell [4].

A completed standard vibration fixture of cellular design is shown in Fig. 4 in the vibration setup for testing of a typical installation for one of the thruster attitude control system pressure spheres used on the Orbital Workshop. This fixture adapts from a 30-in. diameter shaker head to the 48 by 48 in. platform for specimen mounting. Access for the shaker attachment bolts is provided by holes through the foam. This fixture has performed well for many tests.

LARGE VIBRATION SETUP WITH CELLULAR FIXTURES

The cellular fixture shown in Fig. 3 and a similar but smaller fixture are shown in the vibration setup of Fig. 5. The setup is for one axis of vibration for the qualification test of the Orbital Workshop Solar Array System. This is an example of a very large soft mount test using large sections of vehicle structure for specimen mounting.

The specimen is one of the two Orbital Workshop solar array wings. (TRW, a major subcontractor for the McDonnell Douglas Astronautics Company (MDAC), has a contract to design, build, and test the Solar Array System. However, the vibration fixturing for this phase of testing was designed and built by MDAC.)

The overall setup (Fig. 5) is 60 ft long by 14 ft high. The total weight of the solar array wing, plus the forward and aft fixtures with their back-up structures, is approximately 5,000 lb. The beam structures shown surrounding each shaker are support structures to fasten the close tolerance hydraulic bearings required for shaker armature lateral support. These supports are necessary to react a bending moment which would be induced into the armature, caused by the flexibility of the solar array wing and the unsymmetrical attachment of the solar array wing to the back-up structures.

Fig. 4 - Standard adaptor fixture of cellular design

The solar array radial axis vibration test requires the largest fixture ever built at MDAC for testing on an electrodynamic shaker. The required fixturing is so large that two of the largest available electrodynamic shakers are marginal in force capability for some of the test conditions. The cellular fixture design was used for this configuration of fixturing because they are approximately 20 percent lighter than equivalent tubular fixtures.

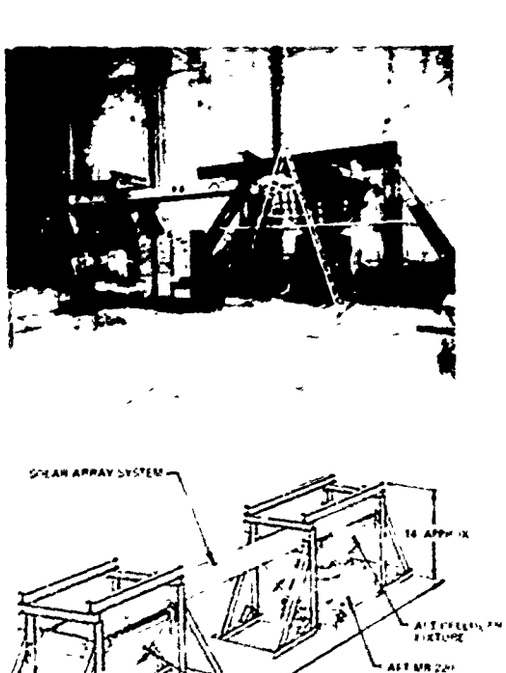

Fig. 5 - Solar array radial axis vibration setup using cellular fixtures

REFERENCES

1. O. J. Zamparo, "Designing Tight Bolted Joints For Vibration Environment," The Shock and Vibration Bull. No. 34, Part 5, pp. 273-277, Feb. 1965

2. L. G. Smith, "The Design of Large Vibration Fixtures S-IVB Stage Design Development and Qualification Program," The Shock and Vibration Bull. No. 34, Part 5, pp. 243-253, Feb. 1965

3. G. T. Klees, "Vibration Frequency Charts," Machine Design, pp. 139-141, Dec. 22, 1960

4. E. F. Shroyer and H. S. Bieniecki, "Effect of a Central Circular Hole On Fundamental Plate Frequency," ASME Publication, 69-VIBR-62

BIBLIOGRAPHY

1. B. S. Klee, D. V. Kimball and W. Tustin, "Vibration and Shock Test Fixture Design," Tustin Institute of Technology

2. R. J. Roark, "Formulas For Stress and Strain," Third Edition, McGray-Hill, 1954

3. "Shock Vibration and Associated Environments," The Shock and Vibration Bull. No. 27, Part IV, June 1959

WALL FLOW NOISE IN A SUBSONIC DIFFUSER

E. F. Timpke
California State College
Long Beach, California

and

R. C. Binder
University of Southern California
Los Angeles, California

This paper presents the results of an experimental investigation of wall flow noise in a variable-angle two-dimensional subsonic diffuser. Measurements were made of the sound pressure level, power spectral density, and the cross-correlation function. Wall noise measurements were made at various locations in the diffuser for flow through a parallel wall channel, flow approaching separation, and separated flow. The sound pressure level increased as the diffuser angle increased, and reached a maximum at flow separation. The sound pressure level was as much as 28 decibels higher at the separation point as compared to the sound pressure level for flow between parallel walls. The magnitude of the root-mean-square wall pressure fluctuations in turbulent flow was 0.0053 times the free stream dynamic pressure. This value compares fairly well with other values reported in the literature. The convection velocity was 0.83 times the free stream velocity for flow in parallel walls and decreased to 0.73 times the free stream velocity beyond separation. An analytical distribution function was developed to describe the spectral noise characteristics of the large scale turbulent eddies as the flow field changed.

INTRODUCTION

Various studies have been made of airflow noise, as for free jets and boundary layers. There is a lack of information on the characteristics of wall flow noise in a subsonic flow, with and without separation. This type of flow noise is common in various channels and piping systems. Some features of this noise have not been fully detailed in the previous literature.

This paper presents the results of an experimental investigation of the wall noise associated with the flow of air in a two-dimensional diffuser. The noise was measured with a microphone in the wall of a diffuser. Measurements were made of the overall sound pressure level, power spectral density, and the cross-correlation function. These measurements were made at various locations in the diffuser wall for flow between parallel walls, flow approaching separation, and flow with separation. Fluid flow parameters measured were wall static pressure, velocity, boundary layer thickness, and diffuser angle. The objective of the study was to relate certain acoustic and fluid flow parameters.

DIFFUSER APPARATUS

Figure 1 is a schematic of the flow test section. A low-noise, low-turbulence fan system was used to develop flow in the variable-angle two-dimensional diffuser. The diffuser had an inlet bell, and a 3 in. by 12 in. throat (3 in. in the plane of two-dimensional flow) with one wall fixed parallel to the approach flow and the other wall movable; each wall was rigid. This arrangement was used to provide a stable flow. With the diffuser walls parallel, the velocities ranged from about 75 to 110 feet per second. The movable wall was instrumented to provide sound pressure level (SPL), power spectral density, and cross-correlation data for the pressure fluctuations adjacent to the surface for different flow field conditions. The angle θ is the diffuser angle.

VELOCITY PROFILES

Velocity profiles are presented non-dimensionally in Figure 2, and show reasonable agreement for the zero pressure gradient case ($\theta = 0$) to those of Schloemer (1). They are typically turbulent profiles and were taken for Reynolds numbers ranging from 4.6 to 8.2 x 10^5. The adverse pressure gradient case ($\theta = 10°$) gives an indication of how the velocity profiles change as flow separation is approached. Velocity data were not obtained immediately adjacent to the movable diffuser wall due to large manometer deflections resulting from flow fluctuations and instabilities as the diffuser angle was increased.

SOUND PRESSURE MEASUREMENTS

All wall sound pressure measurements were made using a Massa 141 B microphone mounted flush with the inside of the movable diffuser wall. The Massa microphone sensing surface has a diameter of 0.5 inch; this size sensor may have caused some cancellation of the high frequency noise; the spectral data indicated little noise at frequencies above 500 cycles per second. A sound level meter was used to measure the SPL and a heterodyne type sonic analyzer (2) was used to determine power spectral density as a function of frequency.

The diffuser angle θ is indicated in Figure 1. Figure 3 presents overall SPL as a function of diffuser angle for velocities of 77.5, 96, and 106 feet per second. These velocities were measured with diffuser walls parallel ($\theta = 0$). For a diffuser angle of 0 degrees, the SPL is approximately the same for all velocities, namely about 56 to 57 decibels (about 15 db above the laboratory background noise, which had essentially a flat spectrum). All curves have the same characteristic shape; the SPL increases until it reaches its maximum value at the separation point, and then decreases as the diffuser angle is increased beyond separation. As the diffuser angle is increased, the SPL is influenced by the velocity; the SPL increases as the velocity increases.

Figure 4 presents the SPL values of Figure 3 as a function of velocity to the fourth power for separated flow (the peak values of Figure 3) and beyond separation ($\theta = 30°$). Figure 4 shows a linear relation between SPL and the fourth power of the velocity. Using the relations presented by Ribner (3) for the power radiated by a monopole source (pulsating sphere model), it can be shown that the sound power is proportional to the fourth power of some characteristic velocity. For this model, Ribner gives the radiated sound P as proportional to $Q^2f^2/\rho c$. For dynamic similar systems of monopole sounds, one can specify that each system be characterized by a typical velocity, U, dimension, L, and frequency, f, proportional to U/L. Since the mass rate, Q, is UA, then the sound power, P, is proportional to U^4L^2/c. Thus a U^4 law is characteristic of the sound power radiated by systems of monopole sources. Figure 4 shows a linear relation between SPL and the fourth power of the velocity. For this separated flow case, if a far acoustic field is developed, then there is the prospect that the sound sources are of the monopole type. At present, there is not sufficient evidence to reach a firm conclusion, one way or the other, for this prospect.

Measurements of power spectral density showed that most of the wall flow noise was in the low frequency range; large amplitudes were found in the range from 100 to 300 cps. Figure 5 shows power spectral density versus frequency for several diffuser angles. Figure 5 indicates that the power spectral density decreased as the diffuser angle was increased. For the case in which the flow separates (θ about 20 degrees), the spectrum is fairly flat and tends to remain flat after separation occurs (θ from 25 to 30 degrees). For flow beyond separation, the power spectral density is similar to the "blow-torch" noise associated with ordinary free jets.

The power spectral density is shown in non-dimensional form in Figure 6. The data of Willmarth (4) and Harrison (5) are also presented for comparison, and illustrates the characteristic decrease in spectral density with increasing frequency. An appreciable decrease in spectral density also occurred at the lowest frequencies measured; this was attributed to the strong influence of boundary layer intermittence on pressure fluctuations at low frequencies. The overall level of spectral density is much higher in the present investigation; this is probably primarily due to the rather thin boundary layers (0.075 in.) studied, and the noise being largely in the low frequency range (less than 300 cps). This last feature implies noise in the diffuser is caused mostly by large scale eddies.

Let k represent the ratio of root-mean-square wall sound pressure fluctuations to the free stream flow dynamic pressure. Willmarth (4, 6) reported two values for this parameter, $k = 0.0035$ and $k = 0.006$, each as being constant, and independent of velocity and Reynolds number. Harrison (5) reported an average value of $k = 0.0095$. In the present investigation, a slight variation with velocity was observed; a value of $k = 0.0053$ was obtained.

CROSS-CORRELATION MEASUREMENTS

Figure 7 shows a schematic of the electronic correlator system used. The microphones were arranged so that the output of the upstream microphone (one closest to the diffuser throat) was fed into a time delay unit. The time delay was accomplished with a variable delay line which permitted a selection of

delay times ranging from 0 to 10 milliseconds. The sound pressure fluctuations (microphone output voltages) were amplified and fed into a sum-difference unit which was designed to have as output, either the sum of the input signals or the difference between them.

The output of the sum-difference unit was fed into a true rms voltmeter. The voltmeter provided as output the rms value of the input signal which, in the case of the sum, is

$$\text{sum} = \sqrt{\overline{(E_1 + E_2)^2}} \qquad (1)$$

and for the difference, the input is

$$\text{difference} = \sqrt{\overline{(E_1 - E_2)^2}} \qquad (2)$$

These outputs are all that is required to compute the cross-correlation function.

Measurements were made for flow with parallel walls, for flow without separation, and for flow with separation. For each case, noise which passes the upstream microphone will be sensed, and at some time later, this noise will pass the downstream microphone and be sensed again. Consequently, the cross-correlation function will be a maximum for some delay time which corresponds to the convection speed of noise adjacent to the diffuser wall. The convection speed, U_c, along the diffuser wall is related to the free stream velocity, U_o, by the relation

$$U_c/U_o = L/TU_o \qquad (3)$$

where T is time delay and L is the distance between sensing ports. Cross-correlation measurements of the sound pressure fluctuations were made for sensing port distances of 0.406, 0.586, and 0.765 inch. For these distances, no dependence of convection velocity on spatial separation was observed. Various time delays were tried until the maximum value of the cross-correlation function was found.

Figure 8 shows a plot of velocity ratio, U_c/U_o, versus angle setting of the movable diffuser wall. With the movable wall set at zero degrees, the velocity ratio, U_c/U_o, was found to be 0.83 which is about 4 percent higher than the results of some other investigations (4, 5, 6). In all cases, the velocity ratio, U_c/U_o, decreased as the angle of the movable wall was increased. It is interesting to note that a strong degree of correlation still exists between the signals being sensed for diffuser angles of 25° and 30°, although the flow is no longer attached to the diffuser wall. Figure 8 indicates that the convection velocity decreases from 0.83 U_o to 0.73 U_o as the diffuser angle is increased from 0° to 30°, which is a decrease in the convection velocity along the diffuser wall of about 12 percent.

AN ANALYTICAL EXPLANATION OF NOISE

The following simple theory, with empirical constants, was developed to describe the change in the noise spectral characteristics as the flow changes from boundary layer flow to separated flow. It should be pointed out that the analysis presented here probably does not apply to boundary layer noise. The noise phenomena reported here for separating flow in a diffuser does not scale with boundary layer thickness; consequently, it is not considered boundary layer noise. Also, the high frequency noise associated with the small eddies characteristic of turbulent boundary layers was not observed. This analysis is based on the assumption that the acoustic energy is primarily a function of frequency and the diffuser angle. The theoretical model used is based on a characteristic time at which large scale turbulent eddies pass by the microphone sensors. This characteristic time is denoted by τ, and is given by

$$\tau = \frac{1}{F} \qquad (4)$$

where F is the characteristic frequency and is given by

$$F = \frac{U_c}{L_c} \qquad (5)$$

where U_c is the noise convection velocity and L_c is a characteristic length defined by

$$L_c = L_t + x \sin \theta \qquad (6)$$

where L_t is the width of the diffuser throat, x is the distance downstream of the diffuser throat, and θ is the diffuser angle.

The characteristic length, L_c, defined by Eq. 6, was used because the experimental data indicated that the frequencies measured scaled fairly well with L_c. This may indicate that large scale turbulent eddies are approximately of the order of the distance between the diffuser walls. L_c is the distance between the diffuser walls at the microphone sensing location for any diffuser angle.

The rate at which the large scale turbulent eddies generate acoustic energy as they pass the test sensing location can be approximated by the following equation:

$$\frac{dE}{dt} \sim -\frac{E}{\tau} \qquad (7)$$

where E is the total acoustic energy. Since t is proportional to 1/f, it follows that

$$\frac{dE}{dt} = \frac{dE}{d(1/f)} = -f^2 \frac{dE}{df}$$

and

$$-f^2 \frac{dE}{df} \sim -\frac{E}{\tau} \qquad (8)$$

Substitution of Eq. (4) into Eq. (8) and rearranging terms yields

$$\frac{dE}{E} \sim F \frac{df}{f^2} \qquad (9)$$

Integration of Eq. (9) gives

$$E = C e^{-F/f} \qquad (10)$$

The spectral acoustic energy, E_f, is related to the total acoustic energy, E, by

$$E_f = \frac{dE}{df} \qquad (11)$$

Substituting for the total acoustic energy, E, from Eq. (10) into Eq. (11) and integrating gives

$$E_f = C_\theta \frac{F}{f^2} e^{-F/f} \qquad (12)$$

Equation (12) is the distribution function that describes the distribution of spectral energy. The constant of integration, C, in Eq. (12) determines the amplitude of the spectral energy, and since the amplitude is dependent upon the flow diffusion angle, θ, C has been replaced by C_θ. Where C_θ is given by the empirical correlation equation

$$C_\theta = 556 \left(118 - \frac{10}{3}\theta\right) \qquad (13)$$

The distribution function, Eq. (12), is shown in Fig. 9 and 10 for values of C_θ at various diffuser angles. The experimental results of Fig. 5 are plotted on Fig. 9 and 10 for comparison, and indicate fair agreement of the theoretical model and the experimental results. The largest deviations occur at the small diffuser angles ($\theta < 15°$) as the frequency increases. The experimental data indicates the spectral energy decreases much faster than the theoretical distribution function would predict.

The experimental spectral results indicate that the maximum value of the spectral energy shifts towards lower frequencies as the flow diffusion angle is increased. The frequency at which the maximum value of the spectral energy occurs can be obtained by differentiating the distribution function (Eq. 12) with respect to the frequency and setting the result equal to zero. That is

$$\frac{d}{df}\left[C_\theta \frac{F}{f^2} e^{-F/f}\right] = 0$$

Performing the differentiation gives

$$f = \frac{F}{2} = \frac{U_c}{2L_c} \qquad (14)$$

For a mean convection velocity of 75 fps, Eq. (14) predicts a frequency of 150 cps for the maximum value of spectral energy at $\theta = 0$, and a frequency of 100 cps for the maximum value of spectral energy at $\theta = 30°$. Both of these theoretical predictions are in good agreement with the experimental results.

The experimental maximum values of the spectral energy correlate very well with Reid's theory (7). Reid has shown the viscous dissipation of energy in turbulent eddies is given by

$$E_f \sim K^2 \qquad (15)$$

where K is the wave number and is given by

$$K = \frac{2\pi F}{c} \qquad (16)$$

where c is the acoustic velocity. These experimentally determined maximum values of the spectral energy are presented as a function of wave number in Fig. 11. The results shown as points on Fig. 11 correlate very well with the equation:

$$E_f = 120 K^2 \qquad (17)$$

CONCLUDING REMARKS

The sound pressure level due to pressure fluctuations adjacent to the diffuser wall was observed to increase as the diffuser angle was increased, and to reach a maximum value at the separation point. The sound pressure level was as much as 28 db higher at the separation point as compared to the

sound pressure level of boundary layer flow. Separation occurred at 20° to 22°, corresponding to velocity changes from 77.5 to 106 fps. For these diffuser angles, the power spectrum was fairly flat, indicating a more uniform distribution of acoustic energy throughout the spectrum.

The magnitude of the root-mean-square wall pressure fluctuations in turbulent flow was found to be 0.0053 times the free stream dynamic pressure. This value compares fairly well with the values 0.0035 and 0.006 reported by Willmarth.

Analysis of the cross-correlation data indicated that the convection velocity of noise along the diffuser wall decreased as the diffuser angle was increased. The convection velocity was 0.83 times the free stream velocity for a diffuser angle of 0° and decreased to 0.73 times the free stream velocity for the maximum diffuser angle of 30°. This represents a 12% decrease in the convection velocity of the noise as the diffuser angle changed from 0° to 30°.

An analytical distribution function was developed to describe the spectral noise characteristics of the large scale, turbulent eddies as the flow field changes. The distribution function is

$$E_f = C_\theta \frac{F}{f^2} e^{-F/f}$$

ACKNOWLEDGEMENT

Material in this paper was adapted from a Ph.D dissertation (8).

NOMENCLATURE

A	surface area
c	speed of sound
C	constant of integration
C_θ	constant defined by Eq. (13)
E	acoustic energy
E_f	special acoustic energy
E_1, E_2	voltage
f	frequency
F	characteristic frequency
k	ratio of rms wall sound pressure fluctuations to free stream dynamic pressure
K	wave number
L	distance
L_c	characteristic length
L_t	diffuser throat width
P	sound power
P(f)	power spectrum
Q	mass flow rate
t	time
T	delay time
U_c	convection velocity
U_o	free stream velocity
x	distance downstream of diffuser throat
δ	boundary layer thickness
θ	diffuser angle
ρ	density
τ	characteristic time

REFERENCES

1. H. H. Schloemer, "Effects of Pressure Gradients on Turbulent-Boundary-Layer-Wall-Pressure Fluctuations," J. Acoust. Soc. Am., 93-113 (1966).

2. J. D. Richard, J. F. Smith, and F. H. Stephens, "Noise Analysis with a Heterodyne-Type Sonic Analyzer," IRE Trans. on Audio AU-3, No. 2, 37-42 (1955).

3. H. S. Ribner, "The Generation of Sound by Turbulent Jets," Advances in Applied Mechanics (Academic Press, New York, 1964), pp. 103-182.

4. W. W. Willmarth, "Space - Time Correlations and Spectra in a Turbulent Boundary Layer," NASA Memorandum 3-17-59W, 1-22 (1959).

5. M. J. Harrison, "Pressure Fluctuations of the Wall Adjacent to a Turbulent Boundary Layer," David Taylor Model Basin Report 1260, 1-14 (1958).

6. W. W. Willmarth, "Wall Pressure Fluctuations in a Turbulent Boundary Layer," NACA TN 4139, 1-39 (1958).

7. W. W. Ried, "The Statistical Theory of Turbulence," Northwestern University, Report 400-01-57, Sept. 1957.

8. E. F. Timpke, Ph.D dissertation, Mech. Eng. Dept., Univ. Southern Calif., Los Angeles (1966).

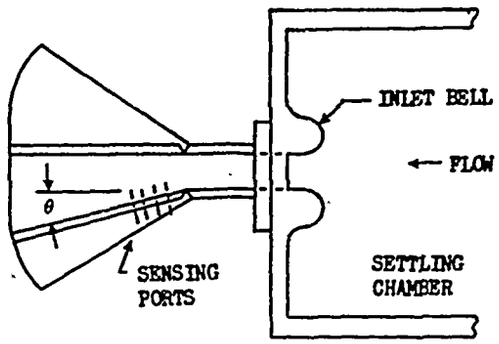

FIG. 1. FLOW SCHEMATIC OF TWO-DIMENSIONAL DIFFUSER

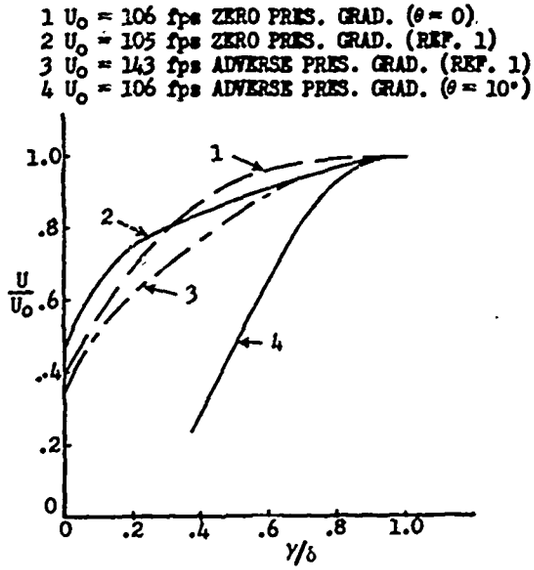

FIG. 2. TYPICAL NONDIMENSIONAL VELOCITY PROFILES

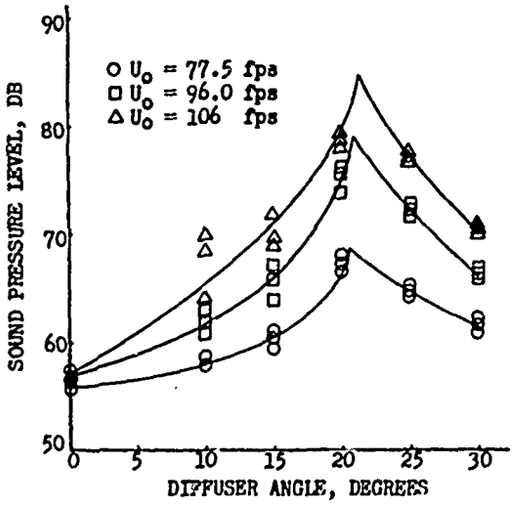

FIG. 3. SOUND PRESSURE LEVEL VERSUS DIFFUSER ANGLE

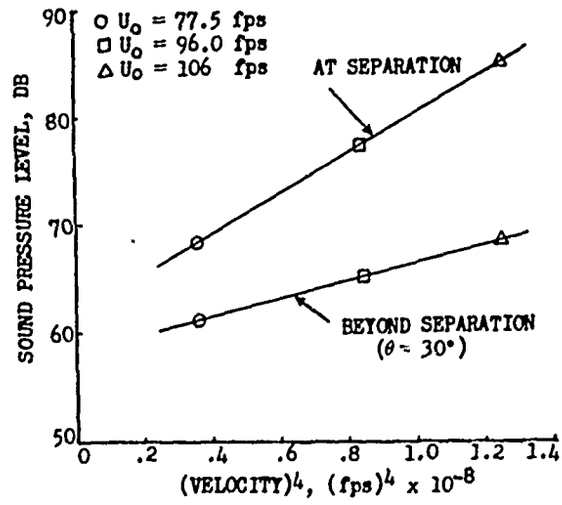

FIG. 4. SOUND PRESSURE LEVEL VERSUS THE FOURTH POWER OF VELOCITY.

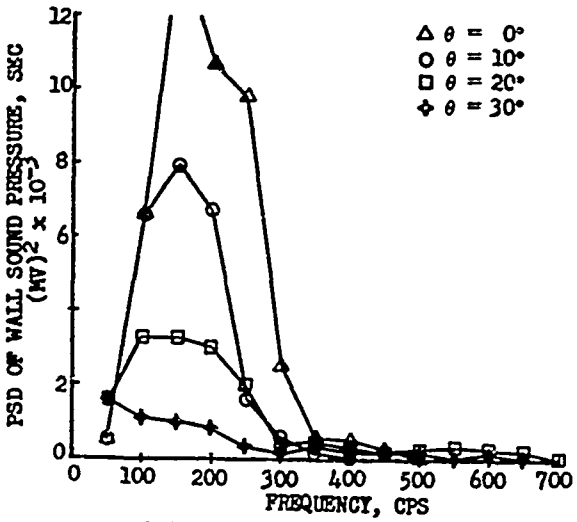

FIG. 5. POWER SPECTRAL DENSITY VERSUS FREQUENCY

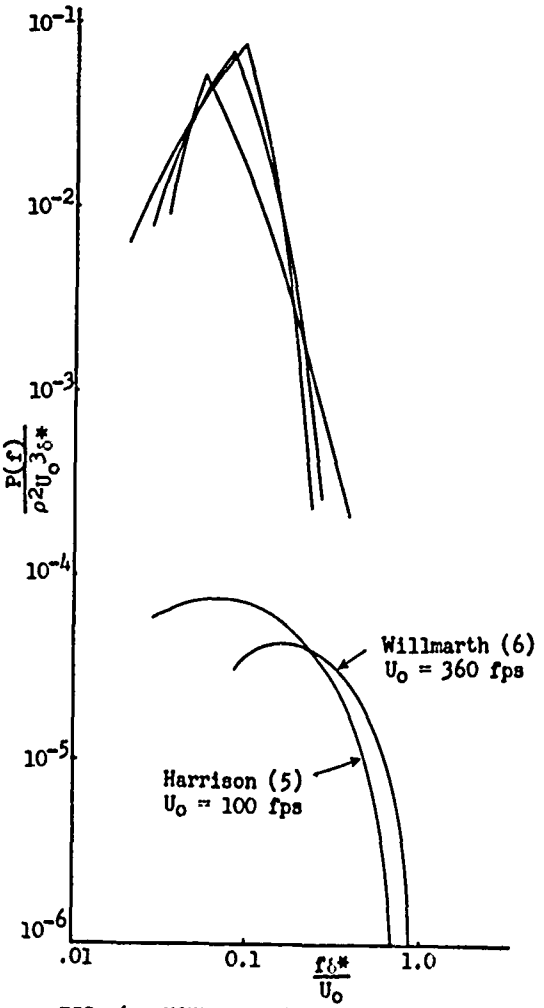

FIG. 6. NONDIMENSIONAL SPECTRAL DENSITY FOR ZERO PRESSURE GRADIENT

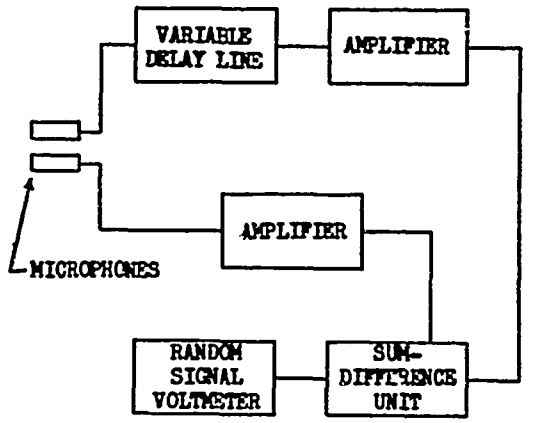

FIG. 7. BLOCK DIAGRAM OF CROSS-CORRELATION FUNCTION MEASUREMENT SYSTEM

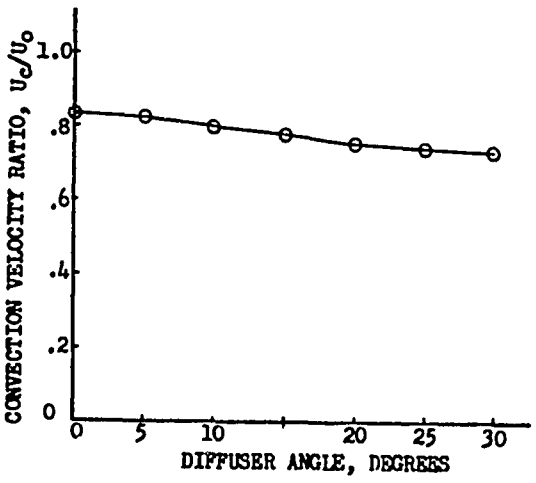

FIG. 8. CONVECTION VELOCITY OF NOISE ALONG THE DIFFUSER WALL

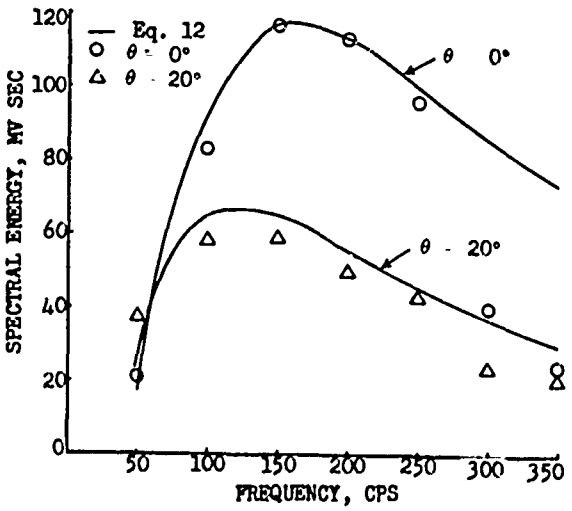

FIG. 9. COMPARISON OF THEORETICAL ENERGY DISTRIBUTION TO EXPERIMENTAL RESULTS

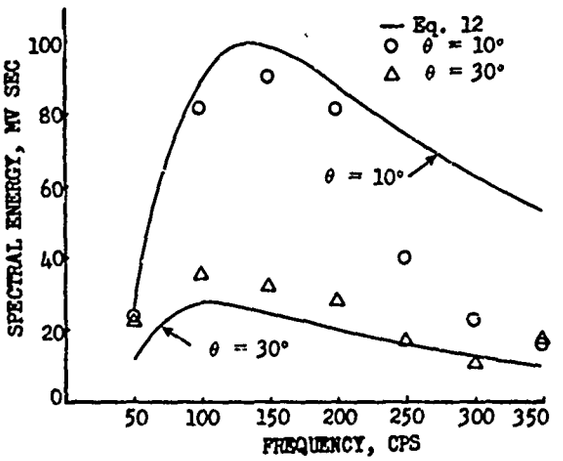

FIG. 10 COMPARISON OF THEORETICAL ENERGY DISTRIBUTION TO EXPERIMENTAL RESULTS

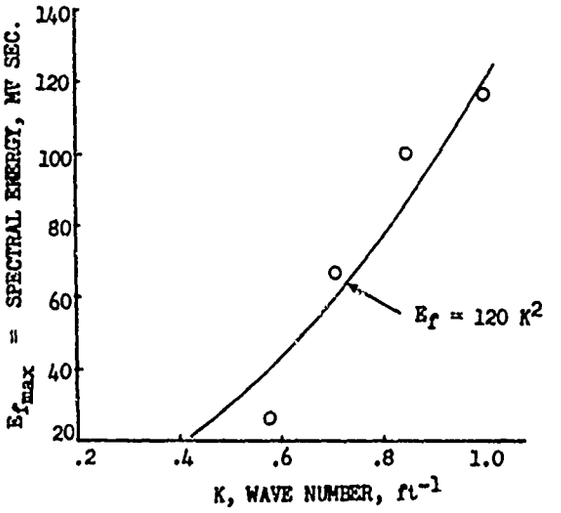

FIG. 11 MAXIMUM VALUE OF THE SPECTRAL ENERGY